

Université de Montréal

Étude de catalyseurs hydrosolubles pour la génération d'hydrogène vert par méthodes photocatalytiques

Présenté par Vincent Picard

Département de chimie, Faculté des sciences et arts

Mémoire présenté en vue de l'obtention du grade de Maître es Science

M.Sc en chimie

Août 2022

© Vincent Picard, 2022

Université de Montréal
Faculté des arts et sciences, département de chimie

Ce mémoire (ou cette thèse) intitulé(e)

Étude de catalyseurs hydrosolubles pour la génération d'hydrogène vert par méthodes photocatalytiques

Présenté par

Vincent Picard

A été évalué(e) par un jury composé des personnes suivantes

Prénom Nom
Nikolay Kornienko

Prénom Nom
Garry S. Hanan

Prénom Nom
Frank Schaper

Résumé

La synthèse de l'hydrogène est une alternative viable à l'utilisation du pétrole. Les méthodes telles que l'électrocatalyse font appel à une source d'énergie primaire, ce qui favorise les déchets générés par ces méthodes, de même que le gaspillage d'énergie. Bien qu'ayant de très faibles rendements, les systèmes photocatalytiques permettent la synthèse d'un hydrogène propre et quasi sans déchets. Une perspective permettant d'améliorer encore leur potentiel serait d'éliminer les solvants organiques tels que le DMF, qui sont nocif pour l'environnement et la santé des êtres vivants. Étant donné que le solvant doit être changé, il faut prendre garde à modifier le donneur d'électron sacrificiel et le photosensibilisateur en conséquence. La production de tels solvants est également source de pollution, ce qui atténue le potentiel environnemental de ces méthodes.

L'objectif de ce travail est de développer et de tester de nouveaux catalyseurs hydro-solubles variés permettant une amélioration des performances photo-catalytiques actuelles ainsi qu'une performance acceptable dans l'eau. L'étude des propriétés catalytiques est réalisée par l'étude de systèmes homogènes conjugués principalement avec le $[\text{Ru}(\text{bpy})_3]^{2+}$ en tant que photosensibilisateur et avec le triéthanolamine (dans le DMF) et l'acide ascorbique (dans l'eau) en tant que donneur d'électron sacrificiel. Les catalyseurs présentés lors de ce travail sont des catalyseurs à base de polypyridyl, de cobaloximes et de N-imidoylamidine.

Les catalyseurs à base de poly-pyridyl ont d'abord été étudiés puisqu'ils sont réputés pour leur performance en milieux aqueux. La seconde approche consistait à produire des catalyseurs à base de cobaloxime qui aient une performance relativement constante tout d'abord dans les solvants organiques, puis d'adapter ces performances en milieu aqueux. La troisième approche a été de tester des catalyseurs à base de N-imidoylamidine, ce type de catalyseurs n'ayant jamais été testé

pour la production d'hydrogène, puis d'en étudier les performances dans l'objectif de paver la voie pour de futures recherches sur le sujet.

Mots-clés : Catalyseurs hydrosolubles, Génération d'hydrogène, Photocatalyse, Énergie verte, Sphères de coordination, Métaux abondants, Photosynthèse artificielle, Photosensibilisateurs, chimie supramoléculaire, Développement de synthèse

Abstract

The synthesis of hydrogen is a viable alternative to the use of petroleum. Methods such as electrocatalysis use a primary energy source, which reduces the waste generated by these methods, as well as the waste of energy. Although having very low yields, photocatalytic systems allow the synthesis of clean hydrogen with virtually no waste. One prospect to further improve their potential would be to eliminate organic solvents such as DMF, which are harmful to the environment and the health of living beings. Giving the fact that we change the solvent, we need to change the electron sacrificial donor and the photosensitizer as well. The production of such solvents is also a source of pollution, which reduces the environmental potential of these methods.

The objective of this work is to develop and test various new water-soluble catalysts allowing an improvement of the current photo-catalytic performances as well as an acceptable performance in water. The study of the catalytic properties is carried out by the study of homogeneous conjugated systems mainly with $[\text{Ru}(\text{bpy})_3]^{2+}$ as photosensitizer and with triethanolamine (in DMF) and ascorbic acid (in water) as a sacrificial electron donor. The catalysts presented during this work are catalysts based on polypyridyl, cobaloximes, and N-imidoylamidine.

Poly-pyridyl-based catalysts were first studied because they are known for their performance in aqueous media. The second approach was to produce cobaloxime-based catalysts that had relatively constant performance first in organic solvents and then to match this performance in aqueous media. The third approach was to test catalysts based on N-imidoylamidine, as this type of catalyst have never been tested to produce hydrogen, then to study their performance to pave the way for future research on the subject.

Keywords: Hydrosoluble catalysts, Hydrogen generation, Photocatalyse, Green energy, Coordination sphere, abundants metals, artificial photosynthesis, Photosensitiser, Supramolecular chemistry, synthesis development

Table des matières

1) Chapitre 1 – Introduction	25
1.1 L'énergie dans la nature et la civilisation	25
1.1.1 L'énergie dans notre monde	25
1.1.2 Pourquoi l'hydrogène.....	29
1.1.3 La photosynthèse naturelle et artificielle	32
1.1.4 Méthodes de production : Un bref aperçu	38
1.1.5 Méthodes d'entreposage : Un bref aperçu.....	44
1.2 Partie 2 : La génération d'hydrogène dans l'eau.....	48
1.2.1 Objectifs de la génération de l'hydrogène dans l'eau	48
1.2.2 Mécanismes réactionnels impliqués.....	49
1.2.3 La photocatalyse dans l'eau	54
1.2.4 Aperçu des systèmes utilisés	55
1.2.5 Limites actuelles du domaine.....	61
2) Chapitre 2 – Synthesis, structure, and hydrogen evolution studies of a heteroleptic Co (III) complex	73
2.1 Abstract.....	73
2.2 Introduction	75
2.3 Experimental.....	77
2.3.1 Materials and physical measurements.....	77
2.3.2 Physical measurements	77
2.3.3 Synthesis and physical measurements of the cobalt(III) complex	78

2.3.4 X-ray crystallography.....	79
2.3.5 Photocatalytic measurements	79
2.4 Results and discussion.....	81
2.4.1 Synthesis.....	81
2.4.2 HRMS analysis.....	81
2.4.3 ^1H and ^{59}Co NMR spectroscopic studies.....	81
2.4.4 UV-visible spectroscopic studies	84
2.4.5 X-ray crystallography.....	85
2.4.6 Electrochemical studies.....	87
2.4.7 Electrocatalytic studies.....	93
2.4.8 Photocatalytic studies.....	94
2.5 Conclusions	96
2.5.1 Acknowledgements	96
2.5.2 References	97
2.6 Supporting Information	100
3) Chapitre 3 – N-substituted 2-pyridinecarbothioamides and polypyridyl mixed-ligand cobalt(III)-containing complexes for photocatalytic hydrogen generation	116
3.1 A B S T R A C T	116
3.2 Introduction	119
3.3 Experimental.....	123
3.3.1 Materials and physical measurements.....	123
3.3.2 DFT calculations	125
3.3.3 Photocatalytic measurements	125
3.3.4 Synthesis of the ligands and cobalt(III) complexes	126

3.3.5	X-ray crystallography.....	129
3.3.6	Results and discussion.....	130
3.4	Conclusions	143
3.5	Declaration of Competing Interest	144
3.6	Acknowledgements	144
3.7	References	145
3.8	Supporting Information	152
3.8.1	General Procedures	152
3.8.2	Additional data	154
3.8.3	Set up of gas chromatography	162
4)	Chapitre 4: Efficient Ru/Co molecular photocatalytic system driven by cyclohexyl-based cobaloximes as HER catalysts.....	166
4.1	Abstract.....	166
4.2	Introduction	169
4.3	Results and discussion	171
4.3.1	Synthesis and NMR analysis.....	171
4.3.2	Crystallographic description	173
4.4	Electrochemistry	175
4.4.1	Spectro-electrochemistry.....	178
4.4.2	Photocatalytic hydrogen evolution.....	180
4.5	Conclusion	184
4.6	Experimental details	185
4.6.1	Synthesis.....	185
4.7	Acknowledgment.....	186

4.8	Conflict of interests	187
4.9	References	187
4.10	Supporting information.....	192
4.10.1	Electrochemistry.....	193
4.10.2	Cyclic voltammetry	194
4.10.3	Spectro-electrochemistry.....	196
4.10.4	Crystallographic study.....	199
4.10.5	Preparation of photoreactions and set up of gas chromatography	206
4.10.6	NMR studies.....	207
4.10.7	References	212
5)	Chapitre 5 - Properties and hydrogen evolution of N-imidoylamidine ligand cobalt(II) containing complexes.....	213
5.1	Abstract.....	213
5.2	Introduction:	215
5.3	Results and discussion	217
5.3.1	Electrochemistry.....	217
5.4	Spectro-Electrochemistry	219
5.4.1	Photocatalytic hydrogen evolution.....	221
5.5	Conclusion	229
5.6	Acknowledgment.....	230
5.7	Bibliography	230
5.8	Supporting information.....	233
5.8.1	Synthesis.....	234
5.8.2	Electrochemistry.....	235

5.8.3	Cyclic voltammetry	235
5.8.4	Spectro-electrochemistry.....	238
5.8.5	Preparation of photoreactions and set up of gas chromatography	244
6)	Chapitre 6 – Conclusions et perspectives	253
6.1	Sommaire.....	253
6.2	Perspectives	255
6.3	Références bibliographiques.....	261

Liste des tableaux

Tableau 1. – Crystal data and structure refinement parameters for [Co(tpy)(phen)Cl](PF ₆) ₂ •0.5CH ₃ CN.....	86
Tableau 2. – Selected bond lengths and angles for [Co(tpy)(phen)Cl](PF ₆) ₂ •0.5CH ₃ CN.	87
Tableau 3. – Comparison of the reduction potentials of complex 1 in H ₂ O and CH ₃ CN with various supporting electrolytes.....	89
Tableau 4. – ⁵⁹ Co NMR spectroscopic data of selected complexes in the respective solvents.	
	101
Tableau 5. – Emission maxima and amplitude of LED light.	114
Tableau 6. – Crystallographic data for the PCA-(CF ₃) ₂	130
Tableau 7. – Redox potentials of the cobalt couples of [Co(N-N) ₂ Cl ₂]PF ₆ and [Co(N-N) ₂ (PCA-(CF ₃) ₂](PF ₆)xH ₂ O in CH ₃ CN at a glassy carbon working electrode vs Ag/AgCl in CH ₃ CN.....	138
Tableau 8. – Emission maxima and amplitude of the LED light.	164
Tableau 9. – Electrochemical potentials (in V vs Fc/Fc ⁺ in DMF) ^a	177
Tableau 10. – Report of interest points of spectro-Echem analysis on complex 1 to 4	199
Tableau 11. – Crystallographic information's for Co(chgH) ₂ (dmap)Cl, (4).....	200
Tableau 12. – Selected angles and bond lengths of crystal structures Co(III)(ChgH) ₂ ClDMAP, the dimer Co(III)(ChgH) ₂ Cl ₂ (4-4bipyridine) and an other structure of the dimer Co(III)(ChgH) ₂ Cl ₂ (4-4bipyridine).	204
Tableau 13. – Maxima, width band of emission spectra, and photon flux of used L.E.D.'s ...	207
Tableau 14. – Electrochemical potentials of the studied complexes (in V vs Fc/Fc ⁺ in DMF) 218	
Tableau 15. – Hydrogen Production Results under Blue-Light Irradiation, vs HEC (450 nm, 62 mW) in DMF	224
Tableau 16. – Hydrogen Production Results under Blue-Light Irradiation, vs PS (450 nm, 62 mW) in DMF	226
Tableau 17. – Hydrogen Production Results under Blue-Light, vs HEC (450 nm, 62 mW) in water	228

Liste des figures et équations

Figure 1.	Concentration du CO ₂ atmosphérique en fonction du temps ¹	26
Figure 2.	Illustration des réserves énergétiques mondiales (figure reproduite avec la permission, référence 14)	28
Figure 3.	Spectre de l'énergie solaire reçu par la terre ¹³	29
Figure 4.	Génération et combustion de l'hydrogène.....	30
Figure 5.	Explosion du dirigeable d'Hindenburg, en 1937, à Lakehurst, New Jersey ¹⁷	31
Figure 6.	Équation simplifiée de la photosynthèse naturelle	32
Figure 7.	Spectre d'absorption des photosensibilisateurs impliqués dans la photosynthèse naturelle ²³	33
Figure 8.	<i>Représentation de la chaîne de réactions impliqués dans la photosynthèse naturelle</i> ²⁴	
	34
Figure 9.	<i>Quelques molécules impliquées dans la photosynthèse naturelle</i>	35
Figure 10.	<i>Schéma de la photosynthèse artificielle</i> ²⁶	36
Figure 11.	<i>Aperçu des différentes méthodes pour la production de l'hydrogène et leur utilité prévue</i> ²⁸	38
Figure 12.	Équations chimiques impliqués dans le reformatage du méthane	39
Figure 13.	Équations chimiques impliqués dans l'électrolyse	42
Figure 14.	<i>Exemples de transporteurs d'hydrogènes étudiés dans la littérature scientifique</i> ⁵¹⁻⁵³	
	45
Figure 15.	<i>Distinction des mécanismes homolytiques et hétérolytiques</i>	50
Figure 16.	<i>Mécanisme hétérolytique de génération d'hydrogène</i> ⁷²	51
Figure 17.	<i>Types de mécanismes hétérolytiques</i> ⁷¹	52
Figure 18.	<i>Voie oxydative et réductive pour l'altération du catalyseur</i>	53
Figure 19.	<i>Catalyseurs à base de cobaloxime (1⁷⁰, 2⁷⁰, 3⁸⁸, 4⁸⁹, 5⁹⁰)</i>	57
Figure 20.	<i>Catalyseurs à base de porphyrine (1⁹¹, 2⁷⁵, 3⁹⁴, 4⁹⁵, 5⁹³, 6⁹²)</i>	58
Figure 21.	<i>Catalyseurs à base de Salen et de dérivés (1,2⁹⁶ 3⁹⁷ 4⁹⁸ 5⁹⁹)</i>	60
Figure 22.	<i>Catalyseurs à base de poly-pyridyl et de dérivés (1⁸⁰ 2¹⁰⁰ 3⁸¹ 4⁷⁹ 5⁸³)</i>	61

Figure 23.	Comparaison entre l'énergie solaire produite et les besoins en énergie du Québec ¹¹⁴	63
Figure 24.	Some examples of cobalt complexes utilised in the catalytic hydrogen evolution reaction.	76
Figure 25.	Synthesis of complex 1 .	81
Figure 26.	¹ H NMR spectra of complex 1 in CD ₃ CN (A) and DMSO- <i>d</i> ₆ (B), and ⁵⁹ Co NMR spectrum of 40 mM complex 1 in CD ₃ CN (C).	83
Figure 27.	UV-visible spectrum of complex 1 in acetonitrile (400-600 nm enhanced view shown in inset).	84
Figure 28.	Structure for the <i>mer</i> -[Co(tpy)(phen)Cl] ²⁺ complex as shown at 50% probability ellipsoids.	85
Figure 29.	A plausible redox behaviour of complex 1 in CH ₃ CN.	89
Figure 30.	Cyclic voltammogram of complex 1 . Solvent = acetonitrile, [complex] = 1.0 mM, [ⁿ Bu ₄ N]ClO ₄ = 0.10 M, working electrode = (A) glassy carbon or (B) Pt, auxiliary electrode = Pt wire, reference electrode = Ag/AgCl, and scan rate = 100 mV s ⁻¹ .	90
Figure 31.	Spectroelectrochemical transformations of complex 1 . Solvent = acetonitrile, [complex] = 14.9 mM, [ⁿ Bu ₄ N]ClO ₄ = 0.10 M, working electrode = Pt mesh wire, auxiliary electrode = Pt wire, reference electrode = Ag/AgCl, held potential = -1.20 V (top) and -1.52 V (bottom), and path length = 1 mm.	92
Figure 32.	Cyclic voltammograms illustrating the electrocatalytic behaviour of complex 1 . Solvent = acetonitrile, [complex] = 1.0 mM, [ⁿ Bu ₄ N]ClO ₄ = 0.10 M, working electrode = glassy carbon, auxiliary electrode = Pt wire, reference electrode = Ag/AgCl, and scan rate = 100 mV s ⁻¹ . The concentration of <i>p</i> -cyanoanilinium tetrafluoroborate was varied from 0.0 mM to 10 mM.	93
Figure 33.	Hydrogen evolution of [Co(dmgH) ₂ Cl(py)] (black) and complex 1 (green). TOF: dotted line. TON: solid line.	95
Figure 34.	ESI MS of [Co(tpy) ₂](PF ₆) _{2/3} in CH ₃ CN.	102
Figure 35.	¹ H NMR spectrum of [Co(tpy) ₂](PF ₆) _{2/3} in CD ₃ CN.	103
Figure 36.	⁵⁹ Co NMR spectrum of [Co(tpy) ₂](PF ₆) ₃ in CD ₃ CN.	104
Figure 37.	¹ H NMR spectra of [Co(tpy) ₂](PF ₆) _{2/3} and [Co(tpy)(phen)Cl](PF ₆) ₂ •0.25CH ₃ CN 1 in CD ₃ CN.	105

Figure 38. HRMS of complex 1 in CH ₃ CN.....	106
Figure 39. ¹ H NMR spectra of complex 1 in DMSO- <i>d</i> ₆	107
Figure 40. ¹ H- ¹ H COSY NMR spectrum of complex 1 in CD ₃ CN.....	108
Figure 41. UV-visible spectra of complex 1 in acetonitrile or a mixture of water:acetonitrile (1:1, v/v) with different sodium salts.....	108
Figure 42. Cyclic voltammograms of [Co(tpy)(phen)Cl]Cl ₂ . Solvent = acetonitrile:water (1:1, v/v), [complex] = 1.0 mM, supporting electrolyte = 0.1 M (NaClO ₄ (black) or NaCl (red)), working electrode = Pt, auxiliary electrode = Pt wire, reference electrode = Ag/AgCl, and scan rate = 100 mV s ⁻¹	109
Figure 43. Cyclic voltammograms of [Co(tpy)(phen)Cl]Cl ₂ . Solvent = water, [complex] = 1.0 mM, supporting electrolyte = 0.1 M (NaClO ₄ (black) or NaCl (red)), working electrode = Pt, auxiliary electrode = Pt wire, reference electrode = Ag/AgCl, and scan rate = 100 mV s ⁻¹	110
Figure 44. Cyclic voltammogram of complex 1 . Solvent = acetonitrile, [complex] = 1.0 mM, [ⁿ Bu ₄ N]ClO ₄ = 0.10 M, working electrode = either Pt or glassy carbon, auxiliary electrode = Pt wire, reference electrode = Ag/AgCl, and scan rate = 100 mV s ⁻¹	111
Figure 45. Spectroelectrochemical spectra of [Co(tpy)(phen)Cl](PF ₆) ₂ •0.25CH ₃ CN 1 . Solvent = acetonitrile, [complex] = 13.3 mM, [ⁿ Bu ₄ N]ClO ₄ = 0.10 mM, working electrode = Pt mesh wire, auxiliary electrode = Pt wire, reference electrode = Ag/AgCl, and held potential = 0.50 V.....	112
Figure 46. Spectroelectrochemical spectra of [Co(tpy)(phen)Cl](PF ₆) ₂ •0.25CH ₃ CN 1 with the supporting electrolyte NaClO ₄ (A and B) or NaCl (C and D) in H ₂ O:CH ₃ CN (1:1, v/v). [complex] = 0.9 – 10.3 mM, [supporting electrolyte] = 0.1 M, working electrode = Pt, auxiliary electrode = Pt wire, and reference electrode = Ag/AgCl.	113
Figure 47. Emission spectrum of blue LED.....	114
Figure 48. Restart of hydrogen evolution of [Co(dmgH) ₂ Cl(py)] (black) and complex 1 (olive) by the addition of fresh photosensitizer (1.25 ml of 0.4 mM [Ru(bpy) ₃](PF ₆) ₂) at the end of activity. TOF: dotted line. TON: solid line.	115
Figure 49. First row transition metal complexes containing either a thiosemicarbazone ligand or polypyridyl ligands [68,72,73].	124
Figure 50. Synthesis of N-(3,5-bis(trifluoromethyl)phenyl)pyridine-2-carbothioamide (PCA-(CF ₃) ₂)	132

Figure 51. Synthesis of complexes 1-4.....	132
Figure 52. Structure of PCA-(CF ₃) ₂ shown as 50% probability ellipsoids. Minor components of the CF ₃ disorder are omitted for clarity.....	134
Figure 53. UV-visible spectra of PCA-(CF ₃) ₂ and complexes 3 and 4 in CH ₃ CN (inset: 300-500 nm expanded view).	135
Figure 54. HOMO-LUMO plots for complex 3.	136
Figure 55. Cyclic voltammograms of complexe 3 (top) and 4 (bottom) in CH ₃ CN with increasing [<i>p</i> -cyanoanilinium tetrafluoroborate]. [complex] = 1.1 mM, supporting electrolyte = 0.1M tetrabutylammonium perchlorate ([ⁿ Bu ₄ N]ClO ₄). Scan rate = 100mV s ⁻¹	141
Figure 56. Mechanism for protonation, electron transfert, and hydrogen evolution.....	143
Figure 57. Hydrogen evolution with [Co(dmgH) ₂ (py)Cl] (black), complex 3 (purple), and complex 4 (green). TOF: dotted line. TON: solid line.....	143
Figure 58. . ESI MS of complexes 3 and 4 in CH ₃ CN	154
Figure 59. FTIR spectra of PCA-(CF ₃) ₂ , complex 3, and complex 4.....	155
Figure 60. ¹ H NMR spectrum of PCA-(CF ₃) ₂ in DMSO- <i>d</i> ₆	156
Figure 61. Crystals of PCA-(CF ₃) ₂	156
Figure 62. Packing of molecules in PCA-(CF ₃) ₂ , viewed along the <i>b</i> -axis.....	157
Figure 63. ¹ H NMR spectra of PCA-(CF ₃) ₂ , and complex 3, and complex 4 in DMSO-d ₆	158
Figure 64. ¹³ C NMR spectra of PCA-(CF ₃) ₂ , and complex 3, and complex 4 in DMSO-d ₆	159
Figure 65. ¹⁹ F NMR spectra of PCA-(CF ₃) ₂ , and complex 3, and complex 4 in DMSO-d ₆ . ..	160
Figure 66. Cyclic voltammograms of 1.0 mM (PCA-(CF ₃) ₂ , <i>bpy</i> , and <i>phen</i> in CH ₃ CN at a glassy carbon working electrode vs Ag/AgCl. Supporting electrolyte = 0.1 M ([ⁿ Bu ₄ N]ClO ₄) and scan rate = 100 mV s ⁻¹	161
Figure 67. Cyclic voltammograms of complexes 1-6 in CH ₃ CN. [complex] = 1.0 mM, supporting electrolyte = 0.1 M ([ⁿ Bu ₄ N]ClO ₄), and scan rate = 100 mV s ⁻¹	162
Figure 68. Emission spectrum of the blue LED.	164
Figure 69. Restart of hydrogen evolution of [Co(dmgH) ₂ Cl(py)] (black), complex 3 (purple), and complex 4 (olive) by the addition of photosensitizer (1.25 ml of 0.4 mM Ru(bpy) ₃ (PF ₆) ₂) at the end of activity. TOF: dotted line. TON: solid line.....	165
Figure 70. cobaloximes catalysts used in the present study	171

Figure 71. Comparison of the different NMR- ¹ H spectra of the catalysts realized in deuterated chloroform)	173
Figure 72. View of the Co(chgH) ₂ Cl(DMAP), atoms are represented at the 50 % probability level.	174
Figure 73. Voltammograms of Co(chgH) ₂ (pyr)Cl (V vs Fc ⁺ /Fc).	177
Figure 74. Turn Over Frequency of hydrogen evolution for Ru(bpy) ₃ ²⁺ in association with cobaloxime catalysts 1 in red, 2 in orange, 3 in green, and 4 in blue.	180
Figure 75. Turn Over Number of hydrogen evolution for Ru(bpy) ₃ ²⁺ in association with cobaloxime catalysts 1 in red, 2 in orange, 3 in green, and 4 in blue.	181
Figure 76. Reduction voltammograms of Co(dmgH) ₂ (pyr)Cl in DMF with triethylammonium PF ₆ as supporting electrolyte	194
Figure 77. Reduction voltammograms of Co(dmgH) ₂ (DMAP)Cl in DMF with triethylammonium PF ₆ as supporting electrolyte	194
Figure 78. Reduction voltammograms of Co(chgH) ₂ (pyr)Cl in DMF with triethylammonium PF ₆ as supporting electrolyte	195
Figure 79. Reduction voltammograms of Co(chgH) ₂ (DMAP)Cl in DMF with triethylammonium PF ₆ as supporting electrolyte	195
Figure 80. Reduction voltammograms of Co(chgH) ₂ Cl ₂ in DMF with triethylammonium PF ₆ as supporting electrolyte	196
Figure 81. Spectro-electrochemistry spectra of the Co(dmgH) ₂ (Pyr)Cl	197
Figure 82. Spectro-electrochemistry spectra of the Co(dmgH) ₂ (DMAP)Cl	197
Figure 83. Spectro-electrochemistry spectra of the Co(chgH) ₂ (Pyr)Cl.....	198
Figure 84. Spectro-electrochemistry spectra of the Co(chgH) ₂ (DMAP)Cl.....	198
Figure 85. View of the Co(chgH) ₂ (DMAP)Cl with hydrogen atoms, atoms are represented at the 50 % probability level. The disorder of position for cyclohexyl conformers is illustrated by two conformers that are modelized with different occupancies.....	201
Figure 86. View of the Co(chgH) ₂ (DMAP)Cl with hydrogen atoms, atoms are represented at the 50 % probability level. The disorder of position for cyclohexyl conformers is illustrated by two conformers that are modelized with different occupancies.....	202

Figure 87. Orientation of N-Heterocycle on cobaloxime derivatives. View of the Co(chgH) ₂ (DMAP)Cl with an indication of the torsion angle between Co-NOxime and C-N of DMAP. Plan 1 describes the commonly observed orientation of 6 membered N-heterocycle on the cobaloxime crystal structure ^[9] . Plan 2 is rare.	205
Figure 88. NMR-H ¹ of the Co(dmgH) ₂ (pyr)Cl.....	208
Figure 89. NMR-H ¹ of the Co(dmgH) ₂ (dmap)Cl.....	209
Figure 90. NMR-H ¹ of the Co(chgH) ₂ (pyr)Cl.....	210
Figure 91. NMR-H ¹ of the Co(chgH) ₂ (dmap)Cl	211
Figure 92. 2D ¹ HNMR Noesy of Co(chgH)2PyrCl CDCl ₃ 400 MHZ. The resolution of the scalar coupling has been decreased to notice the most intense coupling between the protons on the β -carbon positions and δ -carbon of the cyclohexyl moiety.	212
Figure 93. Structure of N-imidoylamidine (ImAm) ligands, catalysts and photosensitiser presented herein.....	216
Figure 94. Spectro-electrochemistry spectra of the [Co ^{II} (Py ₂ ImAm) ₂ Cl ₄] from -2 to 1.6 V..	220
Figure 95.Spectro-electrochemistry spectra of the [Co ^{II} ₃ (Pm ₂ ImAm) ₂ Cl ₄] x5H ₂ O from -2 to 1.8 V ..	221
Figure 96. TON and TOF of Co(Py ₂ ImAm) ₂ (orange, 1-2),Co(dmgH) ₂ Cl ₂ (black, 2-2) and Co ₃ (Pm ₂ ImAm) ₂ x5H ₂ O (green, 3-3) in DMF with 1.0x10 ⁻⁴ M of [Ru(bpy) ₃] ²⁺	223
Figure 97. TON and TOF of Co(Py ₂ ImAm) ₂ (blue) with 25% water and DMF as solvent and Co ₃ (Pm ₂ ImAm) ₂ x5H ₂ O (green) in water with 1.0x10 ⁻⁴ M of [Ru(bpy) ₃] ²⁺	229
Figure 98. Reduction voltammograms of Co(dmgH) ₂ (pyr)Cl in DMF with triethylammonium PF ₆ as supporting electrolyte	235
Figure 99. Reduction voltammograms of Co(dmgH) ₂ (pyr)Cl in DMF with triethylammonium PF ₆ as supporting electrolyte	236
Figure 100. Reduction voltammograms of Co(Py ₂ ImAm) ₂ in DMF with triethylammonium PF ₆ as supporting electrolyte	236
Figure 101. Reduction voltammograms of Co ₃ (Pm ₂ ImAm) ₂ in DMF with triethylammonium PF ₆ as supporting electrolyte	237
Figure 102. Square wave voltammograms of Co(Py ₂ ImAm) ₂ in DMF with triethylammonium PF ₆ as supporting electrolyte	237

Figure 103. Square wave voltammograms of $\text{Co}_3(\text{Pm}_2\text{ImAm})_2$ in DMF with triethylammonium PF ₆ as supporting electrolyte.....	238
Figure 104. Spectro-electrochemistry spectra of the $[\text{Co}^{\text{II}}(\text{Py}_2\text{ImAm})_2\text{Cl}_4]$ from 0 to -2v	239
Figure 105. Spectro-electrochemistry spectra of the $[\text{Co}^{\text{II}}(\text{Py}_2\text{ImAm})_2\text{Cl}_4]$ from 0 to 1.6v ..	240
Figure 106. Zoom-in of the spectro-electrochemistry spectra of the $[\text{Co}^{\text{II}}(\text{Py}_2\text{ImAm})_2\text{Cl}_4]$ (0 to 1.6v)	240
Figure 107. Spectro-electrochemistry spectra of the $[\text{Co}^{\text{II}}(\text{Py}_2\text{ImAm})_2\text{Cl}_4]$ from -2 to 1.6v	241
Figure 108. Spectro-electrochemistry spectra of the $[\text{Co}^{\text{II}}_3(\text{Pm}_2\text{ImAm})_2\text{Cl}_4] \times 5\text{H}_2\text{O}$ from 0 to -2v	242
Figure 109. Spectro-electrochemistry spectra of the $[\text{Co}^{\text{II}}_3(\text{Pm}_2\text{ImAm})_2\text{Cl}_4] \times 5\text{H}_2\text{O}$ from 0 to 1.8v	243
Figure 110. Spectro-electrochemistry spectra of the $[\text{Co}^{\text{II}}_3(\text{Pm}_2\text{ImAm})_2\text{Cl}_4] \times 5\text{H}_2\text{O}$ from -2 to 1.8v	244
Figure 111. Turn Over Frequency of hydrogen evolution for $\text{Co}(\text{dmgH}_2)\text{Cl}_2$ in association with $1 \times 10^{-4}\text{M} [\text{Ru}(\text{bpy})_3]^{2+}$ in DMF	245
Figure 112. Turn Over Frequency of hydrogen evolution for $\text{Co}(\text{Py}_2\text{ImAm})_2\text{Cl}_2$ in association with $1 \times 10^{-4}\text{M} [\text{Ru}(\text{bpy})_3]^{2+}$ in DMF	246
Figure 113. Turn Over Frequency of hydrogen evolution for $\text{Co}_3(\text{Pm}_2\text{ImAm})_2\text{Cl}_2$ in association with $1 \times 10^{-4}\text{M} [\text{Ru}(\text{bpy})_3]^{2+}$ in DMF	247
Figure 114. Turn Over Frequency of hydrogen evolution for $1 \times 10^{-4}\text{M}$ catalyst ($5 \times 10^{-5}\text{M}$ for $\text{Co}_3(\text{Pm}_2\text{ImAm})_2$) in association with $1 \times 10^{-4}\text{M} [\text{Ru}(\text{bpy})_3]^{2+}$ in DMF	248
Figure 115. Turn Over Frequency of hydrogen evolution for $1 \times 10^{-5}\text{M}$ catalyst in association with $1 \times 10^{-4}\text{M} [\text{Ru}(\text{bpy})_3]^{2+}$ in DMF	249
Figure 116. Turn Over Frequency of hydrogen evolution for $1 \times 10^{-6}\text{M}$ catalyst in association with $1 \times 10^{-4}\text{M} [\text{Ru}(\text{bpy})_3]^{2+}$ in DMF	250
Figure 117. Turn Over Frequency of hydrogen evolution for $1 \times 10^{-5}\text{M} \text{ Co}(\text{Py}_2\text{ImAm})_2$ in association with $1 \times 10^{-4}\text{M} [\text{Ru}(\text{bpy})_3]^{2+}$ in DMF, with different amounts of water.....	251
Figure 118. Turn Over Frequency of hydrogen evolution for $\text{Co}_3(\text{Pm}_2\text{ImAm})_2$ in association with $1 \times 10^{-4}\text{M} [\text{Ru}(\text{bpy})_3]^{2+}$ in water.....	252

Figure 119. Structure des catalyseurs cobaloxime à base de sels de potassium prévue dans un projet précédent	255
Figure 120. Structure rayon-x et chemdraw de la molécule obtenue vs la molécule attendue	256
Figure 121. Chemin réactionnel envisagé pour l'obtention du catalyseur aquasoluble à base de cobaloxime	257
Figure 122. Structure des catalyseurs à base de cobaloxime avec fonctions hydrosolubles intégrés	259
Figure 123. Structure proposée par l'auteur pour de futures expériences	260

Liste des sigles et abréviations

°C : Degré Celsius

α : Alpha

ATP : Adénosine triphosphate

COP26 : Conférence de Glasgow de 2021 sur les changements climatiques

EJ : Exajoules (multiplicateur 10^{18} Joules)

ET-PT : Electron transfert-Proton transfert

EY²⁻ : Eosin Y

G20 : Sommet des 20 pays à l'économie la plus développée mondialement

GES : Gaz à effets de serre

HEC : Hydrogen Evolution Catalyst

L-PCET : Ligands-Proton Coupled Electron Transfert

M-PCET : Metal-Proton Coupled Electron Transfert

NADH : Nicotinamide adénine dinucléotide

NADPH : Nicotinamide adénine dinucléotide phosphate

P680: Chlorophylle qui absorbe l'énergie à 680nm

pH : proportion d'hydrogène

PS : Photosensibilisateur

PT-ET : Proton Transfert-Electron Transfert

SED : Sacrificial Electron Donor (donneur d'électron sacrificiel)

TEA : Triethylamine

TEOA : Triethanolamine

TOF : Turn Over Frequency

TON : Turn Over Number

TW : Térawatt (multiplicateur 10^{12} watt)

UV : Ultra Violet

An investment in knowledge pays the best interest.

Benjamin Franklin



Remerciements

Tout d'abord, je tiens à remercier Dr. Garry S. Hanan pour sa confiance et son support. N'étant pas étudiant à l'université de Montréal et étant plutôt difficile d'approche, il a tout de même décidé de m'accorder un stage dans son laboratoire. Il m'a également permis de découvrir ce que sont les études graduées par la participation aux conférences, aux défenses de thèses, aux séminaires ainsi que par l'étude de plusieurs projets stimulants et innovateurs. Je souhaite le remercier chaleureusement pour son implication à la fois dans mon développement scolaire et intellectuel que dans mon développement culturel et social.

Je souhaite ensuite remercier les organismes de financements qui m'ont soutenu et qui ont rendue possible mes recherches. Il faut d'abord citer le CRSNG et le FRQNT, qui m'ont tous deux offert des financements de recherche annuels. Ensuite, je souhaite remercier le FESP ainsi que la banque nationale, pour leurs contributions financières, qui m'ont permis de poursuivre mes études avec un niveau d'anxiété plus léger.

Je souhaite également remercier mes proches, soit mes parents, ma fiancée ainsi que mes sœurs et ma belle-famille pour leur soutien moral et leurs curiosités par rapport à mes recherches. Ils ont partagé la joie de mes succès de même que les difficultés rencontrées.

Je souhaite ensuite remercier chaleureusement Olivier Schott, Georges Turner, Thomas Auvray et Frank Schaper pour leur aide, leurs connaissances ou leurs idées ayant contribués indirectement à l'une ou l'autre des sections de ce mémoire. Je souhaite également remercier chaleureusement Daniel Chartrand, Mira Rupp, Fatemeh Dordahan, Guillaume Poissant, Natali Shevchenko, Lucas Morick, Quentin Dusties Touloumet, Simon De Kreijger et Abdullah Abu-Dayyeh que ce soit pour de l'aide dans le laboratoire, la compréhension des phénomènes chimiques, des idées ou même pour les conversations intéressantes autour d'une bonne bière.

1) Chapitre 1 – Introduction

1.1 L'énergie dans la nature et la civilisation

1.1.1 L'énergie dans notre monde

Aux vues des impacts des changements climatiques, il devient primordial de diversifier et de décarboner notre énergie. Il est d'évidence que des changements climatiques sont opérés dans nos sociétés, une situation sans précédent pour notre espèce qui semble attestée par les étés suffocants et l'augmentation drastique du nombre d'inondation à chaque année. Le taux de CO₂ mesuré (414.72ppm en date du 2021-01-12) n'a jamais été aussi haut dans le cycle annuel et continue d'augmenter à chaque année.¹ Le Québec n'est pas innocent à ces changements, en ce qu'il produit annuellement environ 80 mégatonnes de CO₂.² Pour faire face à ces changements au Québec, les principaux secteurs à cibler sont respectivement les transports (43.3% des GES), les rejets industriels (30,5% des GES) et l'entretien des bâtiments (10.3% des GES).² Des efforts sont consentis à la lutte contre les changements climatiques, alors que plusieurs puissances mondiales ont acceptés de réduire leurs émissions de GES de 37,5% d'ici 2030. Alors que la transition énergétique est entamée dans le monde, le Québec avait déjà réduit ses émissions de 9,1% en 2016, au contraire du Canada qui les a augmentées d'environ 15%.³ Il faut dire que l'enjeu climatique, intimement lié à l'enjeu énergétique fait couler beaucoup d'encre. Les protocoles et engagements se sont multipliés, depuis le protocole de Kyoto en 1997. Il y a eu l'accord de Paris en 2015⁴, le G20 en 2019 et maintenant le COP26 en 2022, pour ne citer que les plus connus.

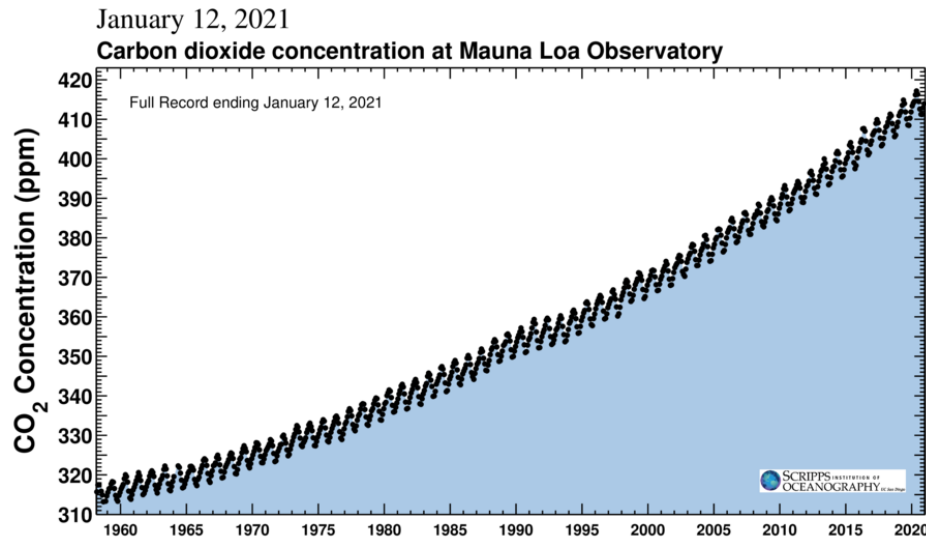


Figure 1. Concentration du CO₂ atmosphérique en fonction du temps ¹

La demande en énergie continue d'augmenter mondialement et il devient primordial d'adopter une stratégie qui peut combler efficacement ce besoin tout en permettant une décarbonation de nos sources d'énergies. La situation du Québec est unique, de par son grand territoire et l'hydroélectricité qu'elle produit abondamment.⁵ Cette dernière pourrait permettre un développement plus rapide et à grande échelle des technologies pour produire l'hydrogène. L'engouement pour l'hydrogène semble déjà être présent, en vue des infrastructures déployées à Bécancour⁶ et très bientôt à Varenne.⁷ L'hydrogène vert, qui pourrait être produit par photocatalyse, est l'une des avenues les plus prometteuses pour l'industrie et pourrait permettre une augmentation marquée de la génération d'énergie renouvelable au Québec. Cette méthode, souvent couplé avec la réduction du CO₂ atmosphérique en raison des processus similaires, permettrait également de produire certains produits à valeur ajouté tel que le méthane, l'acide acétique ou le formate.⁸ Le développement et l'amélioration de cette méthode permettrait également de concurrencer les méthodes de reformatage du méthane en terme de prix, responsable actuellement de la vaste majorité de l'hydrogène produit mondialement (environ 95% de la

production mondiale). Toutefois, le chemin à parcourir est encore considérable. Actuellement, les méthodes photo-électro et méthodes photovoltaïque permettent la production d'hydrogène à respectivement 11.40\$/kg H₂ et 12.10\$/kg H₂, contre 1.39\$/kg H₂ pour les méthodes de reformatage du méthane.⁹

La production d'hydrogène actuelle suffirait à moins de 2% de nos besoins énergétiques, alors que les combustibles fossiles dominent encore largement avec 85% des besoins énergétiques.^{10,11} Le G20 de 2019 a ramené l'utilisation de l'hydrogène sur la table et a permis un consensus vers un financement plus fournis. Puisque l'électricité tarde à devenir le carburant principal, en raison de ses nombreux problèmes, dont le stockage efficace à long terme, plusieurs pays ont accepté d'investir davantage de ressources dans leur recherche pour une nouvelle source d'énergie renouvelable qui gagne en popularité: l'hydrogène. Les carburants renouvelables sont au cœur des enjeux environnementaux actuels, mais ont pour principal problème de devoir être stocké sous forme d'électricité, contrairement à l'hydrogène. De ce fait, le G20 de 2019 à Tokyo, au Japon, avait pour but de définir l'avenir de l'hydrogène dans nos sociétés et de favoriser les ententes pour accorder davantage de ressources pour le développement de ces technologies.¹²

L'énergie solaire est également une réponse plausible aux problèmes d'approvisionnements énergétiques, en ce que l'énergie fournie par le soleil en une heure permettrait de combler entièrement les besoins énergétiques actuels. Effectivement, l'énergie solaire reçue annuellement par la terre (absorbé par les terres et l'océan) est d'environ 3.9 millions d'exajoule (EJ), ce qui correspond annuellement à $3.9 \times 10^{24} \text{ J}$.¹³ La figure ci-dessous permet d'avoir une bonne approximation de ce que ces quantités représentent.¹⁴

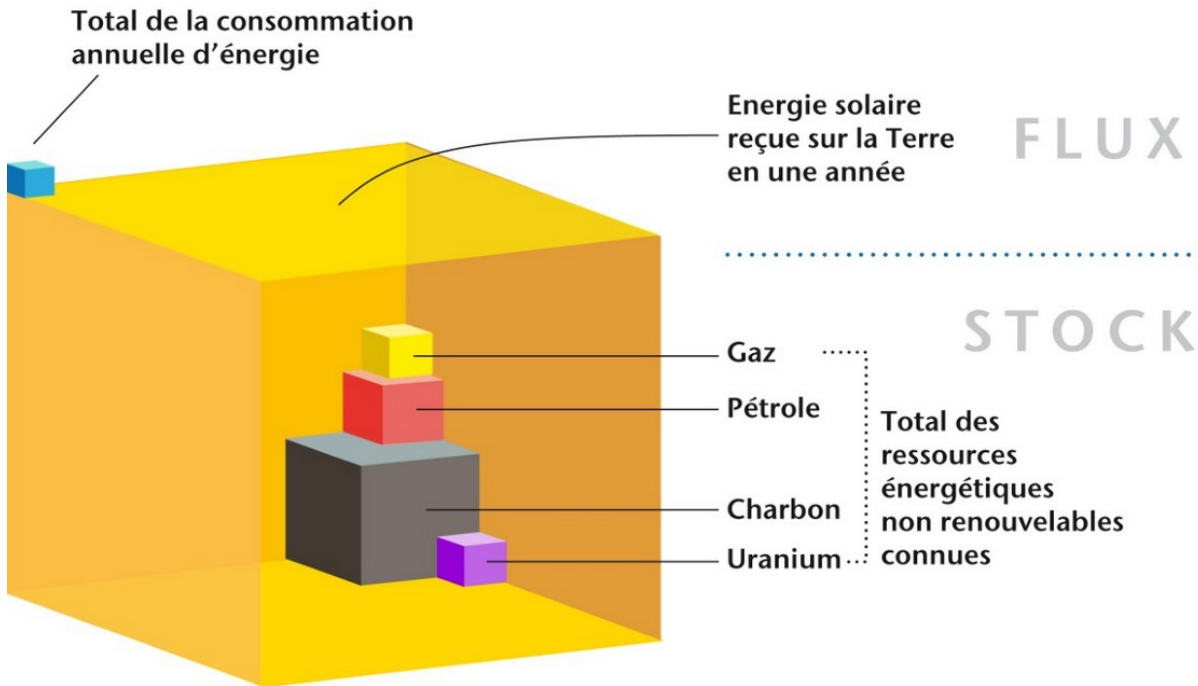


Figure 2. Illustration des réserves énergétiques mondiales (figure reproduite avec la permission, référence 14)

Le potentiel énergétique de l'exploitation de l'énergie solaire est donc énorme et suffirait amplement à combler les besoins énergétiques des civilisations, même si une faible fraction de cette énergie était récupérée. Vincenzo Balzani va jusqu'à affirmer que si on recouvre 0.16% des terres émergées avec des panneaux solaires ayant un rendement énergétique de 10%, cela suffirait à couvrir nos besoins énergétiques, en générant 20TW d'électricité.¹¹ C'est pourquoi il est primordial de développer des antennes solaires analogues à celles que crée la nature. Pour ce faire, il faut développer des molécules avec des systèmes conjugués, de manière à récupérer les ondes infrarouges et dans l'UV-visible, qui sont les deux types d'ondes les plus abondantes dans le spectre solaire. Ainsi, il serait possible d'obtenir davantage d'énergie pour un même rendement. De plus, l'exploitation des ondes de plus faible énergie est meilleure pour la durabilité des molécules du système, en ce qu'elles limitent les réactions indésirables. L'idéal serait de synthétiser des

molécules dont les transitions énergétiques sont presque exactement en concordance avec l'énergie fournis par une gamme de longueur d'onde, puis de s'assurer d'éliminer les autres longueurs d'ondes du spectre, afin d'assurer une durabilité optimale.

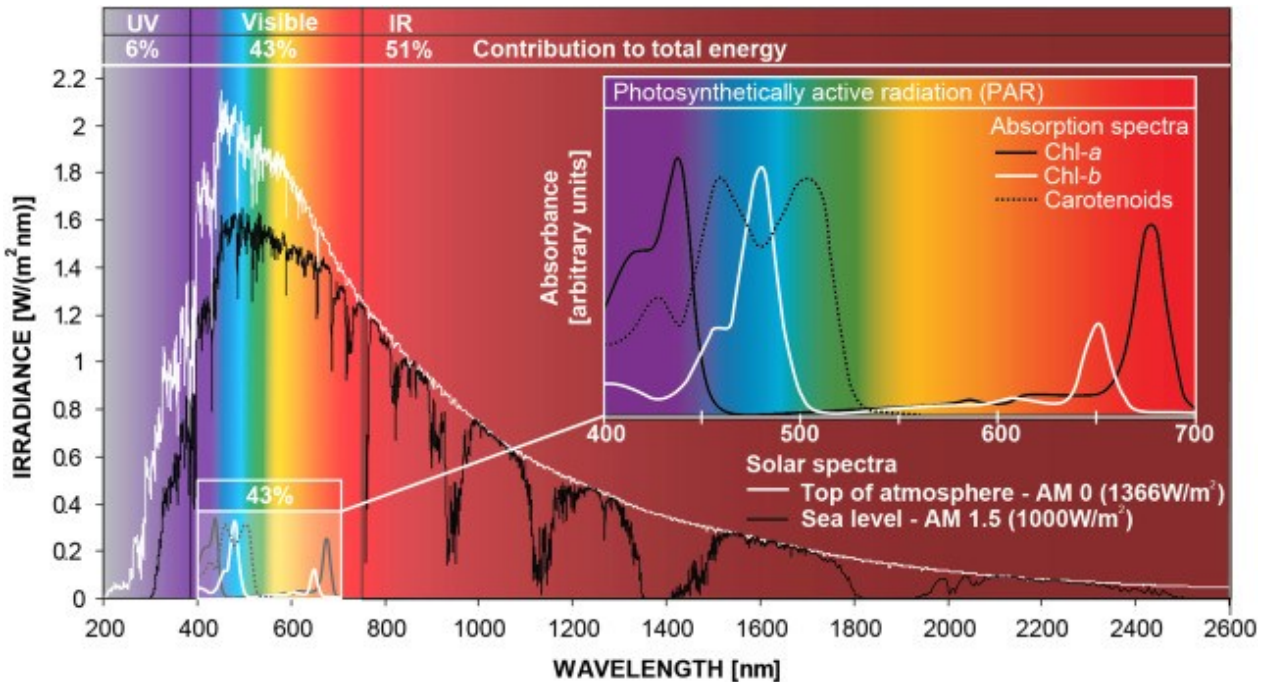


Figure 3. Spectre de l'énergie solaire reçue par la terre¹³

1.1.2 Pourquoi l'hydrogène

Les avantages de l'hydrogène sont multiples. En plus d'être nettement plus facile à stocker que l'électricité en raison de ses propriétés physiques et de sa forme, il est stable à plus long terme. Nous avons besoin d'une source d'énergie abondante et l'hydrogène répond bien à cette demande, en ce qu'il constitue environ 75% de la masse connue dans l'univers.¹⁶ De plus, l'hydrogène produit approximativement 2.2 fois plus d'énergie que le gaz naturel pour une même masse de carburant. Dans les avantages indiscutables de l'hydrogène, il faut ajouter que lorsqu'il est brûlé, il produit simplement de l'eau, selon la formule suivante :¹⁷

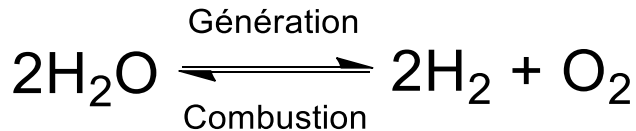


Figure 4. Génération et combustion de l'hydrogène

La génération d'eau en tant que produit de combustion fait de l'hydrogène un carburant environnemental miracle, qui produit un déchet utile à notre société. Bien évidemment, cette eau n'est pas propre à la consommation en raison des contaminants probables, mais peut être utilisé à bien des égards comme par exemple en tant que liquide de refroidissement ou comme diluant dans les eaux de rejets.¹⁶

L'hydrogène souffre du préjugé d'être très dangereux et explosif. Évidemment, la majorité des gens ont déjà entendu parler de l'explosion du dirigeable Hindenburg en 1937, qui était gonflé à l'hydrogène. Malgré qu'à l'époque, certains scientifiques travaillaient déjà sur un moteur alimenté à l'hydrogène, l'explosion du dirigeable a mis un terme à ces projets, sans équivoque. Cela a mis un frein à l'ascendance de l'hydrogène en tant que future source d'énergie de l'époque et a certainement retardé nettement la recherche à ce sujet. Toutefois, il faut savoir que dans ce dirigeable, l'hydrogène servait à la fois de gaz léger, destiné à aider le dirigeable à s'élèver, mais également un gaz de sustentation, c'est-à-dire qu'il servait à équilibrer le dirigeable ainsi qu'à réduire les chocs que provoquent les turbulences aériennes. Il fut choisi par rapport à l'hélium entre autres à cause de son prix exponentiellement plus bas, mais également parce que son potentiel de sustentation est plus élevé que celui de l'hélium, améliorant le confort des passagers.¹⁸

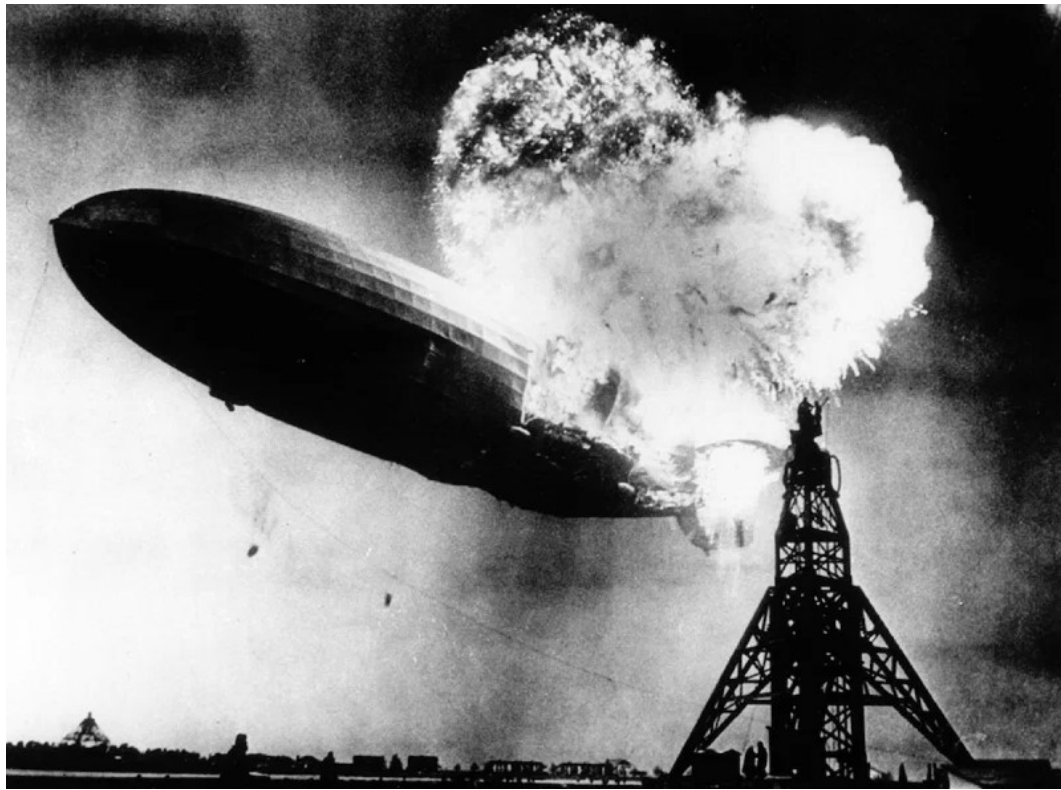


Figure 5. Explosion du dirigeable d'Hindenburg, en 1937, à Lakehurst, New Jersey¹⁷

Au niveau des propriétés de l'hydrogène, il s'agit d'un gaz très léger qui a tendance à s'échapper rapidement par la moindre fissure. Cela constitue un avantage car cela évite l'entrée d'air dans un réservoir d'hydrogène brisé, limitant nettement les risques d'explosion. De plus, on peut dire que sa limite d'inflammabilité se situe entre 4% et 74.2%. Cela signifie qu'il n'y a aucun risque d'explosion si une étincelle est créée dans le réservoir, car au-dessus de 74.2%, l'hydrogène est trop concentré pour exploser. S'il y a moins de 4% d'hydrogène dans l'atmosphère, également aucun risque d'explosion car il n'y a pas assez d'hydrogène pour alimenter la réaction.^{20,21} Vu sa volatilité, pour obtenir une concentration d'hydrogène dangereuse, il faudrait que l'hydrogène soit relâché à l'intérieur dans une pièce assez étanche pour que l'hydrogène s'accumule plus rapidement qu'il ne s'échappe.

Au niveau de la construction automobile, les piles à hydrogène assurent le fonctionnement des unités, mais ces véhicules sont encore très très peu répandus sur le marché et une poignée de constructeurs automobiles ont, pour le moment, des modèles viables. Il faut dire que l'aspect sécurité (en lien avec l'incident Hindenburg) a laissé des séquelles importantes dans la mémoire des gens et incitent la méfiance des consommateurs. Les manufacturiers indiquent que les mesures maximales sont prises pour diminuer au minimum les risques de fuite ou d'explosion de l'hydrogène. Ces mesures comportent entre autres la limitation des risques liés au relâchement accidentelle ou intentionnel de l'hydrogène. On peut citer en exemple les tests de tirs à balles réelles sur le réservoir, le couloir d'évacuation au sein du châssis en cas de fuite involontaire et le dispositif de relâchement de l'hydrogène à l'extérieur en cas d'incendie. Il faut toutefois dire que la technologie n'est pas encore au point pour assurer un prix concurrentiel de l'hydrogène.²²

1.1.3 La photosynthèse naturelle et artificielle

Photosynthèse naturelle

La photosynthèse est un processus connu mais compris partiellement, dans lequel la lumière permet l'oxydation de l'eau et la conversion du CO₂ en dioxygène et en glucose, selon l'équation suivante :

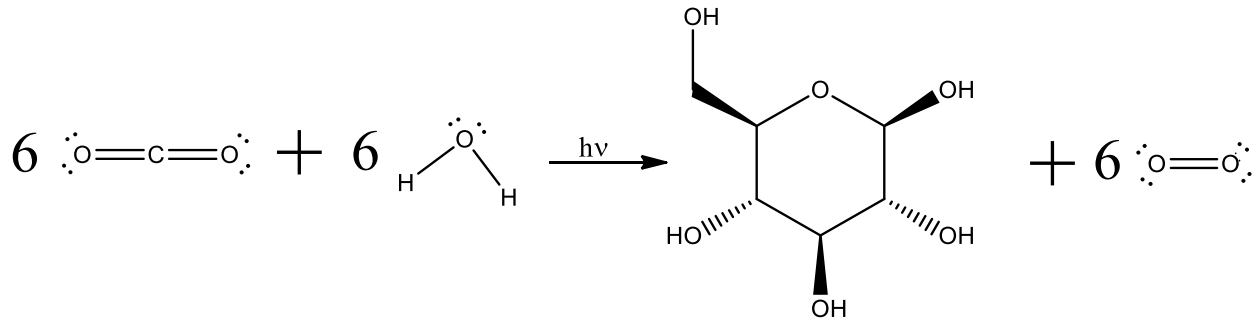


Figure 6. Équation simplifiée de la photosynthèse naturelle

La photosynthèse, bien qu’ayant un rendement très faible, est la principale source de génération du dioxygène sur terre et est donc, par le fait même, indispensable à la vie pluricellulaire que nous connaissons. Cette réaction fonctionne par l’intermédiaire de quatre sous-unités, soit le cytochrome b₆f, le F-ATPase (synthèse de l’ATP), le photosystème I (réduction du NADH⁺) et le photosystème II (Oxydation de l’eau et production de O₂). La photosynthèse se produit dans la membrane thylakoïde par l’intermédiaires de complexes qui absorbent la lumière, appelés photosensibilisateurs (PS), soit une combinaison de chlorophylles dans les deux systèmes, des carotènes dans le cas du photosystème I et de caroténols dans le cas du photosystème II. La principale différence est que le photosystème I absorbe jusqu’à 680nm alors que le photosystème II absorbe jusqu’à 700nm. Les molécules en présence ont des longueurs d’ondes d’absorption complémentaires, de sorte qu’elles peuvent capter la vaste majorité des ondes incidentes afin d’alimenter en énergie les différentes réactions impliquées dans la photosynthèse. Les caroténols ont également un rôle protecteur contre l’oxydation des molécules du système.²³

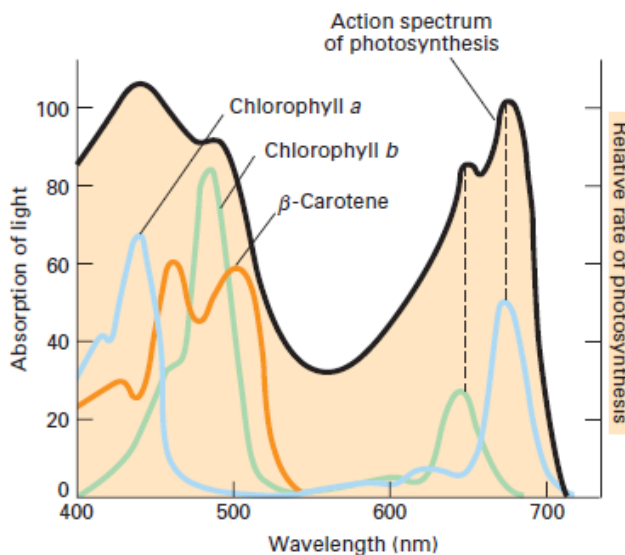


Figure 7. Spectre d'absorption des photosensibilisateurs impliqués dans la photosynthèse naturelle²³

La photosynthèse peut être séparée en deux : Les réactions claires et les réactions sombres. Les réactions claires conduisent à la photolyse de l'eau, générant l'oxygène et les protons disponibles (H^+). Elles sont, comme le nom l'indique, les réactions demandant de la lumière. Celles-ci intègrent la majorité des réactions comprises dans le processus de photosynthèse naturelle et comporte les réactions d'intérêt pour la génération d'hydrogène par photosynthèse artificielle. Les réactions sombres sont celles qui impliquent la fixation du CO_2 par le cycle de Calvin. Ces réactions tirent leur énergie de l'hydrolyse des molécules d'ATP et du NADPH.²⁴

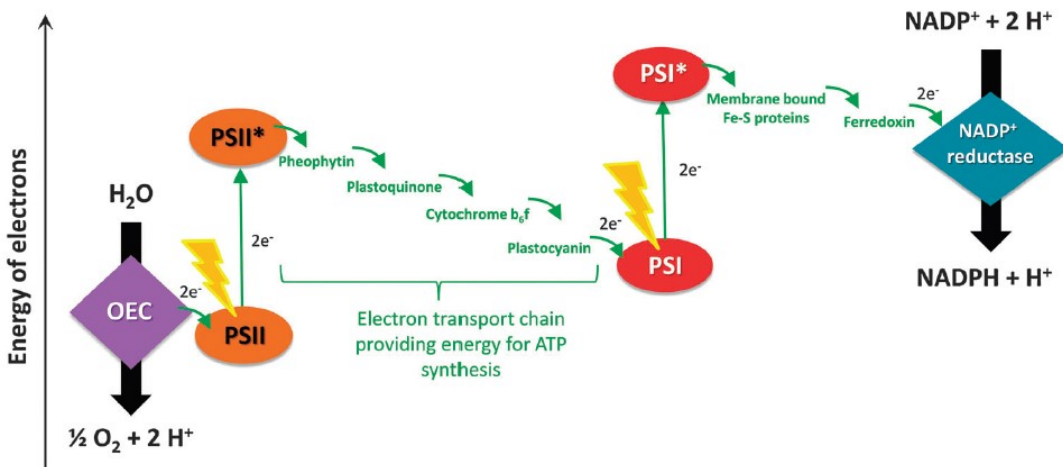


Figure 8. Représentation de la chaîne de réactions impliqués dans la photosynthèse naturelle²⁴

La réaction commence dans le photosystème II, alors que les chlorophylles α qui vont d'environ 670 à 720 (le chiffre indiquant la longueur d'onde préférentielle) et les caroténols, dans les complexes photo-absorbants, absorbent la lumière solaire et transmettent l'énergie d'une molécule à l'autre jusqu'au P680. Suite à quelques transferts, libérant chacun un peu d'énergie, l'électron arrive finalement au P680, qui est le centre réactionnel du photosystème II. Celui-ci convertie l'énergie lumineuse en énergie chimique, provoquant la séparation de charge. Le P680 est responsable de la scission des molécules d'eau, entraînant la libération de l'oxygène. Ensuite, l'électron est transféré à l'accepteur primaire, le pheophytine. Cet électron voyage ainsi jusqu'au

plastocyanine, permettant en chemin la génération d'adénosine triphosphate (ATP). Cette molécule est indispensable pour les organismes vivants, car elle sert en quelque sorte de banque d'énergie pour les réactions métaboliques. Une fois l'électron arrivé au plastocyanine, il est transmis au P700, centre réactionnel du photosystème I. Celui-ci absorbe également la lumière par le biais de complexes d'antenne, qui sont principalement composés de carotènes et de chlorophylle. Ces électrons seront éventuellement transmis à un accepteur primaire, qui à son tour va donner cet électron à la ferrédoxine. Celle-ci conduit une chaîne de transfert d'électrons qui mène éventuellement à la réduction du NADP⁺ en NADPH, nécessaire au cycle de Calvin. Ce cycle est responsable de la synthèse de glucide de la photosynthèse.²⁶

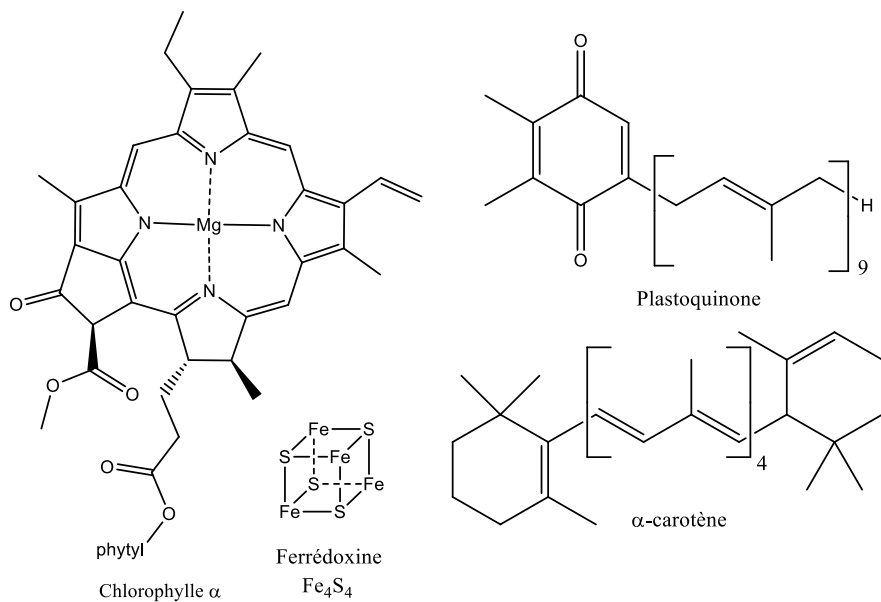


Figure 9. Quelques molécules impliquées dans la photosynthèse naturelle

Photosynthèse artificielle

La photosynthèse est le système d'inspiration des méthodes de génération d'hydrogène par photocatalyse. L'objectif est de répliquer la fonction du système sans répliquer sa complexité. On vise à réduire l'eau de la même manière que la photosynthèse naturelle permet l'oxydation de l'eau afin de produire l'oxygène. Pour ce faire, il faut suivre les 4 étapes clés de la photosynthèse : Absorption de la lumière (photosensibilisateur), transfert d'énergie (système conjugué), séparation de charge (centre réactionnel) et catalyse (catalyseur) pour le clivage de l'eau. Le système de photosynthèse artificielle est connexe au système naturel, à la différence que le photosensibilisateur utilise un centre métallique en tant que centre réactionnel pour procéder à l'état de charge séparé, état qui permet l'oxydation et la réduction du photosensibilisateur, établissant par le fait même la viabilité du système. Le centre métallique sert également à favoriser les transferts d'électrons, dans le but de limiter la dégradation des molécules, qui ne peuvent être que difficilement régénérée dans un système artificiel. L'énergie entrante est l'énergie solaire et on cherche à la convertir en énergie chimique, de manière à la stocker dans les molécules.¹¹

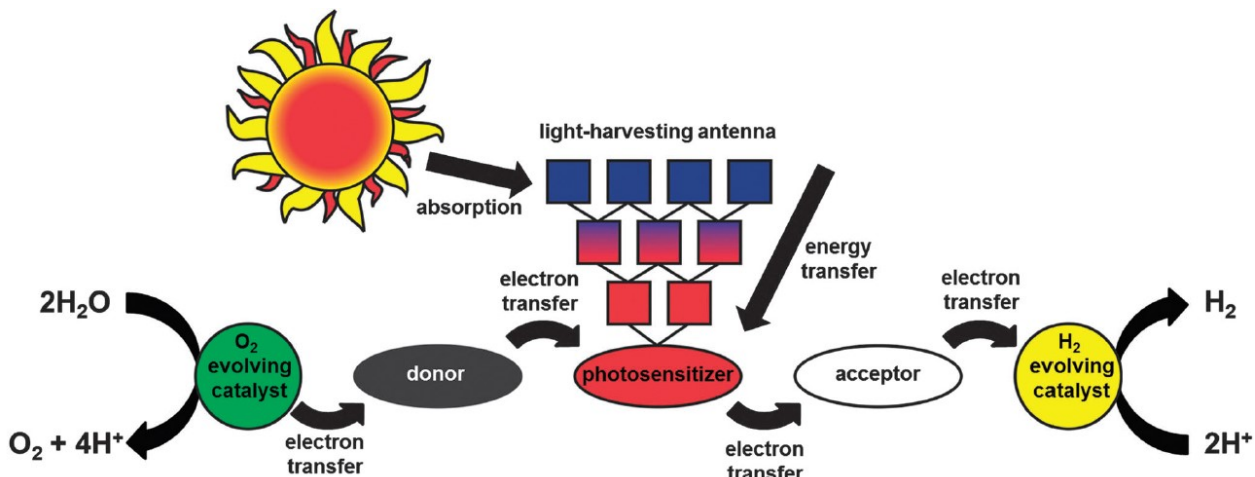


Figure 10. Schéma de la photosynthèse artificielle²⁷

La photosynthèse artificielle procède de la sorte : En premier, la lumière incidente est absorbée par des molécules conjugués, les photosensibilisateurs, qui entrent alors dans un état excité, appelé l'état de charge séparé. Cet état a la propriété de permettre au photosensibilisateur d'être à la fois facilement oxydé et réduit, de manière à favoriser l'oxydation et la réduction de l'eau. S'ensuit un transfert de charge vers un catalyseur pour la formation d'hydrogène ou d'oxygène. La nature de ces molécules dépend fortement des conditions réactionnelles et de nombreuses possibilités sont envisagées. Le problème principal, outre le rendement très faible en comparaison du prix coûtant, reste de combiner la séparation de charge (processus d'un proton et d'un électron) avec la génération d'oxygène, qui est un processus à 4 électrons.²⁸

La photosynthèse artificielle est un processus relativement complexe, malgré sa simplicité par rapport à la photosynthèse naturelle. C'est pourquoi les chercheurs concentrent généralement leur attention uniquement l'une des deux demi-réactions, soit l'oxydation ou la réduction de l'eau. L'objectif est de simplifier le système, de manière à visualiser l'effet des changements apportés au système en intégrant le minimum de variables possible pour que le système fonctionne. On soustrait donc le catalyseur approprié et ont défini le donneur ou l'accepteur comme facteur limité du système. Normalement, d'autres paramètres du système vont devenir le facteur limitant, tel que la dégradation du catalyseur ou du photosensibilisateur, mais si ceux-ci sont très stables, le donneur ou l'accepteur peuvent limiter la réaction, puisqu'ils ne sont pas régénérés par la seconde demi-réaction.

1.1.4 Méthodes de production : Un bref aperçu

Il y a de nombreuses méthodes pour produire de l'hydrogène, mais toutes ne comportent pas les mêmes avantages et inconvénients. L'objectif de cette section est de donner une vue d'ensemble plus complète au lecteur sur le potentiel de l'hydrogène dans nos besoins énergétiques, ainsi que de souligner le potentiel à long terme de la photocatalyse par l'étude d'autres méthodes de production d'hydrogène. C'est pourquoi seront présentés brièvement les méthodes les plus utilisées pour produire de l'hydrogène industriel.

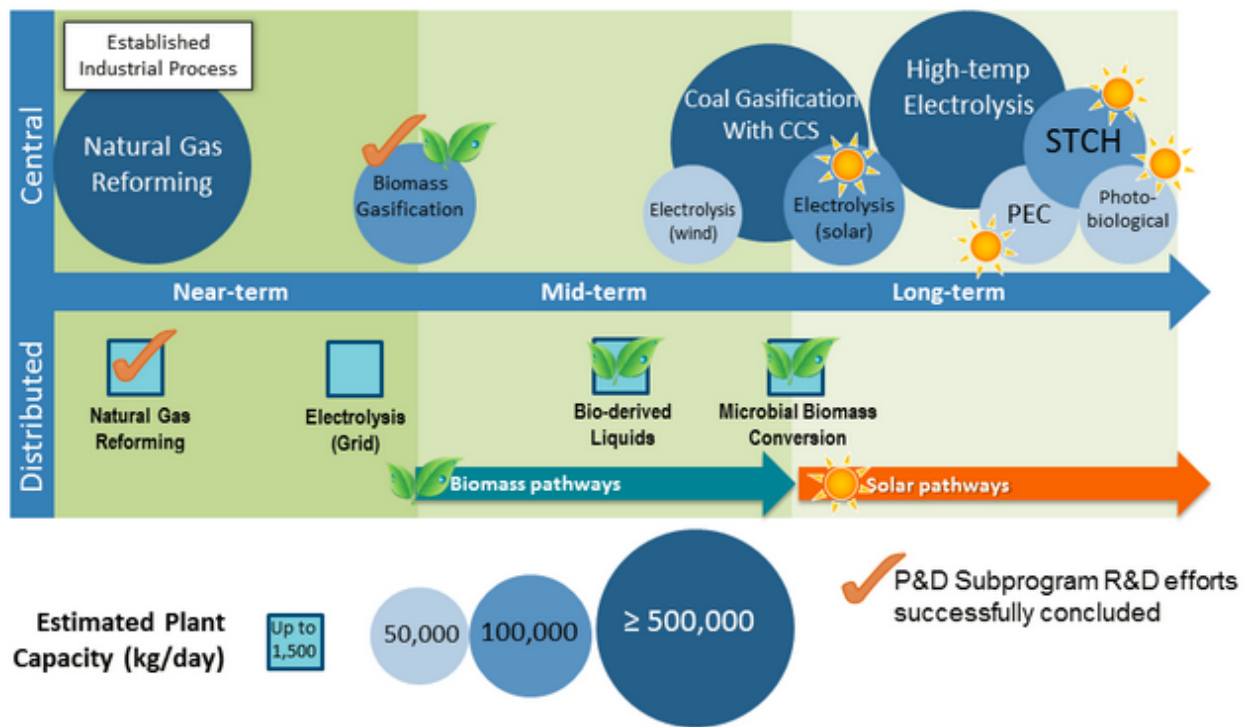


Figure 11. Aperçu des différentes méthodes pour la production de l'hydrogène et leur utilité prévue

28

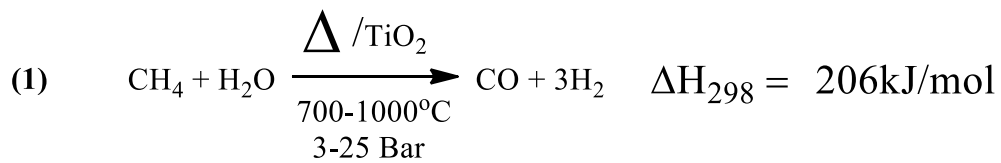
Les méthodes tel que le reformatage du méthane et l'électrolyse sont celles qui sont le plus utilisées présentement, mais ont comme désavantage principal respectivement la production de CO₂ et la perte d'une partie de l'énergie utilisée. Dans un avenir à moyen terme, l'utilisation de biomasse est souhaitable, de manière à éliminer partiellement la production de CO₂ et le gaspillage énergétique.

Sur le long terme, on souhaite favoriser la production d'hydrogène par l'énergie solaire pour éviter d'autres problèmes potentiels, tel que l'utilisation des terres pour la production de bio-carburant, par des méthodes tel que la photocatalyse, qui est une alternative optimale pour l'environnement.

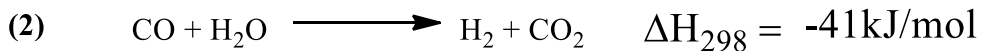
Reformatage du methane (Steam reforming)

Ce procédé se base sur le réarrangement des hydrocarbures (ici le méthane), comme décrit par l'équation suivante (1) :

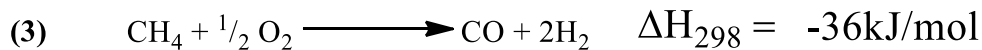
Steam reforming of methane



Water gaz shift



Partial oxidation of methane



Dry reformating of methane



Figure 12. Équations chimiques impliqués dans le reformatage du méthane

La première étape permet la formation de monoxyde de carbone très réactif et sera généralement complété par le water gaz shift (2), générant du dioxyde de carbone, déchet nuisible contribuant aux changements climatiques. La production de CO est désirable, puisqu'il peut être transformé en méthanol, éthanol, formate, etc. Sa relative simplicité, l'abondance du méthane et son faible prix ont permis la production à grande échelle de l'hydrogène par ce procédé, qui domine actuellement 95% du marché de la production d'hydrogène. Le besoin d'une haute température et de fortes

pressions, de même que la production du CO₂ sont deux faiblesses de ce procédé, mais des efforts conséquents sont déployés afin d'en minimiser l'importance.³⁰⁻³² Par ailleurs, l'utilisation directe de la lumière solaire³³, de même que l'oxydation partielle du méthane (**3**), procédé souvent couplé avec le reformatage du méthane, permet d'économiser un peu d'énergie et d'augmenter le rendement de cette réaction. De nouvelles études visent à combiner toutes les méthodes (**1**) à (**4**), afin de limiter les désavantages de chacune d'elles, par exemple limiter la formation de coke, qui réduit généralement la durée de vie du catalyseur, diminuer l'énergie requise au procédé par des réactions exothermiques tel que (**2**) et (**3**) et modifier les ratios d'H₂/CO en modifiant les intrants du système.³⁴

Il est également possible de faire le reformatage de l'éthanol ou du méthanol, mais d'autres problèmes sont alors à considérer comme le besoin d'un catalyseur différent (avec une bande de conduction adapté à l'énergie requise au procédé) ainsi que des produits de dégradation différents.³⁵

Production d'hydrogène à partir de la biomasse

La production d'hydrogène à partir la biomasse est une méthode réputée pour être plus verte que le reformatage du méthane, mais qui a également plusieurs désavantages. D'une part, elle ne consomme pas de méthane, mais produit tout de même du CO₂, ce qui est pire au niveau environnemental, puisque le méthane n'est pas soustrait de l'atmosphère. D'autre part, elle requiert tout de même, en tant qu'intrant, une matière assez variable qui demande l'utilisation des terres agricole.³⁶

La première génération de biocarburants utilise des matières tels que le maïs ou du sucre. Le principal problème est l'utilisation de terres agricoles pour la production de carburants. Alors qu'il y a toujours bon nombre de gens sur terre qui ne peuvent pas manger à leur faim, ceci pose un

important problème éthique. La principale méthode proposée consiste à utiliser les rejets alimentaires, mais cela ne peut heureusement pas combler toute la demande.

La seconde génération de biocarburants est générée à partir de bois ou de déchets organiques. On observe toutefois un gaz moins pur en raison du CO et du CO₂ généré. Beaucoup d'efforts sont déployés dans le but de purifier le gaz résultant à moindre coûts, mais les catalyseurs développés font encore défaut, soit par leur prix, soit par leur efficacité.³⁷ L'utilisation de matières humides provoque toutefois la génération accrue d'oxydes et augmente le coût et la difficulté de séparation, ce qui limite l'utilité des bio-carburants produits par cette méthode.³⁸

La troisième génération de biocarburants provient de micro-organismes. Cette méthode a pour principaux avantages d'être renouvelable, son faible coût et son rendement élevé. Toutefois, elle est encore en plein développement et n'est pas encore tout à fait adaptée au niveau industriel. L'utilisation de compost ou de déchets alimentaires est un point de départ intéressant pour cette méthode, parce qu'elle sert d'intrant principal et que l'intervention humaine requise est très limitée. L'utilisation de catalyseurs aussi abondants que le TiO₂ est également un point fort, puisque les risques de pénuries, même en cas d'utilisation à l'échelle planétaire (ce qui est déjà le cas pour ses usages alimentaires et pharmaceutiques), sont très faibles.³⁹ Cette production peut être réalisée sans lumière ni oxygène. C'est par ailleurs l'une des meilleures méthodes actuelles, en ce qu'elle produit davantage que les méthodes traditionnelles et permet de produire des molécules utiles telles que du méthane ou des alcools. C'est toutefois un problème qu'il faudra résoudre tôt ou tard, en ce que le méthane (CH₄) contribue à l'effet de serre.⁴⁰ En modulant les conditions initiales (pH, température), de même que les souches de bactéries utilisées et les matières à dégrader, il est possible d'influencer à la fois le rendement et la production de déchets nuisibles tel que le CO₂.⁴¹

En définitive, les méthodes de production d'hydrogène à partir de la biomasse ont un certain potentiel. Toutefois, les méthodes de reformatage du méthane sont nettement moins chères et produisent moins de CO₂ (11kg de CO₂ par kg d'hydrogène contre 15 à 18kg de CO₂ pour les méthodes de production d'hydrogène à partir de la biomasse). Des projections prévoient que les prix ainsi que le dégagement de CO₂ devraient diminuer nettement dans les prochaines années.⁴²

Électrolyse de l'eau (water electrolysis)

L'électrolyse de l'eau est l'utilisation d'une source d'énergie (le plus souvent l'électricité) pour fragmenter les molécules d'eau en hydrogène et en oxygène. Cette méthode, bien que viable dans l'industrie, souffre également de plusieurs défauts qu'il faut adresser. Entre autres, l'utilisation d'une source d'énergie (l'électricité) qui génère elle-même ses propres déchets et la perte d'énergie résultant de sa conversion en hydrogène en est le principal facteur limitant. Ce facteur diminue l'efficacité du procédé en raison de l'augmentation des coûts ainsi que de la perte d'énergie durant le processus. Ce processus permet néanmoins de générer de l'hydrogène à partir de l'électricité excédentaire produite, ce qui est une bonne chose.

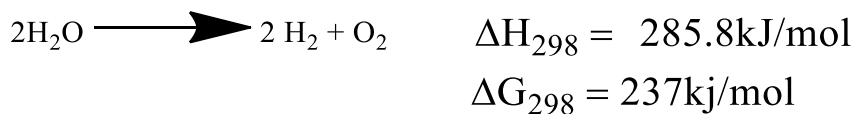


Figure 13. Équations chimiques impliqués dans l'électrolyse

De plus en plus, la recherche se concentre sur la photocatalyse, afin de pallier cet inconvénient majeur. Toutefois, il faut dire que celle-ci est encore en plein développement et souffre de très faible rendement. La photocatalyse devait pallier ces pertes, mais ses rendements sont malheureusement loin d'être compétitifs sur le marché. La dégradation rapide des

photosensibilisateurs rend le processus difficile et non rentable. Certaines méthodes hybrides telles que la photo-électrocatalyse ont pour objectif de réduire le coût en utilisant l'énergie solaire en tant que source partielle de l'énergie requise, ce qui permet non seulement la réduction des pertes mais également un rendement acceptable. Bien que le prix soit plusieurs fois celui du reformatage du méthane, comme mentionné précédemment, on prévoit une chute du coût dans les prochaines années pour ce type de méthodes.^{43,44}

L'électrolyse au plasma est une variante fort intéressante qui se concentre sur la production de plasma pour la production de l'hydrogène localement, ce qui permet de sauver une quantité importante de courant, réduisant par le fait même le coût de la production.⁴⁵ La migration de l'hydrogène dans le plasma est beaucoup plus rapide que dans une solution, ce qui permet une production accrue et une collecte plus efficace.⁴⁶

Photocatalyse de l'eau

La méthode qui concerne cette thèse, la photocatalyse, est celle qui a le plus grand potentiel à long terme. Sans retourner dans le détail (voir section 1.1.3 pour plus d'information sur le développement de la méthode et son origine, et la section 1.2.3 pour plus de détails sur le fonctionnement des catalyseurs dans l'eau), on peut affirmer le potentiel extraordinaire de cette méthode, puisqu'elle ne génère pas de déchets nuisibles. Les deux seuls points à adresser concernant la protection de l'environnement sont l'utilisation d'un solvant moins nocif (tel que l'eau) et la récupération sécuritaire des molécules utilisées dans le processus. D'un point de vue industriel, seul le rendement, très inférieur à celui des autres méthodes, pose problème à l'utilisation de cette méthode.

1.1.5 Méthodes d'entreposage : Un bref aperçu

L'hydrogène, contrairement à l'électricité, n'a pas de problème de stockage. La principale difficulté en est plutôt le transport. Effectivement, il peut être stocké de nombreuses manières comportant toutes différents avantages et inconvénients. On décline généralement les méthodes de stockage par état de la matière, soit sous formes de gaz, liquides ou solides.

Stockage sous forme gazeuse

La forme classique est le gaz sous pression. C'est de loin la méthode la plus répandue. Bien que l'hydrogène soit relativement difficile à comprimer à cause de sa petite taille, cette méthode a comme principal avantage de permettre la compression d'une grande quantité d'hydrogène dans un espace restreint, jusqu'à une pression d'environ 700Bar. Cette méthode a comme principal désavantage la question de la sécurité. Effectivement, si un seul cylindre devait briser, les dégâts seraient très importants et les risques de blessures sont énormes. En raison des risques de rouille des cylindres, une solution probable est de former les futurs cylindres avec plusieurs couches dont au moins une est dépourvue de métaux oxydables, dans le but de limiter les dommages possibles s'il y a un accident.⁴⁷ Dans un futur proche, il est probable que des matériaux encore plus résistants soient développés et permettent de compresser l'hydrogène à des pressions encore plus grandes, améliorant le potentiel de cette méthode.

Stockage sous forme liquide

L'hydrogène peut également être stocké sous forme liquide, réduisant nettement les risques de blessures. Toutefois, pour passer sous la forme liquide, il faut atteindre une température d'environ -252°C, ce qui semble peu efficace et très dispendieux. Le seul moyen de rendre cette méthode

rentable serait d'utiliser un isolant thermique, de manière à rendre presque nulle la diffusion thermique. Ce type de liquéfaction est toutefois possible si on utilise certains systèmes, tel que l'isolation multicouches combinée à un bouclier refroidisseur de vapeur (vapor-cooled shield), permet une diffusion presque nulle, ce qui permet un stockage efficace de l'hydrogène à faible coûts.^{48,49} Ce type de stockage est encore très peu courant au Canada, mais pourrait devenir prometteur rapidement.⁵⁰

Pourtant, il existe une autre solution. Il est possible de dissoudre l'hydrogène dans un 'transporteur' liquide. L'idée est de procéder à une réaction de condensation pour libérer l'hydrogène ou une réaction d'addition, pour le stocker. La figure suivante présente quelques exemples rapportés dans la littérature :

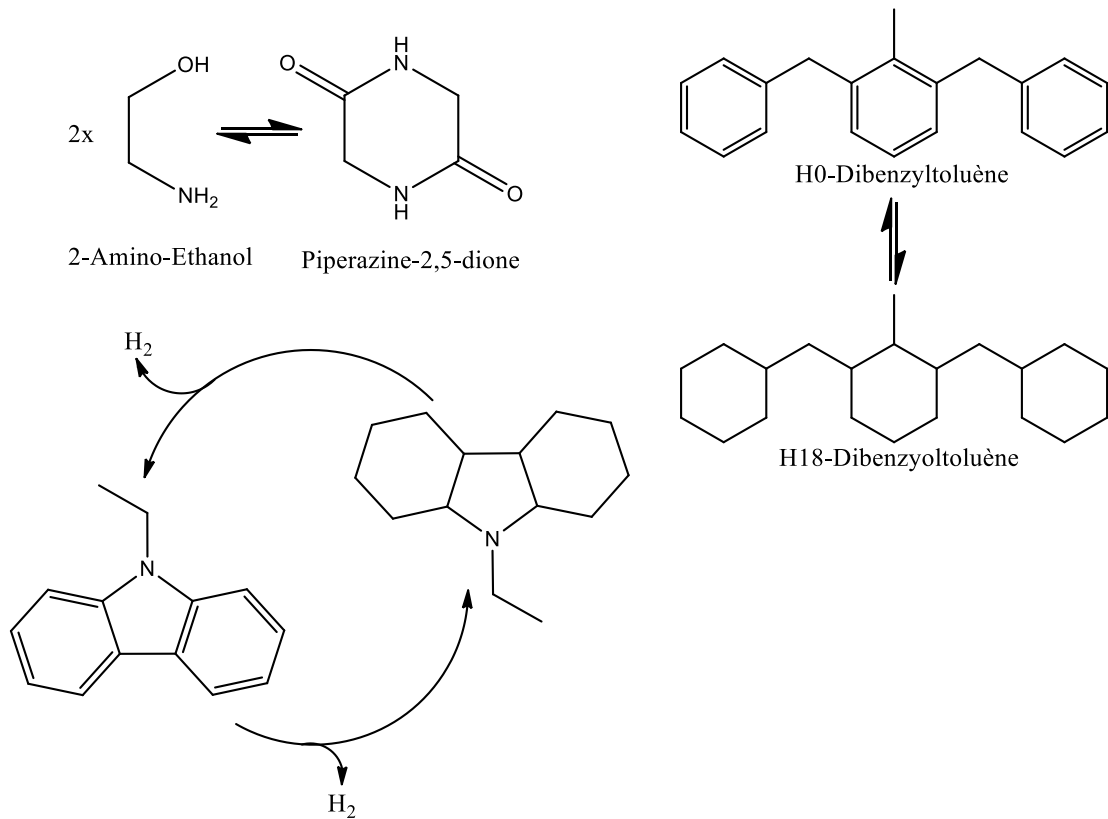


Figure 14. Exemples de transporteurs d'hydrogènes étudiés dans la littérature scientifique⁵¹⁻⁵³

Bien que nettement moins dispendieux que la liquéfaction de l'hydrogène, les transporteurs d'hydrogène ont tout de même plusieurs désavantages. Les principaux désavantages sont la faible quantité qui peut être condensée dans ces molécules (environ 5% en masse) ainsi que la faible cinétique de diffusion, qui pourrait entraver l'utilisation directe de l'hydrogène dissous dans ces liquides.⁵¹⁻⁵³

Stockage sous forme solide

L'hydrogène stocké sous forme solide peut être divisé en deux catégories distinctes : L'hydrogène stocké par physisorption et l'hydrogène stocké par chimisorption.

Processus de chimisorption

L'hydrogène stocké par chimisorption est lié chimiquement soit par liens ioniques ou covalent, soit par insertion de l'hydrogène dans les trous octaédriques ou tétraédriques de la structure. L'hydrure de magnésium (MgH_2) est le candidat principal du stockage de l'hydrogène par chimisorption en raison de ses propriétés particulières, tel que le stockage théorique de 7.6%wt d'hydrogène ainsi que le stockage supplémentaire dans les trous octaédriques (forme hexagonale compacte). Toutefois, il faut mentionner les deux principaux points négatifs le concernant. En premier, sa cinétique de libération d'hydrogène est très lente et est difficile à obtenir car l'énergie d'activation est grande, ce qui réduit nettement l'efficacité de cette méthode de stockage. En second, les processus de désorption sont partiellement irréversibles, réduisant la capacité de stockage à chaque nouveau cycle. Ces deux problèmes peuvent être amoindris en utilisant des alliages à base de magnésium.^{54,55} Une autre sorte de complexe est très étudié actuellement, les complexes de type hydrazinoborane, permettent un stockage de 15-20% d'hydrogène, ce qui est exceptionnel. Toutefois, elle souffre de désavantages significatifs tel que la libération de produits indésirables

(NH_3 , $\text{B}_3\text{N}_3\text{H}_6$) et le besoin d'un catalyseur stable permettant de libérer l'hydrogène en phase aqueuse.^{56,57}

Il est également possible de stocker l'hydrogène dans des "complexes" organiques, tel que LiAlH_4 ou NaBH_4 . Le désavantage principal de cette technique est la haute température requise pour la désorption de l'hydrogène et la réactivité des complexes, rendant le stockage moins sécuritaire que par d'autres méthodes.^{58,59}

Processus de physisorption

Les processus de physisorption impliquent une adsorption de l'hydrogène à la surface de la structure par des interactions de van der Waals, ce qui implique une adsorption proportionnelle à la surface et à la porosité du matériel. De plus en plus de travaux se concentrent sur la recherche de matériaux bidimensionnels, tel que les nanotubes de carbone, qui permettraient de stocker l'hydrogène sous forme de feuillets. Le graphite est le candidat principal à ce genre d'application en raison de sa surface de contact exponentiellement plus grande que les molécules traditionnelles, mais ces recherches sont en pleine expansion et de nouvelles voies potentielles sont explorées. Un exemple récent est le plumbene, qui a une capacité théorique de 6.74%wt, mais qui a pour avantage une modulation des cycles absorption/désorption en fonction du courant électrique appliqué.⁶⁰ Plusieurs travaux de recherches se concentrent sur la combinaison entre le graphène et des catalyseurs métalliques qui pourront réduire l'énergie requise pour stocker l'hydrogène et le désorber plus efficacement. L'avantage principal de cette méthode est qu'elle ne demande pas une grande pression et que le processus est répétable sur plusieurs cycles, en autant qu'on parvient à éviter l'oxydation de la surface des tubes.⁶¹ L'ajout de magnésium à des dispositifs de stockage permet de renforcer les liens et donc de stocker le graphite à des températures plus grandes, mais réduisent légèrement la capacité de stockage.⁶²

1.2 Partie 2 : La génération d'hydrogène dans l'eau

1.2.1 Objectifs de la génération de l'hydrogène dans l'eau

L'utilisation de l'eau en tant que solvant pour la photocatalyse de l'hydrogène est un objectif qui est depuis longtemps dans la mire des chercheurs.⁶³ La découverte de plusieurs types de catalyseurs solubles dans l'eau, tel que les porphyrines et les catalyseurs poly-pyridyl (voir section 1.2.3) sont un bon pas dans ce sens. L'utilisation de l'eau, qui abonde au Canada, permettrait plusieurs avantages marquants. En premier, la réduction des déchets liés à l'utilisation massive de solvant organique constituerait un avantage marquant de cette méthode comparée à la majorité des autres méthodes de production et permettrait d'égaliser le score avec l'électrocatalyse, qui est presque exclusivement réalisée dans l'eau. Cela permettrait également de réduire le coût de ces systèmes, ce qui serait bénéfique à son utilisation. En second, on réduirait massivement les dangers liés à l'application industrielle de ces procédés.

Les défis de la photocatalyse dans l'eau sont nombreux. La dégradation des catalyseurs est généralement nettement plus rapide en raison de l'encombrement généré par la taille des molécules (voir section 1.2.2 pour plus de détails). Également, l'utilisation de l'eau nous limite à l'utilisation des donneurs d'électrons sacrificiels tels que le triéthanolamine, le triéthylamine et l'acide ascorbique.⁶⁴ Lorsque l'acide ascorbique (ou un tampon ascorbate) est utilisé, il faut considérer le pH comme un nouveau facteur décisif des performances du système. Tel que démontré dans la section 1.2.2, le pH optimal change d'un système à l'autre et même d'un catalyseur à l'autre, même s'ils sont très semblables, modifiant par conséquent les performances catalytiques. Un facteur d'importance, en particulier dans les pays du nord, est l'ensoleillement. Effectivement, la production d'énergie solaire n'est pas un point fort du Canada, en raison de son climat particulier.

La capacité de production d'énergie solaire a passé de moins de 500Mw en 2010 à plus de 3000Mw en 2018, ce qui n'est pas négligeable, mais tout de même très loin d'être suffisant.⁶⁵ L'amérique du nord produisait en 2018 57 118mW avec l'énergie solaire, ce qui veux dire que le Canada produit moins de 6% de l'énergie solaire en amérique du nord.⁶⁶ Pour cette raison et en raison du climat particulier du Canada, la photocatalyse a un potentiel plus limité qu'il ne le devrait. Toutefois, si les scientifiques canadiens ont du succès à monter des systèmes efficaces, cela permettrait une application de ces technologies à l'échelle mondiale, d'où l'importance capitale de mener à bien des recherches sur ce sujet.

1.2.2 Mécanismes réactionnels impliqués

Mécanismes réactionnels

Bien que peu de preuves définitives appuient le mécanisme généralement accepté de formation de l'hydrogène, il semble faire l'unanimité dans ses différentes étapes. Deux types de mécanismes sont généralement acceptés : Le mécanisme homolytique et le mécanisme hétérolytique. Dans les deux cas, on peut obtenir la génération d'hydrogène soit avec le Co^{II} ou le Co^{III}. Celle-ci dépend des conditions réactionnelles, tel que le pH^{67,68}, la température ainsi que des concentrations utilisées⁶⁸.

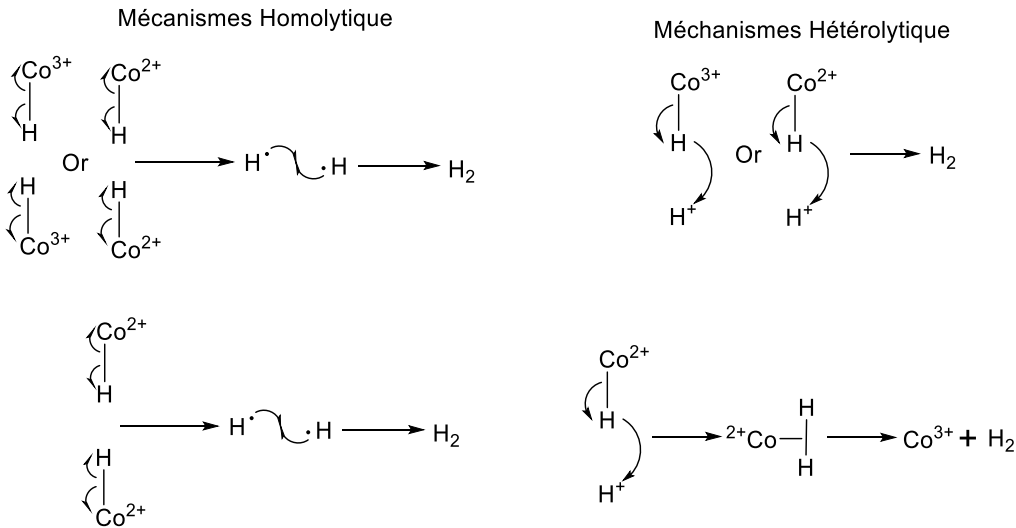


Figure 15. Distinction des mécanismes homolytiques et hétérolytiques

Là où le sujet se corse, c'est quand on arrive à la formation de l'hydrure métallique. Plusieurs mécanismes ont été proposés sur cette étape, mais il est difficile d'arriver à un consensus puisque le mécanisme est mesuré indirectement. Au sujet des catalyseurs à base de cobaloxime, on observe généralement une réduction du centre métallique et l'ajout d'un proton en deux séquences distinctes, ce qui mène à la génération d'hydrogène par mécanisme hétérolytique, tel qu'illustre par la figure 1. La prise du second proton est généralement l'étape limitante, puisque le catalyseur est alors plus encombré et la réaction a par conséquent moins de chances de se produire.⁶⁹

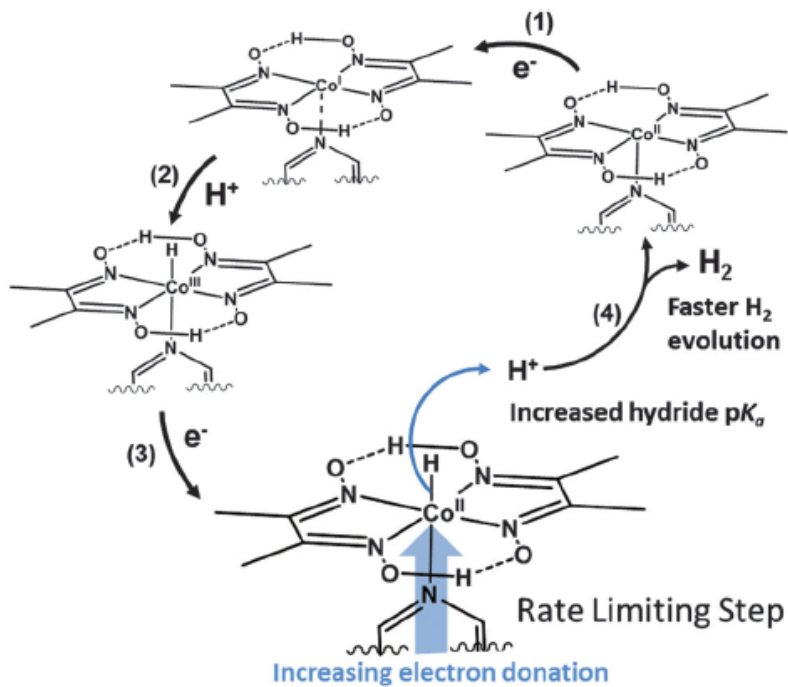


Figure 16. Mécanisme hétérolytique de génération d'hydrogène⁷²

Le mécanisme homolytique, qui semble plutôt rare en photocatalyse et en électrocatalyse organo-métallique, est tout simplement la formation de deux hydrures identiques qui vont réagir ensemble suite au rapprochement des deux catalyseurs, selon un mécanisme d'élimination réductrice pour dégager de l'hydrogène. Ce mécanisme est généralement défavorisé à cause de l'encombrement stérique généré par la taille importante des catalyseurs ainsi que par la faible concentration de catalyseur utilisé. Si un tel mécanisme était actif, il faudrait lui laisser un temps considérable pour faire son effet, excepté si un effet en solution favorise la proximité des catalyseurs. Ce pourrait être le cas par exemple s'il y avait des charges électrostatiques sur les molécules de catalyseurs.⁷⁰ Il est donc probable qu'il s'applique surtout aux alliages métalliques, qui offrent davantage de sites de coordination, tous plus près les uns des autres que ne le seraient ces sites, dans un catalyseur organo-métallique. La vaste majorité des systèmes organo-métalliques publiés prône le modèle hétérolytique, mais pas forcément le même. Il existe dans la littérature 4 types distincts de

mécanismes hétérolytiques (voir figure 17). Les types 1 (ET-PT) et 3 (PT-ET) sont respectivement la réduction du centre métallique (gain d'électron), suivis d'une protonation (gain d'un H⁺), et le processus inverse. Les types 2 (M-PCET) et 4 (L-PCET) consistent en la protonation suivis par le transfert d'électron. La différence entre ces deux mécanismes est que le type 2 est centré sur le métal, alors que le type 4, sur le ligand. On peut noter également que le mécanisme de type 1 se fait en deux étapes distinctes alors que les mécanismes de type 2, 3 et 4 sont réalisés en une seule étape. Il est donc possible de les distinguer à l'aide de leur constante de vitesse.

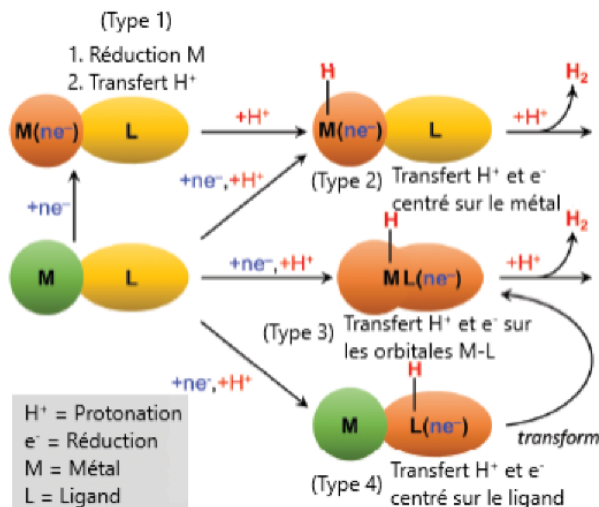


Figure 17. Types de mécanismes hétérolytiques⁷¹

Malgré toutes ces différentes expressions de mécanismes, il faut ajouter qu'il est également possible que ces mécanismes aient lieu par voie oxydative ou réductive (voir figure 18). Tout d'abord, suite à l'exposition à la lumière, un électron du photosensibilisateur (PS) est promu à l'orbitale supérieure, formant l'état de charge séparé. S'ensuit ensuite un transfert d'électron du PS vers le catalyseur (HEC), puis du donneur d'électron sacrificiel (SED) vers le photosensibilisateur

(voie oxydative). La voie réductrice suit également l'excitation du PS, mais le transfert d'électron entre SED et PS a lieu avant le transfert d'électron vers le HEC.⁸¹

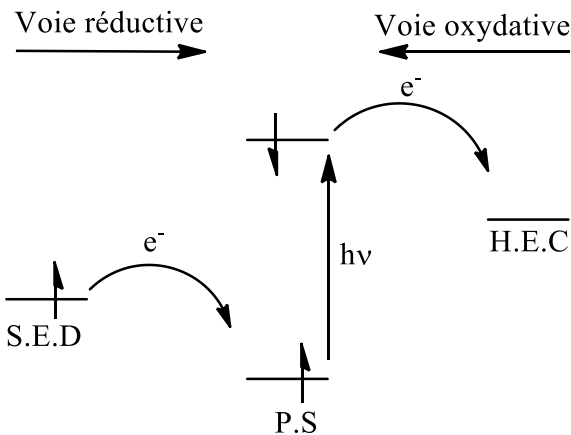


Figure 18. Voie oxydative et réductive pour l'altération du catalyseur

Finalement, il faut donner un mot sur les antécédents des cobaloximes. Le premier exemple de cobaloxime standard a été développé en 1983 par l'équipe de Jean-Marie Lehn, employant le $[\text{Ru}(\text{bpy})_3]^{2+}$ en tant que photosensibilisateur et le TEOA comme donneur d'électron sacrificiel.⁷²

La dégradation des cobaloximes est comme une légende urbaine. Tout le monde sait que ceux-ci se dégradent par oxydation ou réduction du double lien (dépendant des conditions réactionnelles), mais personne ne semble l'avoir démontré dans les conditions usuelles de photocatalyse. La dégradation en milieu fortement acide implique théoriquement la dissociation des liens avec le centre métallique et la dégradation de l'un des deux doubles liens du cobaloxime.⁷³ Les mécanismes de dégradation des cobaloximes ne sont pas démontrés, mais il est possible d'affirmer que généralement, plus les états de transitions des catalyseurs ont de faibles durées de vie, moins la dégradation est rapide, puisque le temps pour les réactions secondaires est réduit. Le Co^{I} semble également être l'espèce qui conduit à la dégradation, dans le cas des cobaloximes.⁷⁴ Ce point pourrait par ailleurs expliquer la formidable stabilité des porphyrines, puisque des études ont

démontré que celles-ci sont très stable malgré une réduction $\text{Co}^{\text{II}}/\text{Co}^{\text{I}}$ courante et généralement facile, ce qui suggère que son mécanisme réactionnel diffère de celui des cobaloximes, mais qui n'a malheureusement, à notre connaissance, pas encore été élucidé. Selon ce même article, le couple de réduction $\text{Co}^{\text{II}}/\text{Co}^{\text{I}}$ peut être observé à des pH compris entre 6.3 et 9, démontrant la forte relation entre le pH et le mécanisme réactionnel.⁷⁵ De plus, il est possible d'affirmer que le mécanisme réactionnel dépend en grande partie de la présence d'eau dans le solvant, rendant la production d'hydrogène moins efficace en milieu purement organique.⁶⁸

1.2.3 La photocatalyse dans l'eau

Le mécanisme généralement accepté pour les cobaloximes, dans la littérature pour la génération d'hydrogène dans l'eau est le même que dans les autres solvants, soit la perte initiale d'un ligand axial, pour permettre la production d'hydrogène sur ce site, gain d'un proton et d'un électron, gain d'un second électron puis réaction avec un proton en solution, qui libère de l'hydrogène (voir section 1.2.2 pour plus de détails).⁷⁶ Toutefois, il y a deux facteurs qui modifient l'approche à apporter à de tels systèmes. La première est la polarité du solvant, qui change évidemment la solubilité des molécules impliqués et permet le passage d'un système homolytique à hétérolytique. Cette considération change le mécanisme impliqué et peut augmenter ou diminuer l'efficacité de la production d'hydrogène.⁷⁷

Le second paramètre est le pH optimal pour la génération d'hydrogène. Celui-ci est évidemment beaucoup influencé par la structure du catalyseur ainsi que sa résistance aux milieux acido-basique. Le pH généralement considéré comme optimal dans la littérature avec l'acide ascorbique est un pH de 5.0.^{67,78} Toutefois, ce n'est pas toujours le cas. On pourrait croire que l'état du donneur d'électron, c'est-à-dire à quel point il est protoné est le seul facteur qui influence la production

d'hydrogène, mais en réalité, il est tout aussi important de considérer la solubilité du catalyseur (qui peut varier en fonction du pH) ainsi que ses groupes fonctionnels, qui peuvent parfois contribuer aux interactions électrostatiques qui favorise le rapprochement entre les molécules qui jouent un rôle clé dans la catalyse.⁷⁰ On retrouve différents systèmes ayant des pH optimaux tels qu'un pH 4⁷⁹⁻⁸², pH 4.5^{83,84}. Il est intéressant de constater que des systèmes sont testés jusqu'à pH 7⁷⁹, mais jamais au-delà, pour les catalyseurs organo-métalliques dans l'eau.

1.2.4 Aperçu des systèmes utilisés

Avant d'entamer cette section, il faut mentionner que des reviews concernant les donneurs d'électrons sacrificiels⁶⁴, les photosensibilisateurs^{25,85,86} ainsi que les catalyseurs^{69,76,86,87} sont disponibles. Le présent projet de recherche se concentrant sur les catalyseurs, c'est sur ces molécules que se concentre cette section.

Dans l'optique de produire de l'hydrogène en générant le minimum de déchets, de nombreux catalyseurs ont été développés en se basant sur des exemples naturels. On peut citer par exemple la porphyrine, qui est analogue à la chlorophylle alors que les photosensibilisateurs visent la conjugaison, de manière analogue aux carotènes. Un autre bon exemple sont les cobaloximes, qui sont analogues à la vitamine B12. On distingue généralement 4 familles de catalyseurs pour la génération d'hydrogène. Il y a les porphyrines, les cobaloximes, les dérivés de salen et les polypyridyl. Il y a bien sur d'autres catalyseurs qui ne sont pas membre de l'une des familles précédemment nommées, mais ils sont plutôt divers et il est difficile de tenter de les regrouper par similitudes. Ils tentent généralement d'imiter un design de la nature, tel que la ferrédoxine.

Les cobaloximes sont considéré comme la référence par excellence pour les systèmes de production d'hydrogène. Ils sont généralement utilisés dans le DMF, mais on observe de plus en plus de

systèmes qui les intègrent en phase aqueuse, avec un succès variable, en raison de la faible solubilité de la molécule de base. Alors que les catalyseurs de cobaloximes sont modérément stables, il est notable de constater un besoin d'affinité entre les molécules du système. On peut effectivement constater que les catalyseurs **1C** et **2C**, une fois associés (TON de 640), produisent moins d'hydrogène que lorsqu'ils sont utilisés individuellement (TON DE 1100 pour **1C** et 700 pour **2C**).⁷⁰ **3C** a la particularité d'être efficace à des concentrations très faibles (à l'état de trace en solution) et d'être stable en milieu acide, ce qui permet des usages alternatifs et surtout, permettant l'usage d'acide ascorbique en tant que donneur d'électron sacrificiel. Les milieux acides permettent habituellement une décoordination du centre métallique, ce qui conduit à une dégradation accrue du catalyseur en solution.⁸⁸ D'autres catalyseurs tels que le **4C** et le **5C** intègrent des groupements axiaux particuliers permettant d'améliorer l'activité catalytique de la molécule à l'étude. Le **4C** possède une fonction acide carboxylique (groupement électro attracteur) qui permet une médiation électronique plus facile en réduisant le potentiel requis pour oxyder le photosensibilisateur, ce qui rend plus facile la production d'hydrogène.⁸⁹ Les donneurs tels que le TEA et le TEOA sont souvent plus efficaces en milieu basiques (pH d'environ 7.5 à 10), ce qui limite parfois l'activité des catalyseurs. Ils ont toutefois une activité optimale en pH basique, dans les milieux organiques. D'autres complexes tels que le **5C** permettent de diminuer potentiellement la complexité des systèmes, en ce qu'ils regroupent le catalyseur et le photosensibilisateur dans une seule et même molécule. L'efficacité est très variable, mais de manière générale, elle est moindre que dans les systèmes dissociés.⁹⁰

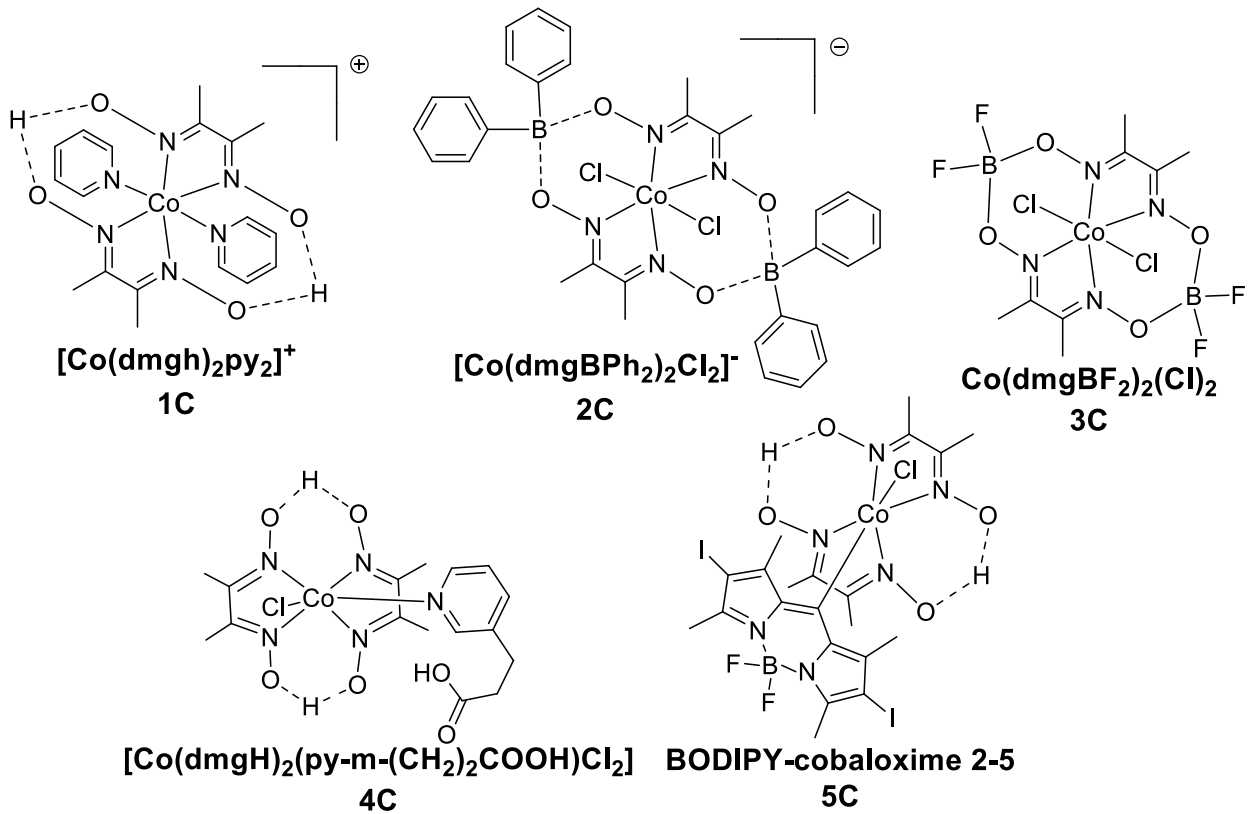


Figure 19. Catalyseurs à base de cobaloxime (1⁷⁰, 2⁷⁰, 3⁸⁸, 4⁸⁹, 5⁹⁰)

Un autre type de catalyseur très en vogue est la porphyrine. Celle-ci a le double avantage d'être très stable et d'être soluble dans les milieux entièrement aqueux. Le pH optimal pour l'usage de la porphyrine est aux environs de 6.8^{91,92} pour la plupart des systèmes, ce qui est particulier, puisque les systèmes utilisant l'acide ascorbique sont optimaux aux environs d'un pH de 5, habituellement.⁶⁷ D'autres systèmes sont rapportés directement au pH 5 en raison des résultats publiés précédemment, ce qui leur a directement permis de trouver des indices sur le mécanisme réactionnel, qui diffère selon le pH.⁷⁵ Le pH est un facteur clé de la performance catalytique, mais son implication exacte est encore mal comprise. Il est clair qu'il influence fortement les performances puisque beaucoup d'espèce en dépendent. Par exemple, l'acide ascorbique peut être déprotoné à deux reprises et son état est certainement caractéristique des performances, puisque

cela modifie la quantité de protons disponibles. Un autre point est la modulation des propriétés de quenching envers le photosensibilisateur. Plus le donneur peut quencher l'état excité du photosensibilisateur, plus la performance du système augmente, puisqu'on laisse peu de temps pour la formation de réaction secondaire indésirable.⁷⁵ Un autre composé, isolé d'une algue, permettrait une bonne activité catalytique. Le point principal de ce composé est qu'il agit à la fois en tant que catalyseur et en tant que photosensibilisateur, ce qui permet de réduire le nombre de composés impliqués ainsi que la complexité du système.⁹³

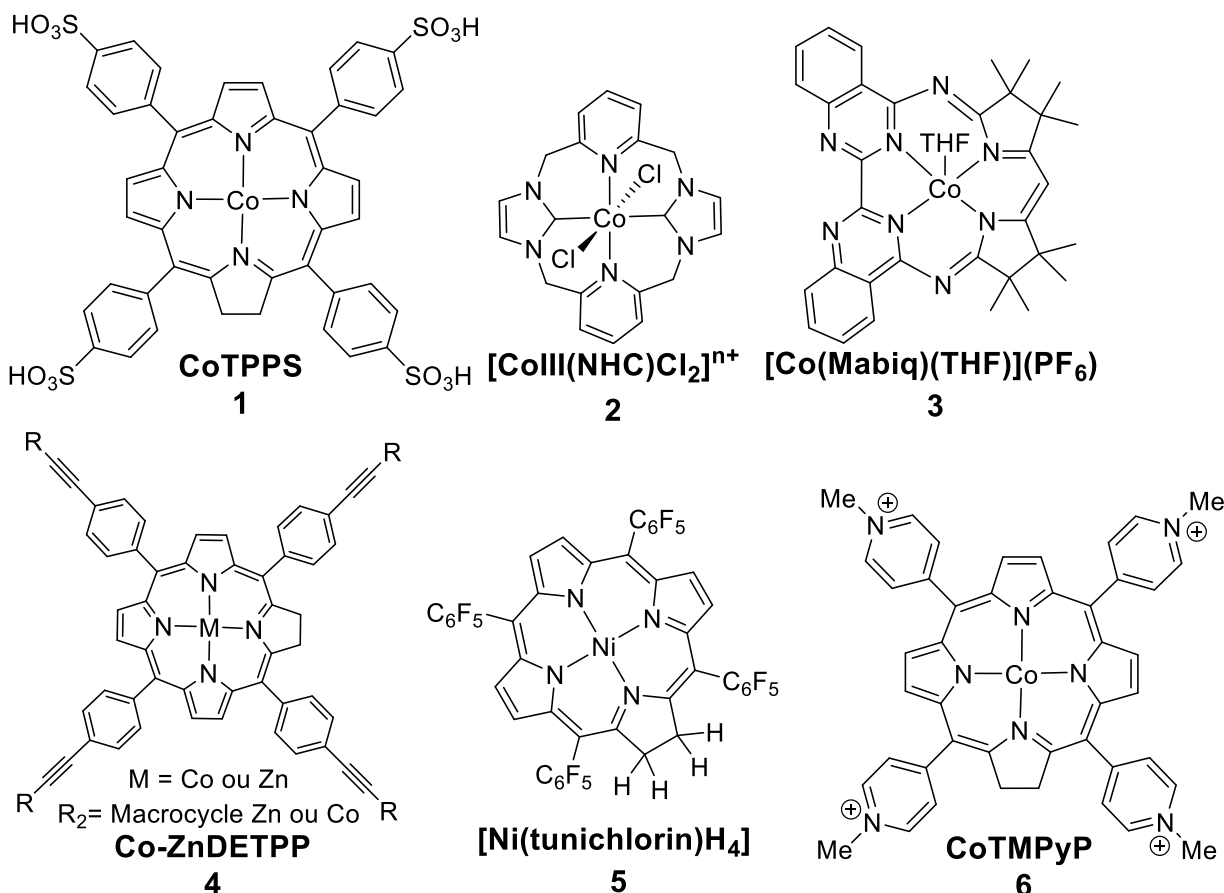


Figure 20. Catalyseurs à base de porphyrine (1⁹¹, 2⁷⁵, 3⁹⁴, 4⁹⁵, 5⁹³, 6⁹²)

Les dérivés de salen sont relativement rares, puisqu'ils sont également utilisés avec davantage de succès dans la réduction du CO₂ et la production de peroxyde d'hydrogène, mais on retrouve tout de même plusieurs exemples significatifs pour la production d'hydrogène. L'avantage principal de ces molécules est la synthèse très simple. Il suffit de placer de l'éthylènediamine et du N,N'-bis(salicylaldehyde)-éthylènediimine dans l'éthanol à reflux, en absence d'oxygène. Leur solubilité dans les solvants polaires, tel que l'eau, le méthanol et l'acétonitrile est avérée, ce qui en fait des molécules utiles pour la génération d'hydrogène en milieu aqueux. Les salen possèdent un côté très encombré et un autre, très peu encombré, ce qui aide à la formation de l'hydrure. Cette propriété a l'avantage de limiter les possibilités concernant le mécanisme réactionnel. Il serait peut-être possible de préciser ce mécanisme plus facilement à partir de ce type de molécules. Les catalyseurs 1 et 2 ont une activité surprenante, mais expliqués par la présence d'un PS particulièrement stable, les nanorodes de CdS.⁹⁶ Les dérivés de salen ont l'avantage d'être efficace dans une grande variété de pH, allant des pH relativement acides, requis pour l'utilisation de l'acide ascorbique, aux pH basiques requis pour l'utilisation d'autres SED tels que le TEA et le TEOA.^{97,98} Un autre avantage de ces catalyseurs est leur stabilité à long terme. Effectivement, dans les cas où ils ont été testés jusqu'à dégradation, ils pouvaient atteindre une durée de vie productive allant jusqu'à 37h.⁹⁹

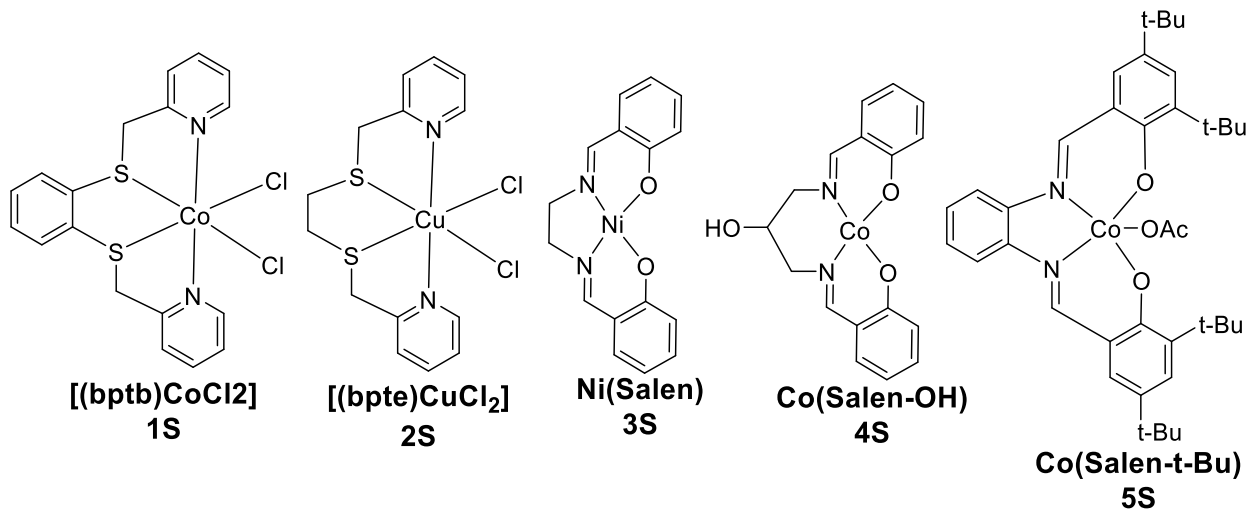


Figure 21. Catalyseurs à base de Salen et de dérivés (1,2⁹⁶ 3⁹⁷ 4⁹⁸ 5⁹⁹)

Pour terminer, il y a les catalyseurs à base de poly-pyridyl, dont l'objectif principal est d'imiter les photosensibilisateurs, pour plusieurs raisons. D'une part, il serait utile de combiner les propriétés du catalyseur et du photosensibilisateur dans une seule et même molécule pour à la fois réduire les coûts de production et simplifier le système. Toutefois, ces molécules ne peuvent pas produire d'hydrogène de manière suffisante sans l'ajout d'un photosensibilisateur. Un second objectif est d'accorder les niveaux énergétiques des deux molécules pour favoriser les transferts électroniques entre les molécules, ce qui tend à favoriser la production d'hydrogène. Les catalyseurs poly-pyridyl ont plusieurs avantages tels que leur solubilité dans l'eau ainsi que leur stabilité dans les milieux autant basiques qu'acides.⁸³ Ils sont très variables dans leur stabilité. Alors que certains peuvent durer jusqu'à une journée⁸⁰, d'autre ne restent intacts que quelques heures.^{79,100}

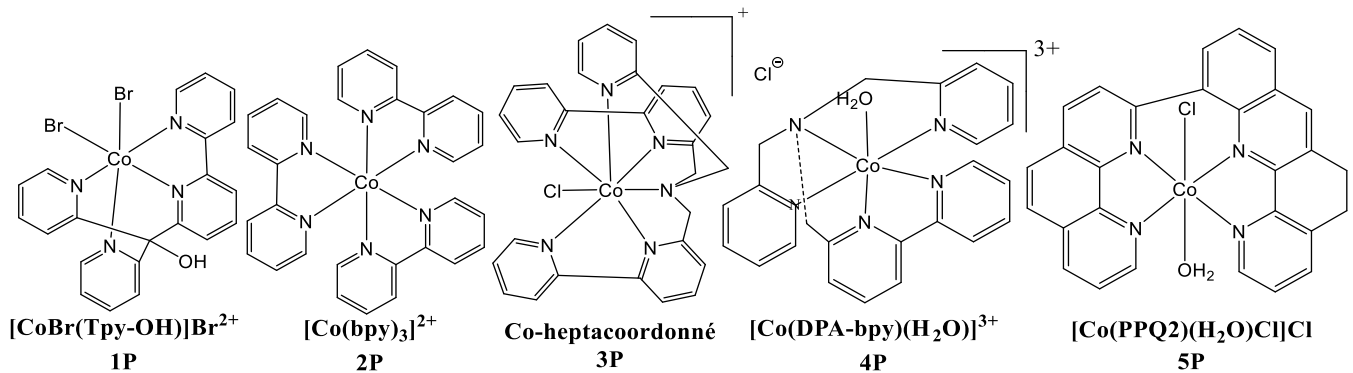


Figure 22. Catalyseurs à base de poly-pyridyl et de dérivés (1⁸⁰ 2¹⁰⁰ 3⁸¹ 4⁷⁹ 5⁸³)

1.2.5 Limites actuelles du domaine

La photocatalyse appliquée à la production d'hydrogène souffre actuellement de plusieurs limitations importantes. Il faut citer la dégradation rapide des molécules, leur faible rendement, la rareté et le coût des matériaux, le manque de récupération des composants, l'utilisation de solvants organiques nocifs et la disponibilité variable de l'énergie solaire à travers le monde.

La principale limitation à l'utilisation à l'échelle mondiale est la dégradation rapide des systèmes, en particulier des photosensibilisateurs. Plusieurs pistes ont été apportées dans le but de régler ce problème, mais cela a en général conduit à des molécules stables, mais dont la production d'hydrogène était tout de même très faible¹⁰¹, ce qui nous amène au second point. La faible production d'hydrogène est associée à l'instabilité des systèmes, mais également à un manque de compatibilité chimique. Notre groupe de recherche est principalement axé sur cette dernière problématique, en ce qu'il cherche à favoriser les transferts électroniques directionnels entre photosensibilisateurs et catalyseurs.^{102,103} Un fort engouement est présent pour ce type d'approche, parce que les systèmes associés ont en général de meilleures performances que les systèmes

dissociés, résultant en une plus grande production d'hydrogène que les systèmes dissociés, ce qui semble démontrer la pertinence de cette approche.¹⁰⁴⁻¹⁰⁸

D'autres problématiques, tel que la pénurie probable de certains éléments du tableau périodique, tel que l'hélium, qui est très discuté ces derniers temps, mais également le lithium, le cobalt et autres métaux semi-précieux est à prévoir.¹⁰⁹⁻¹¹¹ La difficulté de récupération de la plupart des métaux est un enjeu supplémentaire, sur lequel de nombreux groupes de recherches, autant académiques qu'industriels, se sont penchés.¹¹²

Il est plutôt difficile de valoriser le mérite environnemental d'un procédé qui utilise des solvants organiques en tant que solvant principal. L'utilisation de l'eau en tant que solvant est un avantage que seul l'électrolyse permet actuellement et il serait profitable que la photolyse de l'eau en bénéficie également. Dans cette optique, plusieurs molécules ont été testés dans l'eau. L'objectif était donc de paver la voie à de nouveaux systèmes stables dans l'eau et ayant une bonne production d'hydrogène.

Le climat particulier du Québec est un autre enjeu préoccupant dans ce domaine. La disponibilité de l'énergie solaire est généralement inverse à la demande, qui augmente lorsque la lumière solaire n'est plus disponible. On peut également ajouter que la quantité de lumière reçue et la grande variété de climats du Québec ajoute du défi à cette problématique déjà de taille. Ce faisant, il est primordial de la stocker, mais également d'améliorer la récupération de la lumière solaire pour pouvoir répondre à la demande.¹¹³

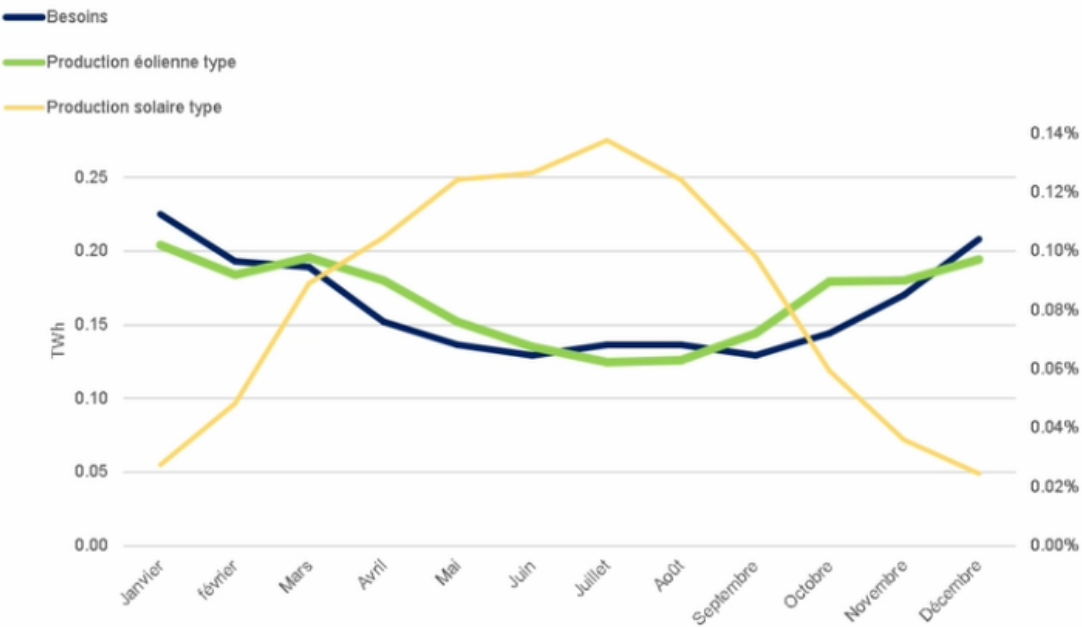


Figure 23. Comparaison entre l'énergie solaire produite et les besoins en énergie du Québec¹¹⁴

La durée d'une maîtrise étant plutôt limitée, il n'était pas possible d'adresser tous ces problèmes. C'est pourquoi il a été nécessaire de faire un choix dans la problématique à travailler. Ayant plusieurs collègues déjà concentrés sur les problématiques du transfert électronique directionnel ainsi que sur la stabilité à long terme des photosensibilisateurs, l'évidence s'imposait que la direction à prendre était celle des systèmes solubles dans l'eau. Le développement, la conception et la validation de ces système est une tâche très ambitieuse et plusieurs directions différentes ont été explorés. La première étape était de se décider sur la famille de molécule à étudier. Des catalyseurs à base de poly-pyridyl nous ont été apportés par l'équipe du Dr. Alvin Holder. Nous avons ensuite porté notre attention sur les catalyseurs à base de cobaloxime. Les deux principaux problèmes de ces catalyseurs en lien avec notre étude sont leur instabilité en solution et leur insolubilité dans l'eau. Nous avons exploré, en collaboration avec Olivier Schott, une modification de la structure qui pourrait s'avérer prometteuse. L'étude de systèmes solubles dans l'eau a été entreprise, mais en même temps, on nous a apporté une famille de molécule inédite pour la

production d'hydrogène : les catalyseurs à base de ligands N-imidoyl amidine. Un choix a été nécessaire étant donné le peu de temps restant à la formation. Puisque l'étude d'une nouvelle famille de molécule est une avenue prometteuse et inédite, cette avenue fut privilégiée, au détriment des catalyseurs hydro-solubles de cobaloxime. Cette étude était concordante avec les buts visés par la formation et nous a permis de renouveler l'intérêt scientifique envers la découverte de nouvelles familles de catalyseurs pour la photolyse de l'eau.

Pour conclure, les nombreuses limitations de la photocatalyse en font une méthode très peu compétitive à l'heure actuelle, mais son potentiel justifie que ces nombreux problèmes soient adressés, dans le but de réduire l'empreinte carbone de nos sociétés et de permettre l'accès à une source d'énergie abondante et sécuritaire.

Bibliographie

- (1) Keeling, C. D. The Keeling Curve.
- (2) Lamarre, S.; Delisle, F.; Leblond, V.; Nolet, E.; Nolet, S.; Normandin, A.; Rioux, C.; Rousseau, P.-L.; Turcotte, V.; Paradis, J. *Inventaire Québécois Des Émissions de Gaz à Effet de Serre En 2017 et Leur Évolution Depuis 1990*; 2019.
- (3) *Indicateurs canadiens de durabilité de l'environnement - Émissions de gaz à effet de serre*; 2020; p 24.
- (4) Gouvernement du Canada. *L'accord de Paris*.
- (5) Whitmore, J.; Pineau, P.-O. *État de l'énergie au Québec 2019*; 2018; p 68.
- (6) Baril, H. La Redécouverte de l'hydrogène. *La presse*. January 27, 2021.
- (7) Hydro-Québec exploitera l'un des électrolyseurs les plus puissants du monde pour la production d'hydrogène vert. December 8, 2020.
- (8) Xia, B.; Zhang, Y.; Shi, B.; Ran, J.; Davey, K.; Qiao, S.-Z. Photocatalysts for Hydrogen Evolution Coupled with Production of Value-Added Chemicals. *Small Methods* **2020**, 4 (7), 2000063. <https://doi.org/10.1002/smtd.202000063>.
- (9) Shaner, M. R.; Atwater, H. A.; Lewis, N. S.; McFarland, E. W. A Comparative Technoeconomic Analysis of Renewable Hydrogen Production Using Solar Energy. *Energy Environ. Sci.* **2016**, 9 (7), 2354–2371. <https://doi.org/10.1039/C5EE02573G>.
- (10) Armaroli, N.; Balzani, V. The Hydrogen Issue. *ChemSusChem* **2011**, 4 (1), 21–36. <https://doi.org/10.1002/cssc.201000182>.
- (11) Balzani, V.; Credi, A.; Venturi, M. Photochemical Conversion of Solar Energy. *ChemSusChem* **2008**, 1, 26–58. <https://doi.org/10.1002/cssc.200700087>.
- (12) Report from the international energy agency. The Future of Hydrogen. 9.
- (13) Moriarty, P.; Honnery, D. *Rise and Fall of the Carbon Civilisation: Resolving Global Environmental and Resource Problems*; Springer: New York, 2011.
- (14) Manifeste négaWatt. *LnWI Ressources gr315 hr.ai*; 2012.
- (15) Ringsmuth, A. K.; Landsberg, M. J.; Hankamer, B. Can Photosynthesis Enable a Global Transition from Fossil Fuels to Solar Fuels, to Mitigate Climate Change and Fuel-Supply Limitations? *Renewable and Sustainable Energy Reviews* **2016**, 62, 134–163. <https://doi.org/10.1016/j.rser.2016.04.016>.
- (16) Jin Zhong Zhang; Jinghong Li; Yat Li; Yiping Zhao. *Hydrogen Generation, Storage and Utilization*; John Wiley & sons. Inc and ScienceWise publishing: New Jersey, 2014.
- (17) Curtin, S.; Ganghi, J. State of the states: Fuel cells in America 2017, 2018.
- (18) Duggan, J. LZ129 Hindenburg - The Complete Story. In *LZ129 Hindenburg - The complete story*; 2002.
- (19) De syon, G. Why the Hindenburg Disaster Is Still Worth Remembering. May 5, 2017.
- (20) Airgas. Safety Data Sheet: Hydrogen.
- (21) Sigma Aldrich. Safety Data Sheet: Hydrogen.
- (22) Toyota: Voiture à l'hydrogène.
- (23) Mazliak, P.; Laval-Martin, D. *Physiologie végétale I - Nutrition et métabolisme*; Hermann: Paris, 1995.
- (24) Darnell, J. E.; Lodish, H.; Baltimore, D. *Molecular cell biology*; Scientific American Books, 1986.

- (25) Berardi, S.; Drouet, S.; Francàs, L.; Gimbert-Suriñach, C.; Guttentag, M.; Richmond, C.; Stoll, T.; Llobet, A. Molecular Artificial Photosynthesis. *Chem. Soc. Rev.* **2014**, *43* (22), 7501–7519. <https://doi.org/10.1039/C3CS60405E>.
- (26) Faucher, J.; Lachaîne, R. *Campbell BIOLOGIE*, 4th ed.; ERPI, 2012.
- (27) Frischmann, P. D.; Mahata, K.; Würthner, F. Powering the Future of Molecular Artificial Photosynthesis with Light-Harvesting Metallosupramolecular Dye Assemblies. *Chem. Soc. Rev.* **2013**, *42* (4), 1847–1870. <https://doi.org/10.1039/C2CS35223K>.
- (28) *From Non-Covalent Assemblies to Molecular Machines*; Sauvage, J.-P., Gaspard, P., Eds.; Wiley-VCH: Weinheim, 2011.
- (29) U.S Energy Information Administration. *Hydrogen Explained*.
- (30) Kujirai, T.; Yamaguchi, A.; Fujita, T.; Abe, H.; Miyauchi, M. Active Site Separation of Photocatalytic Steam Reforming of Methane Using a Gas-Phase Photoelectrochemical System. *Chem. Commun.* **2021**. <https://doi.org/10.1039/D1CC02914B>.
- (31) Wang, J.; Wei, S.; Wang, Q.; Sundén, B. Transient Numerical Modeling and Model Predictive Control of an Industrial-Scale Steam Methane Reforming Reactor. *International Journal of Hydrogen Energy* **2021**, *46* (29), 15241–15256. <https://doi.org/10.1016/j.ijhydene.2021.02.123>.
- (32) Ma, R.; Xu, B.; Zhang, X. Catalytic Partial Oxidation (CPOX) of Natural Gas and Renewable Hydrocarbons/Oxygenated Hydrocarbons-A Review. *Catalysis Today* **2019**, *338*. <https://doi.org/10.1016/j.cattod.2019.06.025>.
- (33) Han, B.; Wei, W.; Li, M.; Sun, K.; Hu, Y. H. A Thermo-Photo Hybrid Process for Steam Reforming of Methane: Highly Efficient Visible Light Photocatalysis. *Chem. Commun.* **2019**, *55* (54), 7816–7819. <https://doi.org/10.1039/C9CC04193A>.
- (34) Pham, X.-H.; Ashik, U. P. M.; Hayashi, J.-I.; Pérez Alonso, A.; Pla, D.; Gómez, M.; Pham Minh, D. Review on the Catalytic Tri-Reforming of Methane - Part II: Catalyst Development. *Applied Catalysis A: General* **2021**, *623*, 118286. <https://doi.org/10.1016/j.apcata.2021.118286>.
- (35) Valecillo, J.; Iglesias-Vázquez, S.; Landa, L.; Remiro, A.; Bilbao, J.; Gayubo, A. G. Insights into the Reaction Routes for H₂ Formation in the Ethanol Steam Reforming on a Catalyst Derived from NiAl₂O₄ Spinel. *Energy Fuels* **2021**. <https://doi.org/10.1021/acs.energyfuels.1c01670>.
- (36) Babatabar, M. A.; Saidi, M. Hydrogen Production via Integrated Configuration of Steam Gasification Process of Biomass and Water-Gas Shift Reaction: Process Simulation and Optimization. *International Journal of Energy Research* **2021**, *n/a* (n/a). <https://doi.org/10.1002/er.7087>.
- (37) Zhao, B.; Yang, H.; Zhang, H.; Zhong, C.; Wang, J.; Zhu, D.; Guan, H.; Sun, L.; Yang, S.; Chen, L.; Xie, H. Study on Hydrogen-Rich Gas Production by Biomass Catalytic Pyrolysis Assisted with Magnetic Field. *Journal of Analytical and Applied Pyrolysis* **2021**, *157*, 105227. <https://doi.org/10.1016/j.jaap.2021.105227>.
- (38) Yong, Y. S.; Abdul Rasid, R. Process Simulation of Hydrogen Production through Biomass Gasification: Introduction of Torrefaction Pre-Treatment. *International Journal of Hydrogen Energy* **2021**. <https://doi.org/10.1016/j.ijhydene.2021.07.010>.
- (39) Zhang, T.; Jiang, D.; Li, Y.; Zhang, H.; Zhang, Z.; Petracchini, F.; Paolini, V.; Zhang, Y.; Yue, T.; Zhang, Q. Study of the Interrelationship between Nano-TiO₂ Addition and Photo-Fermentative Bio-Hydrogen Production of Corn Straw. *Bioresource Technology* **2021**, *338*, 125549. <https://doi.org/10.1016/j.biortech.2021.125549>.

- (40) Łukajtis, R.; Hołowacz, I.; Kucharska, K.; Glinka, M.; Rybarczyk, P.; Przyjazny, A.; Kamiński, M. Hydrogen Production from Biomass Using Dark Fermentation. *Renewable and Sustainable Energy Reviews* **2018**, *91*, 665–694. <https://doi.org/10.1016/j.rser.2018.04.043>.
- (41) Liu, H.; Ru, G.; Zhang, Z.; Li, Y.; Xia, C.; Lu, C.; Zhang, Q. Experimental Study on Optimization of Initial PH for Photo-Fermentation Bio-Hydrogen under Different Enzymatic Hydrolysis of Chlorella Vulgaris. *Bioresource Technology* **2021**, *338*, 125571. <https://doi.org/10.1016/j.biortech.2021.125571>.
- (42) Hosseinzadeh, A.; Zhou, J. L.; Li, X.; Afsari, M.; Altaee, A. Techno-Economic and Environmental Impact Assessment of Hydrogen Production Processes Using Bio-Waste as Renewable Energy Resource. *Renewable and Sustainable Energy Reviews* **2022**, *156*, 111991. <https://doi.org/10.1016/j.rser.2021.111991>.
- (43) Dincer, I.; Acar, C. Review and Evaluation of Hydrogen Production Methods for Better Sustainability. *International Journal of Hydrogen Energy* **2015**, *40* (34), 11094–11111. <https://doi.org/10.1016/j.ijhydene.2014.12.035>.
- (44) Bhandari, R.; Shah, R. R. Hydrogen as Energy Carrier: Techno-Economic Assessment of Decentralized Hydrogen Production in Germany. *Renewable Energy* **2021**, *177*, 915–931. <https://doi.org/10.1016/j.renene.2021.05.149>.
- (45) Saksono, N.; Batubara, T.; Bismo, S. Hydrogen Production by Plasma Electrolysis Reactor of KOH-Ethanol Solution. *IOP Conf. Ser.: Mater. Sci. Eng.* **2016**, *162* (1), 012010. <https://doi.org/10.1088/1757-899X/162/1/012010>.
- (46) Chaffin, J. H.; Bobbio, S. M.; Inyang, H. I.; Kaanagbara, L. Hydrogen Production by Plasma Electrolysis. *Journal of Energy Engineering* **2006**, *132* (3), 104–108. [https://doi.org/10.1061/\(ASCE\)0733-9402\(2006\)132:3\(104\)](https://doi.org/10.1061/(ASCE)0733-9402(2006)132:3(104)).
- (47) Züttel, A. Hydrogen Storage Methods. *Naturwissenschaften* **2004**, *91* (4), 157–172. <https://doi.org/10.1007/s00114-004-0516-x>.
- (48) Jiang, W.; Sun, P.; Li, P.; Zuo, Z.; Huang, Y. Transient Thermal Behavior of Multi-Layer Insulation Coupled with Vapor Cooled Shield Used for Liquid Hydrogen Storage Tank. *Energy* **2021**, *231*, 120859. <https://doi.org/10.1016/j.energy.2021.120859>.
- (49) Xu, X.; Xu, H.; Zheng, J.; Chen, L.; Wang, J. A High-Efficiency Liquid Hydrogen Storage System Cooled by a Fuel-Cell-Driven Refrigerator for Hydrogen Combustion Heat Recovery. *Energy Conversion and Management* **2020**, *226*, 113496. <https://doi.org/10.1016/j.enconman.2020.113496>.
- (50) Krenn, A.; Desenberg, D. Return to Service of a Liquid Hydrogen Storage Sphere. *IOP Conf. Ser.: Mater. Sci. Eng.* **2020**, *755*, 012023. <https://doi.org/10.1088/1757-899X/755/1/012023>.
- (51) Verevkin, S. P.; Konnova, M. E.; Zherikova, K. V.; Pimerzin, A. A. Sustainable Hydrogen Storage: Thermochemistry of Amino-Alcohols as Seminal Liquid Organic Hydrogen Carriers. *The Journal of Chemical Thermodynamics* **2021**, *163*, 106591. <https://doi.org/10.1016/j.jct.2021.106591>.
- (52) Wu, Y.; Guo, Y.; Yu, H.; Jiang, X.; Zhang, Y.; Qi, Y.; Fu, K.; Xie, L.; Li, G.; Zheng, J.; Li, X. Nonstoichiometric Yttrium Hydride-Promoted Reversible Hydrogen Storage in a Liquid Organic Hydrogen Carrier. *CCS Chemistry* **2020**, *3* (3), 974–984. <https://doi.org/10.31635/ccschem.020.202000255>.
- (53) Lee, S.; Kim, T.; Han, G.; Kang, S.; Yoo, Y.-S.; Jeon, S.-Y.; Bae, J. Comparative Energetic Studies on Liquid Organic Hydrogen Carrier: A Net Energy Analysis. *Renewable and Sustainable Energy Reviews* **2021**, *150*, 111447. <https://doi.org/10.1016/j.rser.2021.111447>.

- (54) He, J. H.; Zhang, J.; Zhou, X. J.; Chen, J. N.; Yu, L. P.; Jiang, L. K.; Lu, X. Z.; Chen, X. M.; Zhou, D. W. Hydrogen Storage Properties of Mg_{98.5}Gd₁Zn_{0.5} and Mg_{98.5}Gd_{0.5}Y_{0.5}Zn_{0.5} Alloys Containing LPSO Phases. *International Journal of Hydrogen Energy* **2021**. <https://doi.org/10.1016/j.ijhydene.2021.07.140>.
- (55) Zhang, J.; Li, Z.; Wu, Y.; Guo, X.; Ye, J.; Yuan, B.; Wang, S.; Jiang, L. Recent Advances on the Thermal Destabilization of Mg-Based Hydrogen Storage Materials. *RSC Adv.* **2018**, *9* (1), 408–428. <https://doi.org/10.1039/C8RA05596C>.
- (56) Akbayrak, S.; Özkar, S. Ammonia Borane as Hydrogen Storage Materials. *International Journal of Hydrogen Energy* **2018**, *43* (40), 18592–18606. <https://doi.org/10.1016/j.ijhydene.2018.02.190>.
- (57) Castilla-Martinez, C. A.; Roussignol, L.; Demirci, U. B. Magnesium Hydrazinidoborane: Synthesis, Characterization and Features for Solid-State Hydrogen Storage. *International Journal of Hydrogen Energy* **2021**. <https://doi.org/10.1016/j.ijhydene.2021.07.169>.
- (58) Ghellab, T.; Charifi, Z.; Baaziz, H.; Uğur, Ş.; Uğur, G.; Soyalp, F. First Principles Study of Hydrogen Storage Material NaBH₄and LiAlH₄compounds: Electronic Structure and Optical Properties. *Phys. Scr.* **2016**, *91* (4), 045804. <https://doi.org/10.1088/0031-8949/91/4/045804>.
- (59) Mao, J. F.; Yu, X. B.; Guo, Z. P.; Poh, C. K.; Liu, H. K.; Wu, Z.; Ni, J. Improvement of the LiAlH₄–NaBH₄ System for Reversible Hydrogen Storage. *J. Phys. Chem. C* **2009**, *113* (24), 10813–10818. <https://doi.org/10.1021/jp808269v>.
- (60) Vivek; Sharma, M.; Sharma, R. Plumbene: A next Generation Hydrogen Storage Medium. *International Journal of Hydrogen Energy* **2021**. <https://doi.org/10.1016/j.ijhydene.2021.07.159>.
- (61) Feng, D.; Zhou, D.; Zhao, Z.; Zhai, T.; Yuan, Z.; Sun, H.; Ren, H.; Zhang, Y. Progress of Graphene and Loaded Transition Metals on Mg-Based Hydrogen Storage Alloys. *International Journal of Hydrogen Energy* **2021**. <https://doi.org/10.1016/j.ijhydene.2021.07.155>.
- (62) Li, X.; Fu, Y.; Xie, Y.; Cong, L.; Yu, H.; Zhang, L.; Li, Y.; Han, S. Effect of Ni/Tubular g-C₃N₄ on Hydrogen Storage Properties of MgH₂. *International Journal of Hydrogen Energy* **2021**. <https://doi.org/10.1016/j.ijhydene.2021.07.166>.
- (63) Xu, Y.-J. Promises and Challenges in Photocatalysis. *Frontiers in Catalysis* **2021**, *1*, 6. <https://doi.org/10.3389/fctls.2021.708319>.
- (64) Pellegrin, Y.; Odobel, F. Sacrificial Electron Donor Reagents for Solar Fuel Production. *Comptes Rendus Chimie* **2017**, *20* (3), 283–295. <https://doi.org/10.1016/j.crci.2015.11.026>.
- (65) Canada, N. R. *renewable-energy-facts*. <https://www.nrcan.gc.ca/science-and-data/data-and-analysis/energy-data-and-analysis/energy-facts/renewable-energy-facts/20069> (accessed 2021-11-16).
- (66) Statistica. *Capacité de production d'énergie solaire Amérique du Nord* **2018**. Statista. <https://fr.statista.com/statistiques/828857/capacite-production-energie-solaire-amerique-du-nord/> (accessed 2021-11-16).
- (67) Natali, M. Elucidating the Key Role of PH on Light-Driven Hydrogen Evolution by a Molecular Cobalt Catalyst. *ACS Catal.* **2017**, *7* (2), 1330–1339. <https://doi.org/10.1021/acscatal.6b03087>.
- (68) Chen-Hsiung, H.; Belete B., B. Photocatalytic Hydrogen Evolution from Neutral Aqueous Solution by a Water-Soluble Cobalt(II) Porphyrin. **2018**, *2*, 2036–2043. <https://doi.org/10.1039/c8se00253c>.

- (69) Wakerley, D. W.; Reisner, E. Development and Understanding of Cobaloxime Activity through Electrochemical Molecular Catalyst Screening. *Phys. Chem. Chem. Phys.* **2014**, *16* (12), 5739–5746. <https://doi.org/10.1039/C4CP00453A>.
- (70) Hofmeister, E.; Woo, J.; Ullrich, T.; Petermann, L.; Hanus, K.; Rau, S.; Kahnt, A.; von Delius, M. *Cobaloxime-Based Double Complex Salts as Efficient and Versatile Catalysts for the Light-Driven Hydrogen Evolution Reaction*; preprint; 2020. <https://doi.org/10.26434/chemrxiv.11537661.v1>.
- (71) Koshiba, K.; Yamauchi, K.; Sakai, K. Consecutive Ligand-Based PCET Processes Affording a Doubly Reduced Nickel Pyrazinedithiolate Which Transforms into a Metal Hydride Required to Evolve H₂. *Dalton Trans.* **2019**, *48* (2), 635–640. <https://doi.org/10.1039/C8DT04497J>.
- (72) Hawecker, J.; Lehn, J. M.; Ziessel, R. Efficient Homogeneous Photochemical Hydrogen Generation and Water Reduction Mediated by Cobaloxime or Macroyclic Cobalt Complexes. *Nouv. J. Chim* **1983**, *7*, 271–277.
- (73) Alcock, N. W.; Golding, B. T.; Hall, D. R.; Horn, U.; Watson, W. P. Degradation of Cobaloximes to Derivatives of Imidazo[1,2-a]Pyridine. *J. Chem. Soc., Perkin Trans. I* **1975**, No. 4, 386–394. <https://doi.org/10.1039/P19750000386>.
- (74) Smolentsev, G.; Cecconi, B.; Guda, A.; Chavarot-Kerlidou, M.; van Bokhoven, J. A.; Nachtegaal, M.; Artero, V. Microsecond X-Ray Absorption Spectroscopy Identification of CoI Intermediates in Cobaloxime-Catalyzed Hydrogen Evolution. *Chemistry – A European Journal* **2015**, *21* (43), 15158–15162. <https://doi.org/10.1002/chem.201502900>.
- (75) Kawano, K.; Yamauchi, K.; Sakai, K. A Cobalt–NHC Complex as an Improved Catalyst for Photochemical Hydrogen Evolution from Water. *Chem. Commun.* **2014**, *50* (69), 9872–9875. <https://doi.org/10.1039/C4CC03493G>.
- (76) Artero, V.; Chavarot-Kerlidou, M.; Fontecave, M. Splitting Water with Cobalt. *Angewandte Chemie International Edition* **2011**, *50* (32), 7238–7266. <https://doi.org/10.1002/anie.201007987>.
- (77) Artero, V.; Fontecave, M. Some General Principles for Designing Electrocatalysts with Hydrogenase Activity. *Coordination Chemistry Reviews* **2005**, *249* (15), 1518–1535. <https://doi.org/10.1016/j.ccr.2005.01.014>.
- (78) Krishnan, C. V.; Sutin, N. Homogeneous Catalysis of the Photoreduction of Water by Visible Light. 2. Mediation by a Tris (2, 2'-Bipyridine) Ruthenium (II)-Cobalt (II) Bipyridine System. *Journal of the American Chemical Society* **1981**, *103* (8), 2141–2142.
- (79) Singh, W. M.; Baine, T.; Kudo, S.; Tian, S.; Ma, X. A. N.; Zhou, H.; DeYonker, N. J.; Pham, T. C.; Bollinger, J. C.; Baker, D. L.; Yan, B.; Webster, C. E.; Zhao, X. Electrocatalytic and Photocatalytic Hydrogen Production in Aqueous Solution by a Molecular Cobalt Complex. *Angewandte Chemie International Edition* **2012**, *51* (24), 5941–5944. <https://doi.org/10.1002/anie.201200082>.
- (80) Guttentag, M.; Rodenberg, A.; Bachmann, C.; Senn, A.; Hamm, P.; Alberto, R. A Highly Stable Polypyridyl-Based Cobalt Catalyst for Homo- and Heterogeneous Photocatalytic Water Reduction. *Dalton Trans.* **2012**, *42* (2), 334–337. <https://doi.org/10.1039/C2DT31699D>.
- (81) Lucarini, F.; Fize, J.; Morozan, A.; Marazzi, M.; Natali, M.; Pastore, M.; Artero, V.; Ruggi, A. Insights into the Mechanism of Photosynthetic H₂ Evolution Catalyzed by a Heptacoordinate Cobalt Complex. *Sustainable Energy Fuels* **2020**, *4* (2), 589–599. <https://doi.org/10.1039/C9SE00434C>.

- (82) Wang, F.; Wang, W.-G.; Wang, X.-J.; Wang, H.-Y.; Tung, C.-H.; Wu, L.-Z. A Highly Efficient Photocatalytic System for Hydrogen Production by a Robust Hydrogenase Mimic in an Aqueous Solution. *Angewandte Chemie International Edition* **2011**, *50* (14), 3193–3197. <https://doi.org/10.1002/anie.201006352>.
- (83) Tong, L.; Kopecky, A.; Zong, R.; Gagnon, K. J.; Ahlquist, M. S. G.; Thummel, R. P. Light-Driven Proton Reduction in Aqueous Medium Catalyzed by a Family of Cobalt Complexes with Tetradentate Polypyridine-Type Ligands. *Inorg. Chem.* **2015**, *54* (16), 7873–7884. <https://doi.org/10.1021/acs.inorgchem.5b00915>.
- (84) Reynal, A.; Pastor, E.; Gross, M. A.; Selim, S.; Reisner, E.; Durrant, J. R. Unravelling the PH-Dependence of a Molecular Photocatalytic System for Hydrogen Production. *Chem. Sci.* **2015**, *6* (8), 4855–4859. <https://doi.org/10.1039/C5SC01349F>.
- (85) Yuan, Y.-J.; Yu, Z.-T.; Chen, D.-Q.; Zou, Z.-G. Metal-Complex Chromophores for Solar Hydrogen Generation. *Chem. Soc. Rev.* **2017**, *46* (3), 603–631. <https://doi.org/10.1039/C6CS00436A>.
- (86) Dalle, K. E.; Warnan, J.; Leung, J. J.; Reuillard, B.; Karmel, I. S.; Reisner, E. Electro- and Solar-Driven Fuel Synthesis with First Row Transition Metal Complexes. *Chem. Rev.* **2019**, *119* (4), 2752–2875. <https://doi.org/10.1021/acs.chemrev.8b00392>.
- (87) Queyriaux, N.; Jane, R. T.; Massin, J.; Artero, V.; Chavarot-Kerlidou, M. Recent Developments in Hydrogen Evolving Molecular Cobalt(II)-Polypyridyl Catalysts. *Coordination Chemistry Reviews* **2015**, *304–305*, 3–19. <https://doi.org/10.1016/j.ccr.2015.03.014>.
- (88) Connolly, P.; Espenson, J. H. Cobalt-Catalyzed Evolution of Molecular Hydrogen. *Inorg. Chem.* **1986**, *25* (16), 2684–2688. <https://doi.org/10.1021/ic00236a006>.
- (89) Wang, J.; Li, C.; Zhou, Q.; Wang, W.; Hou, Y.; Zhang, B.; Wang, X. Enhanced Photocatalytic Hydrogen Production by Introducing the Carboxylic Acid Group into Cobaloxime Catalysts. *Dalton Trans.* **2015**, *44* (40), 17704–17711. <https://doi.org/10.1039/C5DT02645H>.
- (90) Bartelmess, J.; Francis, A. J.; El Roz, K. A.; Castellano, F. N.; Weare, W. W.; Sommer, R. D. Light-Driven Hydrogen Evolution by BODIPY-Sensitized Cobaloxime Catalysts. *Inorg. Chem.* **2014**, *53* (9), 4527–4534. <https://doi.org/10.1021/ic500218q>.
- (91) Beyene, B. B.; Hung, C.-H. Photocatalytic Hydrogen Evolution from Neutral Aqueous Solution by a Water-Soluble Cobalt(II) Porphyrin. *Sustainable Energy Fuels* **2018**, *2* (9), 2036–2043. <https://doi.org/10.1039/C8SE00253C>.
- (92) Zhang, X.; Cibian, M.; Call, A.; Yamauchi, K.; Sakai, K. Photochemical CO₂ Reduction Driven by Water-Soluble Copper(I) Photosensitizer with the Catalysis Accelerated by Multi-Electron Chargeable Cobalt Porphyrin. *ACS Catal.* **2019**, *9* (12), 11263–11273. <https://doi.org/10.1021/acscatal.9b04023>.
- (93) Wu, Z.-Y.; Xue, H.; Wang, T.; Guo, Y.; Meng, Y.-S.; Li, X.; Zheng, J.; Brückner, C.; Rao, G.; Britt, R. D.; Zhang, J.-L. Mimicking of Tunichlorin: Deciphering the Importance of a β-Hydroxyl Substituent on Boosting the Hydrogen Evolution Reaction. *ACS Catal.* **2020**, *10* (3), 2177–2188. <https://doi.org/10.1021/acscatal.9b03985>.
- (94) Tok, G. C.; Freiberg, A. T. S.; Gasteiger, H. A.; Hess, C. R. Electrocatalytic H₂ Evolution by the Co-Mabiq Complex Requires Tempering of the Redox-Active Ligand. *ChemCatChem* **2019**, *11* (16), 3973–3981. <https://doi.org/10.1002/cctc.201900953>.
- (95) Chen, Z.; Wang, J.; Zhang, S.; Zhang, Y.; Zhang, J.; Li, R.; Peng, T. Porphyrin-Based Conjugated Polymers as Intrinsic Semiconducting Photocatalysts for Robust H₂ Generation

- under Visible Light. *ACS Appl. Energy Mater.* **2019**, *2* (8), 5665–5676. <https://doi.org/10.1021/acsaem.9b00811>.
- (96) Zhen-Lang, X.; Wen-Xing, J.; Shu-Zhong, Z.; Song-Ping, W. Design, Synthesis and Characterization of a Co-Photocatalyst Based on a Copper (II) Complex of S,S'-Bis(2-Pyridylmethyl)-1,2-Thioethane for Hydrogen Production under Visible Light. *Inorganic Chemistry Communications* **2019**, *107*. <https://doi.org/10.1016/j.inoche.2019.107464>.
- (97) Li, C.-B.; Chu, Y.; He, J.; Xie, J.; Liu, J.; Wang, N.; Tang, J. Photocatalytic Hydrogen Production Based on a Serial Metal-Salen Complexes and the Reaction Mechanism. *ChemCatChem* **2019**, *11* (24), 6324–6331. <https://doi.org/10.1002/cctc.201901656>.
- (98) Li, C.-B.; Gong, P.; Yang, Y.; Wang, H.-Y. Cobalt(II)-Salen Complexes for Photocatalytic Hydrogen Production in Noble Metal-Free Molecular Systems. *Catal Lett* **2018**, *148* (10), 3158–3164. <https://doi.org/10.1007/s10562-018-2509-y>.
- (99) Chen, H.; Sun, Z.; Ye, S.; Lu, D.; Du, P. Molecular Cobalt–Salen Complexes as Novel Cocatalysts for Highly Efficient Photocatalytic Hydrogen Production over a CdS Nanorod Photosensitizer under Visible Light. *Journal of Materials Chemistry A* **2015**, *3* (30), 15729–15737. <https://doi.org/10.1039/C5TA03515E>.
- (100) Goldsmith, J. I.; Hudson, W. R.; Lowry, M. S.; Anderson, T. H.; Bernhard, S. Discovery and High-Throughput Screening of Heteroleptic Iridium Complexes for Photoinduced Hydrogen Production. *J. Am. Chem. Soc.* **2005**, *127* (20), 7502–7510. <https://doi.org/10.1021/ja0427101>.
- (101) Auvray, T.; Sahoo, R.; Deschênes, D.; Hanan, G. S. Heteroleptic Ruthenium Bis-Terpyridine Complexes Bearing a 4-(Dimethylamino)Phenyl Donor and Free Coordination Sites for Hydrogen Photo-Evolution. *Dalton Trans.* **2019**, *48* (40), 15136–15143. <https://doi.org/10.1039/C9DT02613D>.
- (102) Lentz, C.; Schott, O.; Auvray, T.; Hanan, G. S.; Elias, B. Design and Photophysical Studies of Iridium(Iii)-Cobalt(Iii) Dyads and Their Application for Dihydrogen Photo-Evolution. *Dalton Trans.* **2019**, *48* (41), 15567–15576. <https://doi.org/10.1039/c9dt01989h>.
- (103) Schott, O.; Pal, A. K.; Chartrand, D.; Hanan, G. S. A Bisamide Ruthenium Polypyridyl Complex as a Robust and Efficient Photosensitizer for Hydrogen Production. *Chemsuschem* **2017**, *10* (22), 4436–4441. <https://doi.org/10.1002/cssc.201701543>.
- (104) Xiao, W.-C.; Tao, Y.-W.; Zhao, Y.; Luo, J.-X.; Lai, W.-Z. Synthesis, Crystal Structure and Photochemical H₂ Generation of a Co-Based Supramolecular Assembly Containing a Bisthietyl Bodipy Sensitizer. *Inorganic Chemistry Communications* **2020**, *113*. <https://doi.org/10.1016/j.inoche.2020.107800>.
- (105) Lyu, S.; Massin, J.; Pavone, M.; Muñoz-García, A. B.; Labrugère, C.; Toupane, T.; Chavarot-Kerlidou, M.; Artero, V.; Olivier, C. H₂-Evolving Dye-Sensitized Photocathode Based on a Ruthenium–Diacetylde/Cobaloxime Supramolecular Assembly. *ACS Appl. Energy Mater.* **2019**, *2* (7), 4971–4980. <https://doi.org/10.1021/acsaem.9b00652>.
- (106) Winter, A.; Schubert, U. S. Metal-Terpyridine Complexes in Catalytic Application – A Spotlight on the Last Decade. *ChemCatChem* **2020**, *12* (11), 2890–2941. <https://doi.org/10.1002/cctc.201902290>.
- (107) Hironobu Ozawa, M. H. and K. S. A Photo-Hydrogen-Evolving Molecular Device Driving Visible-Light-Induced EDTA-Reduction of Water into Molecular Hydrogen. *J Am Chem Soc* **2006**, *128*, 4926. <https://doi.org/10.1021/ja058087h>.
- (108) Fihri, A.; Artero, V.; Pereira, A.; Fontecave, M. Efficient H₂-Producing Photocatalytic Systems Based on Cyclometalated Iridium- and Tricarbonylrhenium-Diimine

- Photosensitizers and Cobaloxime Catalysts. *Dalton Trans.* **2008**, No. 41, 5567–5569. <https://doi.org/10.1039/B812605B>.
- (109) BP Statistical Review of World Energy 2018., Data compiled by the Centre for Energy Economics Research and Policy, Heriot-Watt University, ceerp.hw.ac.uk. *Statistical Review of World Energy 2021*; 2021.
- (110) ACS Green chemistry. Endangered Elements.
- (111) Rhodes, C. J. Endangered Elements, Critical Raw Materials and Conflict Minerals. *Science Progress* **2019**, 102 (4), 304–350. <https://doi.org/10.1177/0036850419884873>.
- (112) Letarte, M. Vers Le Recyclage Des Batteries de Véhicules Électriques. **2019**.
- (113) Hydro Québec. *PHOTOVOLTAIC SOLAR POWER*; 2021.
- (114) Hydro Québec Distribution. *ÉTAT D'AVANCEMENT 2020 DU PLAN D'APPROVISIONNEMENT 2020-2029*; 2020; p 57.

2) Chapitre 2 – Synthesis, structure, and hydrogen evolution studies of a heteroleptic Co (III) complex

2.1 Abstract

$[Co(tpy)(phen)Cl](PF_6)_2 \bullet 0.25CH_3CN$ (where tpy = 2,2';6',2''-terpyridine and phen = 1,10-phenanthroline) was prepared from a one pot mixture involving stoichiometric quantities of tpy and phen. The structure of $[Co(tpy)(phen)Cl](PF_6)_2 \bullet 0.25CH_3CN$ was confirmed by elemental analysis, high resolution mass spectroscopy (HRMS), various spectroscopic analyses, and X-ray crystallography. Density functional theory calculations were also carried out. The crystal structure of $[Co(tpy)(phen)Cl](PF_6)_2 \bullet 0.25CH_3CN$, which was grown from acetonitrile, revealed a monoclinic crystal system with a C2/c space group. The cyclic voltammogram which was acquired in acetonitrile revealed reversible $Co^{III/II}$, $Co^{II/I}$, and $Co^{I/0}$ mixed with ligand-based redox couples at $E_{1/2}^\circ = +0.35$, -0.81 , and -1.37 V (vs Ag/AgCl), respectively. In the presence of p-cyanoanillinium tetrafluoroborate with acetonitrile as the solvent, $[Co(tpy)(phen)Cl](PF_6)_2 \bullet 0.25CH_3CN$ displayed electrocatalytic hydrogen evolution activity at a 830 mV overpotential, as evidenced by a catalytic wave which was observed in the voltammogram, and by the detection of hydrogen in the headspace of the reaction vessel of a controlled potential electrolysis experiment. Photocatalytic hydrogen evolution studies with $[Co(tpy)(phen)Cl](PF_6)_2 \bullet 0.25CH_3CN$ produced a turnover frequency (TOF) of $3300\text{ mmol H}_2\text{ mol}^{-1}\text{ CAT min}^{-1}$ when compared to $[Co(dmgH)_2(py)Cl]$ (where $dmgH$ = dimethylglyoximato), which had a TOF of $4500\text{ mmol H}_2\text{ mol}^{-1}\text{ CAT min}^{-1}$ under the same conditions. $[Co(tpy)(phen)Cl](PF_6)_2 \bullet 0.25CH_3CN$ produced a turnover number (TON) of 79 when compared to 141 for $[Co(dmgH)_2Cl(py)]$ in DMF in ca 3 h.

Published in Inorganica chemical Acta, volume 517, 2021-03-01

Synthesis, structure, and hydrogen evolution studies of a heteroleptic Co (III) complex

Michael J. Celestine,^a Mark A.W. Lawrence,^b Olivier Schott,^c Vincent Picard,^c Garry S. Hanan,^c Emily M. Marquez,^a Chekeyl G. Harold,^a Cole T. Kuester,^d Blaise A. Frenzel,^d Christopher G. Hamaker,^e Sean E. Hightower,^d Colin D. McMillen,^f and Alvin A. Holder*^a

^aDepartment of Chemistry and Biochemistry, Old Dominion University, 4541 Hampton Boulevard, Norfolk, VA 23529, U.S.A.

^bDepartment of Chemistry, University of the West Indies, Mona Campus, Kingston 7, Jamaica

^cDépartement de Chimie, Université de Montréal, Montréal, Canada

^dDepartment of Chemistry, University of North Dakota, 151 Cornell St., Stop 9024, Grand Forks, ND 58202-9024, U.S.A.

^eDepartment of Chemistry, Illinois State University, Campus Box 4160, Normal, IL, 61790-4160, U.S.A.

^fDepartment of Chemistry, Clemson University, 379 Hunter Laboratories, Clemson, SC 29634, U.S.A.

Corresponding author's e-mail: aholder@odu.edu

Contribution: I prepared all the solutions for the hydrogen evolution, and I took several data myself. I also created several graphics (used or not for the final version). I helped to find relevant references for the article.

Inorganica Chimica Acta, volume 517, 1 March 2021, 120195

Published: 2020-12-11

Doi: <https://doi.org/10.1016/j.ica.2020.120195>

Chapitre 2 – Synthesis, structure, and hydrogen evolution studies of a heteroleptic Co (III) complex

2.2 Introduction

The finite nature of fossil fuels, and the lasting adverse effects caused by the by-products of their combustion [1, 2] has created the need for a viable yet clean alternative fuel source. Hydrogen has been, and continues to be examined as a suitable candidate [1-5]. There are many drawbacks to the storage and transportation of hydrogen, mainly due to its highly flammable nature. As such, its generation on site and on demand is desired. A convenient way to produce hydrogen through sustainable means would be the conversion of solar energy to chemical energy through the reduction on water [6-8]. Whereas water splitting is appealing, the difficulties associated with the kinetics and thermodynamics of this multi-electron process have made the reduction of protons more appealing for the hydrogen evolution reaction (HER). Some platinum catalysts capable of reducing water to hydrogen with rates that are close to thermodynamic equilibrium have been reported in the literature [9, 10]. However, due to the high cost of noble metals such as Pt, Rh, Ir, etc., there is a search for catalysts based on cheaper and slightly more abundant first row transition metals, for instance, Fe, Co, and Ni [11-17].

Cobalt-containing complexes (Figure 24) such as the cobaloximes [18, 19], polypyridyl-containing cobalt(II/III) complexes [20-23], and cobalt(II) salen complexes [10], just to list a few, have been reported as promising candidates. In 2014 Chen *et al.* [11] reported on the use of a cobalt(II) catalyst, $[\text{Co}(\text{tpy})(\text{phen})\text{Cl}]\text{Cl}$, when immobilized on the surface of an electrode was able to produce hydrogen with a turn over number (TON) of about 2.2×10^6 after about 50 hours. Other efforts to make HER practical included the development of photocatalytic systems. These systems are typically heterometallic in nature, with one site acting as a light antenna and the other as the catalytic site [6, 8, 24-27]. The polypyridyl system as developed by Chang *et al.* [11] may also possess photocatalytic properties, as polypyridyl ligands are known to stabilize the excited state of certain metal centres.

Whether electrocatalytic or photocatalytic in nature, the formation of either +1 or 0 oxidation state is required from the precatalyst in most cases. This is so, as these oxidation states can facilitate the oxidative addition of a proton to form the reactive $\text{M}^{\text{III or II}}-\text{H}$ as an important species in the catalytic cycle of the HER. The choice of the ligand is thus crucial, as a change in the oxidation state may be accompanied by a change in the preferred geometry around the metal centre.

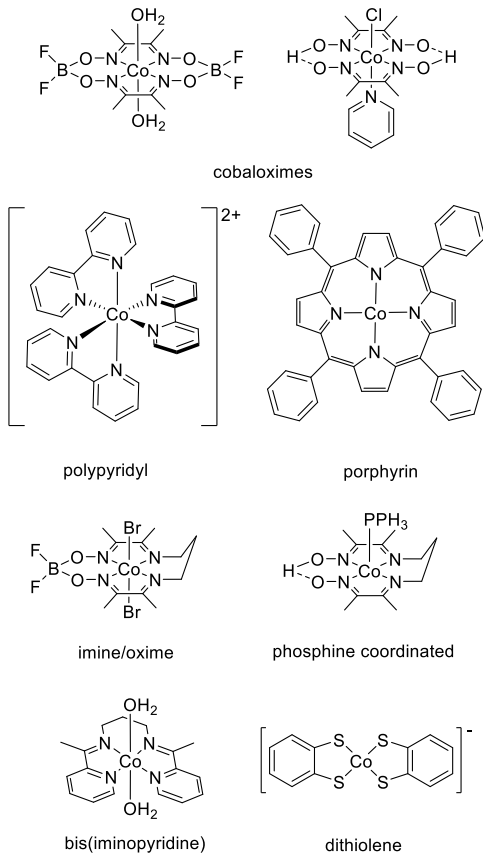


Figure 24. Some examples of cobalt complexes utilised in the catalytic hydrogen evolution reaction.

In many studies involving a cobalt-based catalyst, it is common that upon production of a cobalt(I) species that the complex undergoes a geometric change through the loss of a ligand, with nitrogen-based ligands being favoured in the coordination sphere over aqua and halogen ligands [12, 19, 28, 29].

Herein, this paper we report the crystal structure, spectroscopic, and cyclic voltammetric properties, as well as the electrocatalytic and photocatalytic hydrogen evolution studies of $[\text{Co}(\text{tpy})(\text{phen})\text{Cl}](\text{PF}_6)_2 \bullet 0.25\text{CH}_3\text{CN}$ **1** in non-aqueous media. These studies are geared towards establishing the potential of this species as a photocatalyst in the HER, starting from the Co(III) analogue of the species in comparison to the Co(II) species as reported by Chen *et al.* [11]. Also, to establish the stability of the reduced oxidation states by cyclic voltammetry, and also as a part of a series of studies [30] aimed at correlating the effect of the ancillary ligand on the photocatalytic response of Co(III) complexes in HER.

2.3 Experimental

2.3.1 Materials and physical measurements

All chemicals and reagents were purchased from commercial sources and were used without further purification.

2.3.2 Physical measurements

^{59}Co NMR spectra were acquired on a Bruker 400 MHz spectrometer with $\text{K}_3[\text{Co}(\text{CN})_6]$ as an external reference in either $\text{DMSO}-d_6$ ($\delta = 289$ ppm [31]) or CD_3CN ($\delta = 293$ ppm [31]) at room temperature. ^1H NMR spectra were acquired on a Bruker AVANCE III 400 MHz spectrometer with $\text{DMSO}-d_6$ as solvent. All NMR spectra were processed with the ACD/NMR Processor Academic Edition software which was available from Advanced Chemistry Development¹.

Microanalyses (C, H, and N) were performed by Intertek Chemical and Pharmaceuticals, 291 Route 22 East, Salem Industrial Park, Building #5, Whitehouse, NJ 08888, U.S.A.

HRMS spectra were acquired via positive electrospray ionization on a Bruker 12 Tesla APEX-Qe FTICR-MS with an Apollo II ion source at the College of Sciences Major Instrument Cluster (COSMIC), Old Dominion University, Norfolk, VA 23529, U.S.A. Samples were dissolved in acetonitrile before being introduced by direct injection using a syringe pump with a flow rate of $2 \mu\text{l s}^{-1}$. The data was processed using Bruker Daltonics Data Analysis Version 3.4.

All electrochemical experiments were carried out on a BAS Epsilon C3 under an argon atmosphere in CH_3CN at room temperature (ca 20 °C). A standard three electrode configuration was employed consisting of a glassy carbon working electrode (3 mm diameter) and a Pt wire as auxiliary electrode. For the reference electrode, AgCl/Ag (BASi, 3.0 M NaCl) was employed, which was separated from the analytical solution by a Vicor® frit, against which ferrocene shows a reversible wave at +0.43 V. The ionic strength was maintained at 0.1 M using $[^\text{n}\text{Bu}_4\text{N}]^\text{+}\text{ClO}_4^-$.

¹ ACD, Inc., 8 King Street East, Suite 107, Toronto, Ontario M5C 1B5, Canada.

Spectroelectrochemical measurements were carried out at 20 °C with a thermostatted water bath/circulator (Thermo Scientific®). Absorbance data were acquired on an Agilent® 8453A diode array spectrophotometer. A Pt gauze and a Pt wire were utilised as working and auxiliary electrodes, respectively, and AgCl/Ag (BASi, 3.0 M NaCl) was utilised as a reference electrode. The ionic strength was maintained at 0.10 M as stated above. Each solution was purged with Ar for at least two minutes in the spectroelectrochemical cuvette (1 mm path length) prior to acquisition of the data.

2.3.3 Synthesis and physical measurements of the cobalt(III) complex

Synthesis of $[\text{Co}(\text{tpy})(\text{phen})\text{Cl}](\text{PF}_6)_2 \bullet 0.25\text{CH}_3\text{CN}$ 1

A mixture of 2,2':6',2"-terpyridine (0.98 g, 4.2 mmol), 1,10-phenanthroline (0.76 g, 4.2 mmol), and $\text{CoCl}_2 \bullet 6\text{H}_2\text{O}$ (1.00 g, 4.2 mmol) were stirred in ethanol (320 mL) for 3 hours. Iodine (1.31 g, 5.2 mmol) in ethanol (60 mL) was added dropwise to the resulting solution with stirring. The solution was filtered; then the filtrate was collected and NH_4PF_6 (6.86 g, 42 mmol) in methanol (60 mL) was added. The resulting mixture was filtered; then the residue air dried. The crude product was then dissolved in acetonitrile; then the solution was filtered. The filtrate which contained the crude product was purified three times by chromatography with Sephadex LH-20 as the stationary phase and acetonitrile as eluent. The product was worked up. Yield = 1.17 g (34%) A single crystal of complex **1** was grown as an acetonitrile solvate by slow evaporation at first in acetonitrile solution; followed by the addition of acetone. calculated for $\text{C}_{27.5}\text{H}_{19.75}\text{N}_{5.25}\text{ClP}_2\text{F}_{12}$: C 40.88, H 2.46, N 9.10, Cl 4.39%. Found C 40.85, H 2.51, N 9.17, Cl 4.21%. HRMS (positive mode, found (calc.): $[\text{M}-1\text{PF}_6^-]^+ = 652.0247$ (652.0247). ^1H NMR (400 MHz, CD_3CN , δ/ppm) 10.21 (d, $J = 5.06$ Hz, 1 H, phen-j'), 9.30 (d, $J = 8.14$ Hz, 1 H, phen-h'), 8.89 (d, $J = 6.82$ Hz, 1 H, tpy-h), 8.80 - 8.86 (m, 2 H, tpy-g), 8.67 (d, $J = 8.14$ Hz, 1 H, phen-a'), 8.61 (dd, $J = 7.92, 5.94$ Hz, 1 H, phen-i'), 8.48 - 8.57 (m, 3 H, tpy-a and phen-e'), 8.29 (d, $J = 9.02$ Hz, 1 H, phen-f'), 8.18 (t, $J = 7.59$ Hz, 2 H, tpy-b), 7.64 (dd, $J = 7.59, 5.83$ Hz, 1 H, phen-b'), 7.43 (d, $J = 4.84$ Hz, 1 H, phen -c'), 7.33 (t, $J = 6.38$ Hz, 2 H, tpy-c), 7.18 (d, $J = 5.50$ Hz, 2 H, tpy-d). ^1H NMR (400 MHz, $\text{DMSO}-d_6$, δ/ppm) 10.12 (d, $J = 5.06$ Hz) 9.51 (d, $J = 8.14$ Hz) 9.38 (d, $J = 7.92$ Hz) 9.23 (m) 9.10 (m) 8.93 (m) 8.86 (d, $J = 7.92$ Hz) 8.75 (dd, $J = 8.14, 5.50$ Hz) 8.66 (d, $J = 8.80$ Hz) 8.43 (d, $J = 8.80$ Hz) 8.34 (q, $J = 7.92$ Hz) 7.72 (m) 7.46 (m) 7.35 (d, $J = 5.50$

Hz); ^{59}Co NMR (95 MHz, CD₃CN, δ/ppm) 7148; ^{59}Co NMR (95 MHz, DMSO-*d*₆, δ/ppm) 7177; UV-visible (CH₃CN, λ/nm ($10^{-4} \epsilon/\text{M}^{-1} \text{cm}^{-1}$)): 203 (78), 222 (75), 275 (39), 322 (12), and 487 (0.27).

2.3.4 X-ray crystallography

Single crystal X-ray diffraction was carried out at 150 K using a Bruker D8 Quest diffractometer with Mo K α radiation and a Photon 100 detector. The data was collected using phi and omega scans in 0.5 degree oscillations. The structure was solved and refined using the Bruker SHELXTL [32] Software Package. All non-hydrogen atoms were refined anisotropically, and hydrogen atoms were placed in calculated positions using riding models. The crystal was found to be the acetonitrile solvate of the target cobalt complex. The acetonitrile solvent molecule was found to be disordered and partially occupied, having 1/2 occupancy per formula unit of the cobalt(III) complex. Details of data collection and structural solution for [Co(tpy)(phen)Cl](PF₆)₂•0.5C₂H₃N are provided in the supporting crystallographic files (CIF).

2.3.5 Photocatalytic measurements

Hydrogen evolution was monitored using a Perkin Elmer Clarus-580 gas chromatograph (GC) with a thermal conductivity detector, argon as carrier and eluent gas, a 7' HayeSep N 60/80 pre-column, a 9' molecular sieve 13 × 45/60 column and a 1 mL injection loop.

Three distinct solutions for the photosensitizer, [Ru(bpy)₃](PF₆)₂, for the catalyst, and lastly, for the sacrificial electron donor and acid source (HBF₄, 48% water) were prepared: the three solutions were mixed together to obtain 5 mL of sample solutions in standard 20 mL headspace vials. In DMF, the resulting molar concentrations of photocatalytic components were as follows: 1 M for triethanolamine (TEOA), 0.1 M for (HBF₄), 0.56 M for water, 0.1 mM for [Ru(bpy)₃](PF₆)₂, 0.01 mM for complex **1** or [Co(dmgH)₂Cl(py)] (apparent pH = 8.9). Those vials were placed on a LED panel in a thermostatic bath set at 20 °C. They were sealed with a rubber septum pierced with two stainless steel tubes. The first tube carried an argon flow pre-bubbled in spectroscopic grade solvent. The flow rate

was set to 5 mL min⁻¹ (adjusted with a manual flow controller (Porter, 1000) and referenced with a digital flow meter (Perkin Elmer FlowMark)).

The second tube leads the flow to the GC sample loop through a 2 mL overflow protection vial, then through an 8-port stream select valve (VICCI) and finally to the GC sample loop. A microprocessor (Arduino Uno) coupled with a custom PC interface allows for timed injections. For general calibration, stock cylinders of known concentration of H₂ in nitrogen replaced the nitrogen flow (inserted at the pre-bubbler, to keep the vapor matrix consistent). The acquired data, independent of flow rate (under same pressure) were easily converted into a rate of hydrogen by using equation 1. For calibration of H₂ production, a nitrogen bottle of certified 100 ppm hydrogen was set to deliver a specific flow. H₂ production rate at a specific nitrogen flow, a syringe pump (New Era Pump) equipped with a gas-tight syringe (SGE) and a 26s gauge needle (Hamilton) was used to bubble different rates of pure hydrogen gas into the sample, to a minimum of 0.5 µL min⁻¹. This gave a linear fit for peak area for H₂ versus the flow rates of H₂ (Eq. 1). All experiments were carried out in duplicate to verify the reproducibility of results, and an average for the TOF and TON curves was calculated with Origin software. The error associated with the TOF and TON values was estimated to be 10% [33].

$$\text{H}_2 \text{ rate } (\mu\text{L min}^{-1}) = [\text{H}_2 \text{ standard}] \text{ (ppm)} \times \text{N}_2 \text{ flow rate } (\text{L min}^{-1}) \quad 1$$

CCDC no. 1953060 contains the supplementary crystallographic data for [Co(tpy)(phen)Cl]⁺(PF₆)₂•0.5C₂H₃N. These data can be obtained free of charge from The Cambridge Crystallographic Data Centre via www.ccdc.cam.ac.uk/data_request/cif. Supporting information containing additional spectral and voltammetric characterizations are also provided.

2.4 Results and discussion

2.4.1 Synthesis

Complex **1** was synthesized (figure 25) using stoichiometric quantities in one pot, and was purified three times on a Sephadex LH-20 column to ensure the separation of the main by-products $[\text{Co}(\text{tpy})_2](\text{PF}_6)_3$ and $[\text{Co}(\text{phen})_2(\text{solv})](\text{PF}_6)_3$ from complex **1**. Complex **1** was characterized by elemental analysis, HRMS, UV-visible, ^1H and ^{59}Co NMR spectroscopies, X-ray crystallography, and cyclic voltammetry. $[\text{Co}(\text{tpy})_2](\text{PF}_6)_3$ was identified and characterized after the column chromatography via ^1H and ^{59}Co NMR, and ESI MS (See supporting information Figures 32-35).

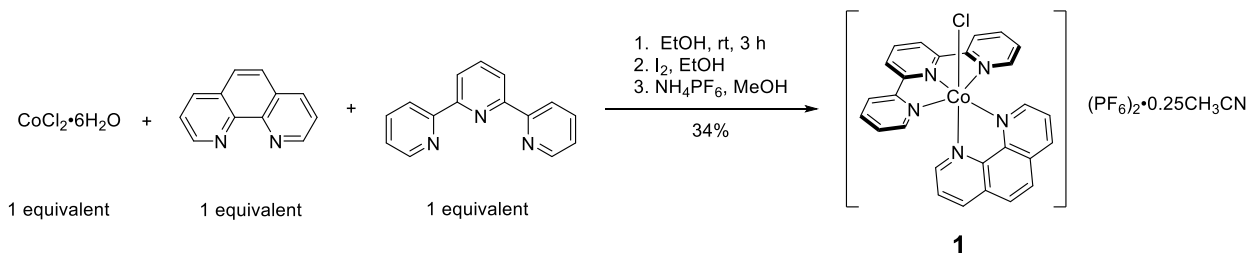


Figure 25. Synthesis of complex **1**.

2.4.2 HRMS analysis

HRMS data were acquired for complex **1** in CH_3CN (Figure 38). In the HRMS, the most intense peak is observed at $m/z = 652.0247$, which corresponded to the loss of one of the PF_6^- counter ions to produce $([\text{Co}^{\text{III}}(\text{tpy})(\text{phen})\text{Cl}](\text{PF}_6))^+$. The HRMS data do complement the elemental analysis data and other spectroscopic characterizations.

2.4.3 ^1H and ^{59}Co NMR spectroscopic studies

In an NMR spectroscopic study, ^1H and ^{59}Co NMR spectra were acquired for complex **1** in CD_3CN or $\text{DMSO}-d_6$ at ambient temperature. The ^1H NMR spectra (Figure 26B, and Figure 39), revealed solvent peaks and aryl resonances.

In the solvent region, the presence of acetonitrile in the isolated solid was confirmed ($\delta = 2.07$ ppm) in $\text{DMSO}-d_6$. In the aromatic region of the ^1H NMR spectrum, there is a significant overlap

of the resonances of the tpy and phen ligands, Figure 26A. The assignment of these peaks was guided by ^1H - ^1H the COSY NMR spectrum (Figure 40); and coordinated tpy protons are assigned to resonances at 7.18, 7.33, 8.18, 8.54, 8.83, and 8.89 ppm. Paramagnetic ^1H NMR measurements on complex **1** showed no resonance between 10 to 120 ppm which suggested the absence of a cobalt(II) species in the isolated solid (see Figure 37). ^1H NMR spectra of polypyridyl cobalt(II) complexes generally display chemical shifts in this region [34]. It should be noted that in the ^1H NMR spectrum of complex **1**, satellite peaks can be seen in the concentrated solutions used to acquire the spectra. These satellite peaks maybe the result of ligand dissociation or trace amounts of the “free” ligand from the synthesis, which the latter is the least probable. The ratio of integrals suggests that the uncoordinated ligand is less than 3% of the mixture.

^{59}Co NMR spectroscopic data as shown in Figure 24 showed one chemical shift at 7148 ppm in CD_3CN and at 7177 ppm in $\text{DMSO}-d_6$. A comparison with other Co(III) complexes such as $[\text{Co}(\text{phen})_3](\text{PF}_6)_3$ ($\delta = 7000$ ppm in $\text{DMSO}-d_6$ [35], 7080 ppm [36]) or $[\text{Co}(\text{phen})_2(\text{bpy})](\text{PF}_6)_3 \bullet 0.5(\text{C}_2\text{H}_5)_2\text{O}$ ($\delta = 6900$ ppm in $\text{DMSO}-d_6$) [35] revealed that the chemical shift of complex **1** is in a similar region to other cobalt(III)-containing polypyridyl complexes, which are shown in Table S1. The ^{59}Co NMR spectroscopic chemical shift of cobalt-containing complexes is very sensitive to the type(s) of ligand(s) in the coordination sphere, as well as the oxidation state of a cobalt metal centre. The absence of other peaks in the 7000 ppm region of the ^{59}Co NMR of the isolated product proved the absence of Co(III) by-products from the synthesis. It should be noted that ^{59}Co NMR on Co(II) species is very difficult to acquire and process. The ^{59}Co NMR spectroscopic data (in conjunction with the ESI-MS data) strongly suggest that cobalt(II) impurities and Co(III) by-products are absent from the isolated product, complex **1**.

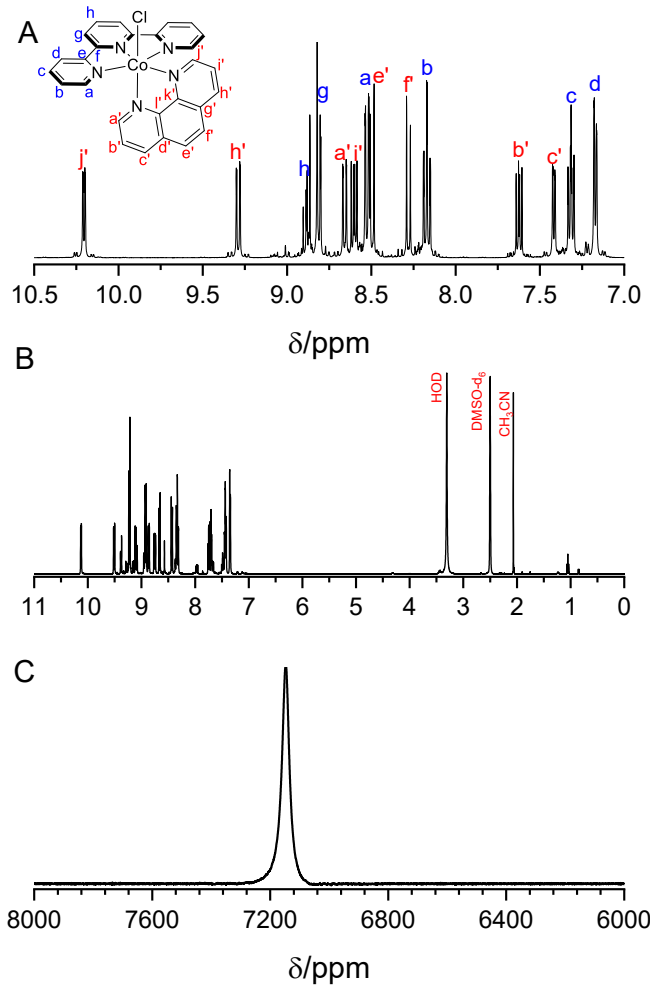


Figure 26. ^1H NMR spectra of complex **1** in CD_3CN (A) and $\text{DMSO}-d_6$ (B), and ^{59}Co NMR spectrum of 40 mM complex **1** in CD_3CN (C).

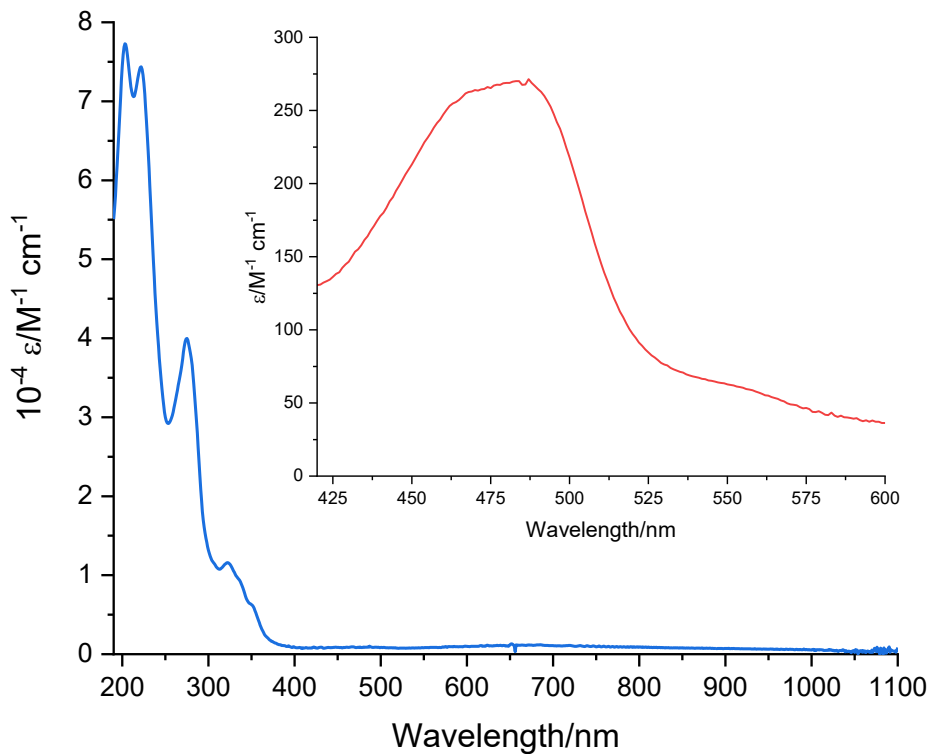


Figure 27. UV-visible spectrum of complex **1** in acetonitrile (400-600 nm enhanced view shown in inset).

2.4.4 UV-visible spectroscopic studies

The UV-visible spectrum of complex **1** in Figure 27 shows transitions that are consistent with d-d transitions (dual bands) at 487 nm, $\pi \rightarrow \pi^*$, intra-ligand, and metal-to-ligand charge transfer bands in the UV region. The molar extinction coefficients are 78×10^4 , 75×10^4 , 29×10^4 , 13×10^4 , and $0.27 \times 10^4 \text{ M}^{-1} \text{ cm}^{-1}$ at 203, 222, 275, 322, and 487 nm, respectively. The dual band at 487 nm in CH_3CN is observed at $\lambda_{\max} = 460 \text{ nm}$ and 491 nm , which had a hypsochromic shift in the $\text{H}_2\text{O}/\text{CH}_3\text{CN}$ (1:1 v/v) mixture to circa 455 nm regardless of the supporting electrolyte used (see Figure 41).

2.4.5 X-ray crystallography

A single crystal of complex **1** was grown as an acetonitrile solvate by slow evaporation at first in acetonitrile solution; followed by the addition of acetone. The X-ray crystal structure for the dication of complex **1** is shown in Figure 4, with selected structure refinement parameters given in Table 1.

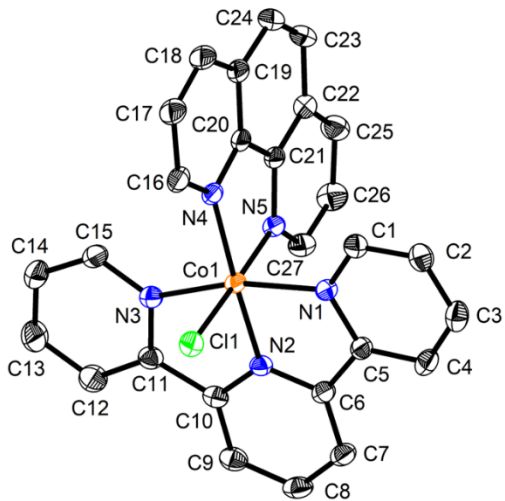


Figure 28. Structure for the *mer*-[Co(tpy)(phen)Cl]²⁺ complex as shown at 50% probability ellipsoids.

Selected bond lengths and angles are shown in Table 2. The structural analysis revealed a distorted octahedral arrangement about to the cobalt(III) metal centre. The tpy ligand is coordinated in a tridentate fashion and is meridionally arranged about the cobalt(III) core with resulting tpy and phen ligands lying in perpendicular coordination planes to each other, with the chloro ligand completing the octahedron. This coordination behaviour, bond lengths, and angles observed here are similar to the analogous [Rh(tpy)(Z)Cl]²⁺ (where Z = bpy or phen) species [37]. In particular, the Co-N bond to the central nitrogen atom of the tpy ligand is the shortest of tpy, and all the tpy Co-N bonds are marginally shorter than those to phen ligand, which is consistent with what is observed in the Rh(III) complex. The N5-Co1-Cl1 bond angle is almost 180°, the bond length is normal for Co–Cl bonds [38]. The charge of complex **1** is counterbalanced by two PF₆[−] anions. In the extended structure, these anions, along with acetonitrile solvent molecules, occupy voids between complex **1**.

Tableau 1. – Crystal data and structure refinement parameters for $[\text{Co}(\text{tpy})(\text{phen})\text{Cl}](\text{PF}_6)_2 \bullet 0.5\text{CH}_3\text{CN}$.

<i>Identification code</i>	$[\text{Co}(\text{tpy})(\text{phen})\text{Cl}](\text{PF}_6)_2$
<i>Chemical formula</i>	$\text{C}_{27}\text{H}_{19}\text{ClCoF}_{12}\text{N}_5\text{P}_2 \bullet 0.5\text{C}_2\text{H}_3\text{N}$
<i>Formula weight (g/mol)</i>	818.32
<i>Crystal system, space group</i>	monoclinic, C2/c
<i>Unit cell dimensions (Å, °)</i>	a = 30.0763(13) b = 14.5703(6) c = 14.9762(6) β = 114.3491(13)
<i>Volume (Å³)</i>	5979.1(4)
<i>Z, Calculated density (g cm⁻³)</i>	8, 1.818
<i>Reflections collected/unique</i>	41055/6133
<i>Data/restraints/parameters</i>	6133/0/461
<i>Final R indices [4838 data; I>2σ(I)]</i>	0.0348, 0.0722
<i>R indices (all data)</i>	0.0531, 0.0796
<i>Largest diff. peak and hole</i>	0.362, -0.421
<i>CCDC no.</i>	1953060

Tableau 2. – Selected bond lengths and angles for $[\text{Co}(\text{tpy})(\text{phen})\text{Cl}](\text{PF}_6)_2 \bullet 0.5\text{CH}_3\text{CN}$.

Bond	Length (Å)	Bond	Length (Å)
Co1-N1	1.945(2)	Co1-N4	1.948(2)
Co1-N2	1.853(2)	Co1-N5	1.953(2)
Co1-N3	1.935(2)	Co1-Cl1	2.2241(8)
Bonds	Bond angle	Bonds	Bond angle
N2–Co1–N1	82.91(9)	N5–Co1–N4	85.04(9)
N2–Co1–N3	83.06(9)	N5–Co1–Cl1	177.80(7)
N1–Co1–N3	165.97(9)	N4–Co1–Cl1	93.86(7)
N2–Co1–N4	177.07(9)	N5–Co1–N3	91.11(9)
N2–Co1–Cl1	88.59(7)	N5–Co1–N1	90.00(9)
N2–Co1–N5	93.49(9)	N3–Co1–N4	98.54(9)
N1–Co1–N4	95.49(9)	N3–Co1–Cl1	89.86(7)
N1–Co1–Cl1	89.54(7)		

2.4.6 Electrochemical studies

The complex, $[\text{Co}(\text{tpy})(\text{phen})\text{Cl}]\text{Cl}$, as reported by Chen *et al.* [11] showed remarkable activity in HER, especially when grafted (via electrochemical polymerization) on a Cu_2O surface. In their work, the $\text{Co}^{\text{IV}/\text{III}}$ and $\text{Co}^{\text{III}/\text{II}}$ couples showed reversible characteristics, however, the $\text{Co}^{\text{II}/\text{I}}$ redox couple showed little reversibility in acetonitrile. It was intriguing that system was an efficient HER

catalyst despite the apparent irreversibility of the $\text{Co}^{\text{II}/\text{I}}$ redox couple. It is therefore of interest to investigate the cyclic voltammetric characteristics of this species, bearing in mind the widely accepted view that a stable Co(I) species capable of undergoing reversible electron transfer is ideal for HER in cobalt-containing systems.

Cyclic and square wave voltammograms of complex **1** in aqueous mixed solvents, and non-aqueous media revealed a series of (quasi-)reversible waves with $i_{\text{pa}}/i_{\text{pc}} = >0.9$ (Table 3). The peak potentials are scan rate dependent and showed negligible potential drift with increasing scan rate, consistent with their reversible nature. The $\text{Co}^{\text{III}/\text{II}}$ redox couple is observed between +0.2 and +0.4 V vs Ag/AgCl, whereas the $\text{Co}^{\text{II}/\text{I}}$ redox couple is observed between -0.8 to -0.9 V depending on the solvent and supporting electrolyte employed (see Figure 42). In aqueous media, cobalt(II)-containing halides are well known to undergo rapid aquation [39], which can only be retarded by the presence of high halide concentration. In water, NaCl supporting electrolyte did not appear to improve the voltammetric reversibility of the electron transfers, and indeed a Co(I) species appears to be more unstable with NaCl compared to NaClO_4 , resulting in a stripping wave on the return scan, due to the deposition of cobalt metal at the electrode surface (see Figure 43). However, in the $\text{H}_2\text{O}/\text{CH}_3\text{CN}$ (1:1, v/v) mixed solvent, improved voltammograms were obtained (see supporting information), and no stripping wave was observed. In the mixed solvent containing NaCl supporting electrolyte, the ΔE_p decreased to 80 mV which is closer to the 57 mV value expected for a one-electron Nernstian process, and was lower than that obtained with the NaClO_4 supporting electrolyte.

In CH_3CN , (Figure 30 and Figure 44), the voltammograms revealed reversible $\text{Co}^{\text{III}/\text{II}}$ and $\text{Co}^{\text{II}/\text{I}}$ redox couples which are slightly sensitive to the working electrode (by ca 60 mV between the GC and Pt electrodes), and are observed at $E_{1/2} = +0.35$ and -0.81 V vs Ag/AgCl, respectively, on a GC working electrode (WE). However, on reductively initiated scans on using Pt WE, a pre-wave is observed before the $\text{Co}^{\text{II}/\text{I}}$ redox couple. This pre-wave is present, albeit somewhat suppressed, on the GC WE and may be related to the enhanced lability of the chloride ligand in the +2 oxidation state, which causes a subtle modification of the layer at the electrode surface. A third reversible wave at $E_{1/2} = -1.37$ V is most likely attributed to a one electron redox couple for one of the polypyridyl ligands. On the return scan upon switching the potential at -2 V, the oxidation waves are slightly distorted and are likely related to the partial dissociation of the polypyridyl ligand(s) in

the highly reduced state [35]. Additionally, as electrons are injected into the system, ΔE_p increased, indicating a drift from Nernstian behaviour. Nevertheless, the Co^{II/I} redox couple showed reversible characteristics in all but the H₂O/NaCl combination.

The overall nature of the voltammogram in CH₃CN suggests that, on the electrochemical time scale, species with all three oxidation states of the cobalt metal centre, viz., +3, +2, and +1, are fairly stable in nature, where complex **1** may potentially be utilised as an electron shuttle in a reaction such as the hydrogen evolution reaction [11] amongst others. A plausible electron transfer mechanism is shown in figure 29.

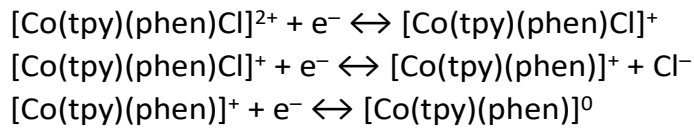


Figure 29. A plausible redox behaviour of complex **1** in CH₃CN

Tableau 3. – Comparison of the reduction potentials of complex **1** in H₂O and CH₃CN with various supporting electrolytes.

Redox couple	$E_{\frac{1}{2}}/\text{V}$	$\square E_p/\text{mV}$	solvent	Electrolyte
Co ^{III/II}	+0.22	320	H ₂ O	NaClO ₄
	+0.23	--	H ₂ O	NaCl
	+0.32	109	H ₂ O/CH ₃ CN	NaClO ₄
	+0.26	80	H ₂ O/CH ₃ CN	NaCl
	+0.35	92	CH ₃ CN	[ⁿ Bu ₄ N]ClO ₄
Co ^{II/I}	-0.90	100	H ₂ O	NaClO ₄
	-1.00	--	H ₂ O	NaCl
	-0.89	87	H ₂ O/CH ₃ CN	NaClO ₄
	-0.88	83	H ₂ O/CH ₃ CN	NaCl
	-0.81	110	CH ₃ CN	[ⁿ Bu ₄ N]ClO ₄

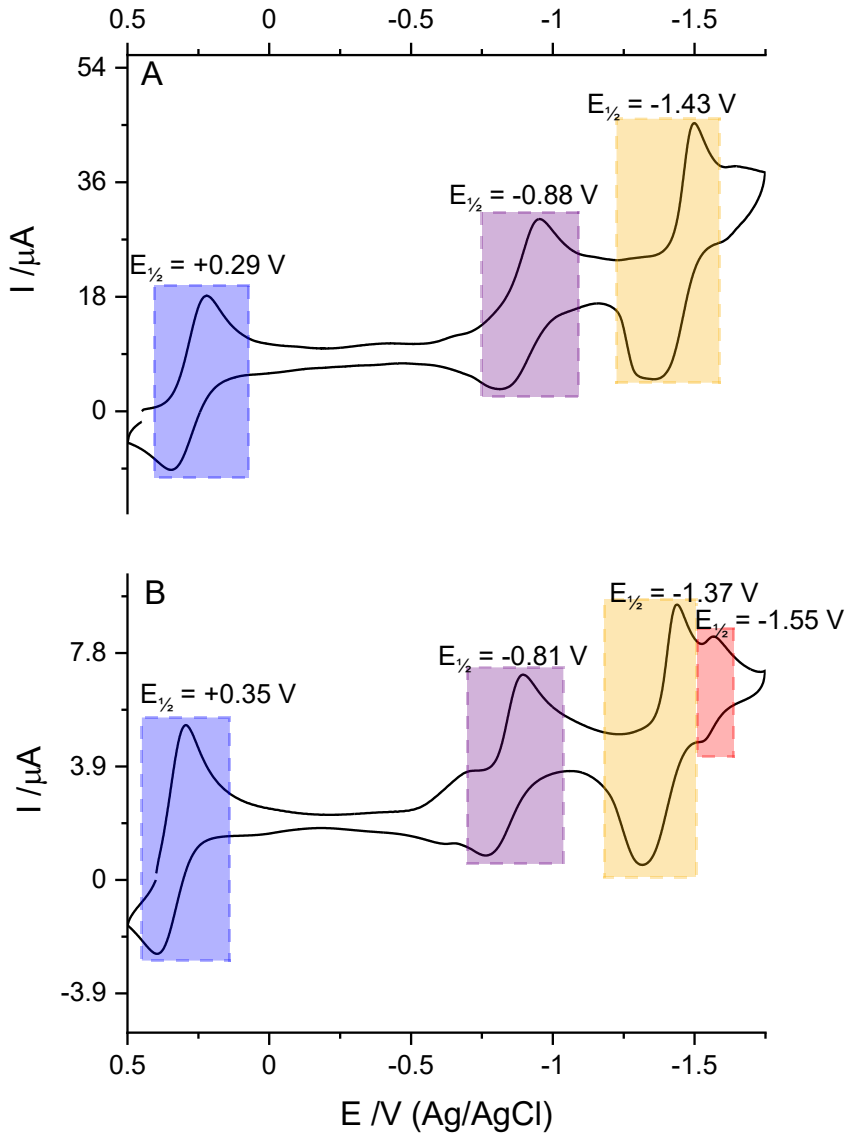


Figure 30. Cyclic voltammogram of complex **1**. Solvent = acetonitrile, [complex] = 1.0 mM, [Bu_4N] ClO_4 = 0.10 M, working electrode = (A) glassy carbon or (B) Pt, auxiliary electrode = Pt wire, reference electrode = Ag/AgCl, and scan rate = 100 mV s⁻¹.

A series of spectroelectrochemical measurements were made on CH₃CN and H₂O/CH₃CN (1:1 v/v) mixed solvent solutions of complex **1** (Figures 30, 45 and 46). In the H₂O/CH₃CN (1:1 v/v) mixed solvent, Figure 46, the Co³⁺ \rightarrow Co²⁺ reduction resulted in a rapid increase in the absorbance at 460 nm along with a blue shift to 450 nm. This is succeeded by a gradual decrease in the absorbance across the spectrum. In the electrolysis of the solution at a potential sufficient to overcome the overpotential for the Co²⁺ \rightarrow Co⁺ reduction, a similar pattern is observed at 460 nm,

albeit a smaller change in the absorbance. A similar electrolysis in CH₃CN caused the peak that is observed circa 480 nm to first have a blue shift to circa 450 nm, followed by a decrease in the absorbance at this wavelength.

In addition to the blue shift in the d-d transitions, there is an increase in the absorbance across the UV region, suggestive of an increase in the charge transfer characteristics of the system associated with formation of a Co(I) species. The complex nature of the spectral transformation clearly indicates that the electrolysis did not have a simple A → B transformation. Here again, the exclusion of the chloride ligand from the coordination sphere maybe the cause of the biphasic nature of the spectral transformation. Electrolysis at -1.52 V (vs Ag/AgCl), also presented a biphasic spectrum, in which there is an initial rapid increase in the absorbance which is followed by decay towards a limiting value that is greater than the value prior to the electrolysis experiment. The transformation at this potential did not appear to share the blue shift observed at the more positive potential, and indeed is suggestive that the reduction involves the polypyridyl ligand(s).

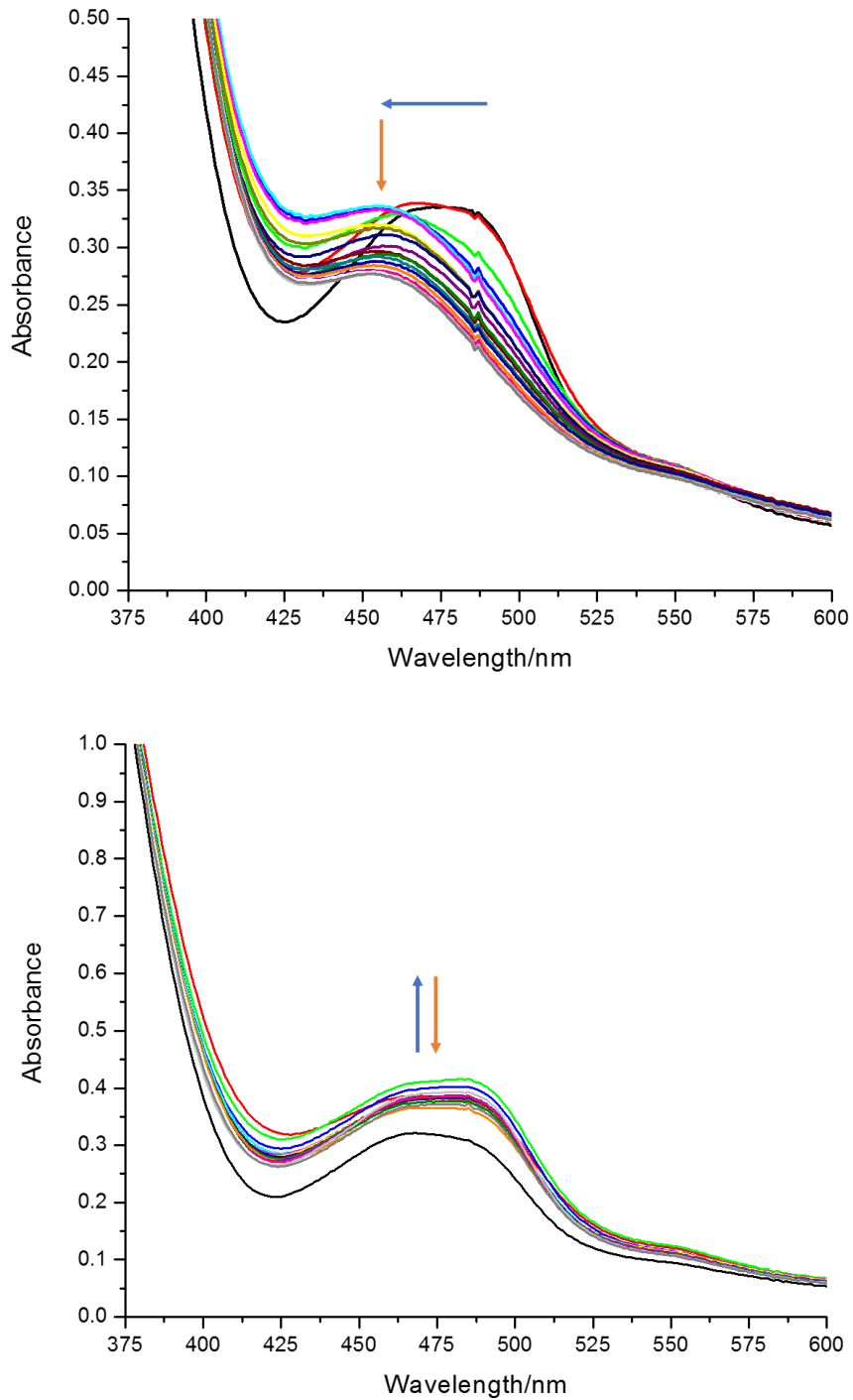


Figure 31. Spectroelectrochemical transformations of complex **1**. Solvent = acetonitrile, [complex] = 14.9 mM, [ⁿBu₄N]ClO₄ = 0.10 M, working electrode = Pt mesh wire, auxiliary electrode = Pt wire, reference electrode = Ag/AgCl, held potential = -1.20 V (top) and -1.52 V (bottom), and path length = 1 mm.

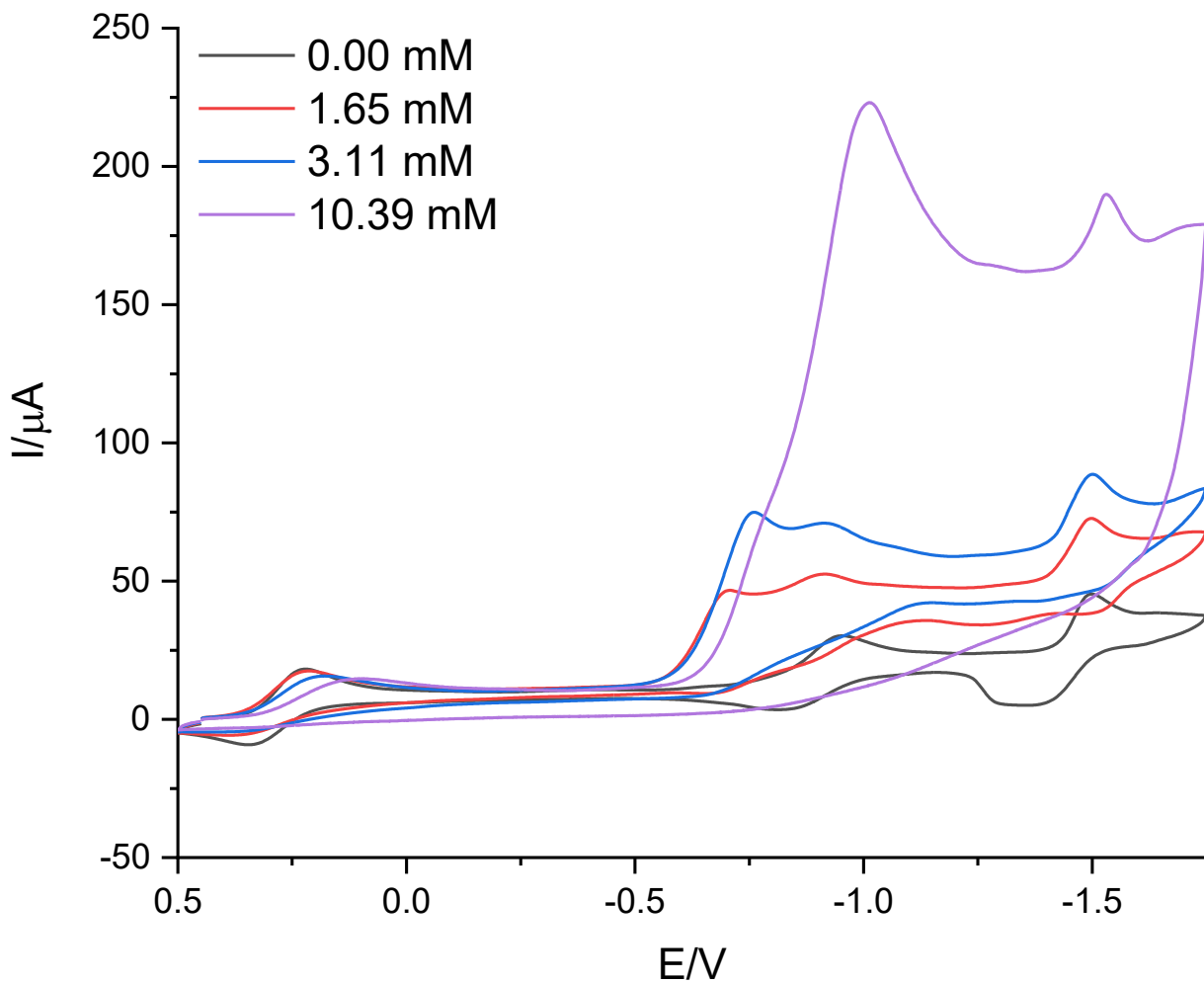


Figure 32. Cyclic voltammograms illustrating the electrocatalytic behaviour of complex **1**. Solvent = acetonitrile, [complex] = 1.0 mM, [${}^n\text{Bu}_4\text{N}\text{ClO}_4$] = 0.10 M, working electrode = glassy carbon, auxiliary electrode = Pt wire, reference electrode = Ag/AgCl, and scan rate = 100 mV s⁻¹. The concentration of *p*-cyanoanilinium tetrafluoroborate was varied from 0.0 mM to 10 mM.

2.4.7 Electrocatalytic studies

The effect of a proton source (*p*-cyanoanilinium tetrafluoroborate) on the voltammograms of complex **1** in CH₃CN was investigated. In the presence of *p*-cyanoanilinium tetrafluoroborate, a new cathodic wave is observed at ca -0.65 V of which the peak current increases with a simultaneous peak potential shift to increasingly negative values with increasing concentration of *p*-cyanoanilinium tetrafluoroborate. The adsorption pre-wave observed in the absence of the proton

source is removed upon the addition of the *p*-cyanoanilinium tetrafluoroborate. The electrocatalytic wave was observed to occur ca 300 mV more positive than the Co^{II/I} reduction wave, and displayed what is considered a “normal” catalysis [40-42], owing the lack of any apparent pre-wave or unexpected diffusional peaks. The production of hydrogen was confirmed from the analysis of the head space of a controlled potential electrolysis experiment involving the complex in the presence of *p*-cyanoanilinium tetrafluoroborate. In CH₃CN, the overpotential associated with the catalysed proton reduction was determined to be 830 mV. The magnitude of the Gibbs free energy for the homolytic and heterolytic hydrogen evolution from *p*-cyanoanilinium tetrafluoroborate in CH₃CN can be determined using the methodology suggested by Kellett and Spiro [43] on the basis of the values for the potentials of the cobalt and HA/H₂ couples versus Fc^{+/-}. From the thermodynamic analysis of the heterolytic and the homolytic pathways, the free energies of ΔG = -15.4 and -56.9 kJ mol⁻¹, respectively, which suggests that the homolytic pathway is favoured thermodynamically.

2.4.8 Photocatalytic studies

Based on the electrochemical and spectroscopic results discussed above, the light driven hydrogen evolution reactions (HERs) for complex **1** and the reference cobaloxime [Co(dmgH)₂Cl(py)] were investigated, as polypyridyl and macrocyclic design for cobalt HER catalysts show promising performances [33, 44-49]. Unfortunately, the weak molar absorptivity of complex **1** in the visible portion of the spectrum suggests that the complex is unlikely to be an intrinsic photosensitizer, and thus requires external activation. The most studied inorganic photosensitizer (PS), [Ru(bpy)₃](PF₆)₂ [33, 46, 50-52] was chosen to photo-reduce the Co HER catalysts. The samples were irradiated with blue LEDs centred at 445 nm, Figure 47 and Tableau 5, in dimethylformamide as solvent, 1 M of triethanolamine as the sacrificial electron donor and 0.1 M aqueous tetrafluoroboric acid as the proton source, 0.1 mM of [Ru(bpy)₃](PF₆)₂, and the cobalt-containing catalysts at 0.01 mM. The [Ru(bpy)₃](PF₆)₂ is fully excited into the ¹MLCT band to drive the photoreactions. The excess of PS permits the evaluation of the maximum TON of HER cobalt-containing catalyst. No hydrogen was detected for the control experiments of the PS in the presence of sacrificial electron donor and HBF₄. When the illumination begins, a peak of activity occurred for both systems after a short lag time due to the required reduction of a Co(III) metal centre to a Co(I) metal centre [33]. The cobaloxime reaches a maximum turn over number (TON) of 4500

$\text{mmolH}_2 \text{ mol}^{-1}_{\text{CAT}} \text{ min}^{-1}$ and complex **1** attains $3300 \text{ mmol H}_2 \text{ mol}^{-1}_{\text{CAT}} \text{ min}^{-1}$ (Figure 31). The activities decrease slowly to end after almost three hours. We observed a TON of 79 for complex **1** and TON of 141 for the cobaloxime in ca 3 h of illumination. Aliquots of fresh photosensitizer and catalyst are added at the end of the photoreactions (Figure 48). For both catalysts, the activity starts again with addition of photosensitizer and no revival is observed in the case of catalyst addition indicating that the photosensitizer decomposes first. These results are comparable to the other systems reported in a smorgasbord study of cobalt containing systems [30].

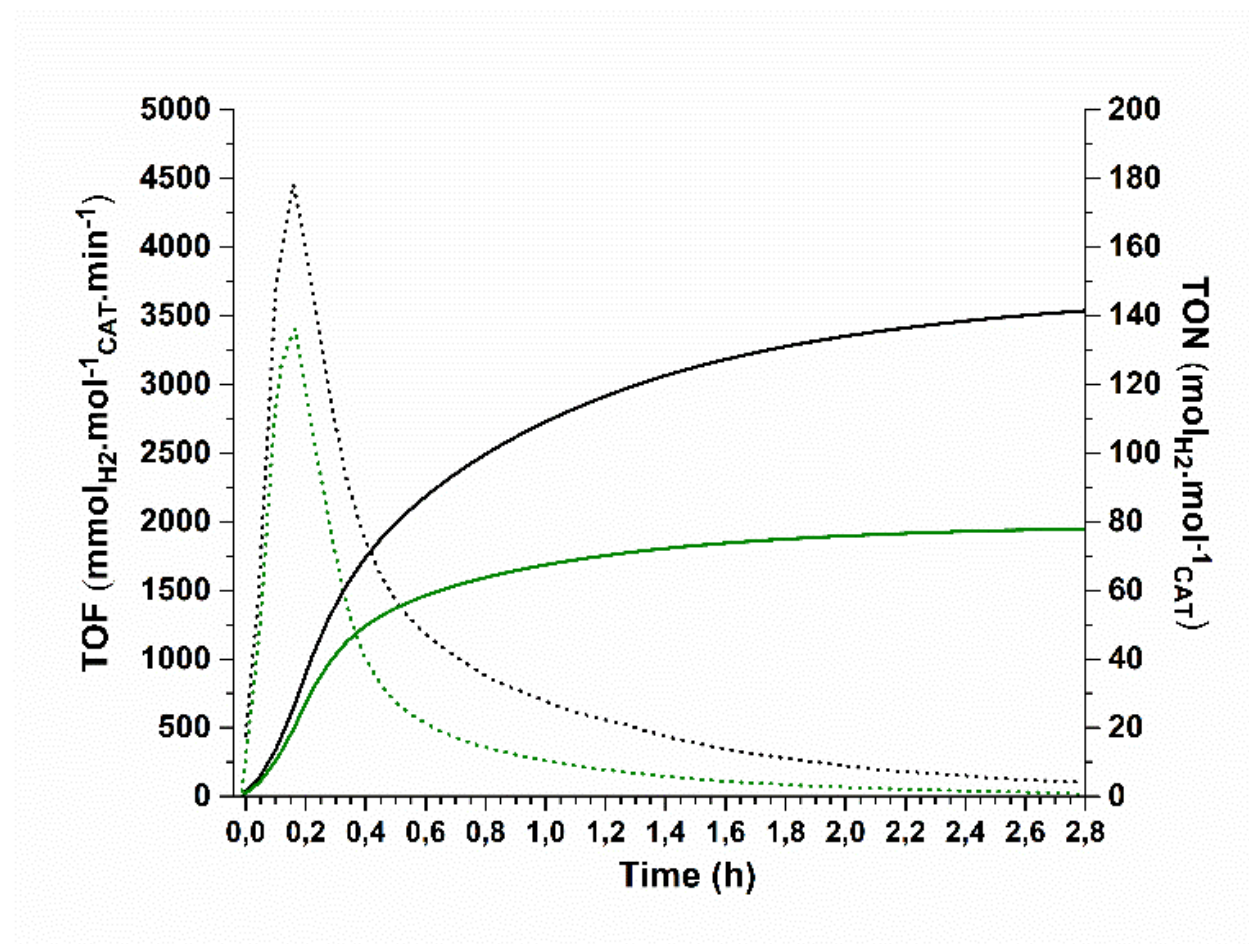


Figure 33. Hydrogen evolution of $[\text{Co}(\text{dmgH})_2\text{Cl}(\text{py})]$ (black) and complex **1** (green). TOF: dotted line. TON: solid line.

2.5 Conclusions

The X-ray crystallographic structure of complex **1** is presented, along with its spectroscopic and cyclic voltammetric properties. Unlike the report of its Co(II) analogue, we have demonstrated that the Co(II/I) couple of complex **1** possesses good reversible characteristics in aqueous and mixed aqueous environments. Like its analogous Co(II) counterpart, complex **1** demonstrated excellent electrocatalytic hydrogen evolution at 830 mV overpotential in CH₃CN, as well as photocatalytic hydrogen evolution with a high turnover number and moderate turnover frequency in DMF over a 3 h period.

2.5.1 Acknowledgements

AAH and MAWL would like to thank Professor Tara P. Dasgupta (sunrise: Wednesday, January 29, 1941 and sunset: Monday, April 20, 2020) for his beloved guidance as a father, a Ph.D. research advisor, and a mentor, to make us what we are today. R.I.P. AAH would also like to thank the National Science Foundation, 2415 Eisenhower Avenue, Alexandria, VA 22314, U.S.A., for a National Science Foundation CAREER Award, as this material is based upon work supported by the National Science Foundation under CHE-14321172 (formerly CHE-1151832). AAH would also like to thank the Old Dominion University startup package that allowed for the successful completion of this work. GSH, OS, and VP thank the Natural Sciences and Engineering Research Council (NSERC) of Canada (grant number 103046) for financial support.

2.5.2 References

- [1] N.S. Lewis, D.G. Nocera, Proc. Natl. Acad. Sci. U.S.A., 103 (2006) 15729.
- [2] D.L. Royer, R.A. Berner, J. Park, Nature, 446 (2007) 530.
- [3] R.B. Gordon, M. Bertram, T.E. Graedel, Proc. Natl. Acad. Sci. U.S.A., 103 (2006) 1209.
- [4] R.F. Service, Science, 309 (2005) 548-551.
- [5] D.Z. Zee, T. Chantarojsiri, J.R. Long, C.J. Chang, Acc. Chem. Res., 48 (2015) 2027-2036.
- [6] V. Artero, M. Chavarot-Kerlidou, M. Fontecave, Angew. Chem. Int. Ed., 50 (2011) 7238-7266.
- [7] T. Autrey, S. Xantheas, L. Li, J. Linehan, J. Franz, D. Katakis, C. Mitsopoulou, Z. Sofianos, T. Bitterwolf, Prepr. Pap. - Am. Chem. Soc., Div. Fuel Chem., 47 (2002) 752-754.
- [8] M. Kobayashi, S. Masaoka, K. Sakai, Angew. Chem. Int. Ed., 51 (2012) 7431-7434.
- [9] A.J. Esswein, D.G. Nocera, Chem. Rev., 107 (2007) 4022-4047.
- [10] C.-B. Li, P. Gong, Y. Yang, H.-Y. Wang, Catal. Lett., 148 (2018) 3158-3164.
- [11] X. Chen, H. Ren, W. Peng, H. Zhang, J. Lu, L. Zhuang, J. Phys. Chem. C, 118 (2014) 20791-20798.
- [12] M.A.W. Lawrence, M.J. Celestine, E.T. Artis, L.S. Joseph, D.L. Esquivel, A.J. Ledbetter, D.M. Cropek, W.L. Jarrett, C.A. Bayse, M.I. Brewer, A.A. Holder, Dalton Trans., 45 (2016) 10326-10342.
- [13] G.A.N. Felton, R.S. Glass, D.L. Lichtenberger, D.H. Evans, Inorg. Chem., 45 (2006) 9181-9184.
- [14] W. Gao, J. Ekström, J. Liu, C. Chen, L. Eriksson, L. Weng, B. Åkermark, L. Sun, Inorg. Chem., 46 (2007) 1981-1991.
- [15] M.L. Helm, M.P. Stewart, R.M. Bullock, M.R. DuBois, D.L. DuBois, Science, 333 (2011) 863-866.
- [16] P.A. Jacques, V. Artero, J. Pecaut, M. Fontecave, Proc. Natl. Acad. Sci. USA, 106 (2009) 20627-20632.
- [17] O.R. Luca, S.J. Konezny, J.D. Blakemore, D.M. Colosi, S. Saha, G.W. Brudvig, V.S. Batista, R.H. Crabtree, New J. Chem., 36 (2012) 1149-1152.
- [18] C. Baffert, V. Artero, M. Fontecave, Inorg. Chem., 46 (2007) 1817-1824.
- [19] X. Hu, B.S. Brunschwig, J.C. Peters, J. Am. Chem. Soc., 129 (2007) 8988-8998.
- [20] J. Wang, C. Li, Q. Zhou, W. Wang, Y. Hou, B. Zhang, X. Wang, Catal. Sci. Technol., 6 (2016) 8482-8489.

- [21] P. Wang, G. Liang, C.L. Boyd, C.E. Webster, X. Zhao, *Eur. J. Inorg. Chem.*, 2019 (2019) 2134-2139.
- [22] P. Wang, G. Liang, M.R. Reddy, M. Long, K. Driskill, C. Lyons, B. Donnadieu, J.C. Bollinger, C.E. Webster, X. Zhao, *J. Am. Chem. Soc.*, 140 (2018) 9219-9229.
- [23] M.A.W. Lawrence, A.A. Holder, *Inorg. Chim. Acta*, 441 (2016) 157-168.
- [24] P. Du, J. Schneider, G. Luo, W.W. Brennessel, R. Eisenberg, *Inorg. Chem.*, 48 (2009) 4952-4962.
- [25] W.T. Eckenhoff, R. Eisenberg, *Dalton Trans.*, 41 (2012) 13004-13021.
- [26] S. Varma, C.E. Castillo, T. Stoll, J. Fortage, A.G. Blackman, F. Molton, A. Deronzier, M.N. Collomb, *Phys. Chem. Chem. Phys.*, 15 (2013) 17544-17552.
- [27] M.G. Pfeffer, B. Schäfer, G. Smolentsev, J. Uhlig, E. Nazarenko, J. Guthmuller, C. Kuhnt, M. Wächtler, B. Dietzek, V. Sundström, S. Rau, *Angew. Chem. Int. Ed.*, 54 (2015) 5044-5048.
- [28] S. Shi, L.M. Daniels, J.H. Espenson, *Inorg. Chem.*, 30 (1991) 3407-3410.
- [29] O.M. Williams, A.H. Cowley, M.J. Rose, *Dalton Trans.*, 44 (2015) 13017-13029.
- [30] R.W. Hogue, O. Schott, G.S. Hanan, S. Brooker, *Chem. - Eur. J.*, 24 (2018) 9820-9832.
- [31] T. Taura, *Bull. Chem. Soc. Jpn.*, 63 (1990) 1105-1110.
- [32] G.M. Sheldrick, in, University of Gottingen, Germany, 2014.
- [33] O. Schott, A.K. Pal, D. Chartrand, G.S. Hanan, *ChemSusChem*, 10 (2017) 4436-4441.
- [34] B. Brisig, E.C. Constable, C.E. Housecroft, *New J. Chem.*, 31 (2007) 1437-1447.
- [35] M.A.W. Lawrence, C.D. McMillen, R.K. Gurung, M.J. Celestine, J.F. Arca, A.A. Holder, *J. Chem. Crystallogr.*, 45 (2015) 427-433.
- [36] A. Yamasaki, F. Yajima, S. Fujiwara, *Inorg. Chim. Acta*, 2 (1968) 39-42.
- [37] M.Y. Kim, W.K. Seok, Y. Dong, H. Yun, *Inorg. Chim. Acta*, 319 (2001) 194-198.
- [38] D.A. House, *Comments Inorg. Chem.*, 19 (1997) 327-350.
- [39] F.P. Rotzinger, *Inorg. Chem.*, 38 (1999) 5730-5733.
- [40] K.J. Lee, B.D. McCarthy, J.L. Dempsey, *Chem. Soc. Rev.*, 48 (2019) 2927-2945.
- [41] C. Costentin, J.-M. Savéant, *ChemElectroChem*, 1 (2014) 1226-1236.
- [42] C. Costentin, H. Dridi, J.-M. Savéant, *J. Am. Chem. Soc.*, 136 (2014) 13727-13734.
- [43] R.M. Kellett, T.G. Spiro, *Inorg. Chem.*, 24 (1985) 2373-2377.
- [44] N. Queyriaux, R.T. Jane, J. Massin, V. Artero, M. Chavarot-Kerlidou, *Coord Chem Rev*, 304-305 (2015) 3-19.

- [45] S. Rajak, O. Schott, P. Kaur, T. Maris, G.S. Hanan, A. Duong, RSC Advances, 9 (2019) 28153-28164.
- [46] R.W. Hogue, O. Schott, G.S. Hanan, S. Brooker, Chemistry, 24 (2018) 9820-9832.
- [47] R.S. Khnayzer, V.S. Thoi, M. Nippe, A.E. King, J.W. Jurss, K.A. El Roz, J.R. Long, C.J. Chang, F.N. Castellano, Energ Environ Sci, 7 (2014) 1477-1488.
- [48] D.Z. Zee, T. Chantarojsiri, J.R. Long, C.J. Chang, Acc Chem Res, 48 (2015) 2027-2036.
- [49] W.K. Lo, C.E. Castillo, R. Gueret, J. Fortage, M. Rebarz, M. Sliwa, F. Thomas, C.J. McAdam, G.B. Jameson, D.A. McMorrان, J.D. Crowley, M.N. Collomb, A.G. Blackman, Inorg Chem, 55 (2016) 4564-4581.
- [50] P. Dongare, B.D.B. Myron, L. Wang, D.W. Thompson, T.J. Meyer, Coord. Chem. Rev., 345 (2017) 86-107.
- [51] E. Rousset, D. Chartrand, I. Ciofini, V. Marvaud, G.S. Hanan, Chem Commun (Camb), 51 (2015) 9261-9264.
- [52] E. Rousset, I. Ciofini, V. Marvaud, G.S. Hanan, Inorg Chem, 56 (2017) 9515-9524.

2.6 Supporting Information

Synthesis, structure, and hydrogen evolution studies of a heteroleptic Co(III) complex

Michael J. Celestine,^a Mark A.W. Lawrence,^b Olivier Schott,^c Vincent Picard,^c Garry S. Hanan,^c Emily M. Marquez,^a Chekeyl G. Harold,^a Cole T. Kuester,^d Blaise A. Frenzel,^d Christopher G. Hamaker,^e Sean E. Hightower,^d Colin D. McMillen,^f and Alvin A. Holder^{*a}

a. Department of Chemistry and Biochemistry, Old Dominion University, 4541 Hampton Boulevard, Norfolk, VA 23529, U.S.A.

b. Department of Chemistry, University of the West Indies, Mona Campus, Kingston 7, Jamaica

c. Département de Chimie, Université de Montréal, Montréal, Canada

d. Department of Chemistry, University of North Dakota, 151 Cornell St., Stop 9024, Grand Forks, ND 58202-9024, U.S.A.

e. Department of Chemistry, Illinois State University, Campus Box 4160, Normal, IL, 61790-4160, U.S.A.

f. Department of Chemistry, Clemson University, 379 Hunter Laboratories, Clemson, SC 29634, U.S.A.

Corresponding author's e-mail: aholder@odu.edu

Tableau 4. – ^{59}Co NMR spectroscopic data of selected complexes in the respective solvents.

Complexes	δ/ppm	Ref.	Complexes	δ/ppm	Ref.
$[\text{Co}(\text{tpy})(\text{phen})\text{Cl}](\text{PF}_6)_2 \bullet 0.25\text{CH}_3\text{CN}^{\text{d}}$	7148	TW ^a	$[\text{Co}(\text{tpy})(\text{phen})\text{Cl}](\text{PF}_6)_2 \bullet 0.25\text{CH}_3\text{CN}^{\text{b}}$	7177	TW ^a
$[\text{Co}(\text{tpy})_2](\text{PF}_6)_3^{\text{d}}$	7039	TW	$[\text{Co}(\text{tpa})(\text{O}_2\text{CO})]\text{ClO}_4 \bullet \text{H}_2\text{O}^{\text{c}}$	7965	¹
$[\text{Co}(\text{phen})_2(\text{O}_2\text{CO})]\text{PF}_6^{\text{b}}$	8362	²	$[{}^n\text{Bu}_4\text{N}][\text{Co}(\text{bpy})_2(\text{solv})]^{\text{d}}$	2934	³
$[\text{Co}(\text{phen})_2(\text{H}_2\text{O})_2](\text{PF}_6)_3^{\text{b}}$	7070	²	$[\text{Co}(\text{ATS})(\text{NH}_3)_2]^{+\text{b}}$	5320	⁴
$[\text{Co}(\text{phen})_2(\text{MeATSC})](\text{NO}_3)_3 \bullet 1.5\text{H}_2\text{O}$	7067	²	$[\text{Co}(\text{ATS})(\text{Im})_2]^{+\text{b}}$	5640	⁴
$[\text{Co}(\text{phen})_2(\text{O}_2\text{CO})](\text{L}) \bullet 6\text{H}_2\text{O}^{\text{c}}$	8377	⁵	$[\text{Co}(\text{ATS})(\text{BnA})_2]^{+\text{b}}$	5600	⁴
$[\text{Co}(\text{phen})_2(\text{O}_2\text{CO})]_2(\text{C}_8\text{H}_4\text{O}_4) \bullet 15\text{H}_2\text{O}^{\text{e}}$	8377	⁶	$[\text{Co}(\text{PTS})(\text{NH}_3)_2]^{+\text{b}}$	5320	⁴
$[\text{Co}(\text{phen})_3]\text{Cl}_3^{\text{d}}$	7080	⁷	$[\text{Co}(\text{PTS})(\text{Im})_2]^{+\text{b}}$	5610	⁴
$[\text{Co}(\text{phen})_3](\text{PF}_6)_3^{\text{b}}$	7000	⁸	$[\text{Co}(\text{PTS})(\text{BnA})_2]^{+\text{b}}$	5590	⁴
$[\text{Co}(\text{phen})_2(\text{bpy})](\text{PF}_6)_3 \bullet 0.5(\text{C}_2\text{H}_5)_2\text{O}^{\text{b}}$	6900	⁸	$[\text{Co}(\text{GTS})(\text{NH}_3)_2]^{+\text{b}}$	5250	⁴
$[\text{Co}(\text{tepa})(\text{O}_2\text{CO})]\text{ClO}_4^{\text{c}}$	10121	¹	$[\text{Co}(\text{GTS})(\text{Im})_2]^{+\text{b}}$	5570	⁴
$[\text{Co}(\text{pmap})(\text{O}_2\text{CO})]\text{ClO}_4^{\text{c}}$	9096	¹	$[\text{Co}(\text{GTS})(\text{BnA})_2]^{+\text{b}}$	5510	⁴
$[\text{Co}(\text{pmea})(\text{O}_2\text{CO})]\text{ClO}_4 \bullet 3\text{H}_2\text{O}^{\text{c}}$	8509	¹			

^a TW = this work^b in DMSO-d₆.^c in D₂O.^d where solv = H₂O and/or CH₃CN) generated *in situ* from [Co(bpy)₂Cl₂] in the presence of 10 equivalents of [nBu₄N]BH₄ in CD₃CN-D₂O (4:1, v/v) at 28 °C.^e in water.

Abbreviations:

ATS = diacetyl bis(thiosemicarbazone)

BnA = benzylamine

C₈H₄O₄²⁻ = terephthalate anion

GTS = glyoxal bis(thiosemicarbazone)

Im = imidazole

L = 4-aminobenzenesulphonate

pmap = bis(2-(2-pyridyl)ethyl)(2-pyridylmethyl)amine

pmea = bis((2-pyridyl)methyl)-2-((2-pyridyl)ethyl)amine

PTS = pyruvaldehyde bis(thiosemicarbazone)
 tepa = tris(2-(2-pyridyl)ethyl)amine
 tpa = tris(2-pyridylmethyl)amine

Characterisation of Co containing by-products

After the one-pot synthesis, complex **1** was purified three times on a Sephadex LH-20 column. The other major product that eluted out was $[\text{Co}(\text{tpy})_2]^{n+}$. From the ESI mass spectrum of $[\text{Co}(\text{tpy})_2]^{n+}$, Figure S13, the cobalt(III) species was observed at the m/z of 335.05 and 815.10, and the cobalt(II) species at the m/z of 262.90 and 670.15. The ^1H NMR spectra of the complex, Figure S4 and S14, further showed that indeed the bis-2:2':6':2''-terpyridinecobalt(II/III) complex was a mixture of the cobalt(II) species and the cobalt(III). Finally Figure S15, the ^{59}Co NMR spectrum of $[\text{Co}(\text{tpy})_2](\text{PF}_6)_3$ chemical shift was observed at 7039 ppm upfield to compared to complex **1**.

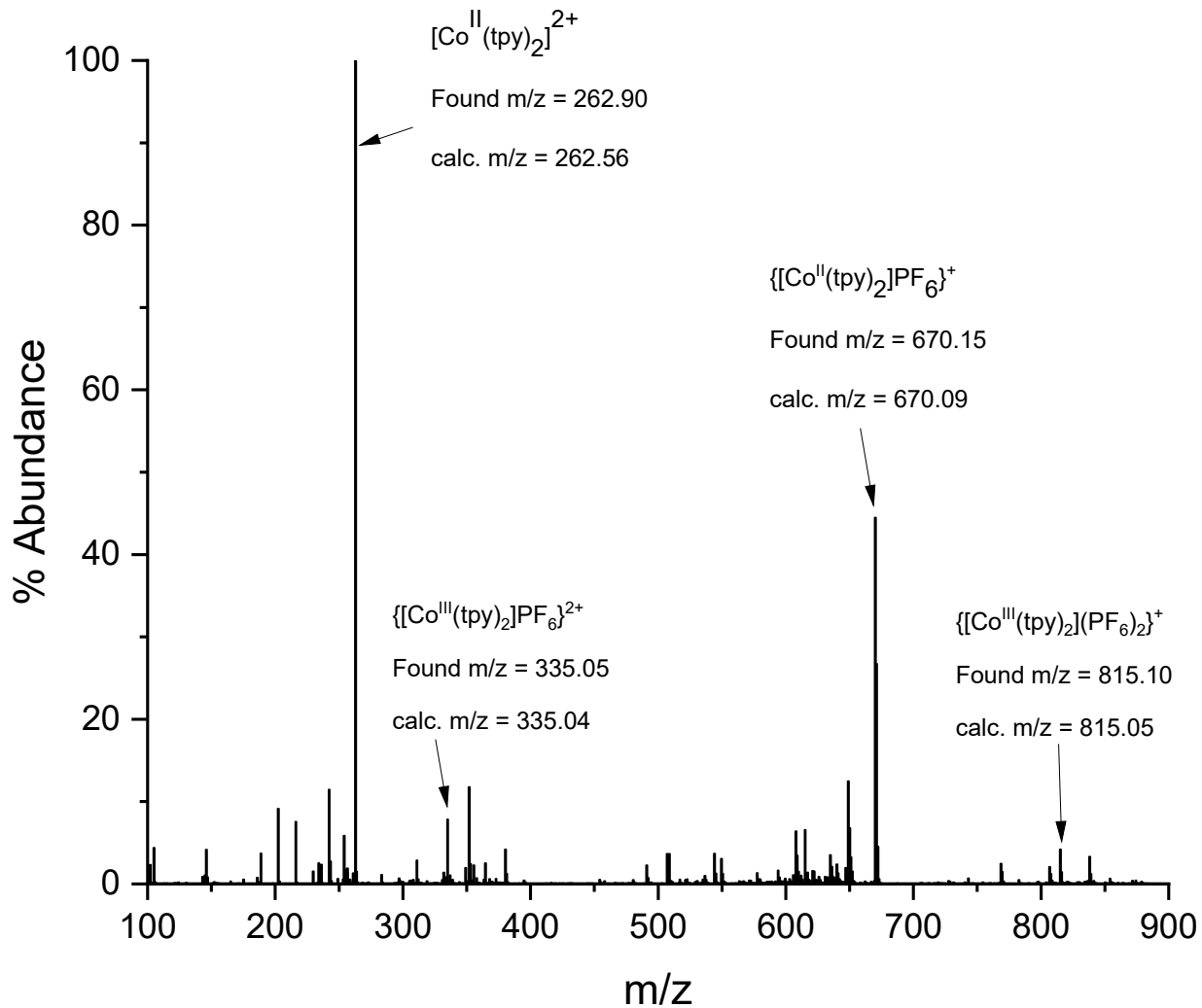


Figure 34. ESI MS of $[\text{Co}(\text{tpy})_2](\text{PF}_6)_{2/3}$ in CH_3CN .

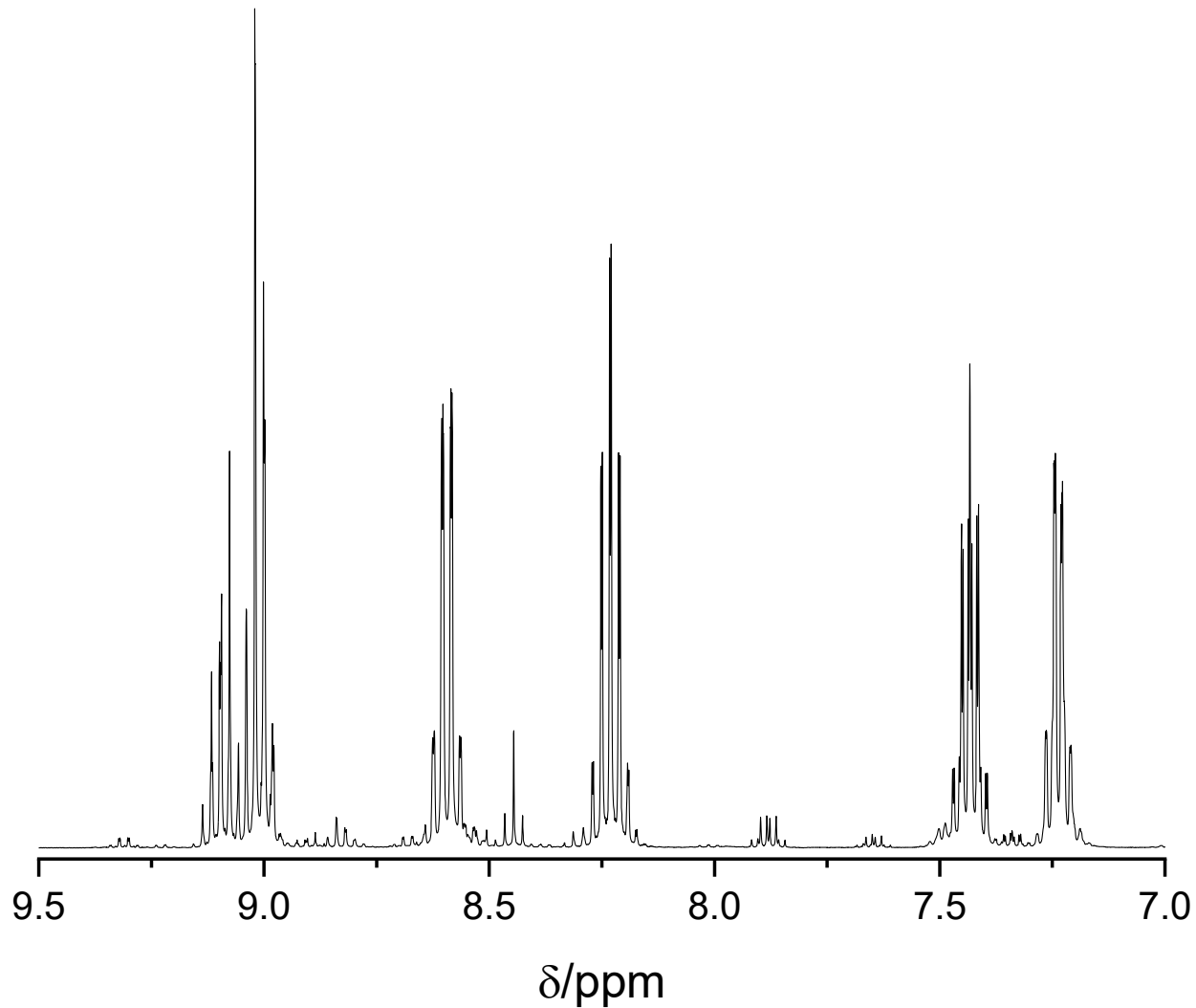


Figure 35. ${}^1\text{H}$ NMR spectrum of $[\text{Co}(\text{tpy})_2](\text{PF}_6)_{2/3}$ in CD_3CN .

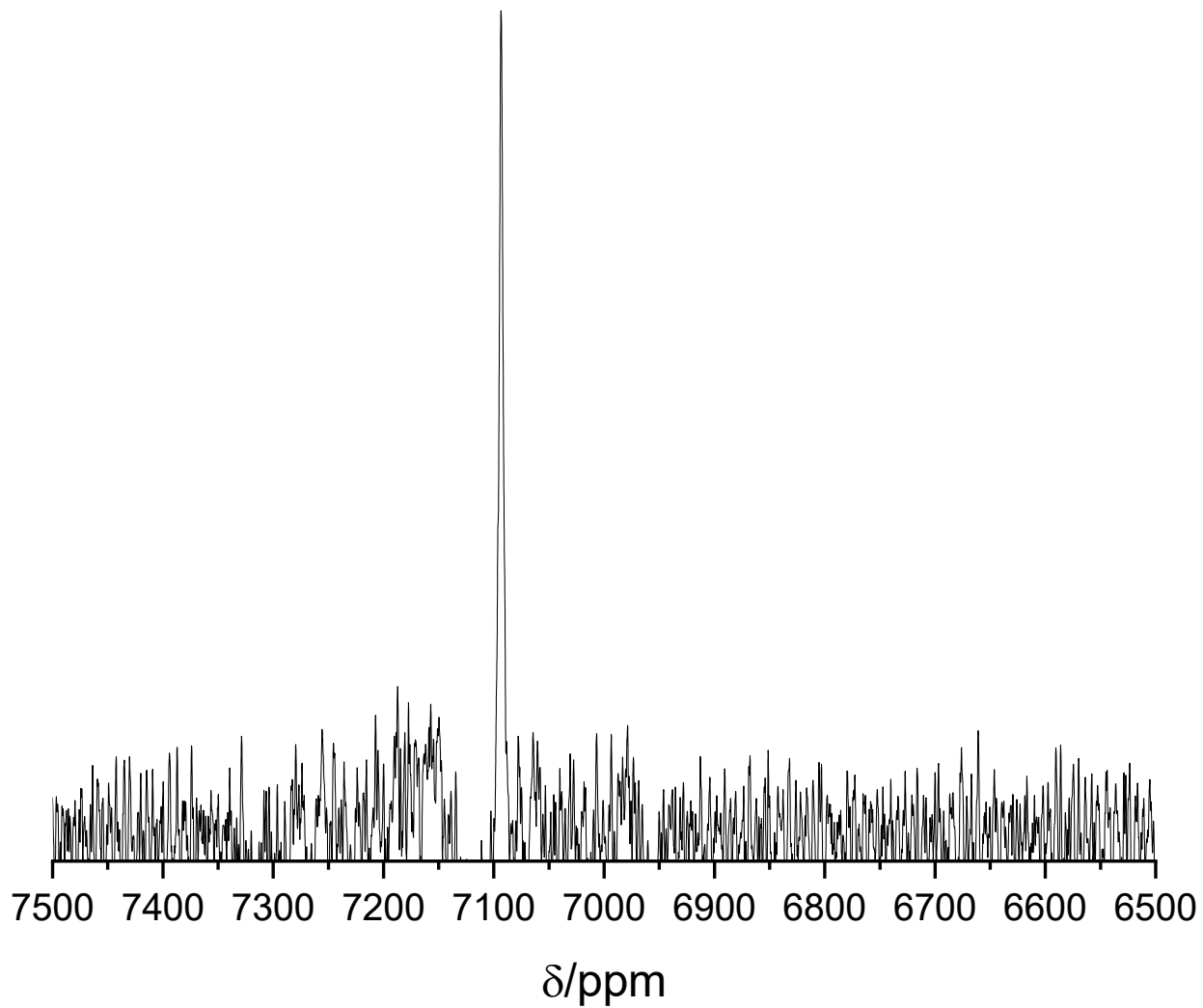


Figure 36. ^{59}Co NMR spectrum of $[\text{Co}(\text{tpy})_2](\text{PF}_6)_3$ in CD_3CN .

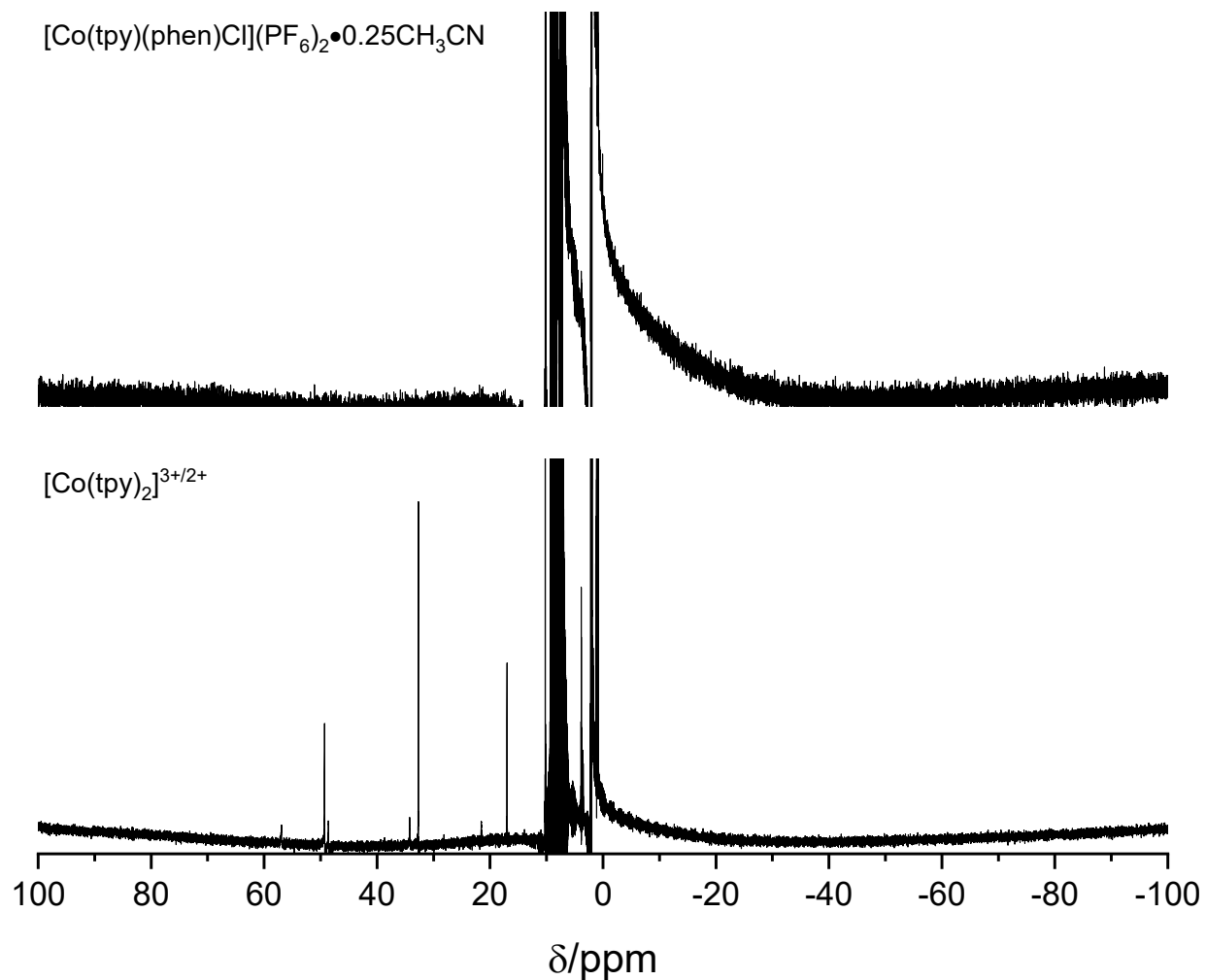


Figure 37. ¹H NMR spectra of $[\text{Co}(\text{tpy})_2](\text{PF}_6)_{2/3}$ and $[\text{Co}(\text{tpy})(\text{phen})\text{Cl}](\text{PF}_6)_2 \bullet 0.25\text{CH}_3\text{CN}$ **1** in CD_3CN .

Additional data for [Co(tpy)(phen)Cl](PF₆)₂•0.25CH₃CN **1**

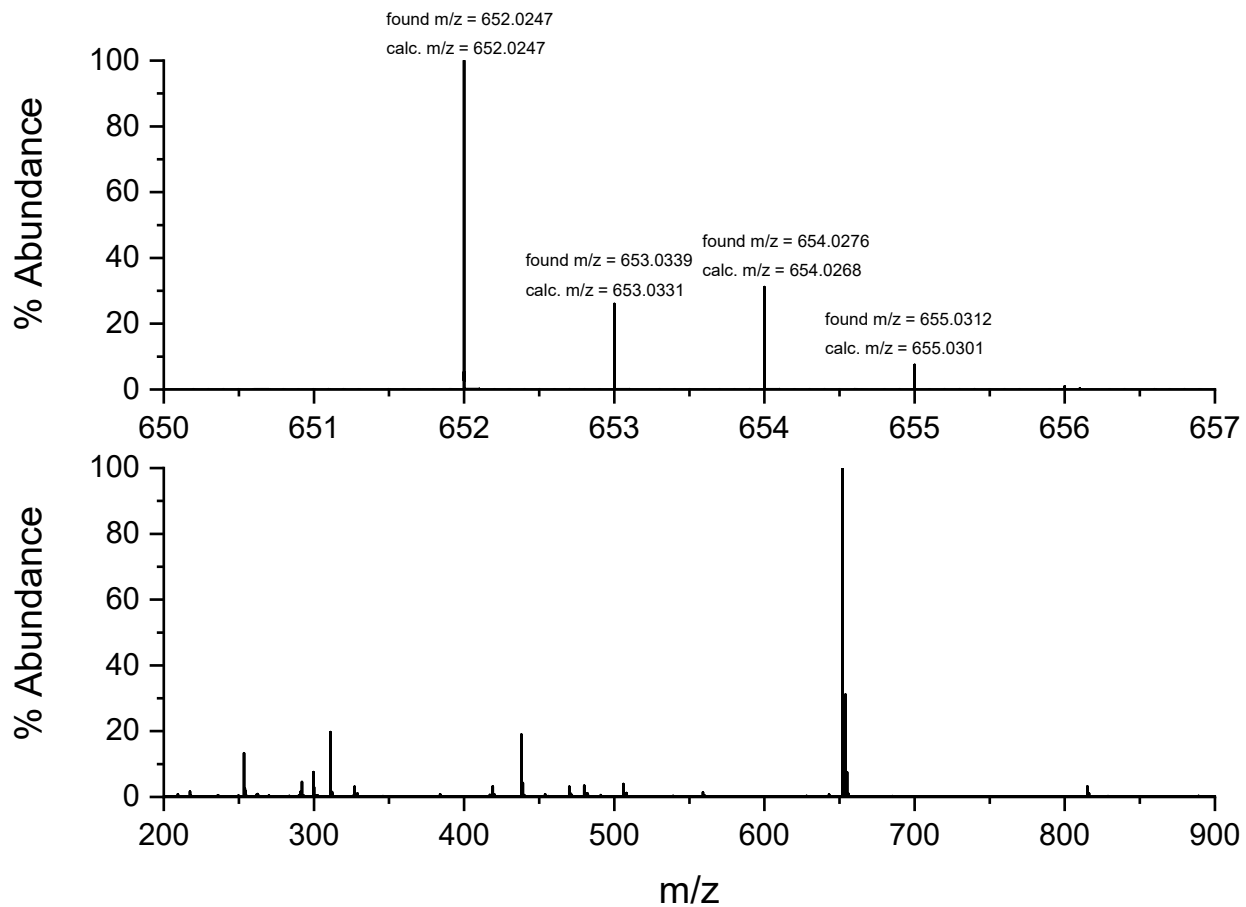


Figure 38. HRMS of complex **1** in CH₃CN

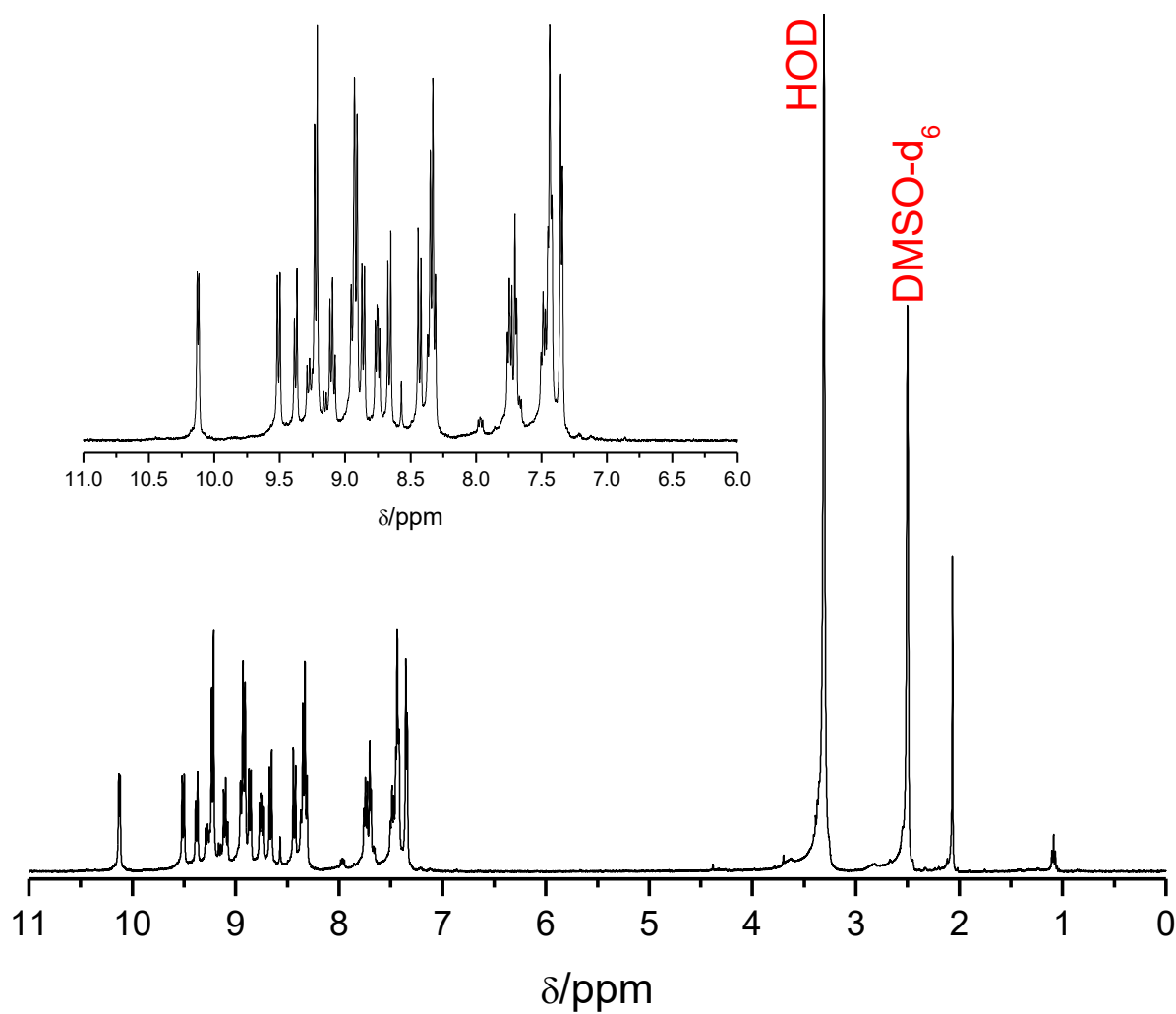


Figure 39. ¹H NMR spectra of complex **1** in DMSO-*d*₆.

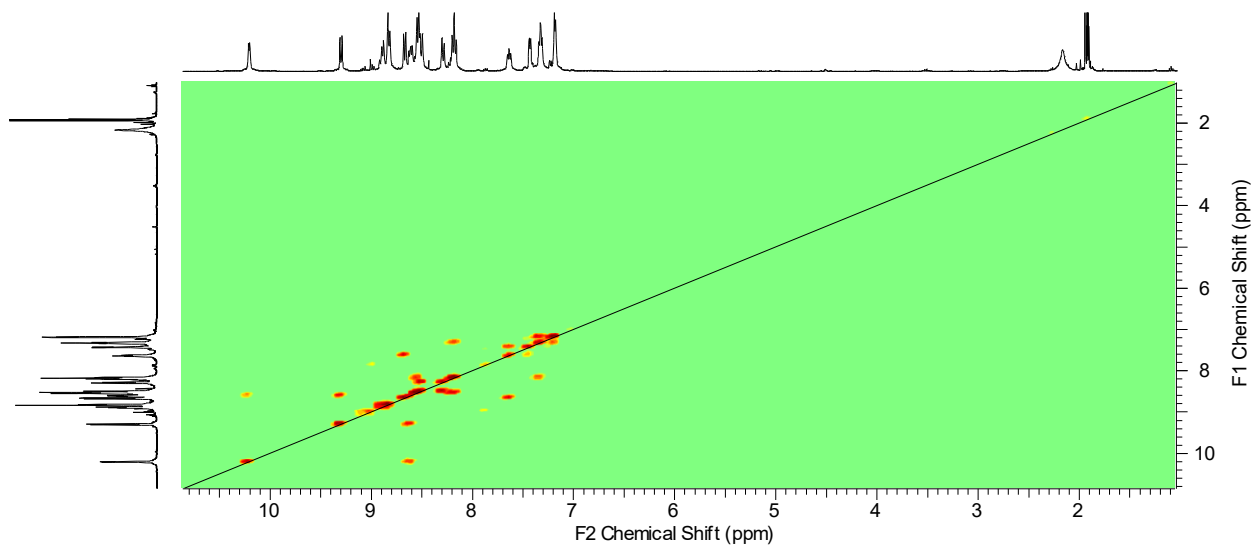


Figure 40. ^1H - ^1H COSY NMR spectrum of complex **1** in CD_3CN .

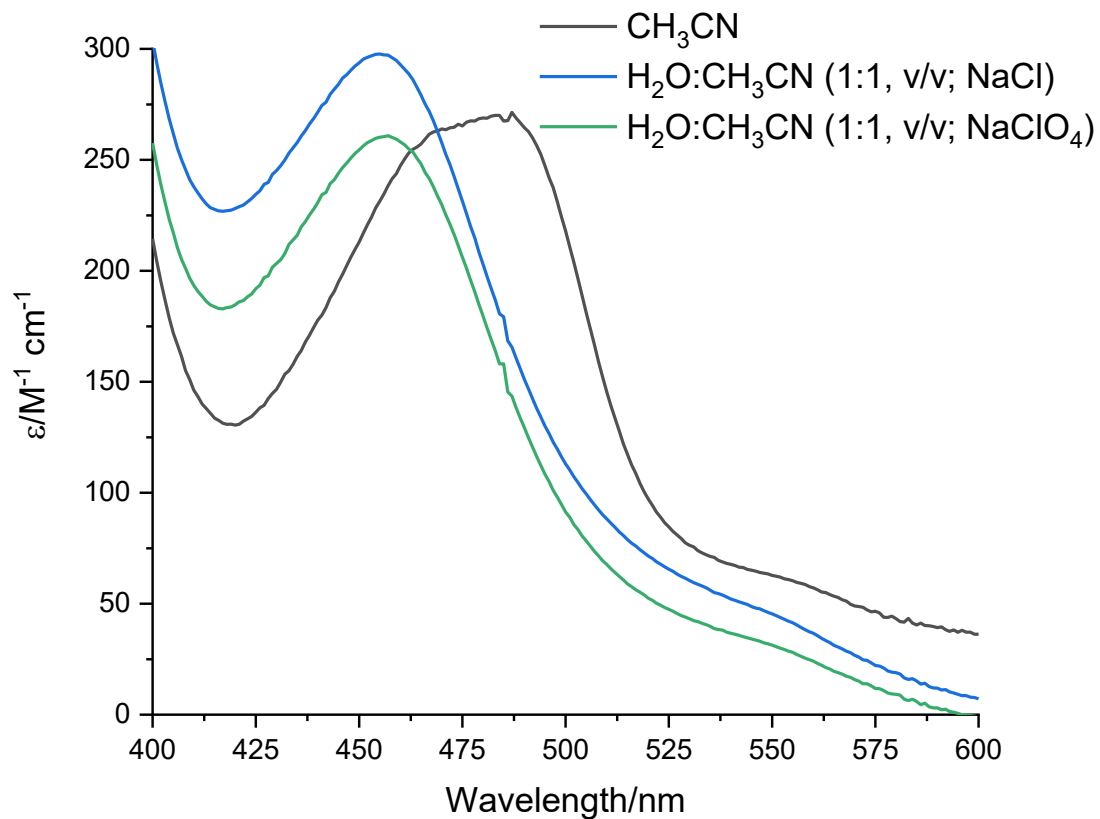


Figure 41. UV-visible spectra of complex **1** in acetonitrile or a mixture of water:acetonitrile (1:1, v/v) with different sodium salts.

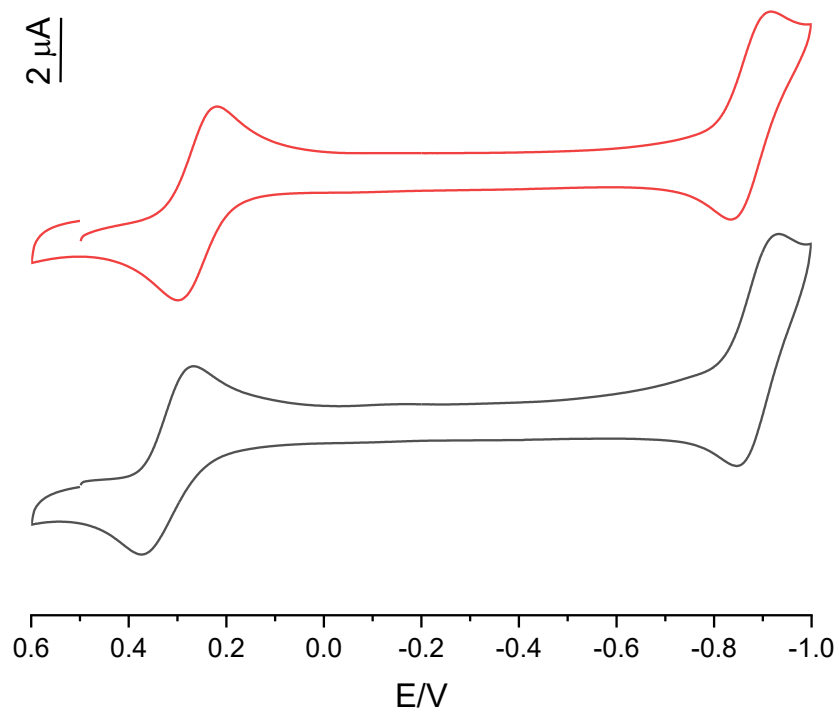


Figure 42. Cyclic voltammograms of $[\text{Co}(\text{tpy})(\text{phen})\text{Cl}]\text{Cl}_2$. Solvent = acetonitrile:water (1:1, v/v), $[\text{complex}] = 1.0 \text{ mM}$, supporting electrolyte = 0.1 M (NaClO_4 (**black**) or NaCl (**red**)), working electrode = Pt, auxiliary electrode = Pt wire, reference electrode = Ag/AgCl , and scan rate = 100 mV s^{-1} .

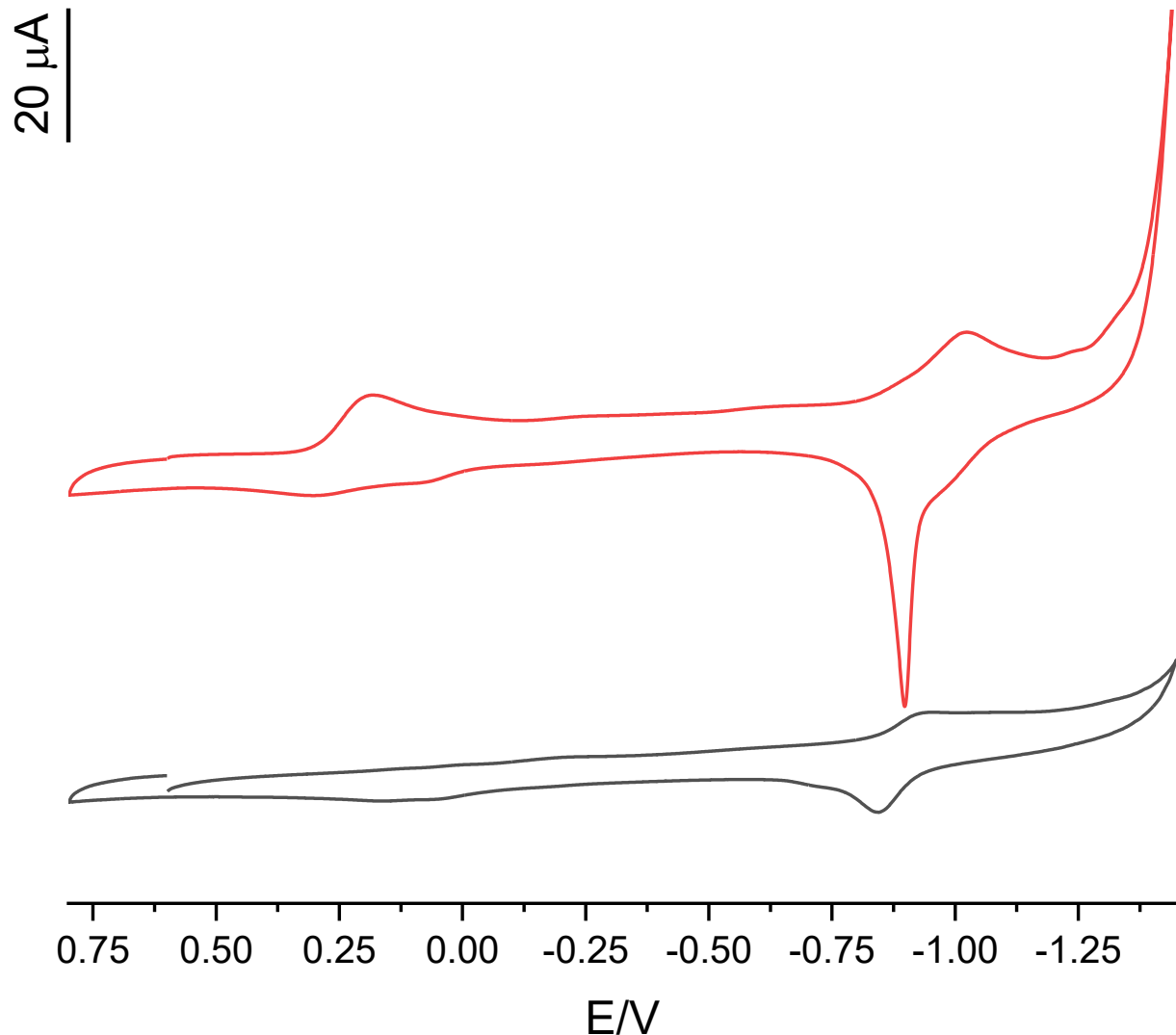


Figure 43. Cyclic voltammograms of $[\text{Co}(\text{tpy})(\text{phen})\text{Cl}]\text{Cl}_2$. Solvent = water, $[\text{complex}] = 1.0 \text{ mM}$, supporting electrolyte = $0.1 \text{ M} (\text{NaClO}_4 \text{ (black)} \text{ or } \text{NaCl} \text{ (red)})$, working electrode = Pt, auxiliary electrode = Pt wire, reference electrode = Ag/AgCl , and scan rate = 100 mV s^{-1} .

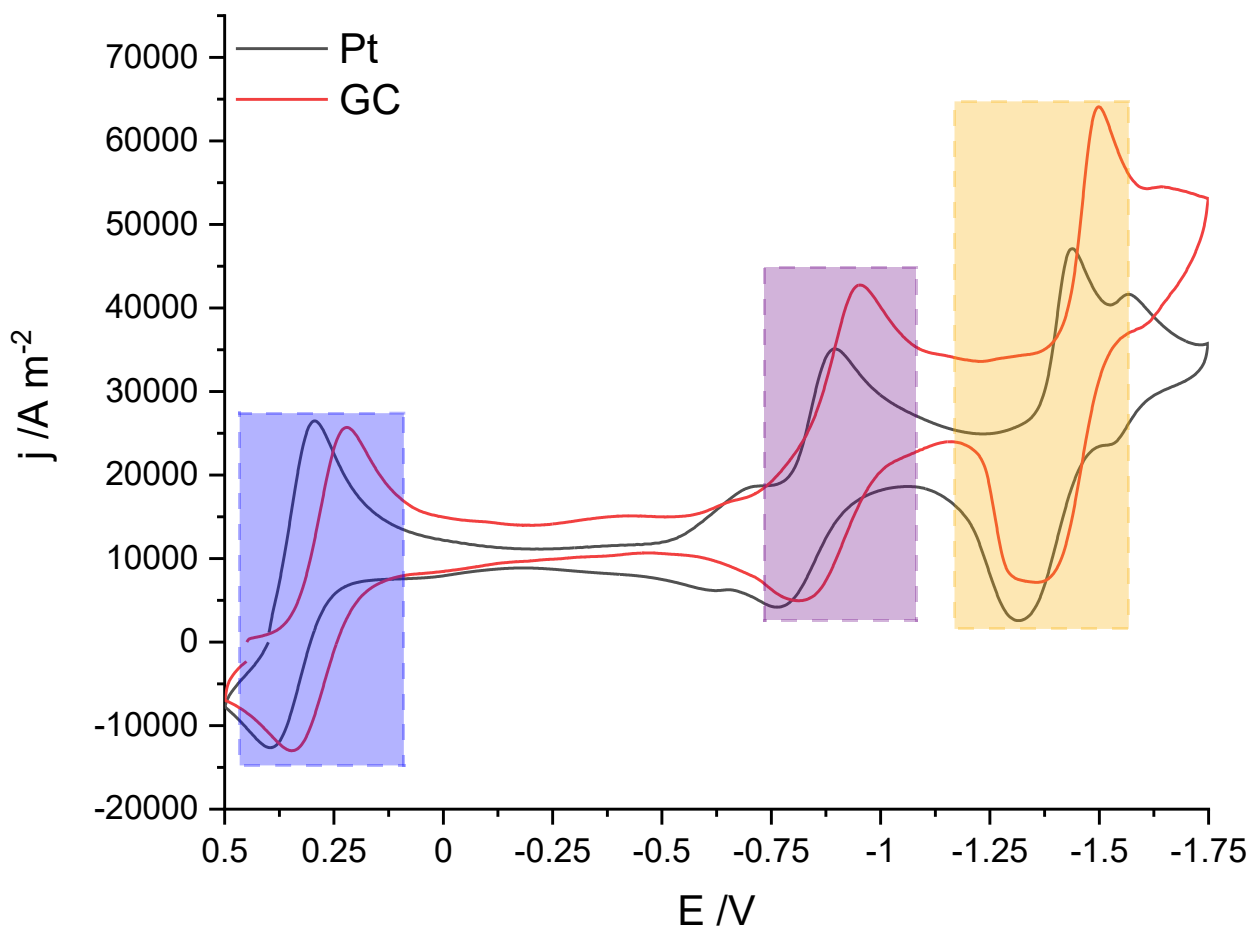


Figure 44. Cyclic voltammogram of complex **1**. Solvent = acetonitrile, [complex] = 1.0 mM, $[{}^n\text{Bu}_4\text{N}] \text{ClO}_4$ = 0.10 M, working electrode = either Pt or glassy carbon, auxiliary electrode = Pt wire, reference electrode = Ag/AgCl, and scan rate = 100 mV s⁻¹.

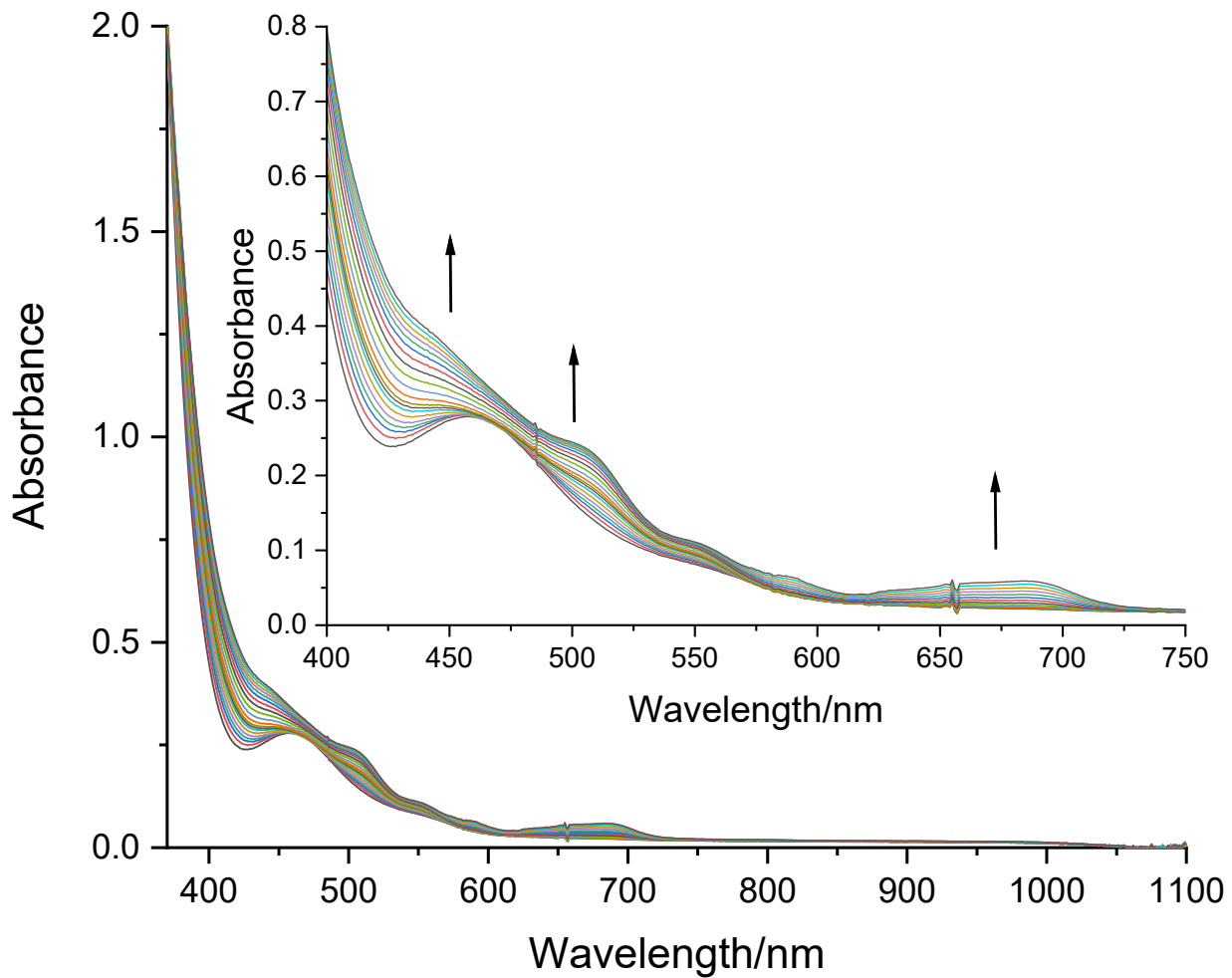


Figure 45. Spectroelectrochemical spectra of $[\text{Co}(\text{tpy})(\text{phen})\text{Cl}](\text{PF}_6)_2 \cdot 0.25\text{CH}_3\text{CN}$ **1**. Solvent = acetonitrile, [complex] = 13.3 mM, [$^n\text{Bu}_4\text{N}\text{ClO}_4$] = 0.10 mM, working electrode = Pt mesh wire, auxiliary electrode = Pt wire, reference electrode = Ag/AgCl, and held potential = 0.50 V.

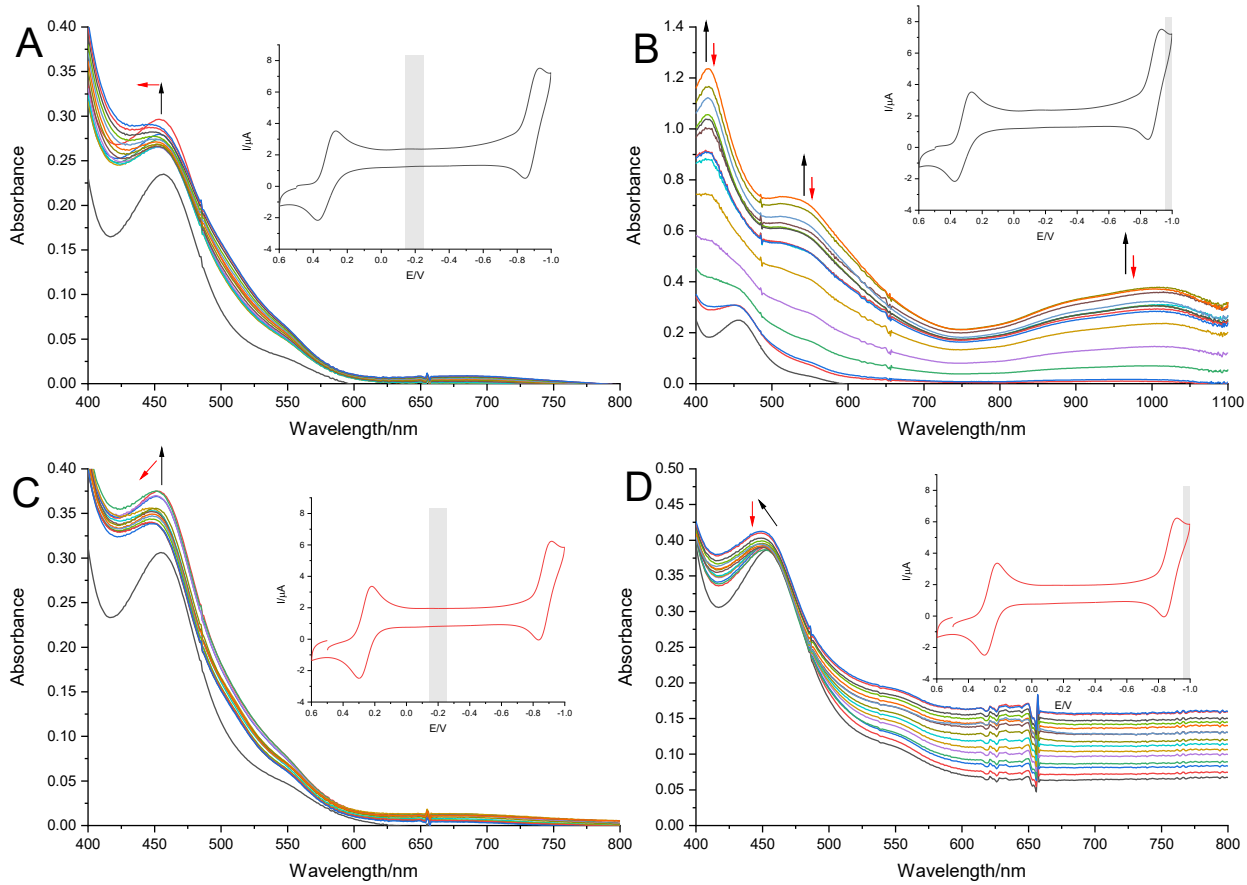


Figure 46. Spectroelectrochemical spectra of $[\text{Co}(\text{tpy})(\text{phen})\text{Cl}](\text{PF}_6)_2 \cdot 0.25\text{CH}_3\text{CN}$ **1** with the supporting electrolyte NaClO_4 (**A** and **B**) or NaCl (**C** and **D**) in $\text{H}_2\text{O}:\text{CH}_3\text{CN}$ (1:1, v/v). $[\text{complex}] = 0.9 - 10.3 \text{ mM}$, $[\text{supporting electrolyte}] = 0.1 \text{ M}$, working electrode = Pt, auxiliary electrode = Pt wire, and reference electrode = Ag/AgCl.

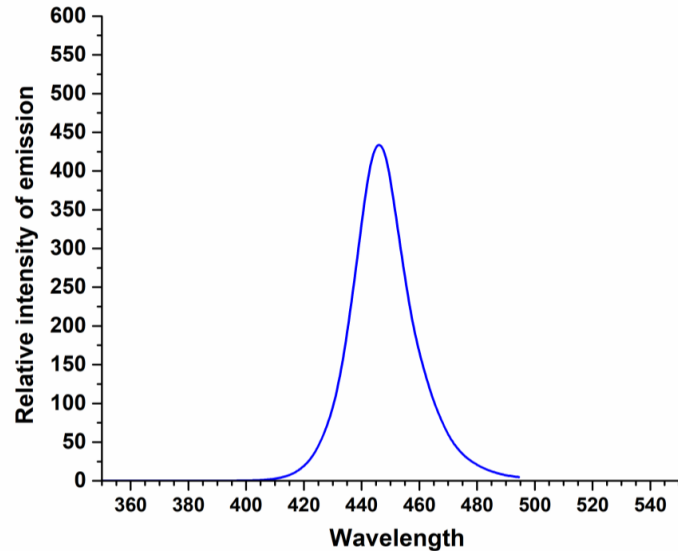


Figure 47. Emission spectrum of blue LED.

Tableau 5. – Emission maxima and amplitude of LED light.

Light source ^a	Blue
$\lambda_{\text{max,em}}/\text{nm}$	445
$\Delta\lambda/\text{nm}$	90
Photon flux in $\mu\text{mol}_{\text{photons}} \text{min}^{-1} \text{cm}^{-2}$ ^b	20

^a A 445 nm blue LED.

^b An analog power-meter PM100A (THORLABS) associated with a compact photodiode power head with silicon detector S120C was used to evaluate the photon flux for the LEDs. Photo-diode detector was placed at the same distance from the LED surface as the bottom of the illuminated vial.

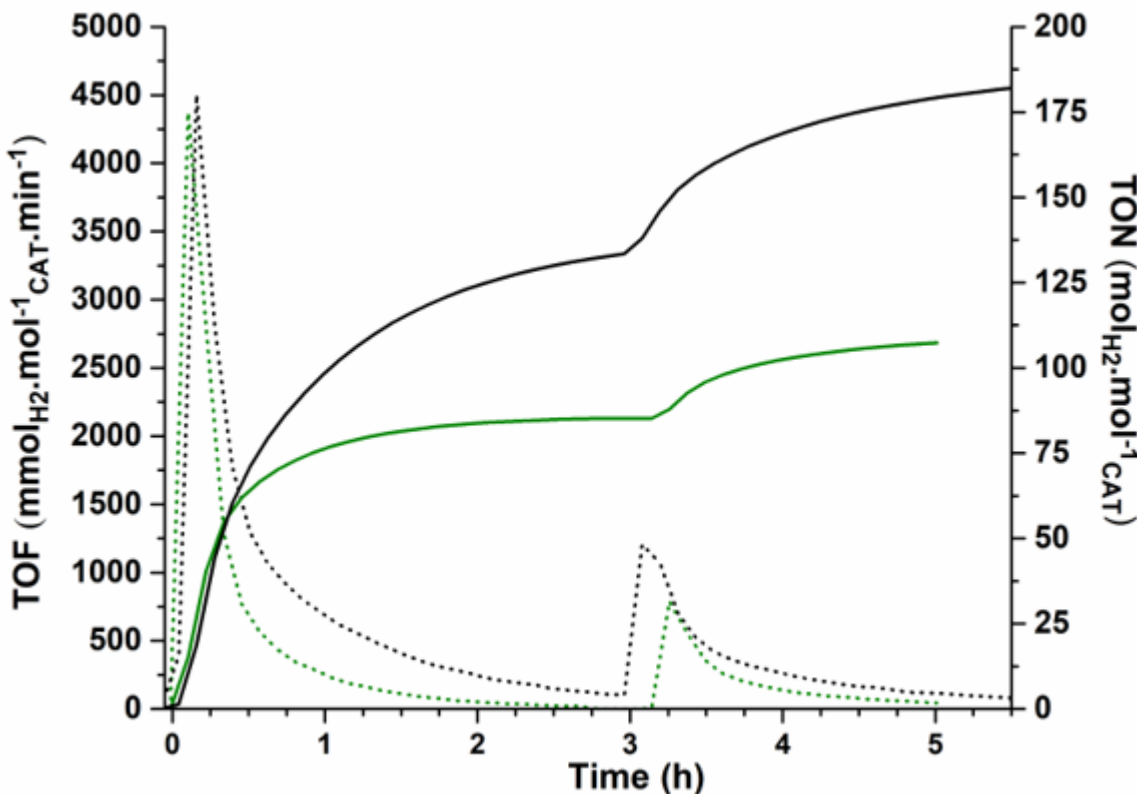


Figure 48. Restart of hydrogen evolution of $[\text{Co}(\text{dmgH})_2\text{Cl}(\text{py})]$ (black) and complex **1** (olive) by the addition of fresh photosensitizer (1.25 ml of 0.4 mM $[\text{Ru}(\text{bpy})_3](\text{PF}_6)_2$) at the end of activity. TOF: dotted line. TON: solid line.

References

1. P. M. Jaffray, L. F. McClintock, K. E. Baxter and A. G. Blackman, *Inorg. Chem.*, 2005, **44**, 4215-4225.
2. S. J. Beebe, M. J. Celestine, J. L. Bullock, S. Sandhaus, J. F. Arca, D. M. Cropek, T. A. Ludvig, S. R. Foster, J. S. Clark, F. A. Beckford, C. M. Tano, E. A. Tonsel-White, R. K. Gurung, C. E. Stankavich, Y.-C. Tse-Dinh, W. L. Jarrett and A. A. Holder, *J. Inorg. Biochem.*, 2020, **203**, 110907.
3. M. A. W. Lawrence and A. A. Holder, *Inorg. Chim. Acta*, 2016, **441**, 157-168.
4. A. P. King, H. A. Gellineau, J.-E. Ahn, S. N. MacMillan and J. J. Wilson, *Inorg. Chem.*, 2017, **56**, 6609-6623.
5. R. P. Sharma, A. Singh, T. Aree and P. Venugopalan, *J. Mol. Struct.*, 2009, **928**, 18-24.
6. R. P. Sharma, A. Singh, P. Venugopalan and W. T. A. Harrison, *J. Mol. Struct.*, 2010, **980**, 72-77.
7. A. Yamasaki, F. Yajima and S. Fujiwara, *Inorg. Chim. Acta*, 1968, **2**, 39-42.
8. M. A. W. Lawrence, C. D. McMillen, R. K. Gurung, M. J. Celestine, J. F. Arca and A. A. Holder, *J. Chem. Crystallogr.*, 2015, **45**, 427-433.

3) Chapitre 3 – N-substituted 2-pyridinecarbothioamides and polypyridyl mixed-ligand cobalt(III)-containing complexes for photocatalytic hydrogen generation

3.1 A B S T R A C T

Two mixed-ligand cobalt(III) complexes containing 2,2'-bipyridine (bpy) or 1,10-phenanthroline (phen), and *N*-(3,5-bis(trifluoromethyl)phenyl)pyridine-2-carbothioamide (PCA-(CF₃)₂) as ligands were synthesized, and characterized by a variety of spectroscopic techniques and elemental analyses. Crystals of the PCA-(CF₃)₂ molecule are of the monoclinic, C2/c crystal system and space group as determined via X-ray crystallography. The voltammetric properties of six cobalt(III) complexes, [Co(bpy)₂Cl₂]Cl **1**, [Co(phen)₂Cl₂]Cl **2**, [Co(bpy)₂(PCA-(CF₃)₂)](PF₆)₂ · H₂O **3**, [Co(phen)₂(PCA-(CF₃)₂)](PF₆)₂ · 1.25H₂O **4**, [Co(bpy)₃](PF₆)₃ **5**, and [Co(phen)₃](PF₆)₃ **6**, were compared to assess the potential influence of the PCA-(CF₃)₂ ligand on the effectiveness of cobalt in the catalytic hydrogen evolution reaction (HER) under electrochemical and photochemical conditions. The PCA-

(CF₃)₂ moiety caused an anodic shift in the reduction potential of CoII/I redox couple of complexes **3** and **4**, in comparison to the other complexes. Complexes **3** and **4** demonstrated catalytic HER in the presence of *p*-cyanoanilinium tetrafluoroborate in CH₃CN, with overpotentials for the HER of 730 and 630 mV for complexes **3** and **4**, respectively. The reduction potentials suggest that the HER was most likely facilitated by a homolytic pathway. Complexes **3** and **4** also demonstrated

photocatalytic HER in the presence of $[\text{Ru}(\text{bpy})_3](\text{PF}_6)_2$ as a photosensitizer and triethanolamine as a sacrificial reductant in DMF. Complexes **3** and **4** attained rates of $2700 \text{ mmol H}_2 \cdot \text{mol}^{-1} \text{ CAT min}^{-1}$ and $2600 \text{ mmol H}_2 \text{ mol}^{-1} \text{ CAT min}^{-1}$, respectively, compared to a standard complex $[\text{Co}(\text{dmgH})_2(\text{py})\text{Cl}]$ which had a rate of $4500 \text{ mmol H}_2 \text{ mol}^{-1} \text{ CAT min}^{-1}$, under similar conditions. Turnover numbers (TON) of 140 were observed for $[\text{Co}(\text{dmgH})_2(\text{py})\text{Cl}]$ and complex **4**, compared to 91 for complex **3**, over a 3 h period.

Contribution: I prepared all the solutions for the hydrogen evolution and I took several data myself. I also created several graphics (used or not for the final version). I helped to find relevant references for the article.

Inorganica Chimica Acta. Volume 510, 24 september 2020, 119726

Published: 2020-04-30

Doi: <https://doi.org/10.1016/j.ica.2020.119726>

Chapitre 3 - N-substituted 2-pyridinecarbothioamides and polypyridyl mixed-ligand cobalt(III)-containing complexes for photocatalytic hydrogen generation

Michael J. Celestine^a, Mark A.W. Lawrence^b, Nicholas K. Evaristo^a, Benjamin W. Legere^a, James K. Knarr^a, Olivier Schott^c, Vincent Picard^c, Jimmie L. Bullock^a, Garry S. Hanan^c, Colin D. McMillen^d, Craig A. Bayse^a, Alvin A. Holder^{a,*}

a Department of Chemistry and Biochemistry, Old Dominion University, 4541 Hampton Boulevard, Norfolk, VA 23529, USA

b Department of Chemistry, the University of the West Indies, Mona Campus, Kingston 7, W.I., Jamaica

c Departement de Chimie, Universite de Montreal, Pavillon J.-A. Bombardier, 5155 Chemin de la Rampe, Montreal, Quebec H3T 2B1, Canada

d Department of Chemistry, Clemson University, 219 Hunter Laboratories, Clemson, SC 29634, USA

* Corresponding author.

E-mail address: aholder@odu.edu (A.A. Holder).

<https://doi.org/10.1016/j.ica.2020.119726>

Received 31 October 2019; Received in revised form 23 April 2020; Accepted 28 April 2020

Inorganica Chimica Acta 510 (2020) 119726

Available online 30 April 2020

0020-1693/ © 2020 Elsevier B.V. All rights reserved.

3.2 Introduction

The increasing consumption of fossil fuels has led to the global energy crisis, environmental degradation, and is significantly contributing to climate change [1,2]. Electrical energy is considered as one of the most promising replacements for end users of fossil fuels; however electricity generation currently accounts for *ca.* 25% of global green-house gas emissions [3]. There is a growing need for efficient systems (that are ideally based on solar powered mechanisms) exploiting inexpensive and robust catalytic materials for the photo- and/or electro-catalytic processes which are applicable to water splitting, photo-voltaic cells, fuel cells, and conversion of waste products (such as CO₂) to chemical fuels [4]. Fuel cells are appealing, and various designs for the hydrogen fuel cell have been explored, owing to the fact that under optimal conditions, the only waste product from the electrochemical process is water [5,6]. Due to the inherent dangers and difficulties in storing and transporting hydrogen [5], there is a growing need for the generation of specific quantities of molecular hydrogen on site, and on demand. Water represents an abundant and convenient energy vector, which in conjunction with sun light, present a viable method for generating clean energy [7-12].

The splitting of water into oxygen and hydrogen has utilized various catalysts [13-16] and others that are derived from expensive and rare noble metals, such as Pt, Pd, Rh, *etc.* [17,18], which are not competitive to fossil fuels, and are thus unsuitable for technologies geared towards meeting global demands [19]. The entire water-to-hydrogen process first requires the oxidation of water to protons and O₂ followed by the reduction of protons to hydrogen. This multi-electron process is difficult to control using simple electro- or photocatalytic systems. The global research output has demonstrated general shift from heterogeneous to homogeneous catalytic processes that are based

on cheaper and more abundant first-row transition metals [20-30]. Success has been achieved on water oxidation [31-33], however, our focus is on the latter reaction designed to produce H₂. While one approach is to mimic the core of natural hydrogenases [34-37], there have also been reports of cobaloxime-containing complexes that are efficient electrocatalysts for hydrogen evolution [38-59]. Fihri *et al.* [22] reported the first multinuclear ruthenium(II)-cobaloxime-based photocatalytic system for hydrogen evolution. The complex $[(bpy)_2Ru(l\text{-}pyr)Co(dmgBF_2)_2(OH_2)]^{2+}$ (where $l\text{-}pyr = (4\text{-pyridine})\text{oxazolo}[4,5-f]\text{phenanthroline}$ and $dmgBF_2 = \text{difluoroboryldimethylglyoximato}$) harvests photons from the $[\text{Ru}(bpy)_3]^{2+}$ moiety and drives electrons to the $[\text{Co}(dmgBF_2)_2]$ moiety, which is a hydrogen evolving catalyst. This complex was able to perform around 105 turnovers over 15 h [22]. This complex requires UV irradiation and is relatively inactive under visible irradiation ($\lambda > 380$ nm). Fihri *et al.* [21] also synthesized two other complexes, $[(dmphen)_2Ru(l\text{-}pyr)Co(dmgBF_2)_2(OH_2)](\text{PF}_6)_2$ (where dmphen = 2,9-dimethyl-1,10-phenanthroline) and $[(ppy)_2Ir(l\text{-}pyr)Co(dmgBF_2)_2(OH_2)]\text{PF}_6$ (where ppy = 2-phenylpyridine), in an attempt to get past the UV requirement. Both complexes were comparable or better than platinum-based systems [21], and were able to produce hydrogen under visible irradiation with a higher number of turnovers (up to 273 turnovers). Their report also showcased the potential of various moieties for hydrogen production, like tricarbonyl(diimine) rhenium, and the first photocatalyst containing an Ir-based photocatalytic moiety.

Cropek *et al.* [52] reported the effects of ligand structure on the photocatalytic production of hydrogen in acidic media. The complexes used were three mixed metal complexes Ru(II) polypyridyl photosensitizer abridged to a $[\text{Co}(dmgBF_2)_2(OH_2)]$ moiety as a catalyst. Photochemical studies done in acetonitrile with *p*-cyanoanilinium tetrafluoroborate as the proton

source, and either triethylamine or triethanolamine as the sacrificial electron donor, concluded that the terminal ligand affects the catalyst and its performance. Likewise, the sacrificial electron donor affects the amount of hydrogen produced and the lifespan of the catalyst. One of the complexes, $[\text{Ru}(\text{pbt})_2(\text{l-pyr})\text{Co}(\text{dmgBF}_2)_2(\text{OH}_2)](\text{PF}_6)_2$, outperformed the other complexes, by producing hydrogen over a 42h period with triethylamine as the sacrificial electron donor [52]. Numerous cobalt(III) complexes have been reported as electro-catalysts for hydrogen production from acidic media in aqueous, non- aqueous, and also mixed-solvents. For example, Peng *et al.* [60] re- ported on a water soluble complex, $[(\text{phen})_2\text{Co}(\text{CN})_2]\text{NO}_3$, capable of producing hydrogen via electrocatalysis from both aqueous acetic acid and an aqueous acetate buffer. In acetonitrile, the complex could produce hydrogen with a turnover frequency of 0.0154 mol of H_2 per mole of catalyst per second at an overpotential of 892 mV. In a neutral aqueous buffer, the turnover frequency was 0.25 mol of H_2 per mole of catalyst per second at an overpotential of 838 mV. Despite his achievement and others [52,60-64], many electrocatalytic HER are performed in non-aqueous or mixed aqueous/non-aqueous solvents largely due to solubility issues.

Carbothioamides are noted as important functional groups in organic synthesis and medicinal chemistry [65,66]. *N*-substituted 2-pyridinecarbothioamides (PCAs) are versatile and easily accessible building blocks for the synthesis of S,*N*-bidentate ligands for organo- metallic, and coordination compounds. The most attractive preparative method to PCAs involves the reaction of a primary amine with sulfur in refluxing 2-methylpyridine in the presence of catalytic $\text{Na}_2\text{S}\cdot 9\text{H}_2\text{O}$ (a modified Willgerodt-Kindler reaction) [67], giving excellent yields (>70%), and the steric and electronic properties of the products are readily tuned by varying the amines used. An increasing number of thiosemicarbazone-containing metal complexes have been observed to act as hydrogen evolution catalyst with the S- and N-atoms acting as proton relays for the

complex [68- 71]. This type of relay stems back to the effects and influence of heteroatoms within the second coordination sphere of ligand, capturing the protons which are then transferred toward the active site of the complex. PCAs, as a group, have similar characteristics to thiosemi-carbazones, thus may also give rise to this second coordination sphere effect as well. With the coordination modes corresponding to $\kappa^2\text{-N}_{\text{pyr}}\text{S}_{\text{thioamide}}$ or $\kappa^2\text{-N}_{\text{pyr}}\text{N}_{\text{thioamide}}$ being the most likely scenario, and the protonation of the uncoordinated thione or the uncoordinated nitrogen may aid in the production of hydrogen by acting as a proton shuttle to the cobalt metal center. This would be similar to the mechanisms/ pathways proposed for HER by the complex **a** in figure 49 in which the azine nitrogen that is coordinated to the nickel(II) metal center is protonated [68]. With the complexes **b** and **c** in figure 49, the protonation site is proposed at either the ammine nitrogen or the nitrogen of one of the pyridyl rings of the cobalt(II) and cobalt(III) complexes [72,73].

When producing hydrogen the stability of the complex is very important as they have to cycle over and over; the addition of the poly-pyridyl ligands have been known to increase the overall stability of the complex, especially in aqueous media, by removing the possibility of hydrolysis [72,74-92]. The polypyridyl ligands are also able to participate in π back-bonding which would stabilize the cobalt(I) species when formed [91]. The electronic and steric effects from these ligands control not only the redox properties of the complexes, but also their catalytic properties [73]. In the 1980s, Sutin investigated 2,2'-bipyridine with a Co(III) metal center for hydrogen photocatalysis. The lability of 2,2'-bipyridine in $[\text{Co}(\text{bpy})_3]^{2+}$ generated free sites in the Co (III) metal center coordination sphere to form a hydride species critical for catalysis [93]. The design of polypyridyl cobalt-containing complexes for the hydrogen evolving reaction (HER) has since used ligand tailoring to change the metal environment [84,91,94-98], including a few

examples of bidendantate pyridine-containing derivatives for HER cobalt-containing catalysts [60,93,98].

This work reports the synthesis and characterization of two mixed ligand cobalt(III) complexes bearing polypyridyl ligands with a pyridyl carbothioamide moiety. The inclusion of the pyridyl carbothioamide is anticipated to modify the electrochemical and photochemical properties of the metal centre. Indeed both mixed ligand species produced molecular hydrogen at respectable rates under photocatalytic conditions. The crystal structure of *N*-(3,5-bis(trifluoromethyl)phenyl)pyridine-2-carbothioamide (PCA-(CF₃)₂) is also reported.

3.3 Experimental

3.3.1 Materials and physical measurements

All the chemicals including solvents were obtained from Sigma- Aldrich (St. Louis, MO, U.S.A), Fisher Scientific, VWR, or other commercial vendors, and used as received.

Microanalyses (C, H, and N) were performed by Intertek Pharmaceutical Services, P.O. Box 470, Salem Industrial Park, Building #5, Whitehouse, NJ 08888, U.S.A. FTIR and ATR data were acquired on a Nicolet AVATAR 370 DTGS spectrometer. ¹H, ¹³C, and ¹⁹F spectra were acquired on a Bruker 400 MHz NMR spectrometer in the respective solvent and were referenced internally to the residual protons of the incompletely deuterated solvent; except where all ¹⁹F NMR spectra which were acquired in DMSO-*d*₆. Here CF₃CO₂H ($\delta = -76.55$ ppm) was used as an external reference at room temperature. All NMR spectra were processed with the ACD Spectrus Processor 2012 software.[†]

ESI MS spectra were acquired via positive electrospray ionization on a Bruker 12 Tesla APEX

–Qe FTICR-MS with an Apollo II ion source at the College of Sciences Major Instrument Cluster (COSMIC), Old Dominion University. Samples were dissolved in methanol before being introduced by direct injection using a syringe pump with a flow rate of $2 \mu\text{L s}^{-1}$. The data was processed using Bruker Daltonics Data Analysis Version 3.4.

Voltammograms were acquired on a Bioanalytical Systems Inc. Epsilon workstation on a C3 cell stand at room temperature in acetonitrile containing 0.10 M tetra-*n*-butylammonium perchlorate (TBAP) as supporting electrolyte, using a three electrode system consisting of a glassy carbon working electrode, a platinum wire auxiliary electrode, and a Ag/AgCl reference electrode, against which ferrocene shows a reversible wave at +0.43 V. Solutions were saturated with argon for 15 min prior to each acquisition, and a blanket of argon gas was maintained throughout the measurements.

All UV–visible spectra were acquired on an Agilent 8453 diode array spectrophotometer using a quartz cuvette with a path length of 1.0 cm for standard measurements, and a quartz cuvette with a path length of 0.1 cm for the spectroelectrochemical measurements.

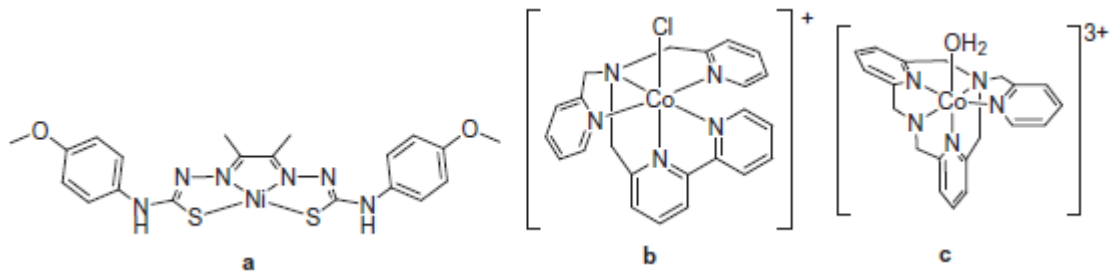


Figure 49. First row transition metal complexes containing either a thiosemicarbazone ligand or polypyridyl ligands [68,72,73].

3.3.2 DFT calculations

Geometries were optimized in the gas- and solvent-phase using the mPW1PW91 exchange correlation functional and Gaussian 09. Implicit solvation in acetonitrile was modeled with the integral equation formalism variant of the polarizable continuum model (IEF-PCM) [99]. Cobalt was represented by the Wachters-Hay all-electron basis set [100,101]. The Dunning triple- ξ basis was used for all other atoms [102]. Diffuse functions were added to N, O, F, and S. Optimized structures were confirmed as minima on the potential energy surface by vibrational analysis. Vertical electronic excitations were calculated using time-dependent DFT (TD-DFT) from the optimized structures.

3.3.3 Photocatalytic measurements

Hydrogen evolution was measured using a Perkin Elmer Clarus-580 gas chromatograph (GC) with a thermal conductivity detector, argon as carrier and eluent gas, a 7' HayeSep N 60/80 pre-column, a 9' molecular sieve 13 \times 45 /60 column and a 1 mL injection loop. Three distinct solutions were prepared for the photosensitizer $[\text{Ru}(\text{bpy})_3](\text{PF}_6)_2$, the respective catalyst, and last, the sacrificial electron donor and the acid source (HBF_4 , 48% water): the three solutions were mixed together to obtain 5 mL of sample solutions in standard 20 mL head-space vials.

In DMF, the resulting molar concentrations of photocatalytic components were: 1 M for triethanolamine (TEOA), 0.1 M for (HBF_4), 0.56 M for water, 0.1 mM for $[\text{Ru}(\text{bpy})_3](\text{PF}_6)_2$, 0.01 mM for $[\text{Co}(\text{tpy})(\text{phen})\text{Cl}](\text{PF}_6)_2$ or $[\text{Co}(\text{dmgH})_2\text{Cl}(\text{py})]$ (apparent pH = 8.9). Those vials were placed on a LED panel in a thermostatic bath set at 20 °C. They were sealed with a rubber septum pierced with two stainless steel tubes. The first tube carried an argon flow pre-

bubbled in spectroscopic grade solvent. The flow was set to 5 mL min⁻¹ (adjusted with a manual flow controller (Porter, 1000) and referenced with a digital flowmeter (Perkin Elmer FlowMark). The second tube leads the flow to the GC sample loop through a 2 mL overflow protection vial, then through an 8-port stream select valve (VICCI) and finally to the GC sample loop. A microprocessor (Arduino Uno) coupled with a custom PC interface allows for timed injections.

For general calibration, stock cylinders of known concentration of H₂ in nitrogen replaced the nitrogen flow (inserted at the pre-bubbler, to keep the vapor matrix consistent). The measured results, in- dependent of flow rate (under same pressure) can be easily converted into a rate of hydrogen following equation 1 in the [supporting information](#). For calibration of H₂ production, a nitrogen bottle of certified 100 ppm hydrogen was set to deliver a specific flow. H₂ production rate at a specific nitrogen flow, a syringe pump (New Era Pump) equipped with a gas-tight syringe (SGE) and a 26 s gauge needle (Hamilton) was used to bubble different rates of pure hydrogen gas into the sample, to a minimum of 0.5 µL min⁻¹ (see [supporting information](#) for additional details).

3.3.4 Synthesis of the ligands and cobalt(III) complexes

i. N-(3,5-bis(trifluoromethyl)phenyl)pyridine-2-carbothioamide (PCA-(CF₃)₂)

A mixture of 3,5-bis(trifluoromethyl)aniline (3.41 mL, 21.6 mmol), sulfur (2.01 g, 65.4 mol) and sodium sulfide nonahydrate (0.24 g, 2 mol%) in 2-methylpyridine (30 mL) was refluxed for 48h. After cooling and removal of all volatiles *in vacuo*, the dark brown oil residue was taken up in CHCl₃/MeOH (20:1) and was purified using column chromatography on silica

gel. Fractions containing the desired product were combined and the filtrate was evaporated under reduced pressure to yield a yellow solid. A single crystal suitable for X-ray analysis was grown via the slow evaporation technique from chloroform. Yield = 5.90 g (77%). FTIR (ν/cm^{-1}): 3170 (NH, m); 1380 (C=S, s); 1278 (C-F, vs). ^1H NMR (400 MHz, CDCl_3 , δ/ppm): 12.38–12.28 (m, 1H), 8.76 (d, J = 7.8 Hz, 1H), 8.67 (s, 2H), 8.61–8.54 (m, 1H), 7.93 (dt, J = 1.6, 7.8 Hz, 1H), 7.77 (s, 1H), 7.54 (ddd, J = 1.2, 4.7, 7.4 Hz, 1H). ^{13}C NMR (101 MHz, CDCl_3 , δ/ppm): 189.4, 150.7, 146.6, 140.0, 137.8, 132.4, 132.1, 126.7, 124.9, 122.2, 121.7, 119.5. ^{19}F NMR (376 MHz, CDCl_3 , δ/ppm): -62.94 (s, 6F)

ii. General procedure for the preparation of $[\text{Co}(\text{NeN})_2\text{Cl}_2]\text{Cl}$ (where NeN = bpy (complex 1) or phen (complex 2))

$[\text{Co}(\text{bpy})_2\text{Cl}_2]\text{Cl}$ **1** and $[\text{Co}(\text{phen})_2\text{Cl}_2]\text{Cl}$ **2** were synthesized via the procedure as by Ghosh *et al.* [103].

iii. Synthesis of $[\text{Co}(\text{bpy})_2(\text{PCA-(CF}_3)_2]\text{(PF}_6)_2\text{H}_2\text{O}$ 3

$[\text{Co}(\text{bpy})_2\text{Cl}_2]\text{Cl}$, **1** (0.175 g, 0.366 mmol) and PCA-(CF_3)₂ (0.256 g, 0.733 mmol) were mixed in ethanol (50 mL) and stirred at room temperature for 4 h. The solvent was then removed via rotary evaporation (note that the water bath temperature should NOT exceed 50 °C); then $\overset{\circ}{\text{H}_2\text{O}}$ (10 mL) was added and the mixture was filtered. The residue was washed with H_2O (~20 mL). The filtrate was then collected to which NH_4PF_6 (0.597 g, 3.66 mmol) was added and the resulting mixture was then placed in an ice bath. The mixture was then filtered, and the residue was washed with cold H_2O , followed by Et_2O , and air dried. Yield = 0.389 g (92%). Found C, 39.70; H, 2.38; and N 8.05%, Anal. Calc. for $\text{C}_{34}\text{H}_{25}\text{CoF}_{18}\text{N}_6\text{OP}_2\text{S}$: C,

39.70; H, 2.45; and N, 8.17%. ESI MS (positive mode, CH₃CN): [M–2PF₆[–]]²⁺ 360 (360.05). ¹H NMR (400 MHz, DMSO-*d*6, δ/ppm) 9.43 (d), 9.04 (dd), 8.99 (d), 8.92 (d), 8.75 (d), 8.56 (m), 8.33 (dt), 8.01 (m), 7.91 (m), 7.86 (s), 7.81 (qd), 7.73 (m), 7.68 (m), 7.50 (m), 7.44 (d), 7.16 (d). ¹³C NMR (101 MHz, DMSO-*d*6, δ/ppm) 170.9, 159.4, 156.3, 156.0, 155.4, 155.3, 152.9, 152.3, 151.2, 151.0, 149.9, 142.7, 142.5, 142.2, 142.0, 131.5, 131.2, 131.2, 130.7, 130.3, 130.1, 129.9, 127.0, 126.7, 126.3, 126.2, 125.4, 124.4, 121.7, 121.2. ¹⁹F NMR (376 MHz, DMSO-*d*6, δ/ppm) –61.02, –68.94, and –70.83.

2.4.4. Synthesis of [Co(phen)₂(PCA-(CF₃)₂](PF₆)₂ · 1.25H₂O 4 [Co(phen)₂Cl₂]Cl, **2** (0.175 g, 0.333 mmol) and PCA-(CF₃)₂ (0.233 g, 0.666 mmol) were mixed in ethanol (50 mL) and stirred at room temperature for 4 h. The solvent was then removed via rotary evaporation; then H₂O (10 mL) was added and the mixture was then filtered. The residue was washed with H₂O (~20 mL). The filtrate was then collected to which NH₄PF₆ (0.543 g, 3.33 mmol) was added and the resulting mixture was placed in an ice bath. The mixture was then filtered, and the residue was washed with cold H₂O followed by Et₂O, and air dried. Yield: 0.288 g (72%). Found C, 42.03; H, 2.17; and N 7.74%, Anal. Calc. for C₃₈H_{25.5}CoF₁₈N₆O_{1.25}P₂S: C, 42.22; H, 2.38; and N, 7.77%. ESI MS (positive mode, MeCN): [M–2PF₆[–]]²⁺ 384.1 (384.05). ¹H NMR (400 MHz, DMSO-*d*6, δ/ppm) 9.79 (m), 9.18 (m), 8.83 (d), 8.54 (m), 8.32 (m), 7.94 (m), 7.81 (s), 7.73 (m), 7.60 (m), 7.25 (d). ¹³C NMR (101 MHz, DMSO-*d*6, δ/ppm) 171.2, 159.7, 154.7, 153.5, 152.8, 152.5, 151.6, 151.2, 146.4, 146.0, 145.6, 145.1, 141.9, 141.5, 141.1, 140.5, 131.9, 131.7, 131.6, 131.5, 131.2, 131.1, 130.7, 129.2, 128.8, 128.7, 128.5, 128.4, 128.4, 128.2, 128.0, 126.5, 124.4, 121.6, 121.1. ¹⁹F NMR (376 MHz, DMSO-*d*6, δ/ppm) –60.97, –68.94, and –70.83.

2.4.5. Synthesis of $[Co(NeN)_3](PF_6)_3$ where NeN = bpy (complex 5) or phen (complex 6)

$[Co(bpy)_3](PF_6)_3$ **5** was synthesized following the procedure as by Kim [104]. $[Co(phen)_3](PF_6)_3$ **6** was synthesized from $[Co(phen)_2Cl_2]Cl$ **2** using stoichiometric quantities of complex **2** and 1,10-phenanthroline (see supporting information).

3.3.5 X-ray crystallography

Intensity data were collected using a Rigaku Mercury CCD detector and an AFC8S diffractometer. Data reduction including the application of L_p and absorption corrections used the CRYSTALCLEAR [105] program. The structure was solved by direct methods and subsequent Fourier difference techniques, and refined anisotropically, by full-matrix least squares, on F^2 using SHELXTL [106,107]. Hydrogen atom positions in the ligand were calculated from ideal geometry with coordinates riding on the parent atom. Ammonium hydrogen coordinates were determined from a difference Fourier and fixed at those values. A summary of the data collection and refinement for the ligand is shown in Table 1. The crystallographic data has been deposited with the CCDC, deposition number 1956421.

Tableau 6. – Crystallographic data for the PCA-(CF₃)₂

Identification code	PCA-(CF ₃) ₂
Chemical formula	C ₁₄ H ₈ F ₆ N ₂ S
Formula weight (g mol ⁻¹)	350.28
Crystal size (mm)	0.50 × 0.33 × 0.26
Crystal system, space group	monoclinic, C2/c
Unit cell dimensions (Å, °)	$a = 14.326(2)$ $b = 8.5708(13)$ $c = 24.713(4)$ $\beta = 103.100(5)$
Volume (Å ³)	2955.4(8)
Z, Calculated density (g cm ⁻³)	8, 1.575
Absorption coefficient (mm ⁻¹)	0.283
F(0 0 0)	1408
Θ range for data collection (°)	2.79 to 25.25
Reflections collected/unique	11137/2649
Max. and min. transmission	0.8638, 1.0000
Data/restraints/parameters	2649/93/268
Goodness-of-fit on F ²	1.187
Final R indices [4838 data; I > 2σ(I)]	0.0561, 0.1482
R indices (all data)	0.0639, 0.1566
Largest diff. peak and hole	0.200, -0.258
CCDC no.	1956421

3.3.6 Results and discussion

3.1. Synthesis and characterization

3.1.1. N-(3,5-bis(trifluoromethyl)phenyl)pyridine-2-carbothioamide (PCA-(CF₃)₂)

The synthesis of N-(3,5-bis(trifluoromethyl)phenyl)pyridine-2-carbothioamide (PCA-(CF₃)₂) followed a one-pot protocol as reported by Klingele and Brooker [67] under aerobic conditions (see figure 50). The desired product was isolated in good yield, and of sufficient purity, as determined from X-ray crystallography and a series of spectroscopic measurements. The structure of the PCA-(CF₃)₂ ligand is shown in figure 52. The molecule is generally planar, excepting the fluorine atoms of the CF₃ groups, with the aromatic rings inclined to one another at an angle of 6.15(13)°. Planarity is also reinforced by the N-H · · N intramolecular hydrogen bond (N-H =

0.89(4) Å, H···N = 1.99(3) Å, \angle N-H···N = 120(3) $^\circ$). In the extended structure, the molecules are stacked in layers along the c-axis with localized fluorous regions where the CF₃ groups are concentrated (Figure 61). The aromatic rings of neighboring molecules overlap at a centroid distance of 3.783 Å, suggesting weak assisting π stacking interactions. Selected bond lengths (Å): C6-S1 = 1.637(2), C1-N1 = 1.333(3), C5-N1 = 1.332(4), C6-N2 = 1.346(3), C7-N2 = 1.409(3). In the FTIR spectrum (Figure 58), the diagnostic stretching frequency of the v(N-H) of the thioamide was observed at 3200 cm⁻¹ and the corresponding bend (amide II) at 1550 cm⁻¹. These values are comparable to those of other thioamide systems [108,109]. In the ¹H NMR spectrum (Figure 59) the NH proton is observed resonating circa 12.33 ppm, integrating for a single proton, and the aryl region integrated for a total of seven protons, all consistent with the desired product PCA-(CF₃)₂. In the ¹³C NMR spectrum, the thioamide resonance was observed at 189.4 ppm along with the aryl resonances and a single resonance at -62.94 ppm for the trifluoromethyl carbons, indicating their equivalence in the molecule. The DFT optimized structures of PCA-(CF₃)₂ is near planar with a short NH···N distance of 1.917 Å, consistent with the X-ray structure (figure 52). The amide NH bending mode is found at 1607 cm⁻¹ and the overall spectrum in agreement with experiment (Figure 59). Calculated structures of complex **3** are similar in the gas phase and the solvent phase. The Co-N bond distances for the bpy ligand *trans* to the Co-S bond to PCA-(CF₃)₂ are slightly longer than for the bpy *trans* to the pyridyl ring of PCA. The imine C=N stretching frequency mixes with the C-C stretch for two bands at 1657 and 1678 cm⁻¹.

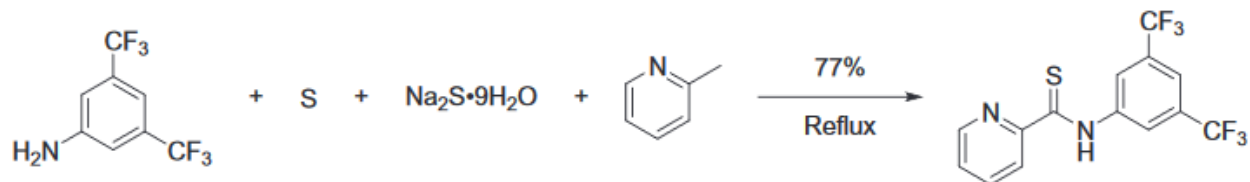


Figure 50. Synthesis of N-(3,5-bis(trifluoromethyl)phenyl)pyridine-2-carbothioamide (PCA-(CF₃)₂)

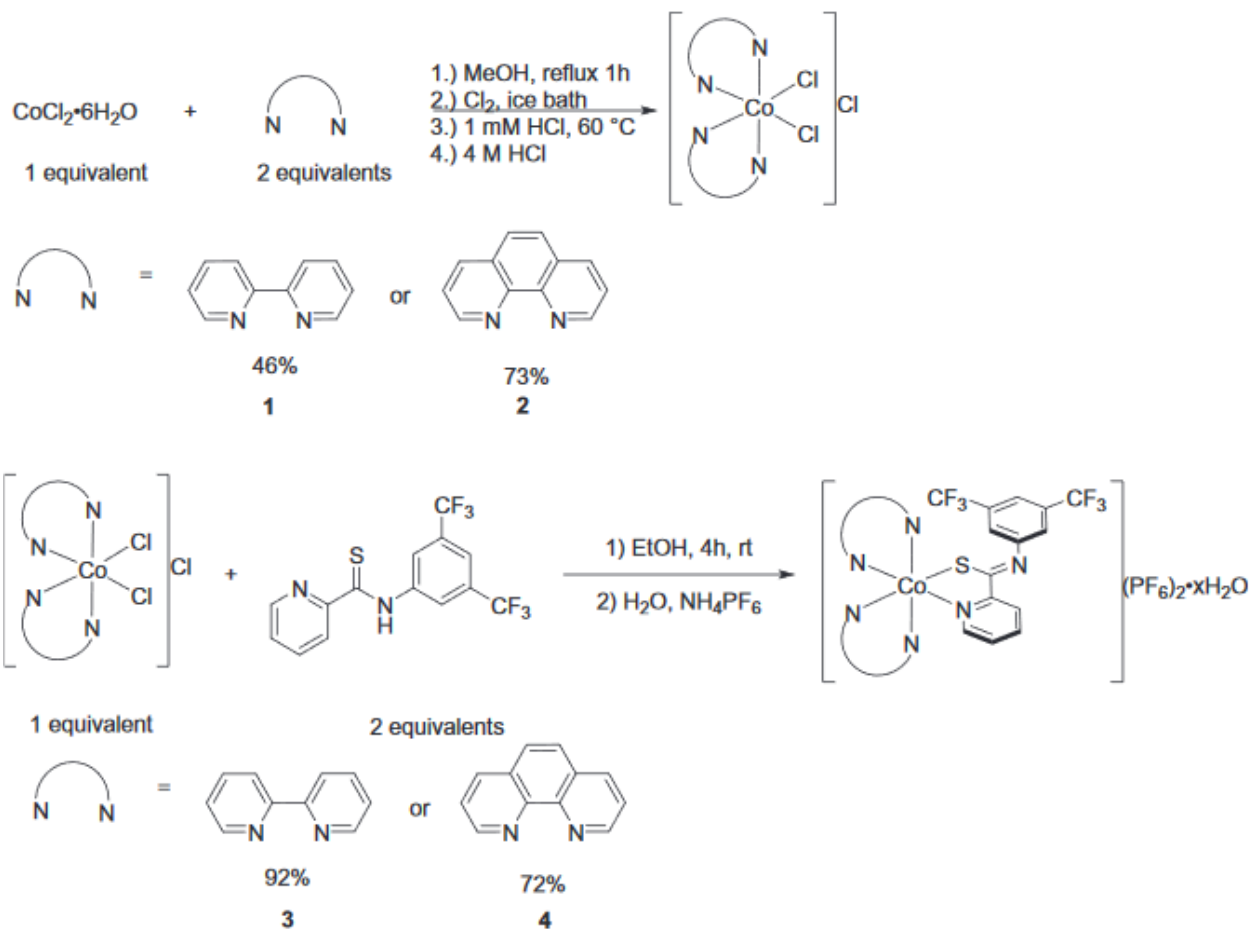


Figure 51. Synthesis of complexes 1-4

3.1.2. $[Co(N-N)2(PCA-(CF_3)_2)](PF_6)_2 \cdot xH_2O$ (where N-N = bpy ($x = 1$) or phen ($x = 1.25$))

The syntheses of the complexes **3** and **4** were achieved via a two step protocol, from complexes **1** and **2** ($[\text{Co}(\text{N-N})\text{Cl}_2]\text{Cl}$ species) which were prepared by a literature method [103]. Complexes **1** and **2** were then reacted with two equivalences of the PCA-(CF₃)₂ in ethanol (figure 51). $[\text{Co}(\text{N-N})_2(\text{PCA-(CF}_3)_2)](\text{PF}_6)_2 \cdot x\text{H}_2\text{O}$ (complexes **3** and **4**) were isolated in good to excellent yields as red-brown (complex **3**) or green–brown (complex **4**) colored solids using this simple protocol. The identities of complexes **3** and **4** were confirmed form their elemental analyses and a series of spectroscopic measurements. In the infrared spectra of complexes **3** and **4**, a key feature is the disappearance of the $\nu(\text{N-H})$ stretch and bend, in going from the free PCA-CF₃ ligand, signaling coordination via thioamide sulfur with concomitant tautomerization to the imino thiolate [108-110]. A second feature is the appearance of a broad $\nu(\text{O-H})$ stretching frequency signaling the presence of water in the solids (Figure 59).

In the ¹H NMR spectra of complexes **3** and **4** (–the NH resonance observed in the PCA-(CF₃)₂ ligand is absent in both complexes, which is consistent with the FTIR spectra. Similarly, in the ¹³C NMR spectra of complexes **3** and **4**, the thioamide resonance at 189.4 ppm, which is observed in the “free” PCA-(CF₃)₂ is absent. These data are consistent with coordination by the thiolate's sulfur as a result of tautomerization of PCA-(CF₃)₂ to the imino thiolate. In the ¹⁹F NMR spectra of the complexes (figure 61), the formation of the PF₆⁻ salt is evident from the appearance of two new peaks due to P-F coupling. ESI MS of the complexes in acetonitrile (Figure 62) revealed an intense molecular ion for the $[\text{M}-\text{H}-2\text{PF}_6^-]^{2+}$. All of the spectroscopic data support the proposed formulations of coordination through the thiolate.

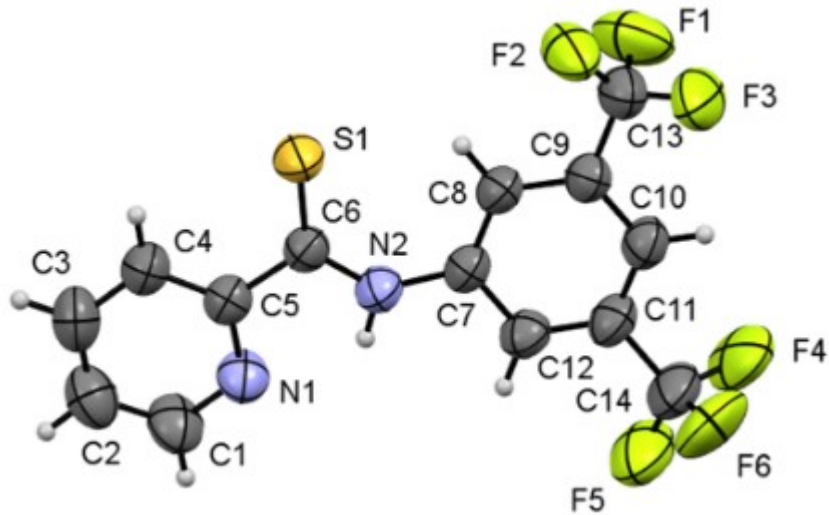


Figure 52. Structure of PCA-(CF₃)₂ shown as 50% probability ellipsoids. Minor components of the CF₃ disorder are omitted for clarity

The UV-visible spectra of complexes **3** and **4** (Fig 53) revealed d-d transitions of the Co(III) mixed with n → π* and π → π* electronic transitions of the ligand between 450 and 330 nm. This is accompanied by intense metal-to-ligand charge transfer (MLCT), ligand-to-metal charge transfer (LMCT), and mixed with intra-ligand charge transfer (ILCT) bands between 330 and 190 nm, as revealed by the large molar extinction coefficient values. TD-DFT calculations in acetontirile are consistent with the experimental assignment of the UV-visible spectrum. Three transitions with significant intensity occur at 375 (f = 0.0170), 367 (f = 0.0875), and 357 (f = 0.0407) nm. These transitions consist of excitations from the HOMO to the LUMO (375 nm) and linear combinations of LUMO + 1 and LUMO + 3 orbitals (367 and 357 nm), see figure 54. The HOMO is localized on the imine-thiolate of PCA-(CF₃)₂ with slight antibonding with the Co t_{2g}-type atomic orbital. The LUMO and LUMO + 1 are the combinations of the bpy π* and LUMO + 3 consists of π*-character on the pyridine ring of PCA-(CF₃)₂. These three excitations are consistent with the assignment of the absorption between 450 and 330 nm as n → π* and π → π*. An additional set of closely spaced excitations between 320 and

275 nm involve excitations from HOMO-1 through HOMO-3 (occupied ligand π and metal t_{2g} -type orbitals) to the π^* LUMOs, consistent with the experimental assignment of absorptions at a wavelength less than 330 as LMCT and ILCT excitations.

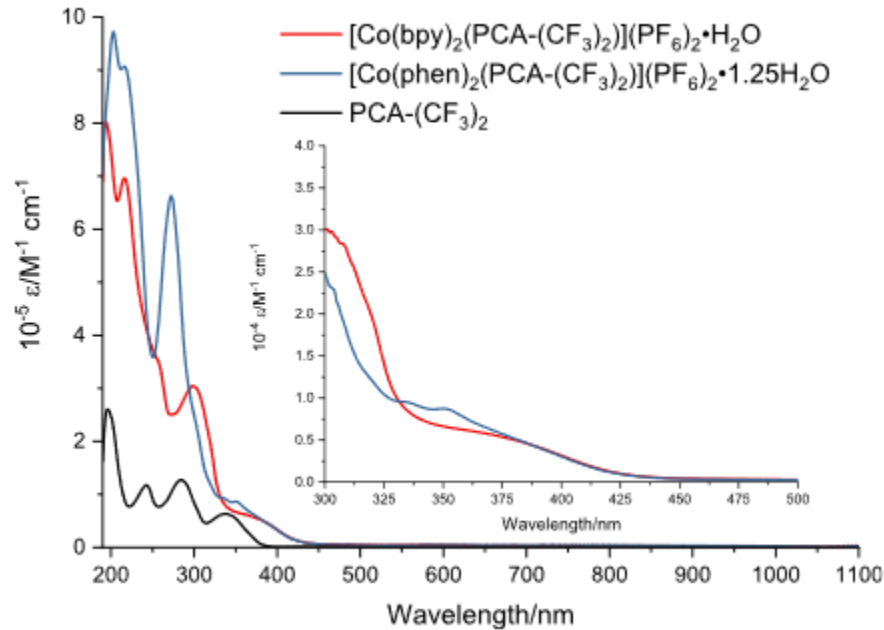


Figure 53. UV-visible spectra of $\text{PCA-(CF}_3)_2$ and complexes 3 and 4 in CH_3CN (inset: 300-500 nm expanded view).

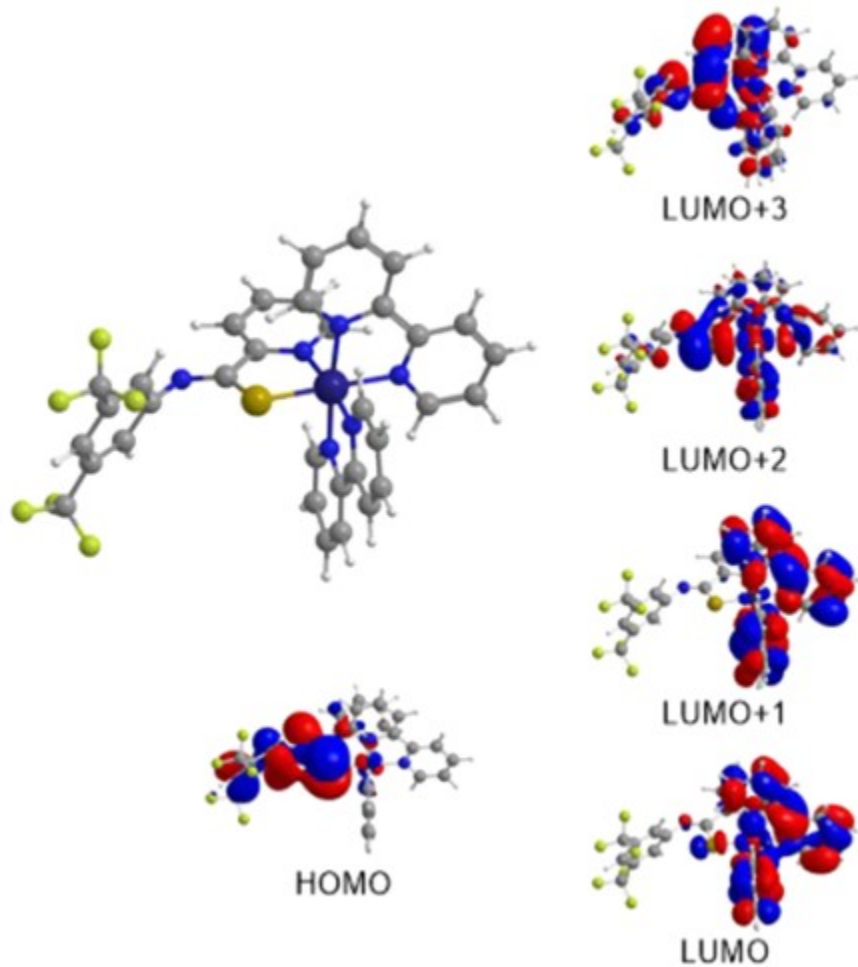


Figure 54. HOMO-LUMO plots for complex 3.

3.2 Electrochemical studies

Voltammograms of PCA-(CF₃)₂ measured between +2.0 and -2.5 V in CH₃CN revealed a reversible one electron reduction of the thioamide moiety at $E_{1/2} = -1.40$ V vs Ag/AgCl, and the thioamide moiety is oxidized via an irreversible two electron process at $E_{pa} = +1.50$ V vs Ag/AgCl (Figure 66). In the voltamograms of complexes **3** and **4**, there are a series of one electron quasi-reversible electron transfers (Figure 55). There was no anodic current at potentials more positive than + 0.20 V indicating the absence of the thioamide moiety in

complexes **3** and **4**. The coordination of PCA-(CF₃)₂ to [Co(N-N)Cl₂]⁺, in general, resulted in the reduction potentials of the cobalt shifting to more negative values (tableau 7 and Figure 64), whilst maintaining their quasi-reversible characteristics. Of note, the coordination of PCA-(CF₃)₂ had a pronounced effect on the Co^{III/II} and Co^{II/I} redox couples, shifting the potential more negative by 100–200 mV. Secondly, ΔE_p for the Co^{III/II} redox couple is less in the [Co(N-N)₂(PCA-(CF₃)₂)](PF₆)₂ (complexes **3** and **4**) in comparison to the [Co(N-N)₂Cl₂](PF₆) species (complexes **1** and **2**) species, making the redox process more Nernstian in its nature. This behavior is similar to that observed in the [Co(N-N)₃](PF₆) (complexes **5** and **6**) species when compared to the [Co(N-N)₂Cl₂](PF₆) species (Figure 64), and is thus related to the enhanced stability introduced by the third bi-dentate ligand, which is more resistant to dissociation in the +2 oxidation state. This is also consistent with the $\kappa^2\text{-S,N}$ coordination of the PCA-(CF₃)₂ ligand. Additionally, the potential shifts of the cobalt redox couples to more negative values in complexes **3** and **4** when compared to complexes **1** and **2**, are consistent with coordination of the soft base, sulfur in which dπ-pπ backdonation can occur. The seemingly haphazard and large ΔE_p values associated with the Co^{III/II} couples can be attributed to the reorganization energy associated with the Co^{III/II} conversion. In complexes **1** and **2**, these reorganization effects coupled with the loss of chloro ligands result in intermediate values relative to complexes **3–6**. The similarity in the Co^{II/I} reduction potentials of complexes **1–4** are likely due to the partial dissociation of the ligand(s) in the +2 oxidation state.

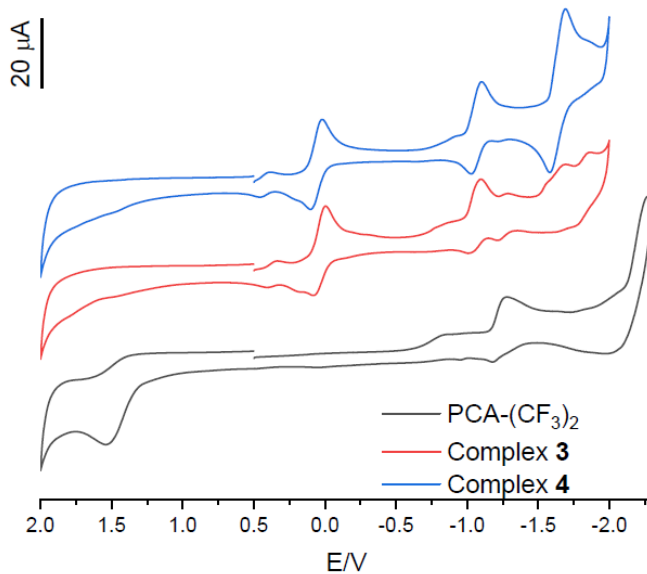


Figure 55. Cyclic voltammograms of PCA-(CF₃)₂ and complexes **3** and **4** in CH₃CN. [complex] = 1.0 mM, supporting electrolyte = 0.1M ([nBu₄N]ClO₄), scan rate = 100 mV s⁻¹.

Tableau 7. – Redox potentials of the cobalt couples of [Co(N-N)₂Cl₂]PF₆ and [Co(N-N)₂(PCA-(CF₃)₂)](PF₆)_xH₂O in CH₃CN at a glassy carbon working electrode vs Ag/AgCl in CH₃CN

Complex	Co ^{III/II} /V (ΔE _p /mV)	Co ^{II/I} /V (ΔE _p /mV)	Co ^{I/0} /V (ΔE _p /mV)
1	+ 0.24 (178)	- 0.92 (66)	- 1.50 (71)
2	+ 0.13 (376)	- 1.08 (144)	- 1.56 (124)
3	+ 0.04 (78)	- 1.05 (86)	-
4	+ 0.05 (120)	- 1.07 (71)	- 1.64 (109)
5	+ 0.39 (180)	- 0.89 (66)	- 1.50 (70)
6	+ 0.44 (140)	- 0.88 (68)	- 1.58 (64)

3.3. Electrocatalytic behavior of [Co(NeN)₂(PCA-(CF₃)₂)](PF₆)_xH₂O in the presence of p-cyanoanilinium tetrafluoroborate in CH₃CN

The addition of *p*-cyanoanilinium tetrafluoroborate to acetonitrile solutions of complexes **1**–**6**, resulted in the appearance of a new cathodic wave in the vicinity of the Co^{II/I} redox couple. In complexes **3** and **4**, the new cathodic wave is observed at ca -0.9 V of which the peak

current increases with a simultaneous peak potential shift to increasingly negative values with increasing [*p*-cyanoanilinium tetra-fluoroborate] (figure 56). In addition to the cathodic wave at -0.9 V, a pre-wave is observed at ca -0.6 V. This pre-wave or “adsorption wave” is postulated to be the result of protonation of the nitrogen of the iminothiol, and may also include hydrogenation of the bond [111,112]. This can be inferred from the initial increase in the current of the pre-wave with the [*p*-cyanoanilinium tetrafluoroborate], however, the peak current quickly plateau at a ratio of ca 1:4, [Co(III) complex]/[proton source], suggesting a slow reaction compared to proton transfer from the *p*-cyanoanilinium tetrafluoroborate in the electrocatalytic process. This 4-H process as suggested by the saturation ratio at -0.6 V would be consistent with the 3H proton coupled reduction required to convert the -C=N- to -H₂CNH- followed by protonation to H₂CNH₂⁺.

This protonated complex may also present (a minor) alternative pathway to the formation of hydrogen from the Co^{III}-H via intra-molecular electron. The peak current observed at -0.9 V did not display any apparent saturation within the concentration range explored, and on the return scan, no stripping wave was observed, suggesting cobalt was not deposited at the electrode, to facilitate heterogeneous catalysis. Nevertheless, such a possibility cannot be excluded without further analysis of the electrode following electrocatalytic experiments [112]. The production of hydrogen was confirmed from the analysis of the head space of a controlled potential electrolysis experiment involving the complex in the presence of *p*-cyanoanilinium tetrafluoroborate. In light of nature of the voltammograms, a mechanism involving the Co(I) species produced upon electro-reduction is proposed (figure 57) and also suggest overpotentials for the HER of 730 and 630 mV for complex **3** and **4**, respectively. The magnitude of the Gibbs free energy for the homolytic and heterolytic H₂ evolution from *p*-

cyanoanilinium tetra- fluoroborate (HA) in CH₃CN can be determined using the methodology suggested by Kellett and Spiro [113], on the basis of the values for the potentials of the cobalt and HA/H₂ couples versus the Fc^{+/0} couple [40]. The heterolytic pathways are calculated at -83 and -86 kJ mol⁻¹, and the homolytic pathways at -120 and -123 kJ mol⁻¹ for complexes **3** and **4**, respectively. From the analyses, it is evident that the thermodynamics of the hydrogen evolution tends to favour the homolytic pathway by about 40 kJ mol⁻¹. This preference for the homolytic pathway is consistent with the deduction made for some cobaloximes [40,43].

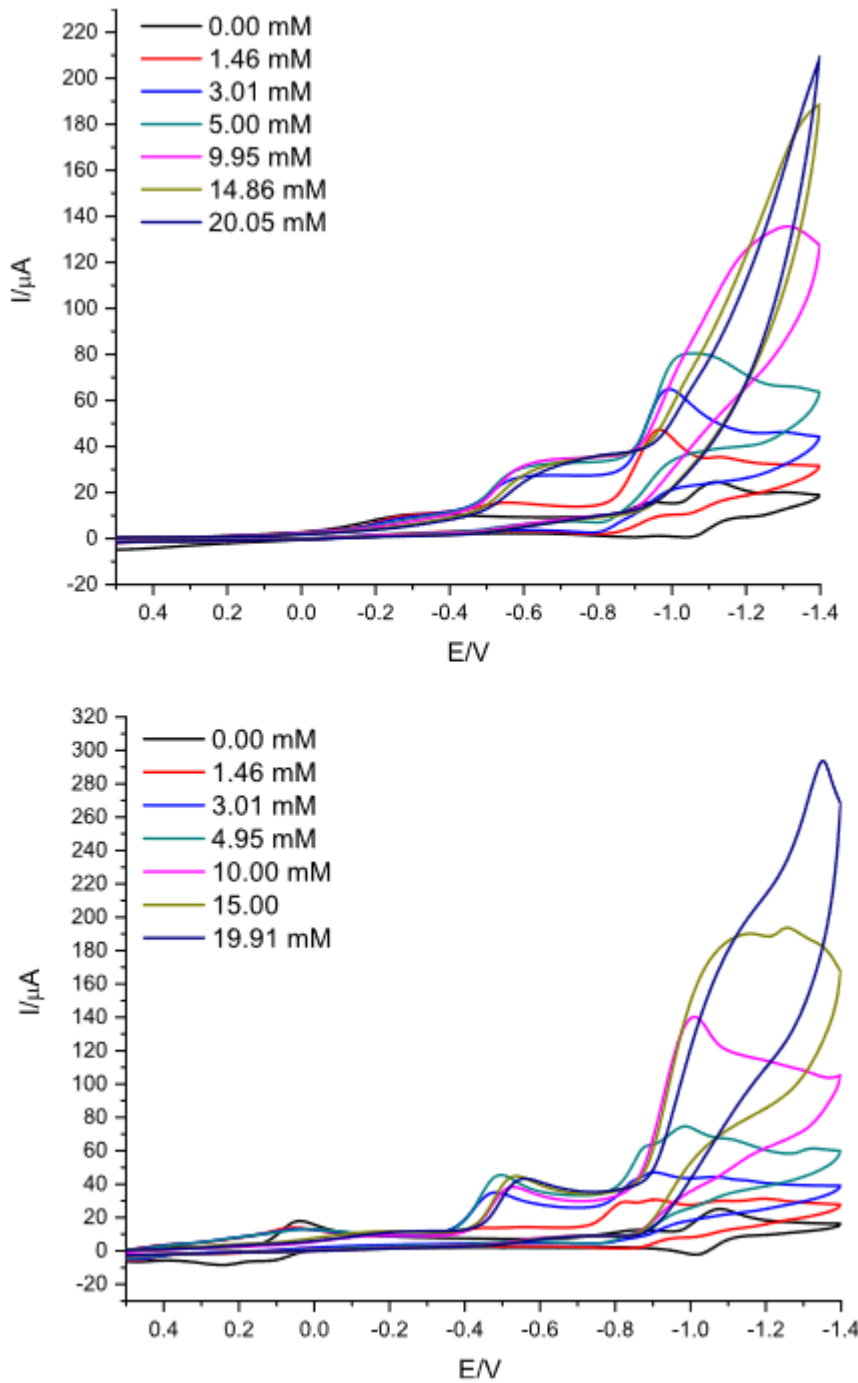


Figure 56. Cyclic voltammograms of complexe 3 (top) and 4 (bottom) in CH₃CN with increasing [*p*-cyanoanilinium tetrafluoroborate]. [complex] = 1.1 mM, supporting electrolyte = 0.1M tetrabutylammonium perchlorate ([ⁿBu₄N]ClO₄). Scan rate = 100mV s⁻¹.

3.4. Photocatalytic hydrogen production

The photosensitizer (PS) $[\text{Ru}(\text{bpy})_3](\text{PF}_6)_2$ [98,114-117] was chosen to photo-reduce the Co HER catalysts. Complex **3**, complex **4**, and the reference catalyst $[\text{Co}(\text{dmgH})_2(\text{Py})\text{Cl}]$ were tested under the same photoreaction conditions (Figure 58). The samples were irradiated with blue LEDs centered at 445 nm, in dimethylformamide as solvent, 1 M of triethanolamine as the sacrificial electron donor and 0.1 M aqueous tetrafluoroboric acid as the proton source, 0.1 mM of $[\text{Ru}(\text{bpy})_3](\text{PF}_6)_2$, and the respective cobalt catalysts at 0.01 mM. The $[\text{Ru}(\text{bpy})_3](\text{PF}_6)_2$ is fully excited into the $^1\text{MLCT}$ band to drive the photo-reactions. The excess of PS permits the evaluation of the maximum TON of HER cobalt-containing catalyst. No hydrogen is detected for the control experiments of the PS in the presence of sacrificial electron donor and HBF_4 . A peak of activity occurred for all the systems when the light is turned on. The cobaloxime reaches a rate of 4500 $\text{mmolH}_2 \cdot \text{mol}^{-1} \text{CAT} \cdot \text{min}^{-1}$, complex **3** and complex **4** attain 2700 $\text{mmolH}_2 \cdot \text{mol}^{-1} \text{CAT} \cdot \text{min}^{-1}$ and 2600 $\text{mmolH}_2 \cdot \text{mol}^{-1} \text{CAT} \cdot \text{min}^{-1}$, respectively. The 2,2'-bipyridine and 1,10-phenanthroline systems react more slowly than the cobaloxime standard and their lower activity is aligned with the loss of ligand on going from Co(III) to Co(I) (d^6 to d^8 , respectively) whereas the dmg in the cobaloxime complex are stable anionic ligands. The activities of all the systems decrease slowly to end after almost three hours, with the 1,10-phenanthroline system decreasing more slowly than the 2,2'-bipyridine system. We observed a TON of 140 for the cobaloxime, and 140 for complex **4** and 91 for complex **3** over a 2.5 h period. Aliquots of fresh photosensitizer and catalyst were added at the end of the photoreactions. For the three catalysts, the activity starts again with addition of photosensitizer and no revival is observed in the case of catalyst addition indicating that the photosensitizer decomposes first.

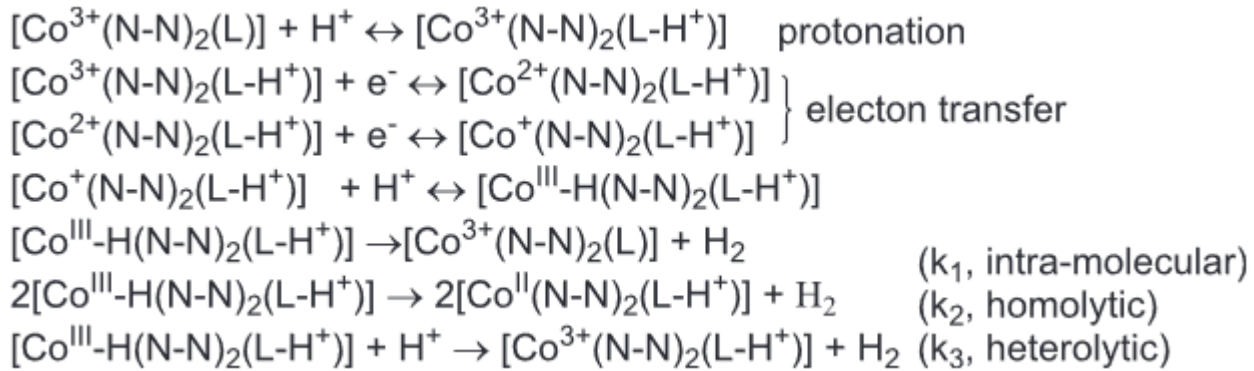


Figure 57. Mechanism for protonation, electron transfer, and hydrogen evolution

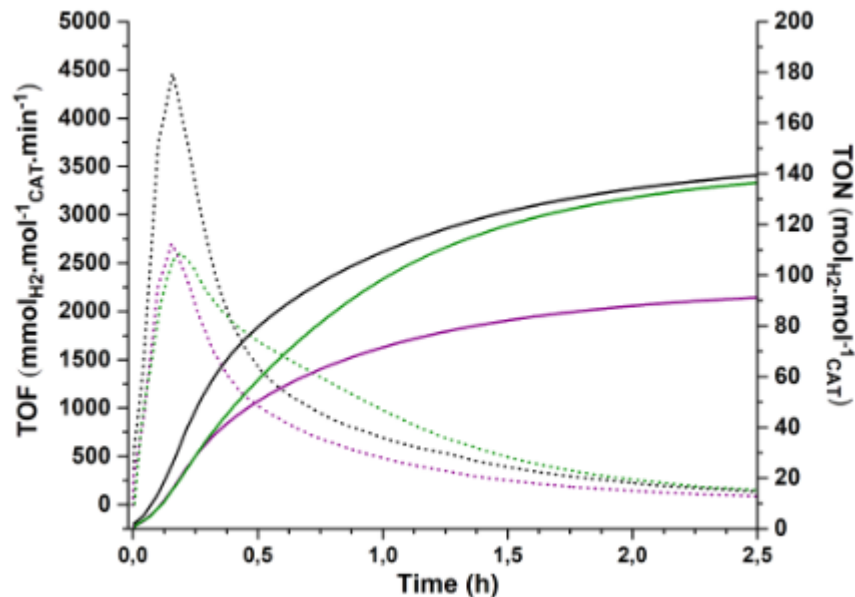


Figure 58. Hydrogen evolution with $[\text{Co}(\text{dmgH})_2(\text{py})\text{Cl}]$ (black), complex 3 (purple), and complex 4 (green). TOF: dotted line. TON: solid line.

3.4 Conclusions

Two new Co(III) complexes (complexes **3** and **4**) bearing a *N*-substituted 2-pyridinecarbothioamide ($\text{PCA}-(\text{CF}_3)_2$) and either bpy or phen ligands were synthesized, and isolated in high purity. Both complexes demonstrated reversible metal-based redox processes in CH_3CN , and yielded a $\text{Co}^{\text{II}}/\text{I}$ redox couple more positive than the polypyridyl analogues

[Co(NeN)₂Cl₂]PF₆ or [Co(NeN)₃](PF₆)₃ (where (NeN) = bpy or phen). Both complexes showed electrocatalytic hydrogen evolution at moderate overpotential in the presence of the acid source, *p*-cyanoanilinium tetrafluoroborate in CH₃CN, and photocatalytic hydrogen evolution in the presence of [Ru(bpy)₃](PF₆)₂ as a photosensitizer and triethanolamine as a sacrificial reductant in DMF.

3.5 Declaration of Competing Interest

The authors declare that they have no known competing financial interests or personal relationships that could have appeared to influence the work reported in this paper.

3.6 Acknowledgements

AAH and MAWL would like to thank Professor Tara P. Dasgupta (sunrise: Wednesday, January 29, 1941 and sunset: Monday, April 20, 2020) for his beloved guidance as a father, a Ph.D. research advisor and a mentor to make us what we are today. R.I.P. AAH would also like to thank the National Science Foundation, 2415 Eisenhower Avenue, Alexandria, VA 22314, U.S.A., for a National Science Foundation CAREER Award, as this material is based upon work supported by the National Science Foundation under CHE-14321172 (formerly CHE-1151832). AAH would also like to thank the Old Dominion University startup package that allowed for the successful completion of this work. GSH, OS, and VP thank the Natural Sciences and Engineering Research Council (NSERC) of Canada (grant number 103046) for financial support. The authors are also grateful for the suggestions made by the reviewers.

Appendix A. Supplementary data

Supplementary data to this article can be found online at

<https://doi.org/10.1016/j.ica.2020.119726>.

3.7 References

- [1] S.A. Asongu, S. Le Roux, N. Biekpe, Energy Policy 111 (2017) 353–361.
- [2] J.-K. He, Adv. Clim. Change Res. 7 (2016) 204–212.
- [3] B. Tranberg, O. Corradi, B. Lajoie, T. Gibon, I. Staffell, G.B. Andresen, arXiv.org, e-Print Arch., Phys., (2018) 1-20.
- [4] A. Munir, K.S. Joya, T. Ulhaq, N.-U.-A. Babar, S.Z. Hussain, A. Qurashi, N. Ullah, I. Hussain, ChemSusChem 12 (2019) 1517–1548.
- [5] F.H. Sobrino, C.R. Monroy, J.L.H. Perez, Renew. Sust. Energ. Rev. 14 (2010) 772–780.
- [6] H. Krassen, S. Ott, J. Heberle, PCCP 13 (2011) 47–57.
- [7] N. Armaroli, V. Balzani, Angew. Chem. Int. Ed. 46 (2007) 52–66.
- [8] R. Eisenberg, D.G. Nocera, Inorg. Chem. 44 (2005) 6799–6801.
- [9] H.B. Gray, Nature Chem. 1 (2009) 112.
- [10] M.I. Hoffert, K. Caldeira, A.K. Jain, E.F. Haites, L.D.D. Harvey, S.D. Potter, M.E. Schlesinger, S.H. Schneider, R.G. Watts, T.M.L. Wigley, D.J. Wuebbles, Nature 395 (1998) 881–884.
- [11] W. Lubitz, W. Tumas, Chem. Rev. 107 (2007) 3900–3903.
- [12] R.F. Service, Science 309 (2005) 548–551.
- [13] H. Ou, P. Yang, L. Lin, M. Anpo, X. Wang, Angew. Chem. Int. Ed. Engl. 56 (2017) 10905–10910.
- [14] S. Preiss, K. Heinze, A. Papcke, S. Lochbrunner, L. Burkhardt, M. Bauer, L. Grossmann, T. Opatz, Chemistry 25 (2019) 5940–5949.
- [15] A. Rauf, M. Ma, S. Kim, S.M.S.A. Sher, C.-H. Chung, J.H. Park, P.J. Yoo, Nanoscale 10 (2018) 3026–3036.

- [16] F. Wang, Q. Li, D. Xu, *Adv. Energy Mater.* 7 (2017) n/a.
- [17] P. Du, K. Knowles, R. Eisenberg, *J. Am. Chem. Soc.* 130 (2008) 12576–12577.
- [18] A.J. Esswein, D.G. Nocera, *Chem. Rev.* 107 (2007) 4022–4047.
- [19] R.B. Gordon, M. Bertram, T.E. Graedel, *Proc. Natl. Acad. Sci. USA* 103 (2006) 1209–1214.
- [20] M. Elvington, J. Brown, S.M. Arachchige, K.J. Brewer, *J. Am. Chem. Soc.* 129 (2007) 10644–10645.
- [21] A. Fihri, V. Artero, A. Pereira, M. Fontecave, *Dalton Trans.* (2008) 5567–5569.
- [22] A. Fihri, V. Artero, M. Razavet, C. Baffert, W. Leibl, M. Fontecave, *Angew. Chem. Int. Ed.* 47 (2008) 564–567.
- [23] J.R. Fisher, D.J. Cole-Hamilton, *J. Chem. Soc., Dalton Trans.* (1984) 809–813.
- [24] J. Hawecker, J.M. Lehn, R. Ziessel, *Nouveau J. Chimie* 7 (1983) 271–277.
- [25] M. Wang, Y. Na, M. Gorlov, L. Sun, *Dalton Trans.* (2009) 6458–6467.
- [26] G.M. Brown, B.S. Brunschwig, C. Creutz, J.F. Endicott, N. Sutin, *J. Am. Chem. Soc.* 101 (1979) 1298–1300.
- [27] C.V. Krishnan, B.S. Brunschwig, C. Creutz, N. Sutin, *J. Am. Chem. Soc.* 107 (1985) 2005–2015.
- [28] C.V. Krishnan, N. Sutin, *J. Am. Chem. Soc.* 103 (1981) 2141–2142.
- [29] C. Fink, G. Laurenczy, *Dalton Trans.* 46 (2017) 1670–1676.
- [30] H. Li, S. Yao, H.-L. Wu, J.-Y. Qu, Z.-M. Zhang, T.-B. Lu, W. Lin, E.-B. Wang, *Appl. Catal., B* 224 (2018) 46–52.
- [31] Z. Huang, Z. Luo, Y.V. Geletii, J.W. Vickers, Q. Yin, D. Wu, Y. Hou, Y. Ding, J. Song, D.G. Musaev, C.L. Hill, T. Lian, *J. Am. Chem. Soc.* 133 (2011) 2068–2071.
- [32] N.S. McCool, D.M. Robinson, J.E. Sheats, G.C. Dismukes, *J. Am. Chem. Soc.* 133 (2011) 11446–11449.
- [33] S.Y. Reece, J.A. Hamel, K. Sung, T.D. Jarvi, A.J. Esswein, J.J.H. Pijpers, D.G. Nocera, *Science* 334 (2011) 645–648.
- [34] X. Li, M. Wang, S. Zhang, J. Pan, Y. Na, J. Liu, B. Aakermark, L. Sun, *J. Phys. Chem. B* 112 (2008) 8198–8202.
- [35] Y. Na, J. Pan, M. Wang, L. Sun, *Inorg. Chem.* 46 (2007) 3813–3815.
- [36] Y. Na, M. Wang, J. Pan, P. Zhang, B. Aakermark, L. Sun, *Inorg. Chem.* 47 (2008)

2805–2810.

[37] B.E. Barton, M.T. Olsen, T.B. Rauchfuss, *Curr. Opin. Biotechnol.* 21 (2010) 292–297.

[38] C. Baffert, V. Artero, M. Fontecave, *Inorg. Chem.* 46 (2007) 1817–1824.

[39] P. Connolly, J.H. Espenson, *Inorg. Chem.* 25 (1986) 2684–2688.

[40] J.L. Dempsey, B.S. Brunschwig, J.R. Winkler, H.B. Gray, *Acc. Chem. Res.* 42 (2009) 1995–2004.

[41] J.L. Dempsey, A.J. Esswein, D.R. Manke, J. Rosenthal, J.D. Soper, D.G. Nocera, *Inorg. Chem.* 44 (2005) 6879–6892.

[42] J.L. Dempsey, J.R. Winkler, H.B. Gray, *J. Am. Chem. Soc.* 132 (2010) 16774–16776.

[43] J.L. Dempsey, J.R. Winkler, H.B. Gray, *J. Am. Chem. Soc.* 132 (2010) 1060–1065.

[44] L. Gong, J. Wang, H. Li, L. Wang, J. Zhao, Z. Zhu, *Catal. Commun.* 12 (2011) 1099–1103.

[45] X. Hu, B.M. Cossairt, B.S. Brunschwig, N.S. Lewis, J.C. Peters, *Chem. Commun.* (2005) 4723–4725.

[46] X.L. Hu, B.S. Brunschwig, J.C. Peters, *J. Am. Chem. Soc.* 129 (2007) 8988–8998.

[47] S. Losse, J.G. Vos, S. Rau, *Coord. Chem. Rev.* 254 (2010) 2492–2504.

[48] O. Pantani, E. Anxolabehere-Mallart, A. Aukauloo, P. Millet, *Electrochim. Commun.* 9 (2006) 54–58.

[49] B. Probst, C. Kolano, P. Hamm, R. Alberto, *Inorg. Chem.* 48 (2009) 1836–1843.

[50] M. Razavet, V. Artero, M. Fontecave, *Inorg. Chem.* 44 (2005) 4786–4795.

[51] P. Zhang, M. Wang, C. Li, X. Li, J. Dong, L. Sun, *Chem. Commun.* 46 (2010) 8806–8808.

[52] D.M. Cropek, A. Metz, A.M. Muller, H.B. Gray, T. Horne, D.C. Horton, O. Poluektov, D.M. Tiede, R.T. Weber, W.L. Jarrett, J.D. Phillips, A.A. Holder, *Dalton Trans.* 41 (2012) 13060–13073.

[53] J. Chen, P.H.L. Sit, *Catal. Today* 314 (2018) 179–186.

[54] D.P. Estes, D.C. Grills, J.R. Norton, *J. Am. Chem. Soc.* 136 (2014) 17362–17365.

[55] K.L. Mulfort, R.A. Jensen, D.M. Tiede, *Prepr. Symp. - Am. Chem. Soc., Div. Fuel Chem.* 56 (2011) 198–199.

- [56] N.M. Muresan, J. Willkomm, D. Mersch, Y. Vaynzof, E. Reisner, *Angew. Chem., Int. Ed.* 51 (2012) 12749–12753.
- [57] I. Ozcesmeci, A. Demir, D. Akyuz, A. Koca, A. Gul, *Inorg. Chim. Acta* 466 (2017) 591–598.
- [58] A. Panagiotopoulos, K. Ladomenou, D. Sun, V. Artero, A.G. Coutsolelos, *Dalton Trans.* 45 (2016) 6732–6738.
- [59] G. Smolentsev, B. Cecconi, A. Guda, M. Chavarot-Kerlidou, J.A. van Bokhoven, M. Nachtegaal, V. Artero, *Chem. - Eur. J.* 21 (2015) 15158–15162.
- [60] Q.-X. Peng, L.-Z. Tang, S.-T. Ren, L.-P. Ye, Y.-F. Deng, S.-Z. Zhan, *Chem. Phys. Lett.* 662 (2016) 152–155.
- [61] M.A. Lawrence, M.J. Celestine, E.T. Artis, L.S. Joseph, D.L. Esquivel, A.J. Ledbetter, D.M. Cropek, W.L. Jarrett, C.A. Bayse, M.I. Brewer, A.A. Holder, *Dalton Trans.* 45 (2016) 10326–10342.
- [62] E. Ahmad, K. Majee, J. Patel, B. Das, S.K. Padhi, *Eur. J. Inorg. Chem.* 2017 (2017) 3409–3418.
- [63] P.-L. Fabre, D. Chen, O. Reynes, N. Chouini-Lalanne, V. Sartor, *J. Electroanal. Chem.* 711 (2013) 25–31.
- [64] W.R. McNamara, Z. Han, P.J. Alperin, W.W. Brennessel, P.L. Holland, R. Eisenberg, *J. Am. Chem. Soc.* 133 (2011) 15368–15371.
- [65] T.S. Jagodziński, *Chem. Rev.* 103 (2003) 197–228.
- [66] R.N. Hurd, G. DeLaMater, *Chem. Rev.* 61 (1961) 45–86.
- [67] M.H. Klingele, S. Brooker, *Eur. J. Org. Chem.* 2004 (2004) 3422–3434.
- [68] S. Panagiotakis, G. Landrou, V. Nikolaou, G. Charalambidis, A.G. Coutsolelos, A. Putri, R. Hardre, J. Massin, M. Orio, *Front Chem* 7 (2019) 405.
- [69] M.J.M. Campbell, *Coord. Chem. Rev.* 15 (1975) 279–319.
- [70] D.L. DuBois, *Inorg. Chem.* 53 (2014) 3935–3960.
- [71] N. Coutard, N. Kaeffer, V. Artero, *Chem. Commun.* 52 (2016) 13728–13748.
- [72] P. Wang, G. Liang, M.R. Reddy, M. Long, K. Driskill, C. Lyons, B. Donnadieu, J.C. Bollinger, C.E. Webster, X. Zhao, *J. Am. Chem. Soc.* 140 (2018) 9219–9229.
- [73] P. Wang, G. Liang, C.L. Boyd, C.E. Webster, X. Zhao, *Eur. J. Inorg. Chem.* 2019 (2019) 2134–2139.

- [74] Y. Sun, J.P. Bigi, N.A. Piro, M.L. Tang, J.R. Long, C.J. Chang, *J. Am. Chem. Soc.* 133 (2011) 9212.
- [75] Y. Sun, J. Sun, J.R. Long, P. Yang, C.J. Chang, *Chem. Sci.* 4 (2013) 118.
- [76] L. Chen, M. Wang, K. Han, P. Zhang, F. Gloaguen, L. Sun, *Energy Environ. Sci.* 7 (2014) 329.
- [77] C. Bachmann, M. Guttentag, B. Spingler, R. Alberto, *Inorg. Chem.* 52 (2013) 6055.
- [78] D. Basu, S. Mazumder, X. Shi, H. Baydoun, J. Niklas, O. Poluektov, H.B. Schlegel, C.N. Verani, *Angew. Chem., Int. Ed.* 54 (2015) 2105.
- [79] J.P. Bigi, T.E. Hanna, W.H. Harman, A. Chang, C.J. Chang, *Chem. Commun.* 46 (2010) 958.
- [80] L. Chen, A. Khadivi, M. Singh, J.W. Jurss, *Inorg. Chem. Front.* 4 (2017) 1649.
- [81] E. Joliat-Wick, N. Weder, D. Klose, C. Bachmann, B. Spingler, B. Probst, R. Alberto, *Inorg. Chem.* 57 (2018) 1651.
- [82] A.E. King, Y. Surendranath, N.A. Piro, J.P. Bigi, J.R. Long, C.J. Chang, *Chem. Sci.* 4 (2013) 1578.
- [83] J.G. Kleingardner, B. Kandemir, K.L. Bren, *J. Am. Chem. Soc.* 136 (2014) 4.
- [84] N. Queyriaux, R.T. Jane, J. Massin, V. Artero, M. Chavarot-Kerlidou, *Coord. Chem. Rev.* 304–305 (2015) 3.
- [85] A. Rodenberg, M. Oraziotti, B. Probst, C. Bachmann, R. Alberto, K.K. Baldridge, P. Hamm, *Inorg. Chem.* 54 (2015) 646.
- [86] S. Schnidrig, C. Bachmann, P. Muller, N. Weder, B. Spingler, E. Joliat-Wick, M. Mosberger, J. Windisch, R. Alberto, B. Probst, *ChemSusChem* 10 (2017) 4570.
- [87] W.M. Singh, T. Baine, S. Kudo, S. Tian, X.A. Ma, H. Zhou, N.J. DeYonker, T.C. Pham, J.C. Bollinger, D.L. Baker, B. Yan, C.E. Webster, X. Zhao, *Angew. Chem., Int. Ed.* 51 (2012) 5941.
- [88] W.M. Singh, M. Mirmohades, R.T. Jane, T.A. White, L. Hammarstrom, A. Thapper, R. Lomoth, S. Ott, *Chem. Commun.* 49 (2013) 8638.
- [89] B.D. Stubbert, J.C. Peters, H.B. Gray, *J. Am. Chem. Soc.* 133 (2011) 18070.
- [90] P. Zhang, M. Wang, F. Gloaguen, L. Chen, F. Quentel, L. Sun, *Chem. Commun.* 49 (2013) 9455.
- [91] D.Z. Zee, T. Chantarojsiri, J.R. Long, C.J. Chang, *Acc. Chem. Res.* 48 (2015)

2027–2036.

- [92] S. Rai, K. Majee, M. Raj, A. Pahari, J. Patel, S.K. Padhi, *Polyhedron* 159 (2019) 127–134.
- [93] C. Creutz, N. Sutin, *Coord. Chem. Rev.* 64 (1985) 20.
- [94] V. Artero, M. Chavarot-Kerlidou, M. Fontecave, *Angew. Chem. Int. Ed.* 50 (2011) 7238–7266.
- [95] K.E. Dalle, J. Warnan, J.J. Leung, B. Reuillard, I.S. Karmel, E. Reissner, *Chem Rev* 119 (2019) 2752–2875.
- [96] R. Gueret, C.E. Castillo, M. Rebarz, F. Thomas, M. Sliwa, J. Chauvin, B. Dautreppe, J. Pecaut, J. Fortage, M.N. Collomb, *Inorg Chem* 58 (2019) 9043–9056.
- [97] R.S. Khnayzer, V.S. Thoi, M. Nippe, A.E. King, J.W. Jurss, K.A. El Roz, J.R. Long, C.J. Chang, F.N. Castellano, *Energy Environ. Sci.* 7 (2014) 1477–1488.
- [98] R.W. Hogue, O. Schott, G.S. Hanan, S. Brooker, *Chemistry* 24 (2018) 9820–9832.
- [99] J. Tomasi, B. Mennucci, R. Cammi, *Chem. Rev.* 105 (2005) 2999–3094.
- [100] P.J. Hay, *J. Chem. Phys.* 66 (1977) 4377–4384.
- [101] A.J.H. Wachters, *J. Chem. Phys.* 52 (1970) 1033–1036.
- [102] T.H. Dunning, *J. Chem. Phys.* 55 (1971) 716–723.
- [103] S. Ghosh, A.C. Barve, A.A. Kumbhar, A.S. Kumbhar, V.G. Puranik, P.A. Datar, U.B. Sonawane, R.R. Joshi, *J. Inorg. Biochem.* 100 (2006) 331–343.
- [104] H.-S. Kim, S.-B. Ko, I.-H. Jang, N.-G. Park, *Chem. Commun.* 47 (2011) 12637–12639.
- [105] N.G. Park, *Hwahak Sekye* 46 (2006) 74–83.
- [106] G. Sheldrick, *Acta Crystallogr. Sect. A* 64 (2008) 112–122.
- [107] G.M. Sheldrick, in, University of Gottingen, Germany, 2014.
- [108] M.A.W. Lawrence, Y.A. Jackson, W.H. Mulder, P.M. Bjoremark, M. Hakansson, *Aust. J. Chem.* 68 (2015) 731–741.
- [109] M.A.W. Lawrence, W.H. Mulder, *ChemistrySelect* 3 (2018) 8387–8394.
- [110] M. Bakir, M.A.W. Lawrence, M. Ferhat, R.R. Conry, *J. Coord. Chem.* 70 (2017) 3048–3064.
- [111] O. Pantani, S. Naskar, R. Guillot, P. Millet, E. Anxolabehere-Mallart, A. Aukauloo, *Angew. Chem., Int. Ed.* 47 (2008) 9948–9950.

- [112] K.J. Lee, B.D. McCarthy, J.L. Dempsey, Chem. Soc. Rev. 48 (2019) 2927–2945.
- [113] R.M. Kellett, T.G. Spiro, Inorg. Chem. 24 (1985) 2373–2377.
- [114] P. Dongare, B.D.B. Myron, L. Wang, D.W. Thompson, T.J. Meyer, Coord. Chem. Rev. 345 (2017) 86–107.
- [115] E. Rousset, D. Chartrand, I. Ciofini, V. Marvaud, G.S. Hanan, Chem. Commun. (Camb) 51 (2015) 9261–9264.
- [116] E. Rousset, I. Ciofini, V. Marvaud, G.S. Hanan, Inorg Chem 56 (2017) 9515–9524.
- [117] O. Schott, A.K. Pal, D. Chartrand, G.S. Hanan, Chemsuschem 10 (2017) 4436–4441.

3.8 Supporting Information

N-substituted 2-pyridinecarbothioamides and Polypyridyl Mixed-ligand Cobalt(III)-Containing Complexes for Photocatalytic Hydrogen Generation

Michael J. Celestine,^a Mark A. W. Lawrence,^b Nicholas K. Evaristo, Benjamin W. Legere, James K. Knarr, Olivier Schott, Vincent Picard, Jimmie L. Bullock, Garry S. Hanan,^c Colin D. McMillen,^d Craig A. Bayse,^a and Alvin A. Holder^{a*}

Author affiliations:

^a Department of Chemistry and Biochemistry, Old Dominion University, 4541 Hampton Boulevard, Norfolk, VA 23529, U.S.A.

^b Department of Chemistry, the University of the West Indies, Mona Campus, Kingston 7, Jamaica W.I.

^c Département de Chimie, Université de Montréal, Bureau 3013, Pavillon J.-A. Bombardier, 5155 Chemin de la Rampe (Rampe Road), Montreal, Quebec, H3T 2B1, Canada

^d Department of Chemistry, Clemson University, 219 Hunter Laboratories, Clemson, SC 29634, U.S.A.

3.8.1 General Procedures

General procedure for the preparation of $[\text{Co}(\text{N-N})_2\text{Cl}_2]\text{Cl}$ (where N-N = bpy (complex 1) or phen (complex 2)) and $[\text{Co}(\text{dmgH})_2\text{Cl}(\text{py})]$

$[\text{Co}(\text{bpy})_2\text{Cl}_2]\text{Cl}$ **1** and $[\text{Co}(\text{phen})_2\text{Cl}_2]\text{Cl}$ **2** were synthesized via the procedure as by Ghosh *et al.* [1]. The $[\text{Co}(\text{dmgH})_2\text{Cl}(\text{py})]$ complex was synthesized as previously described [2].

Synthesis of $[\text{Co}(\text{N-N})_3](\text{PF}_6)_3$ (where N-N = bpy (5) or phen (6))

$[\text{Co}(\text{bpy})_3](\text{PF}_6)_3$ **5** was synthesized following the procedure of Kim [3]. $[\text{Co}(\text{bpy})_3](\text{PF}_6)_2$ (0.176 g, 0.397 mmol) was then dissolved in acetonitrile (15 ml); to this bromine (1.27 g, 408 μ l, 7.92 mmol) was added, and the reaction mixture was allowed to stir for 17.5 hours at room temperature. The reaction mixture was dried via rotary evaporation, and the resulting residue was dissolved in *N,N*-dimethylformamide (3 ml); followed by the addition of ammonium hexafluorophosphate

(0.502 g, 3.08 mmol) and water (10 ml). The resulting precipitate was then filtered, and the residue was washed with cold water, followed by diethyl ether and was air dried. ^1H NMR (400 MHz, $\text{CD}_3\text{CN}-d_3$, δ/ppm) 8.68 (dd, $J = 8.14, 1.10$ Hz, 6 H), 8.44 - 8.50 (m, 6 H), 7.73 (ddd, $J = 7.59, 6.05, 1.54$ Hz, 6 H), 7.24 - 7.29 (m, 6 H).

[Co(phen)₃](PF₆)₃ **6** was synthesized from [Co(phen)₂Cl₂]Cl **2** (0.175 g, 0.334 mmol), dissolved in water (10 ml) followed by the addition of 1,10-phenanthroline (0.124 g, 0.690 mmol). The reaction was then stirred for 20 minutes following which acetone (10 ml) and ammonium hexafluorophosphate (0.230 g, 1.41 mmol) were added. The solvent was removed via vacuum, and the residue was then dissolved in acetonitrile, filtered and diethyl ether was added to the filtrate. The resulting precipitate was then filtered, and the residue was washed with diethyl ether, and allowed to air dry. Yield: 0.270 g (78%). ^1H NMR (400 MHz, DMSO-*d*₆, δ/ppm) 9.16 (dd, $J = 8.14, 0.88$ Hz, 6 H), 8.57 (s, 6 H), 7.97 (dd, $J = 8.25, 5.61$ Hz, 6 H), 7.66 (dd, $J = 5.50, 0.66$ Hz, 6 H).

3.8.2 Additional data

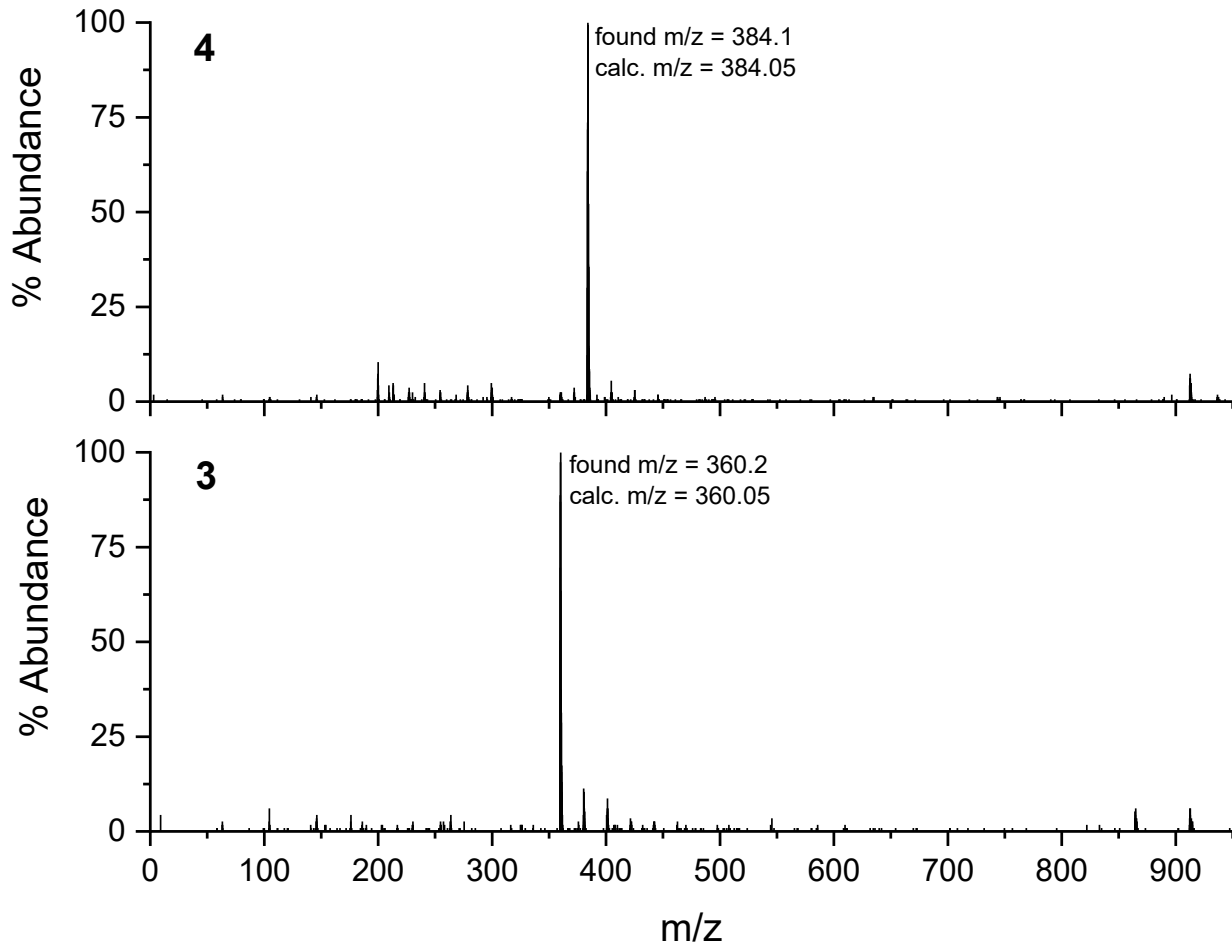


Figure 59. . ESI MS of complexes **3** and **4** in CH₃CN

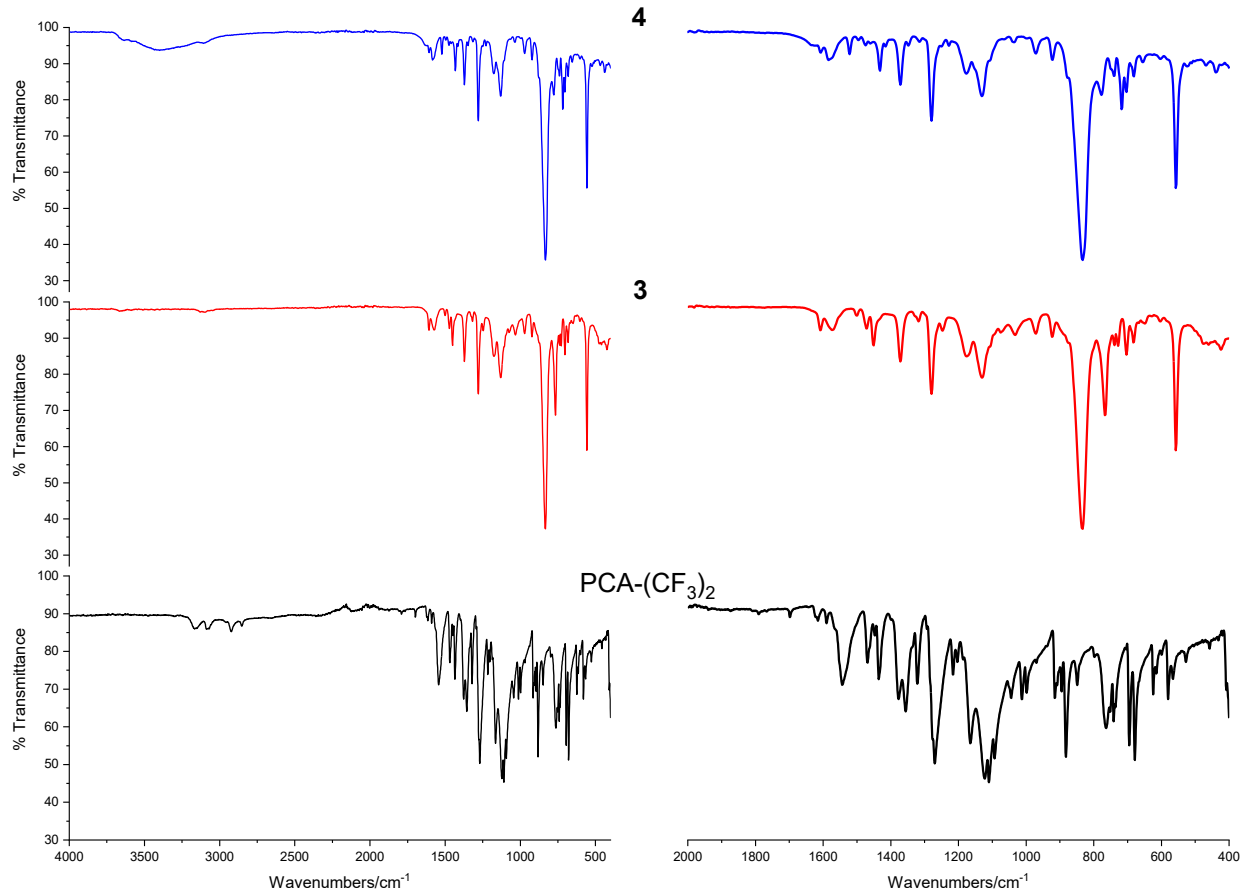


Figure 60. FTIR spectra of PCA-(CF₃)₂, complex 3, and complex 4.

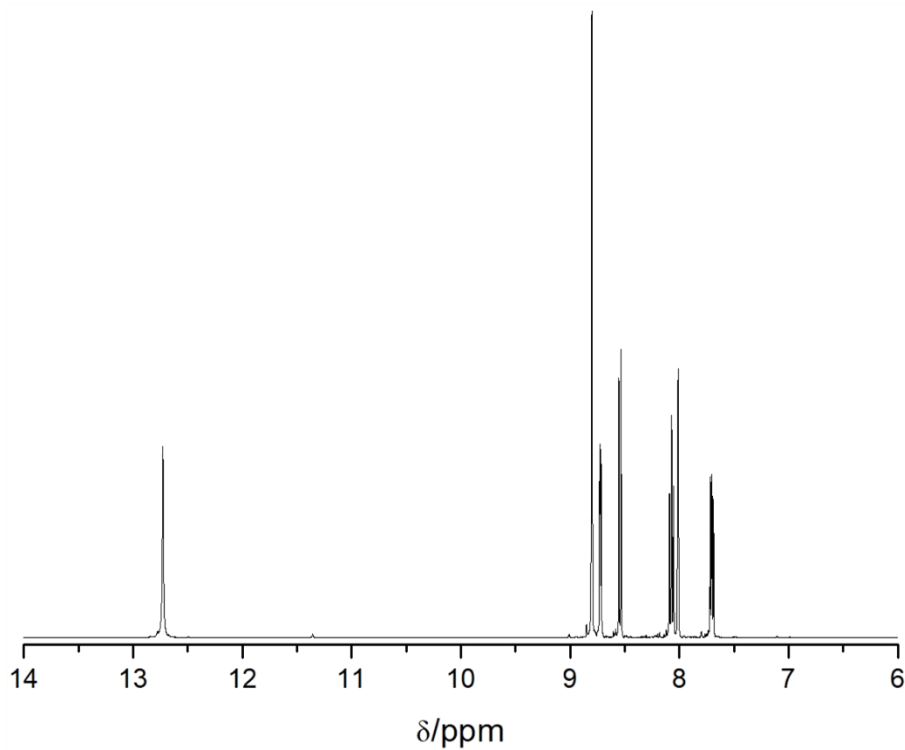


Figure 61. ¹H NMR spectrum of PCA-(CF₃)₂ in DMSO-*d*₆.



Figure 62. Crystals of PCA-(CF₃)₂.

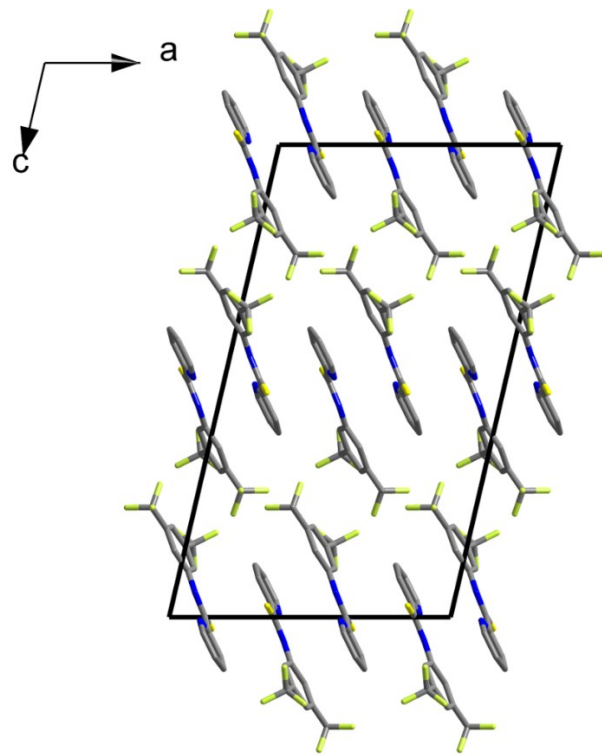


Figure 63. Packing of molecules in PCA- $(CF_3)_2$, viewed along the b -axis.

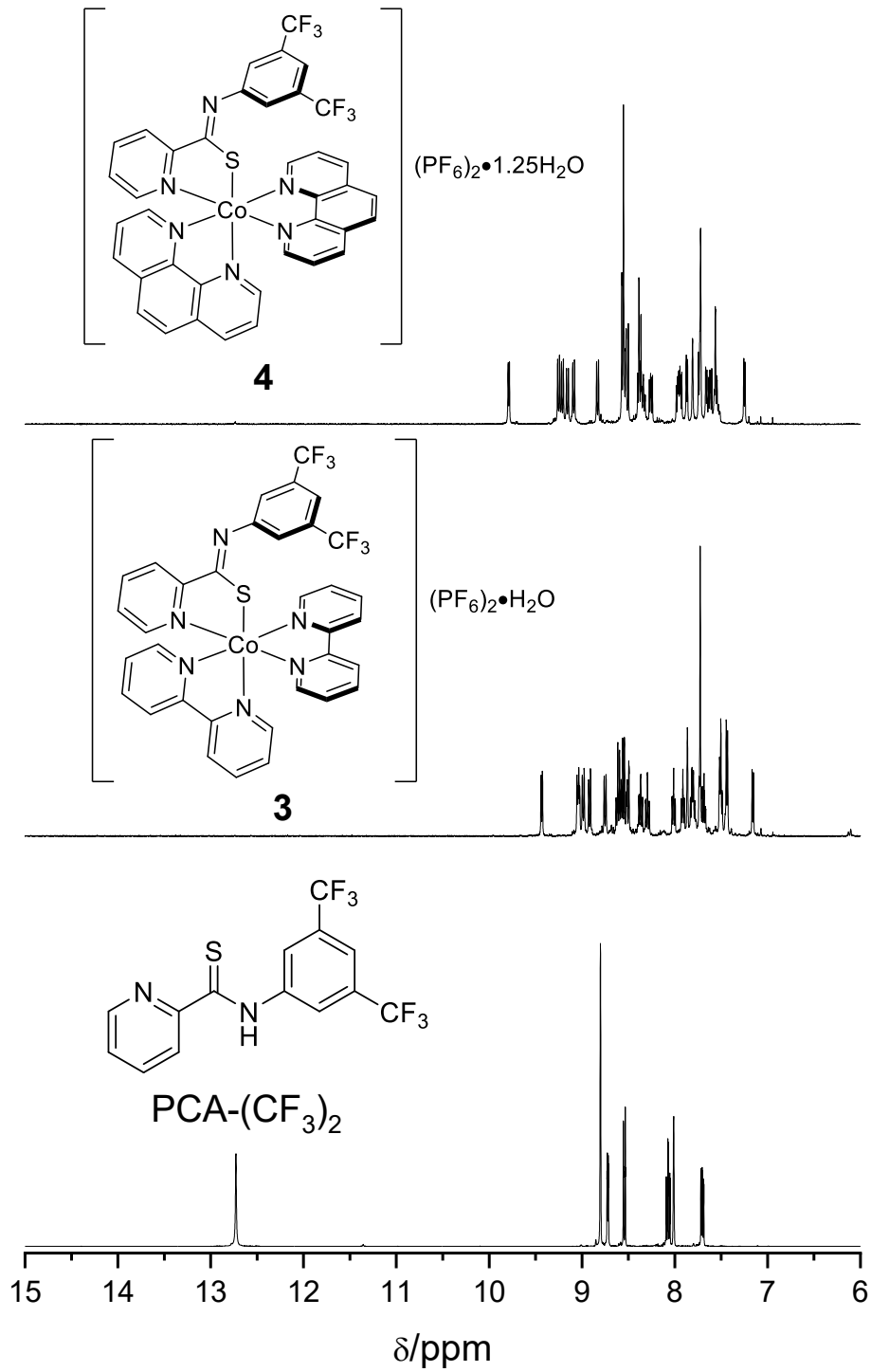


Figure 64. ¹H NMR spectra of PCA-(CF₃)₂, and complex 3, and complex 4 in DMSO-d₆.

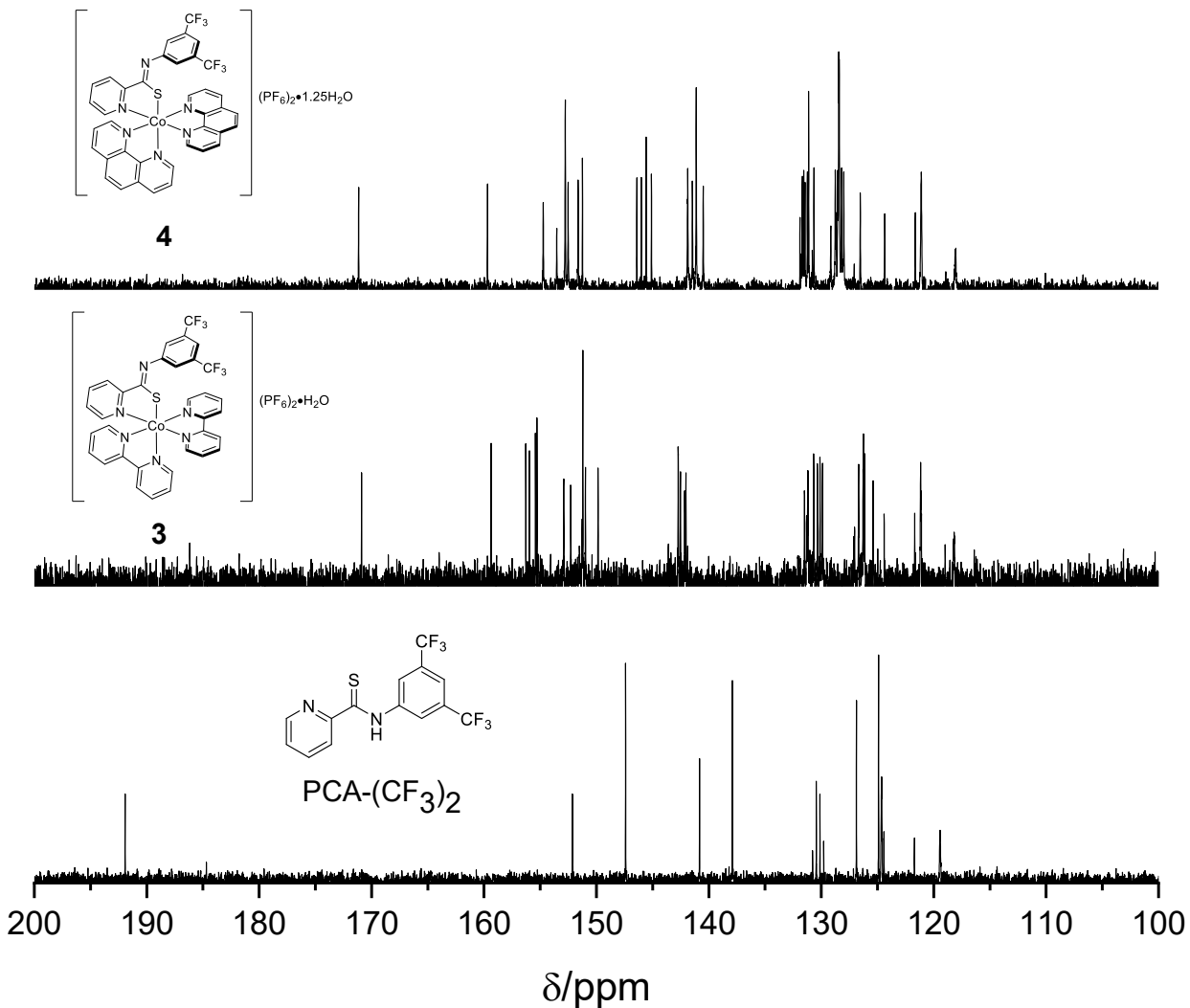


Figure 65. ^{13}C NMR spectra of PCA- $(\text{CF}_3)_2$, and complex 3, and complex 4 in DMSO-d₆.

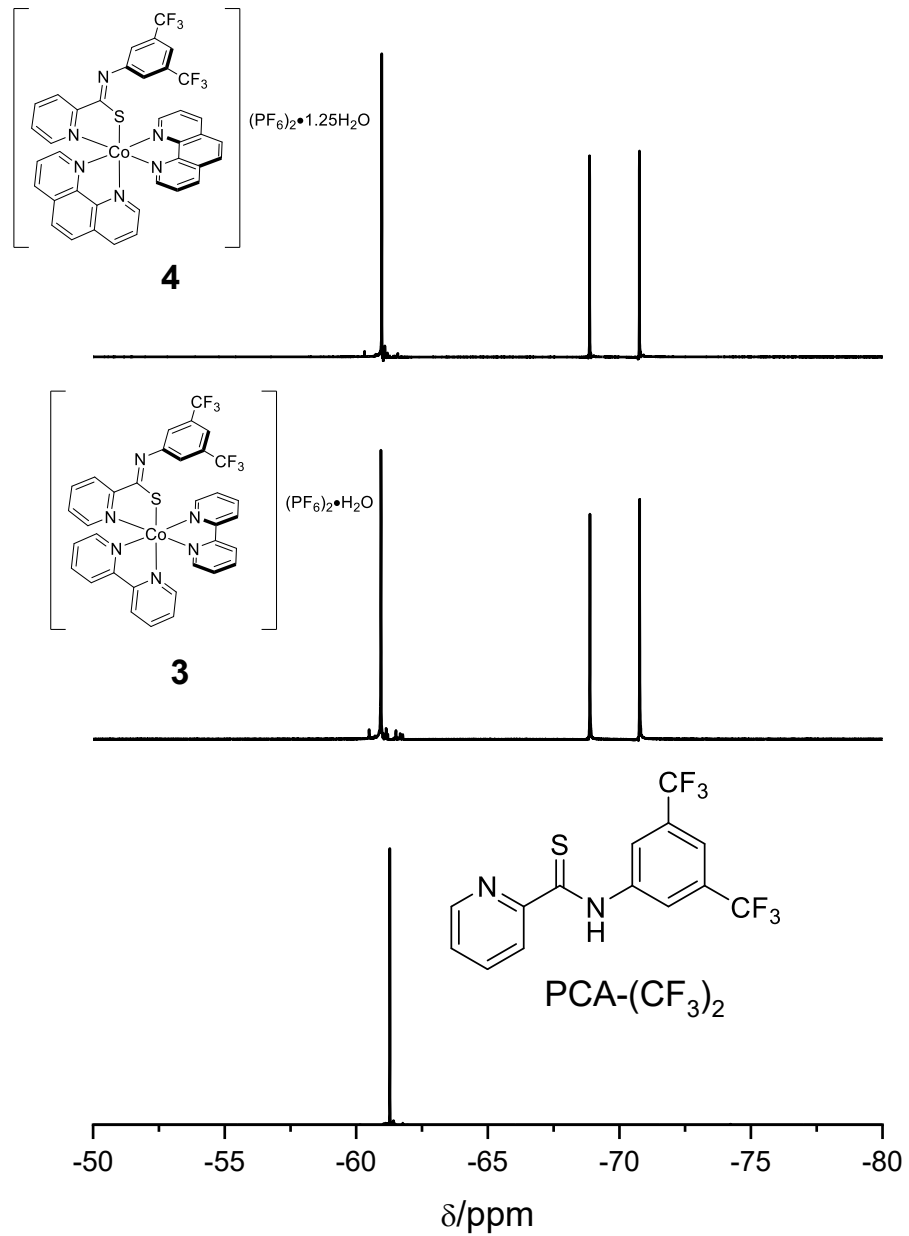


Figure 66. ^{19}F NMR spectra of PCA- $(\text{CF}_3)_2$, and complex **3**, and complex **4** in DMSO-d_6 .

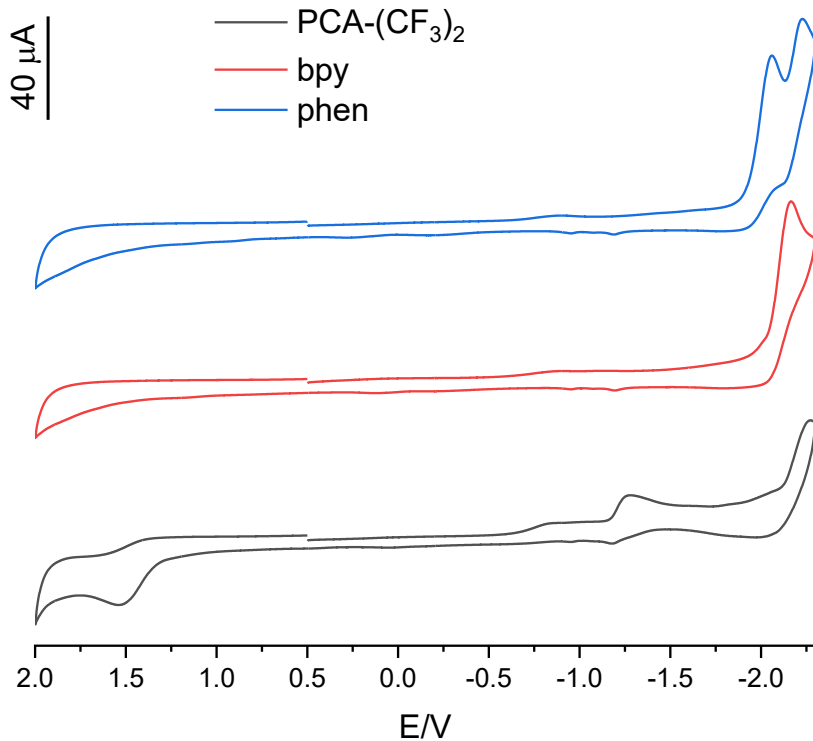


Figure 67. Cyclic voltammograms of 1.0 mM (PCA-(CF₃)₂, *bpy*, and *phen* in CH₃CN at a glassy carbon working electrode vs Ag/AgCl. Supporting electrolyte = 0.1 M ([ⁿBu₄N]ClO₄) and scan rate = 100 mV s⁻¹.

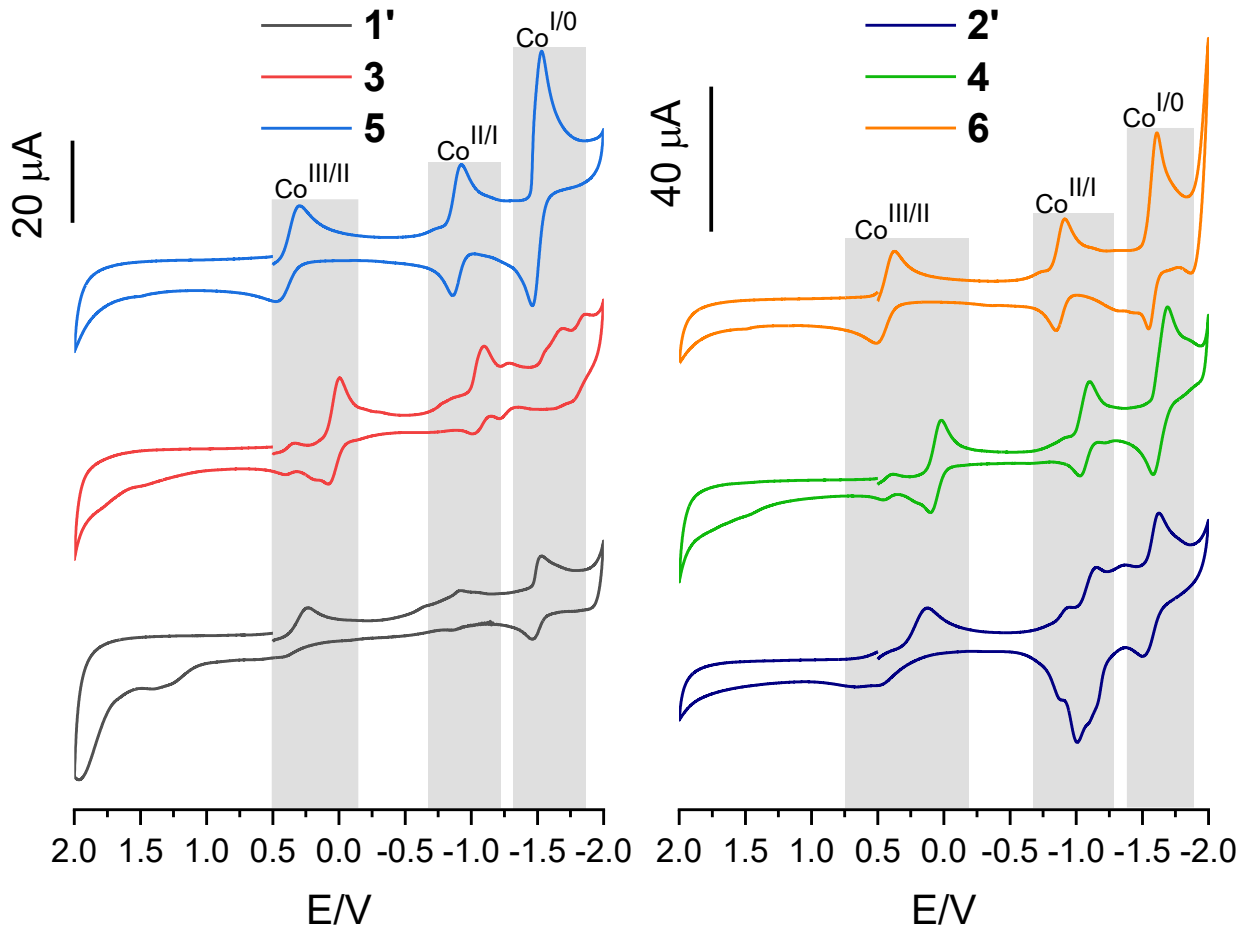


Figure 68. Cyclic voltammograms of complexes **1-6** in CH_3CN . [complex] = 1.0 mM, supporting electrolyte = 0.1 M ($[{}^n\text{Bu}_4\text{N}]\text{ClO}_4$), and scan rate = 100 mV s^{-1} .

3.8.3 Set up of gas chromatography

Hydrogen evolution was measured using a Perkin Elmer Clarus-580 gas chromatograph (GC) with a thermal conductivity detector, argon as carrier and eluent gas, a 7' HayeSep N 60/80 pre-column, a 9' molecular sieve $13 \times 45/60$ column and a 1 mL injection loop. Three distinct solutions were prepared for the photosensitizer $\text{Ru}(\text{bpy})_3(\text{PF}_6)_2$, catalyst and last sacrificial electron donor and acid source (HBF_4 , 48% water): the three solutions were mixed together to obtain 5 mL of sample solutions in standard 20 mL headspace vials. In DMF, the resulting molar concentrations of photocatalytic components were: 1 M for triethanolamine (TEOA), 0.1 M for (HBF_4), 0.56 M for water, 0.1 mM for $\text{Ru}(\text{bpy})_3(\text{PF}_6)_2$, 0.01 mM for $[\text{Co}(\text{tpy})(\text{phen})\text{Cl}](\text{PF}_6)_2$ or

$[\text{Co}(\text{dmgH})_2\text{Cl}(\text{py})]$ (apparent pH = 8.9). Those vials were placed on a LED panel in a thermostatic bath set at 20 °C. They were sealed with a rubber septum pierced with two stainless steel tubes. The first tube carried an argon flow pre-bubbled in spectroscopic grade solvent. The flow was set to 5 mL min⁻¹ (adjusted with a manual flow controller (Porter, 1000) and referenced with a digital flowmeter (Perkin Elmer FlowMark)). The second tube leads the flow to the GC sample loop through a 2 mL overflow protection vial, then through an 8-port stream select valve (VICCI) and finally to the GC sample loop. A microprocessor (Arduino Uno) coupled with a custom PC interface allows for timed injections. For general calibration, stock cylinders of known concentration of H₂ in nitrogen replaced the nitrogen flow (inserted at the pre-bubbler, to keep the vapor matrix consistent). The measured results, independent of flow rate (under same pressure) can be easily converted into a rate of hydrogen following equation 1.

For calibration of H₂ production, a nitrogen bottle of certified 100 ppm hydrogen was set to deliver a specific flow. H₂ production rate at a specific nitrogen flow, a syringe pump (New Era Pump) equipped with a gas-tight syringe (SGE) and a 26s gauge needle (Hamilton) was used to bubble different rates of pure hydrogen gas into the sample, to a minimum of 0.5 µL min⁻¹. This gave a linear fit for peak area for H₂ versus the flow rates of H₂ (Eq. 1). All experiments were done in duplicate to verify the reproducibility of results and an average for the TOF and TON curves is calculated with Origin software. The error associated with the TOF and TON values is estimated to be 10% [4].

$$\text{H}_2 \text{ rate } (\mu\text{L min}^{-1}) = [\text{H}_2 \text{ standard}] \text{ (ppm)} \times \text{N}_2 \text{ flow rate } (\text{L min}^{-1}) \quad 1$$

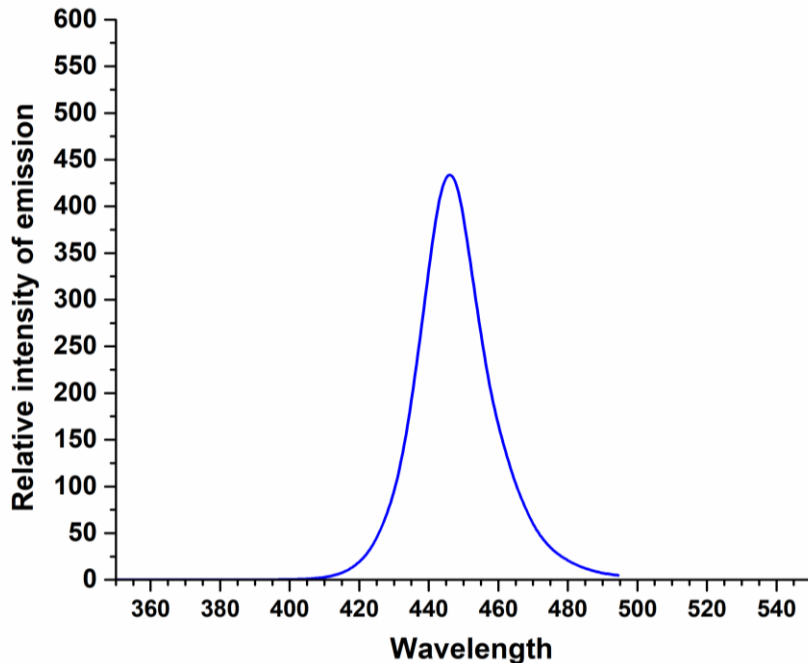


Figure 69. Emission spectrum of the blue LED.

Tableau 8. – Emission maxima and amplitude of the LED light.

Light source ^a	Blue
$\lambda_{\text{max,em}}$ (nm)	445
$\Delta\lambda$ (nm)	90
Photon flux in $\mu\text{mol}_{\text{photons}}.\text{min}^{-1}.\text{cm}^{-2}$ ^b	20

^a blue LED 445 nm.

^b an analog power-meter PM100A (THORLABS) associated with a compact photodiode power head with silicon detector S120C is used to evaluate the photon flux for the LEDs. Photo-diode detector is placed at the same distance from the LED surface as the bottom of the illuminated vial.

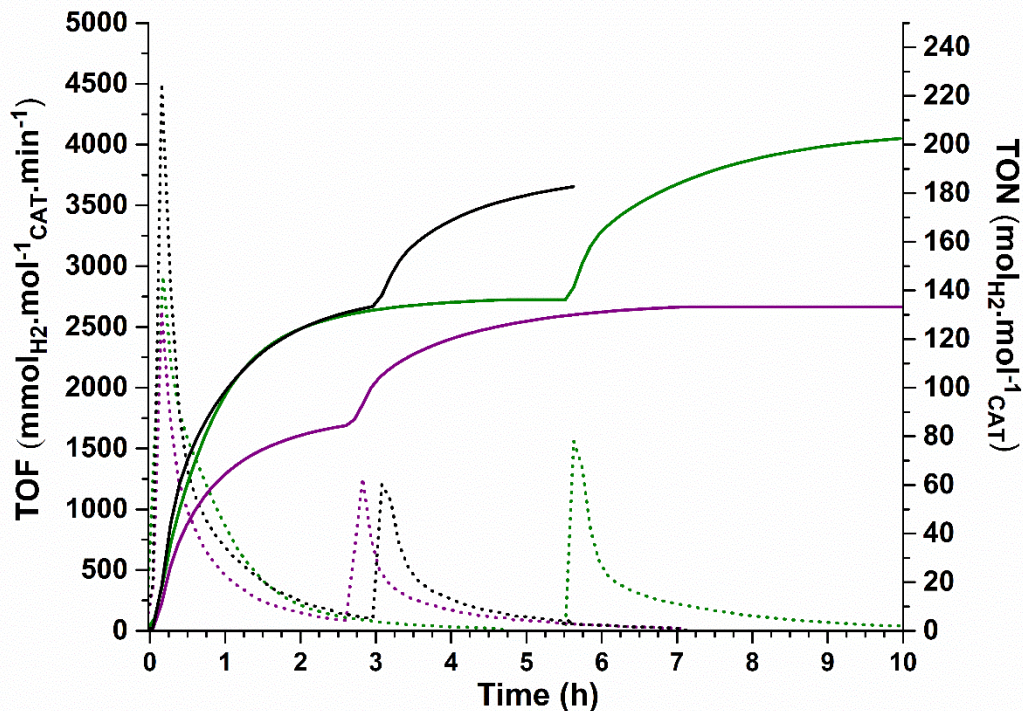


Figure 70. Restart of hydrogen evolution of $[\text{Co}(\text{dmgH})_2\text{Cl}(\text{py})]$ (black), complex 3 (purple), and complex 4 (olive) by the addition of photosensitizer (1.25 ml of 0.4 mM $\text{Ru}(\text{bpy})_3(\text{PF}_6)_2$) at the end of activity. TOF: dotted line. TON: solid line.

References:

- [1] S. Ghosh, A.C. Barve, A.A. Kumbhar, A.S. Kumbhar, V.G. Puranik, P.A. Datar, U.B. Sonawane, R.R. Joshi, *J. Inorg. Biochem.*, 100 (2006) 331-343.
- [2] M. Razavet, V. Artero, M. Fontecave, *Inorg. Chem.*, 44 (2005) 4786-4795.
- [3] H.-S. Kim, S.-B. Ko, I.-H. Jang, N.-G. Park, *Chem. Commun.*, 47 (2011) 12637-12639.
- [4] C. Lentz, O. Schott, T. Auvray, G. Hanan, B. Elias, *Inorg. Chem.*, 56 (2017) 10875-10881.

4) Chapitre 4: Efficient Ru/Co molecular photocatalytic system driven by cyclohexyl-based cobaloximes as HER catalysts

4.1 Abstract

Cyclohexyl-based cobaloximes are studied for photocatalytic hydrogen generation in comparison with dimethylglyoxime-based cobaloximes in association with $[\text{Ru}(\text{bpy})_3]^{2+}$ under blue LED irradiation. Additionally, the effect on the axial position of pyridine substituents with the classical pyridine and dimethylaminopyridine is investigated with regards to the photocatalysis and optoelectronic proprieties of the cobaloximes. X-ray diffraction, NMR, cyclic-voltammetry, spectro-electrochemistry, and monitoring of photocatalytic hydrogen production are used to characterize the four cobaloximes: $\text{Co}(\text{dmgH})_2\text{PyrCl}$, $\text{Co}(\text{dmgH})_2\text{DMAPCl}$, $\text{Co}(\text{chgH})_2\text{PyrCl}$ and $\text{Co}(\text{chgH})_2\text{DMAPCl}$, where Pyr is pyridine and DMAP is dimethylaminopyridine. The cyclohexyl substituent rigidifies the bite angle of the bidentate glyoxime ligand while leaving the optoelectronic proprieties roughly similar to dimethylcobaloximes. Molecular dynamics are illustrated by the free rotation of methyl in dimethyl derivatives and the limited free movement of cyclohexyl conformers that could play a role in the transition catalytic species. The electro-donor dimethylaminopyridine and pyridine tune the Co-hydride proprieties of the complexes. The DMAP influences more than the pyridine the intensity of electronic transitions in the Co^{I} species although optoelectronic measurements are quite similar for the pyridine derivatives and DMAP derivatives. Monitoring the hydrogen evolution exhibits a particular slowly decreasing photocatalytic activity for $[\text{Ru}(\text{bpy})_3]^{2+}$ /cyclohexyl-based cobaloxime systems that leads to the best turnover number of 1650 mol H_2 /mol of photosensitizer among this family vs 60 for dimethyl-based systems.

Keywords: photocatalyst, cobaloxime, photosensitizer, hydrogen evolution, inorganic chemistry, spectroscopy, electrochemistry.

Contribution: J'ai récolté les données d'E-chem et quelques RMN. J'ai participé activement à la rédaction de l'article (section introduction, RMN, E-chem et l'intégralité des infos supplémentaires). Je suis l'auteur de la presque totalité des figures de l'article (incluant les infos supplémentaires) et j'ai procédé seul à la révision de l'article.

Manuscrit accepté avec révision, soumis à inorganica chemica acta ICA-D-22-00871

Efficient Ru/Co molecular photocatalytic system driven by cyclohexyl-based cobaloximes as HER catalysts

Olivier Schott*, Vincent Picard*, Daniel Chartrand, Garry S. Hanan**

Département de Chimie, Université de Montréal 1375 Avenue Thérèse-Lavoie-Roux, Montréal, Québec, H2V-0B3,
Canada. Email: Garry.hanan@umontreal.ca

***Co-First author**

****Corresponding author: Fax: +1 514 343 7586. Tel: +1 514 340 5156.**
Email: Garry.hanan@umontreal.ca

4.2 Introduction

The huge energy consumption of a continuously growing human population causes a looming environmental crisis and a risk for human health^[1]. Manifestations of the pollution on climate change, various ecosystems, and the life of living beings have been more and more widely reported during recent years^[2]. Certainly, the priority must be to slow down the emission of greenhouse gases into the atmosphere, such as carbon dioxide, that induce global warming, and to neutralize and recycle these greenhouse gases^[3]. New developments of clean alternatives to fossil fuels are imperative and the most convenient natural resources of energy is the continual and colossal power of the sun^[1, 4]. Taking inspiration from natural photosynthesis, molecular artificial synthesis offers a promising approach for the conversion of solar energy to chemical bonds in the form of hydrogen gas^[3, 5]. It's high energy density vs fossil fuels or batteries and the benign product of the combustion of hydrogen make it an encouraging form of energy storage^[6]. After recent discussions^[7], the use of hydrogen as a fuel source has been given momentum, as governments around the world see a new opportunity to develop a green economy of hydrogen.^[6b] Commercial hydrogen production from electrolysis uses expensive elements such as platinum^[8] or the steam reforming process, which produces greenhouse gases^[9]. Solar fuels, on the other hand, are the products of the photoreduction of protons or organic derivatives by extracting electrons from water using photocatalysts and light^[3b, 10]. Here, the research aims to develop new inexpensive, clean, efficient, and earth-abundant photocatalytic systems for the hydrogen evolving reaction (HER): half of the water-splitting process. The molecular photosystem is mainly composed of a photosensitizer, a catalyst, and a sacrificial electron donor. As for the photosensitizer, instead of using Ir^[11], Pt^[12], or Re^[13], we exploit the archetypical $[\text{Ru}(\text{bpy})_3]^{2+}$ ^[14] (bpy=bipyridine) due to its lower cost and the higher abundance of Ru over the other metals.

Over the last decade, chemists designed organic ligands to tune the photo-electrocatalytic HER proprieties of earth-abundant first-row transition metals^[15] made of Fe^[13b, 16], Co^[14d, 17], Ni^[18], Cu^[19] that are less expensive than Pt^[20], Pd^[21] and Rh^[22]. Improving the electron transfers between the chromophores and the catalysts by supramolecular interactions such as a pyridine linker^[11c, 23], or introducing basic sites on the ligand to favor the Proton-Coupled Electron Transfer^[24] are strategies of optimization. A variety of ligands with precise geometry and denticity to track the catalytic proprieties of Co coordination chemistry have been investigated with N-heterocycle, Schiff base, sulfur derivatives^[17a]. The cobaloxime is one of the most used and studied because the synthesis of this compound is simple and efficient^[23c]. The glyoxime ligand has an N-bidentate denticity and forms a 5-membered ring with the metal. The soft oxime function, a mediator of protons to the metallic center and an electron relay properties, draws a pseudo-macrocycle by hydrogen bonding around the metallic center, a rare design among inorganic architectures. The literature presents a variety of oxime-based planar ligands derived by a rich diversity of chemical substituents^[17a]. The design of macrocycles, such as tetra-N Schiff base, phthalocyanine or porphyrins^[17a], and recently penta-N membered Schiff^[17j], featuring catalyst built on C-C and C-N bonds around the metal. Indeed, the chelate effect in the pocket of the porphyrin is high, which increases the robustness of the catalyst. The glyoxime pseudo-macrocycle is composed of C-N bonds and hydrogen bonds between the oximes. The axial position has been modified by N-heterocycle and phosphine derivatives to change the proprieties of the Co-hydride intermediates^[25]. The research team of Ott created cobaloxime-Metal-Organic-Frameworks for electrocatalytic HER^[26], while other original system involving quantum dots, using cobaloxime as cocatalyst, along with NiO, have been developed.^[27]

Our hypothesis concerning the improved stability of the Co(dmgH)₂ catalyst is that the cyclohexyl dioxime ligand should rigidify the structure of the catalyst, with favourable effects on ligand and metal orbitals overlap, thus reducing catalyst degradation rate.^[28] We expect that the placement of a strong electron donor in the axial position to raise the rate and the TON of activity^[8a]. The classical pyridine and the strong coordinating N,N-dimethylaminopyridine (DMAP)^[29] axial ligand, which is used notably as anchoring unit for photocathodes^[30] are compared in dimethyl and cyclohexyl based cobaloximes for photocatalytic hydrogen evolution. A growing number of studies discuss the behavior of activity to understand the degradation pathways^[17j, 17l, 23a, 25b, 31].

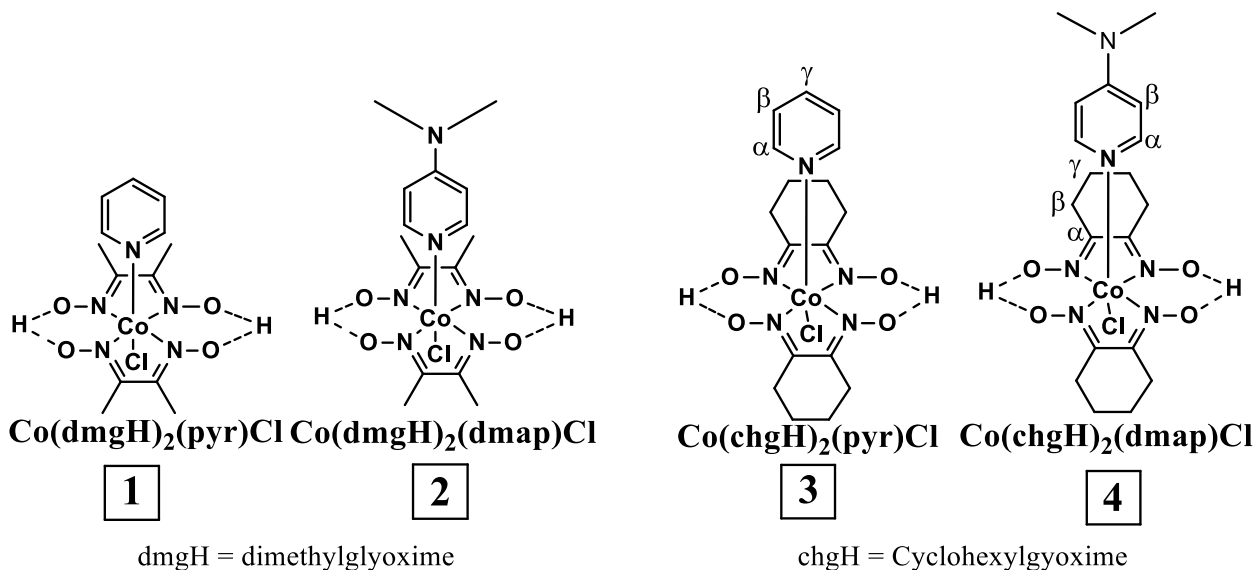


Figure 71. cobaloximes catalysts used in the present study

4.3 Results and discussion

4.3.1 Synthesis and NMR analysis

The cobaloximes were synthesized with pyridine (Pyr) and dimethylaminopyridine (DMAP) as axial ligands with moderate yields of 49 % and 21 % (cobaloxime catalysts **1** and **2**)^[25b, 32], and

33 % and 26 % (cyclohexyls catalysts **3** and **4**), respectively. The catalyst identification was carried by ^1H NMR and Elemental Analysis (see Fig 72 for details). The DMAP derivatives show a less down-shift signal than the pyridine derivatives. The electro-donating substituent DMAP should have a better donor mesomeric effect towards the metal^[29b, 33]. The β protons of DMAP are slightly down-shifted in the case of the cyclohexylcobaloxime as DMAP could share more electronic density in this case vs dmg derivative. For proton signals of the β and γ carbons (see Fig. 71 for positions) of the cyclohexyl ligand, every 8 protons are each divided into two multiplets that integrate for 4, each multiplet corresponds to the protons on the side of the pyridine moieties or below. The chemical shift of the multiplets for the protons on the γ carbon is around 1.7 ppm and those for the protons on the β carbons are around 2.9 ppm. In the X-ray structure, no disorder is modeled for the β positions. The β protons are more affected by the axial position due to the spatial proximity as a bigger shift between the two multiplets than for the γ protons is observed. The NMR signals in the solution are representative of the averaging of the most stable molecular forms that undergo the molecular dynamics. Finally, the singlet signal of the methyl in the dimethylglyoxime manifests a rotation of methyl around the C-C bond. The NMR spectrum of cyclohexyl derivatives exhibits a ligand more complex with less symmetric fragments.

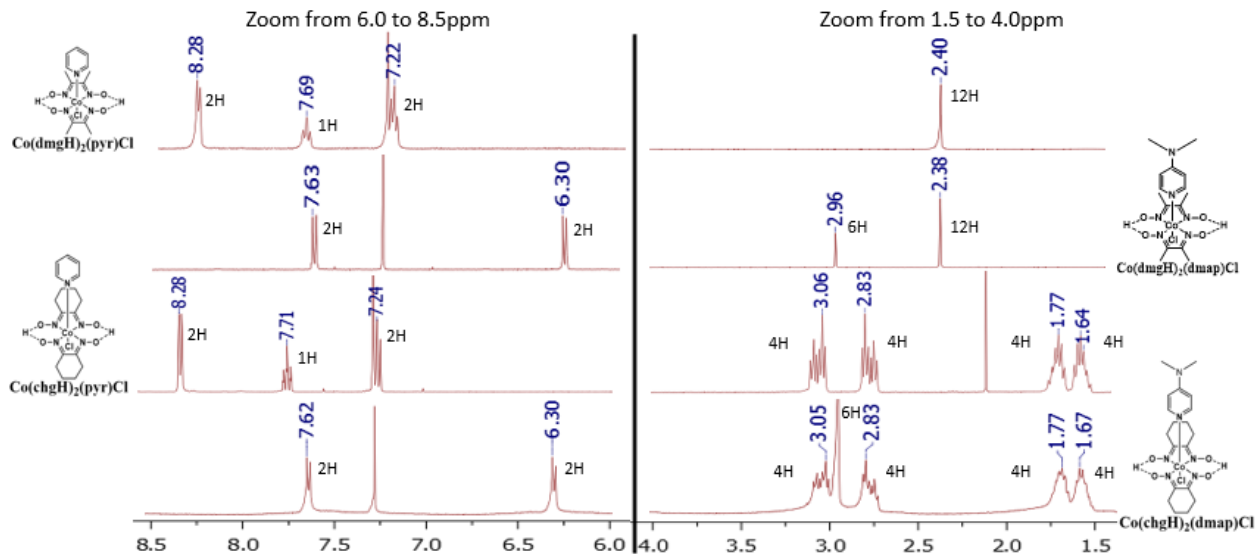


Figure 72. Comparison of the different NMR-¹H spectra of the catalysts realized in deuterated chloroform)

4.3.2 Crystallographic description

The geometric parameters of the coordination sphere in *Co(chgH)₂Cl(DMAP)* are similar to methyl and cyclohexyl derivatives previously reported.^[25c, 28, 34] In the octahedral coordination sphere, the N-oxime plane is described by a length of Co-N bond between 1.88 and 1.92 Å^[25c, 28, 34], in this case, 1.89 Å. The torsion angle between both C-N bonds in each bidentate ligand and the distance out of the plane of Co are in the same range for the cyclohexyl and dimethyl derivatives.^[25c, 28, 34] The electronic body of the inorganic compound is based on strong orbital overlapping of the Co-N bonds in the plane that is the shortest in octahedral coordination sphere. The half-chair conformation of the cyclohexyl ring exhibits 2 λ and 2 β -carbons in the same plane and one of the two δ -carbons is below and the other above or vice-versa depending on offing on the conformer. The pseudo-rotational disorder of the conformers is modelized by 2 β -carbon positions and 4 δ carbon positions on each cyclohexyl (See fig.73, fig.86, fig.87). The X-ray structure informs us about the dynamic exchange between the cyclohexyl conformers compared to

the methyl rotation in dimethyl derivatives. The crystallographic structure of the free ligand 1,2-cyclohexanedionedioxime shows a torsion angle of 26.2° between the two C-N bonds of oximes^[35] while the dimethylglyoxime shows 180° as an anti-configuration^[36]. The constraints of the saturated cycle and the associated rigidity induce fewer variations of torsion between the C-N oxime bonds and an adequate bite angle for coordination chemistry. Those geometric constraints can inhibit decoordination by allowing a better overlapping of orbitals and could enhance the reversibility of the redox states.

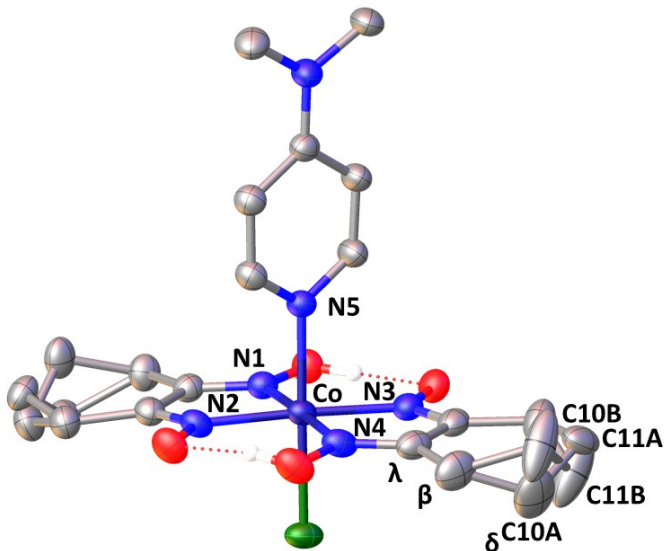


Figure 73. View of the $\text{Co}(\text{chgH})_2\text{Cl}(\text{DMAP})$, atoms are represented at the 50 % probability level.

The 6-membered saturated C-cycle induces a little larger bite angle than for dimethyl derivatives^[37]. In the family of halogeno-cobaloxime pyridine derivatives, the axial bonds Co-N-heterocycle are commonly 0.05 to 0.1 Å longer than the planar Co-N bonds, here 1.9736 (2) Å. For ethyl pyridine-ester in dimethylcobaloximes, the bond is 1.965(3) Å^[34c] and for the electro-donating group o-methoxy pyridine 1.963 (12) Å^[25c]. The normal angle between the N-oxime plane

and the pyridine plane can reach $92.9(4)^\circ$ ^[34a], $82.8(1)^\circ$ ^[34a] or $80.64(2)^\circ$ ^[25c] and $89.09(1)^\circ$ in our mononuclear structure. The supramolecular interaction of the axial ligand implicated in the crystal packing could influence this inclination. The torsion angle between Co-Noxime bonds and C-Npyridine varies between $71.763(1)^\circ$ in our structure, $50.73(1)^\circ$ for $\text{Co}(\text{dmgH})_2\text{DMAP}$ ^[12a], $50.53(10)^\circ$ ^[25c], $53.6(11)^\circ$ for $\text{Co}^{\text{III}}(\text{chgH})_2\text{Cl}_2(4\text{-}4'\text{-bipyridine})$ ^[34a], for another polymorphic structure $57.8(1)^\circ$ $\text{Co}^{\text{III}}(\text{chgH})_2\text{Cl}_2(4\text{-}4'\text{-bipyridine})$ ^[28] (See Fig.85). Over several structures of halogeno-N-heterocycle cobaloximes, we can observe two major kinds of this N-heterocycle orientations around 50° and 70° of torsion angle^[38]. The most labile bonds on the complexes are those of the monodentate axial ligands, chlorine and pyridine. The overlapping orbital of the N-unsaturated cycle with the metal is composed of the σ overlapping between the free electron doublet of the N towards the dz^2 orbital of the Co^{3+} ^[38]. The pyridine shows certain freedom of rotation around the axis and is the most flexible fragment to balance the steric constraints in the crystal packing. The π overlap between the sp^2 empty orbitals of the axial ligand and d_{xz} or d_{yz} Co orbitals mixed with oxime ligand orbitals restrains, however, the orientation of the pyridine. The molecular orbital interaction could be favorable when aromatic π pyridine systems are oriented towards the chelation of oxime ligand. In rare cases, the π system of axial ligand is oriented towards the oxime function^[39] (See Fig.83 and 84). The crystal packing could influence a bit the position. In the trans position, $\text{Co}-\text{Cl}$ is the longest on Co environment around 0.4 \AA more than in the basal plane, 2.23 to 2.245 ^[25c, 28, 34a, 34c], here at $2.2451(6) \text{ \AA}$.

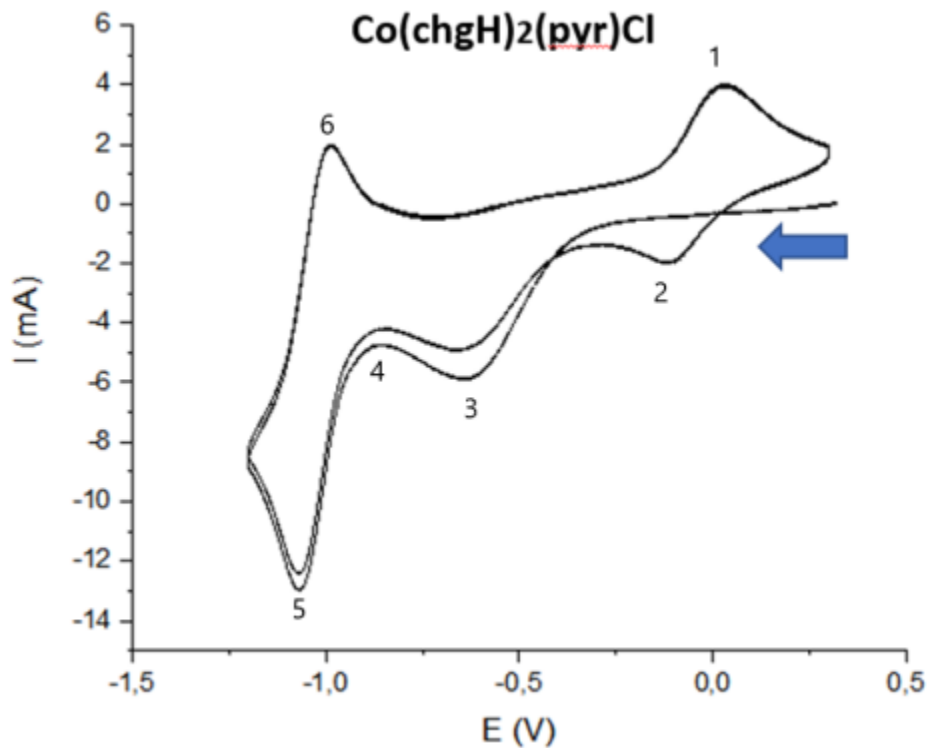
4.4 Electrochemistry

All the cyclic voltammograms of the compounds are collected in dry DMF with 1M of the electrolyte TBAPF_6 (See ESI, Fig 86 to Fig 87.). The cyclic voltammetry responses of all the compounds display similar shapes and the electrochemical potentials of the corresponding redox

events are similar to each other. The reversibility of the electrochemical processes for **1** and **2** are well-known in the literature, as these compounds have been studied in detail.^[12a, 32, 40] [12a] For the first sweep from positive to negative potentials, an irreversible event occurs at -0.66 V (point 3) vs Fc attributed to the monoelectronic reduction Co^{III}Cl/Co^{II}Cl. This peak decreases in intensity for the second scan. We can observe one mono-electronic reversible process around -1.02 V (point 4 and 5) vs Fc, which corresponds to the Co^{II}/Co^I. Then, during the anodic trace, the oxidation of Co^{II} to Co^{III} happens at -0.10 V vs Fc, following by his corresponding cathodic peak at 0.03V during the new forward scan that leads to a quasi-reversible event Co^{III}/Co^{II} couple (see table 9, points 1 and 2). Only one event of oxidation of Co^{II} lets us deduce that the Co(II) coordination sphere releases the chloride, leading to a more stable Co^{II} complex, as reported by Coutsolelos^[25b] and Fontecave^[32]. A molecule of DMF solvent is likely coordinated to the apical position of the octahedral Co^{II} coordination sphere^[41]. The electro-donating character of chloride shifts towards harder reduction of the cathodic peak of Co^{III}Cl/Co^{II}Cl than the one of the redox couple Co^{III}/Co^{II} for the species without chloride anion^[17j]. If the electrochemical solution is agitated, the cathodic event of the Co^{III}/Co^{II} is absent again for the first forward sweep. The pyridine moiety remains coordinated in all redox states as proved by the difference of electrochemical potentials in Co complexes with different N-heterocycle dimethylglyoxime derivatives^[25b] or by spectro-electrochemical measurements^[17t]. Complex **3** shows a slight shift of Co^{III}/Co^{II} potential towards easier reduction compared to the others.

Tableau 9. – Electrochemical potentials (in V vs Fc/Fc⁺ in DMF)^a

Complex	Co ^{III} /Co ^{II}	Co ^{III} Cl/Co ^{II} Cl	Co ^{II} /Co ^I
	(E _{pc} + E _{pa})/2	E _{pc}	(E _{pc} + E _{pa})/2
	Point 1 and 2	Point 3	Point 5 and 6
1	-0.20 (0.18)	-0.76 irr	-1.11 (0.07)
2	-0.19 (0.16)	-0.77 irr	-1.10 (0.07)
3	-0.04 (0.14)	-0.66 irr	-1.02 (0.08)
4	-0.21 (0.18)	-0.84 irr	-1.10 (0.09)

^aAll values in V vs Fc/Fc⁺ potentialFigure 74. Voltammograms of $\text{Co}(\text{chgH})_2(\text{pyr})\text{Cl}$ (V vs Fc⁺/Fc).

4.4.1 Spectro-electrochemistry

All the spectro-electrochemistry data of the compounds are collected in dry DMF with 1M of the electrolyte TBAPF₆ (See ESI, Fig 77 to Fig 81.). Through electroreductive production of hydrogen, Reisner and al. highlight the coordination of the pyridine on the dimethylcobaloxime derivatives by a novel catalytic current in a solution of aqueous phosphate buffer by adding the pyridine in the solution of Co(dmgH₂)(H₂O)₂ vs a sterically hindered 2-6 dimethylpyridine where almost no modification of the catalytic current occurs^[25c]. Holder and al. established absorption spectra of reduced species for Co(dmgBF₂)₂(H₂O)₂ and Co(dmgBF₂)₂(H₂O)(Pyr) and evaluated by spectro-electrochemistry the association constant of the pyridine with the Co^{II} and the Co^I center in various organic solvents.^[17t] The initial compounds at the oxidation state (**III**) are beige-brown for the **1**, same color for **3** but darker and **2** is brown and **4** dark-brown. In the initial spectra of Co^{III}, transitions are mainly ligand centered in the UV range, transfer of charge occurs in the UV-visible, and dd transition in the tailing of absorption spectra^[25d, 42]. The broad transition in the UV-visible suggests multiple orbital mixing between the metal and the ligand. The orbitals implicated in charge transfer transitions are mainly localized on the oxime ligands^[25d]. All compounds show tailing of absorption spectra around 700 nm. While we don't see the usual Co^I shape for the double bands between 550 and 650nm, the shape is still there, but distorted.^[12a, 17n, 43] The reasons for this shape change are still unknown. In the case of DMAP derivatives **2** and **4**, the shoulder at 500 nm is more intense. The application of -0.7 V vs Ag⁺/Ag for a minute lead to the fingerprint spectra of Co^{II}. In the Co^{II} oxidation state, all compounds show a pattern of different shoulders around 430, 570, and 710 nm assigned to charge transfer transitions, which are more intense than for Co^{III}. The spectra tails until 800 nm and a weak very large band characteristic of

Co^{II} low spin around 1200 nm is observable [17^t, 44]. The latter band is absent or not detectable at the concentration of analysis for **1** and **3**, and a maximum is noticed at 1214 nm for **2** and 1220 nm for **4**, although the band is large with 200 nm. The application of -0.5 V vs Ag⁺/Ag for a long period of time (more than 10 min) eventually leads to Co^{II}. This could be due to the lability of monodentate chloride ligand, even in Co^{III}. The application of a current at -1.1 V leads to the increase of the intensity of charge transfer bands in UV-Visible region where the maximum is shifted around 430, 540, and 660 nm and the apparition of an absorption band around 900 nm, that is due to the Co^I form of the complex. The interaction of dimethylaminopyridine with the Co^I increases the intensity of charge transfer bands in the UV-Visible range. For cyclohexyl derivatives **3** and **4**, the maximum of the 900 nm bands is slightly shifted to low energy 919 nm and 921 nm, respectively versus 903 nm for **1** and 893 nm for **2**. The band at 1200 nm is still observable which could be the disproportionation of Co^I and Co^{III} or the same electronic transition that occurs in the Co^{II}. A slight down-shift for the dmap derivatives in the lowest energetic band is noticed 1221 nm for **2** versus 1201 nm for **1**, 1226 nm for **4** versus 1208 nm for the **3**. The interaction of dimethylaminopyridine to Co^I complex have a greater impact on the electronic structure of the compounds than the pyridine. A higher orbital overlapping implicated in π-back donation with low oxidation metallic state^[45] associated with a higher association constant^[29b] with the metal may be an explanation.

4.4.2 Photocatalytic hydrogen evolution

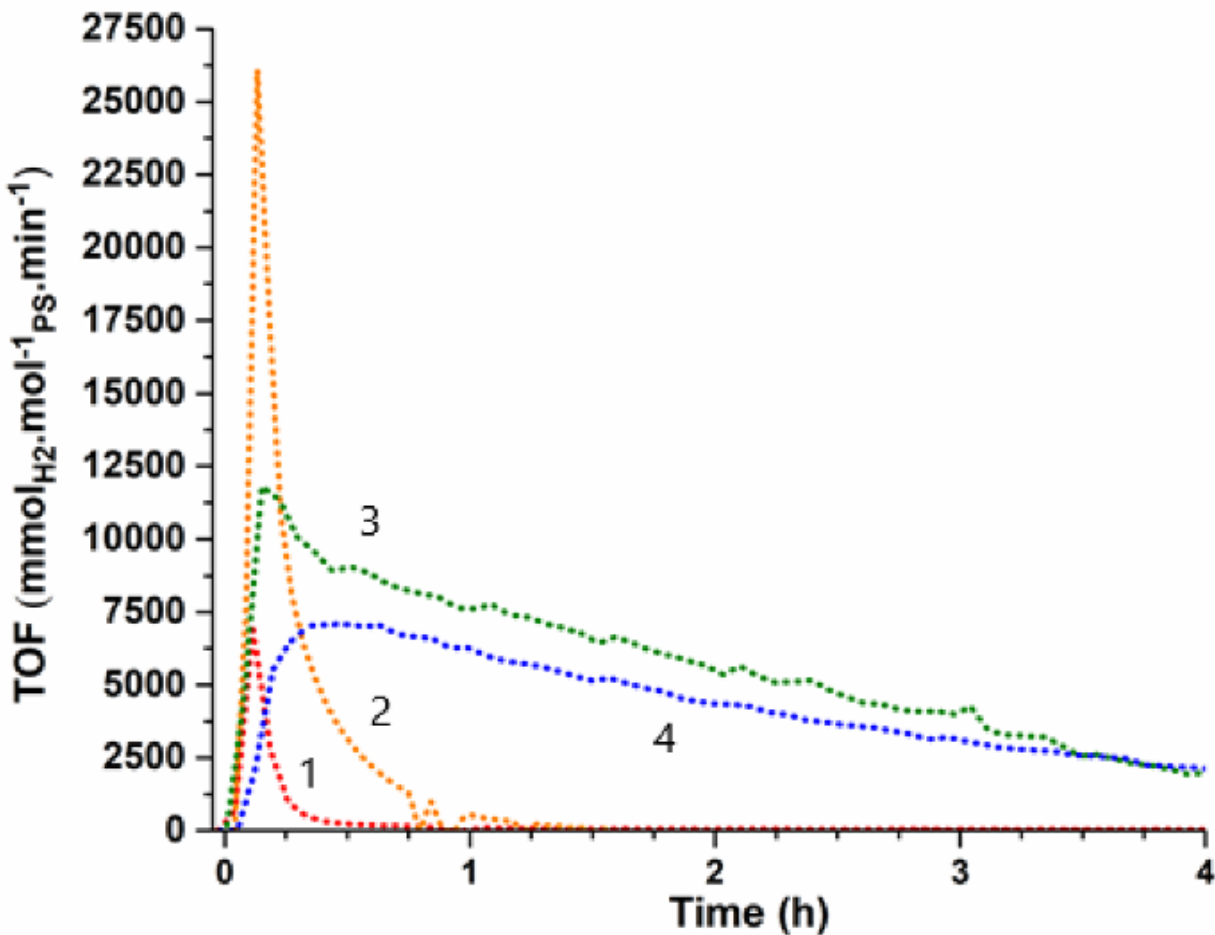


Figure 75. Turn Over Frequency of hydrogen evolution for $\text{Ru}(\text{bpy})_3^{2+}$ in association with cobaloxime catalysts **1** in red, **2** in orange, **3** in green, and **4** in blue.

Photocatalytic experiments are performed with blue Light Emitting Diodes (LEDs) centered at 452 nm irradiation. The LEDs irradiate fully the ¹Metal-to-Ligand-Charge-Transfer of $\text{Ru}(\text{bpy})_3^{2+}$. The solvent of the HER is dimethylformamide, triethanolamine 1 M is the sacrificial electron donor, HBF_4 0.1 M and 0.56 M of water are proton sources. The Co catalysts are analyzed at 0.5 mM in association with the classical photosensitizer $[\text{Ru}(\text{bpy})_3](\text{PF}_6)_2$ at a concentration of 5 µmol. The ratio between both components is 100, which permits the evaluation of the ability to

drive the hydrogen evolving reaction by the cobaloximes in the photocatalytic process and to exploit the maximum turnover of the photosensitizer.

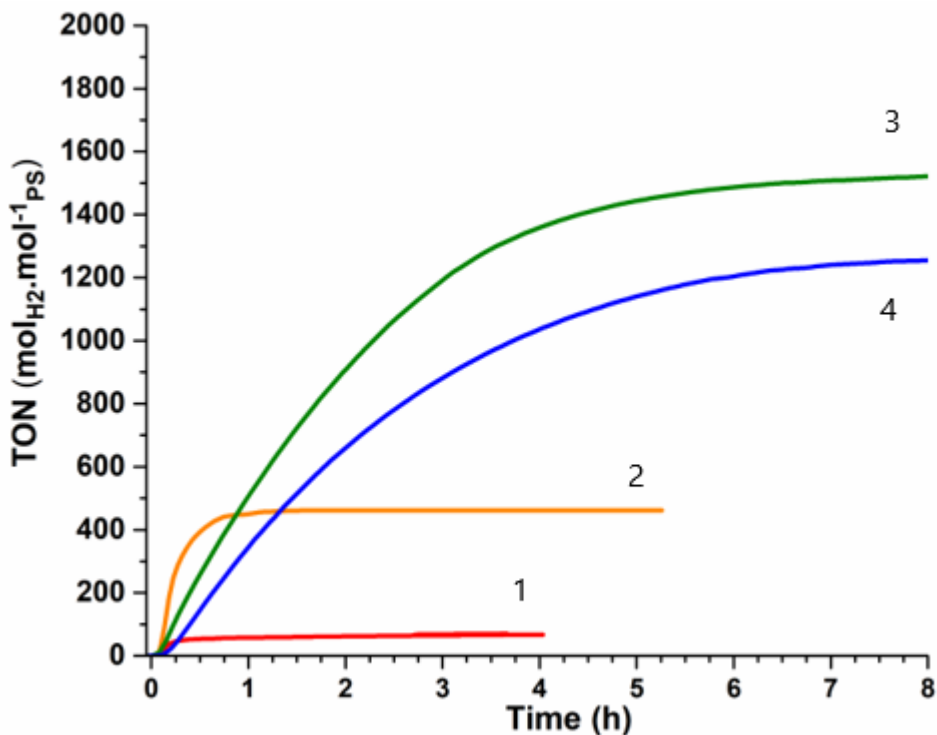


Figure 76. Turn Over Number of hydrogen evolution for $\text{Ru}(\text{bpy})_3^{2+}$ in association with cobaloxime catalysts **1** in red, **2** in orange, **3** in green, and **4** in blue.

The TON and TOF of the photosensitizer are described in the graphics. All four cobaloxime-based systems lack an induction period before the catalytic activity begins. When the light is turning on, all photosystems produce almost instantly a maximum production of hydrogen followed by particular decreasing activities for each system. In the case of methyl derivatives **1** and **2**, a maximum TOF $6900 \text{ mmolH}_2 \cdot \text{mol}^{-1} \text{PS}$ and $26000 \text{ mmolH}_2 \cdot \text{mol}^{-1} \text{PS}$ are attained to decrease quickly towards a TON 60 after 0.7 hours and 460 after 1.5 hours, respectively (Fig 75 and 76). Similar patterns of activity are observed in the case of dimethylcobaloxime derivatives associated with $[\text{Ru}(\text{bpy})_3]^{2+}$ ^[17l, 23a, 23b, 31]. In the case of cyclohexyl-based systems, the first peaks of activities reach

11800 mmolH₂.mol⁻¹_{PS} and 7400 mmolH₂.mol⁻¹_{PS} for **3** and **4**, respectively, to decrease slowly, then attain a final TON of 1500 and 1200, respectively, after 8 hours. For the dimethylaminopyridine cyclohexyl derivative **4**, the photoreaction rate is constant for almost half an hour then decreases faster than the pyridine homolog **3**. Yan and all. highlighted the superiority of hydrogen photocatalysis by a supramolecular binuclear Co(chgH)₂(4-4bipyridine)Cl₂ (TON_{PS}=314) and Co(dmgH)₂(4-4bipyridine)Cl₂ (TON_{PS}=216) compared to the mononuclear homologs Co(dmgH)₂(Pyr)Cl **1** (TON_{PS}=109) and Co(chgH)₂(Pyr)Cl **3** (TON_{PS}=106) [28]. The binuclear cyclohexyl complexes show the best activity. Our results are in concordance with those experiments. Indeed, studies showed that the better the electron transfers occurs from reduced) [Ru(bpy)₃]²⁺ to the catalyst, the less bipyridine dissociates and the less the PS degrades^[46]. Here, the PS at 5 μM is surrounded by 100 equivalents of catalysts at 500 μM. A worse quencher of reduced or excited PS species or an inactive catalyst would increase the decomposition of the PS. The electron transfer ability between the PS and Cat is reflected in the rate and TON of catalytic activity. In similar conditions, at higher concentration of [Ru(bpy)₃]²⁺ of 100 μM, [Ru(bpy)₃]²⁺/Co(dmgH₂)PyrCl couple could attain a TON of 43 vs PS and 9 vs catalyst^[17]. Here, the ratio of concentrations exhibits 0.4 TON for the Co(dmgH)₂PyrCl, then the [Ru(bpy)₃]²⁺ could quickly be deactivated with the Co(dmgH)₂PyrCl as in similar system the TON of **1** could reach 9. Usually, an excess of dimethylglyoxime ligand is used to regenerate the cobaloxime that degrades quickly^[47]. The electronic communication and catalytic activity for system **1** are the lowest of this study. The electron transfers towards **2** and maximum catalytic rate are the fastest of the family due to his maximum activity peak, then a rapid deactivation occurs, possibly induced by the decomposition of both components, but presumably caused by photosensitizer decomposition, because of this lower concentration. As observed in spectro-electrochemical studies, the interaction

of dimethylaminopyridine with the Co^I could be a factor influencing the higher TON. As remarked from electrochemical analysis, energies of HOMO, SOMO, and LUMO orbitals are not the governing factors to differences in H₂ production. In the catalytic cycle, hydride formation and the release of hydrogen are influenced by the oxime planar ligand and axial ligand^[48]. The reduction of the Co^{III}-H could be influenced by the *trans* axial donor group^[25b]. The basicity of Co^{III}-H and the Co^{II}-H should be enhanced in the case of DMAP adducts as it's more electron-donating than Pyr. Several studies highlight the increase of activity rate due to the trans axial donor group^[3a, 25b, 49]. The influence of glyoxime structures on HER performances has been investigated by the comparison of diphenyl vs dimethyl substituents where the diphenyl shows lability on the metal center and poor catalytic activity^[50]. The couple [Ru(bpy)₃]²⁺-cyclohexylcobaloximes are driving an almost constant activity that decreases slowly. The photoredox process of TEOA/[Ru(bpy)₃]²⁺ under this powerful irradiation could generate a higher rate as in the case of **2**, or the PS could decompose via the reduced [Ru(bpy)₃]²⁺ species which is not quickly quenched thereby inducing a decay of hydrogen production. The TOFmax of **3** and **4** systems are lower than **2**. As the activity stays sustainable, the cyclohexyl derivatives are more robust than the dimethyl derivatives. It may lead to a better quenching of the PS excited state, leading to a more active and stable system, as it limit the PS degradation. The photo-redox activity of [Ru(bpy)₃]²⁺ is regulated by the presence of transition states of cyclohexylcobaloximes^[48, 51]. Absorption of irradiation source by the intermediate states of the catalysts and the interaction of electronic configurations between Ru and Co complexes done by energy transfer could influence the longevity of each components in the system. The rate of photodissociation of axial groups are well studied for organocobaloximes^[52] and this fact could play on the catalytic performance. The cyclohexylcobaloxime catalytic activities

in association with $[\text{Ru}(\text{bpy})_3]^{2+}$ and triethanolamine are efficient to drive a sustainable photoreaction in harmony between the photosensitizer and the catalyst.

4.5 Conclusion

This systematic study shows that the bulk of the dioxime substituents can influence drastically the catalytic activity, even with small optoelectronic differences. The X-ray structure exhibits well the directionality through the axial position over the oxime plane that permits one to tune the proprieties of the transition states in the hydrogen evolution of cobaloximes. DMAP boosts the TOF max and TON for dimethyl systems and slows down the rate for cyclohexyl systems, it modifies more the electronic structure of Co^{I} complexes. The NMR analysis and X-ray structure show the difference in molecular dynamics between the facile pseudo rotation of dimethylglyoxime and the rigidification of cyclohexyloximes that could enhance the orbital overlapping between the metal and the N-oxime plane and the stability of the H-bonding macrocycle. The slowly decreasing activity of cyclohexyl systems result in the best TON of the study. Cyclohexylcobaloximes drive in harmony the photoreaction with Ru photosensitizers. Here, we highlight the regulation of catalytic activity by a constructive interaction of the transition species. Correlations between NMR, X-ray, electrochemistry, spectro-electrochemistry, and photocatalytic activity open new perspectives of controlling the photocatalytic proprieties. In the future, the utilization of new photosensitizers in association with cyclohexyl derivatives may help to progress in the fundamental understanding of photoreaction mechanistic regarding photocatalytic hydrogen production.

4.6 Experimental details

4.6.1 Synthesis

All the reagents used for the synthesis were of A.C.S. grade or higher and were used without further purification. The synthesis of **1** and **2** followed the literature procedure.^[32] Synthesis of **3** and **4** were made followed the same procedure, except for the ligand used. First was added respectively the CoCl₂ x 6H₂O (500 mg, 2.15 mmol), the 1,2-cyclohexanedione dioxime (668 mg, 4,70 mmol), and NaOH (86 mg, 2.15 mmol) to the ethanol 95% (20mL), stirred for few minutes between the addition of each reagent, and heated to 45°C. As soon as the temperature is reached, the axial ligand was added (170 mg, 2,15 mmol of pyridine (**3**) or 263 mg, 2.15 mmol of N,N-dimethylaminopyridine (**4**)) and the heat was stopped, but stirring continued. The compound was oxidized by a constant flow of O₂ for about 30 min, giving a brown coloration (oxidation from Co^{II} to Co^{III}). The mixture was stirred for an additional hour before the product filtered. It was washed successively by water (5 mL), ethanol (2 x 5mL), and diethyl ether (3 x 5 mL). The resulting product was extracted with acetone and the product was crystallized by slow solvent evaporation.

Co(dmgH)₂(pyr)Cl (0.130g, 0.322mmol, 49%) ¹H NMR (400MHz, CDCl₃) δ 8,28 (d, J = 5.2Hz, 2H), 7.69 (t, J = 15.1Hz, 1H), 7.23 (t, J = 14.1Hz, 2H) 2.40 (s, 12H) Elemental Analysis: calc for C₁₃H₁₉ClCoN₅O₄ C= 38.68%, H=4.74%, N=17.35% , found C=38.59%, H=4.82%, N=17.12%

Co(dmgH)₂(dmap)Cl (0.179g, 0.401mmol, 21%) ¹H NMR (400MHz, CDCl₃) δ 7.63 (d, J = 7.4Hz, 2H) 6.29 (d, J = 7.6Hz, 2H), 2.97 (s, 6H), 2.39 (s, 12H) Elemental Analysis: calc for C₁₅H₂₄ClCoN₆O₄, C= 40.33 %, H= 5.41%, N= 18.81%, found C=40.42%, H=5.47%, N=18.70%. Yield = 38%, m= 113 mg

Co(chgH)₂(pyr)Cl (0.100g, 0.218mmol, 33%) ¹H NMR (400MHZ, CDCl₃) δ 8.27 (d, J = 7.9Hz, 2H) 7.71 (t, J = 16.6Hz, 1H) 7.23 (t, 14.2Hz, 2H) 3.08 (M, 32.1Hz, 4H) 2.81 (M, 31.9Hz, 4H) 1.79 (M, 35.3Hz, 4H) 1.65 (M, 35.5Hz, 4H) Elemental Analysis: calc for C₁₇H₂₃ClCoN₅O₄, C = 44.80%, H = 5.09%, N = 15.37%, found C = 44.71%, H= 5.16%, N=15.32%

Co(chgH)₂(dmap)Cl (0.084g, 0.175mmol, 26%) ¹H NMR (400MHZ, CDCl₃) δ 7.62 (d, J = 7.5Hz, 2H) 6.30 (d, J = 7.5Hz, 2H) 3.07 (M, 31.7Hz, 4H) 2.98 (S, 6H) 2.81 (M, 31.7Hz, 4H) 1.78 (M, 33.3Hz, 4H) 1.66 (M, 27.7Hz, 4H). ¹³C NMR (400MHZ, CDCl₃) Cyclohexyl (γ)= 21.8 ppm, Cyclohexyl (β) = 26.4 ppm, CMe₂ = 39.6 ppm, Py (β)= 108.5 ppm , Py (α) = 149.4 ppm, Cyclohexyl(α) =153.5 ppm, Py (γ) = 155,0 ppm. Elemental Analysis: calc for C₁₉H₂₈ClCoN₆O₄, C= 45.75%, H= 5.66%, N=16.85%, found C= 45.71%, H = 5.72% N = 16.84%.

4.7 Acknowledgment

We thank the Natural Sciences and Engineering Research Council of Canada for its financial support. We would also like to thank Dr. Daniel Chartrand for the instrumentation. O.S thanks the fonds Québecois de la recherche sur la nature et les technologies for funding.

4.8 Conflict of interests

The authors declare no conflicts of interests

4.9 References

- [1] R. L. House, N. Y. M. Iha, R. L. Coppo, L. Alibabaei, B. D. Sherman, P. Kang, M. K. Brennaman, P. G. Hoertz, T. J. Meyer, *Journal of Photochemistry and Photobiology C: Photochemistry Reviews* **2015**, *25*, 32-45.
- [2] **a)** T. P. Hughes, M. L. Barnes, D. R. Bellwood, J. E. Cinner, G. S. Cumming, J. B. C. Jackson, J. Kleypas, I. A. van de Leemput, J. M. Lough, T. H. Morrison, S. R. Palumbi, E. H. van Nes, M. Scheffer, *Nature* **2017**, *546*, 82; **b)** J. F. Johnstone, C. D. Allen, J. F. Franklin, L. E. Frelich, B. J. Harvey, P. E. Higuera, M. C. Mack, R. K. Meentemeyer, M. R. Metz, G. L. Perry, T. Schoennagel, M. G. Turner, *Front. Ecol. Environ.* **2016**, *14*, 369-378.
- [3] **a)** S. Berardi, S. Drouet, L. Francas, C. Gimbert-Surinach, M. Guttentag, C. Richmond, T. Stoll, A. Llobet, *Chem Soc Rev* **2014**, *43*, 7501-7519; **b)** D. K. Dogutan, D. G. Nocera, *Acc Chem Res* **2019**, *52*, 3143-3148.
- [4] V. Balzani, A. Credi, M. Venturi, *ChemSusChem* **2008**, *1*, 26-58.
- [5] K. E. Dalle, J. Warnan, J. J. Leung, B. Reuillard, I. S. Karmel, E. Reisner, *Coord. Chem. Rev.* **2019**, 2752-2875.
- [6] **a)** N. Armaroli, V. Balzani, *Angew. Chem. Int. Ed.* **2007**, *46*, 52-66; **b)** N. Armaroli, V. Balzani, *ChemSusChem* **2011**, *4*, 21-36.
- [7] D. F. R. S. Ardo, M. A. Modestino, V. Schulze, F. F. A. Greiving, E. Alarcon Llado, V. Artero, K. Ayers, C. Battaglia,, D. B. J.-P. Becker, A. Berger, F. Buda, E. Chinello, B. Dam, V. Di, T. E. Palma, K. Fujii, H. Gardeniers, H. Geerlings, S. M. H., S. H. Hasemi, F. Houle, J. Huskens, B. D. James, K. Konrad,, P. P. K. A. Kudo, D. Lohse, B. Mei, E. L. Miller, G. F. Moore, J., K. L. O. Muller, T. E. Rosser, F. H. Saadi, J.-W. Schüttauf, B., S. W. Seger, W. A. Smith, J. Spurgeon, M. H. Tang, R. van de, P. C. K. V. a. P. W. Krol, *International Energy Agency* **2019**, *11*, 2768-2783.
- [8] A. L. Goff, V. Artero, B. Jousselme, P. D. Tran, N. Guillet, R. Métayé, A. Fihri, S. Palacin, M. Fontecave, *Science* **2009**, *326*, 1384-1387.
- [9] K. Christopher, R. Dimitrios, *Energy & Environmental Science* **2012**, *5*.
- [10] **a)** A. J. Esswein, D. G. Nocera, *Chem. Rev.* **2007**, *107*, 4022-4047; **b)** S. Berardi, S. Drouet, L. Francas, C. Gimbert-Surinach, M. Guttentag, C. Richmond, T. Stoll, A. Llobet, *Chem. Soc. Rev.* **2014**, *43*, 7501-7519.

- [11] **a)** S. Jasimuddin, T. Yamada, K. Fukuju, J. Otsuki, K. Sakai, *Chem Commun (Camb)* **2010**, *46*, 8466-8468; **b)** A. Jacques, O. Schott, K. Robeyns, G. S. Hanan, B. Elias, *European Journal of Inorganic Chemistry* **2016**, *2016*, 1779-1783; **c)** C. Lentz, O. Schott, T. Auvray, G. Hanan, B. Elias, *Inorg Chem* **2017**, *56*, 10875-10881; **d)** P. N. Curtin, L. L. Tinker, C. M. Burgess, E. D. Cline, S. Bernhard, *Inorg Chem* **2009**, *48*, 10498-10506.
- [12] **a)** P. Du, J. Schneider, G. Luo, W. W. Brennessel, R. Eisenberg, *Inorg Chem* **2009**, *48*, 4952-4962; **b)** S. Lin, K. Kitamoto, H. Ozawa, K. Sakai, *Dalton Trans.* **2016**, *45*, 10643-10654.
- [13] **a)** A. Zarkadoulas, E. Koutsouri, C. Kefalidi, C. A. Mitsopoulou, *Coordination Chemistry Reviews* **2015**, *304-305*, 55-72; **b)** H. Y. Wang, G. Si, W. N. Cao, W. G. Wang, Z. J. Li, F. Wang, C. H. Tung, L. Z. Wu, *Chem Commun (Camb)* **2011**, *47*, 8406-8408.
- [14] **a)** P. Dongare, B. D. B. Myron, L. Wang, D. W. Thompson, T. J. Meyer, *Coordination Chemistry Reviews* **2017**, *345*, 86-107; **b)** J. R. Fisher, D. J. Cole-Hamilton, *J. Chem. Soc., Dalton Trans.* **1984**, 809-813; **c)** C. V. Krishnan, B. S. Brunschwig, C. Creutz, N. Sutin, *J. Am. Chem. Soc.* **1985**, *107*, 2005-2015; **d)** C. V. Krishnan, N. Sutin, *J. Am. Chem. Soc.* **1981**, *103*, 2141-2142.
- [15] W. T. Eckenhoff, *Coordination Chemistry Reviews* **2017**.
- [16] **a)** J. Liu, W. Jiang, *Dalton Trans.* **2012**, *41*, 9700-9707; **b)** P. Zhang, M. Wang, Y. Na, X. Li, Y. Jiang, L. Sun, *Dalton Trans.* **2010**, *39*, 1204-1206.
- [17] **a)** V. Artero, M. Chavarot-Kerlidou, M. Fontecave, *Angew. Chem. Int. Ed.* **2011**, *50*, 7238-7266; **b)** C. Baffert, V. Artero, M. Fontecave, *Inorg. Chem.* **2007**, *46*, 1817-1824; **c)** D. Basu, S. Mazumder, X. Shi, H. Baydoun, J. Niklas, O. Poluektov, H. B. Schlegel, C. N. Verani, *Angew. Chem., Int. Ed.* **2015**, *54*, 2105; **d)** J. P. Bigi, T. E. Hanna, W. H. Harman, A. Chang, C. J. Chang, *Chem. Commun.* **2010**, *46*, 958; **e)** G. M. Brown, B. S. Brunschwig, C. Creutz, J. F. Endicott, N. Sutin, *J. Am. Chem. Soc.* **1979**, *101*, 1298-1300; **f)** L. Chen, A. Khadivi, M. Singh, J. W. Jurss, *Inorg. Chem. Front.* **2017**, *4*, 1649; **g)** L. Chen, M. Wang, K. Han, P. Zhang, F. Gloaguen, L. Sun, *Energy Environ. Sci.* **2014**, *7*, 329; **h)** P. Connolly, J. H. Espenson, *Inorg. Chem.* **1986**, *25*, 2684-2688; **i)** J. L. Dempsey, J. R. Winkler, H. B. Gray, *J. Am. Chem. Soc.* **2010**, *132*, 1060-1065; **j)** R. Gueret, C. E. Castillo, M. Rebarz, F. Thomas, M. Sliwa, J. Chauvin, B. Dautreppe, J. Pecaut, J. Fortage, M. N. Collomb, *Inorg. Chem.* **2019**, *58*, 9043-9056; **k)** J. Hawecker, J. M. Lehn, R. Ziessel, *Nouveau J. Chimie* **1983**, *7*, 271-277; **l)** R. W. Hogue, O. Schott, G. S. Hanan, S. Brooker, *Chemistry* **2018**, *24*, 9820-9832; **m)** X. Hu, B. M. Cossairt, B. S. Brunschwig, N. S. Lewis, J. C. Peters, *Chem. Commun.* **2005**, 4723-4725; **n)** X. L. Hu, B. S. Brunschwig, J. C. Peters, *J. Am. Chem. Soc.* **2007**, *129*, 8988-8998; **o)** Z. Huang, Z. Luo, Y. V. Geletii, J. W. Vickers, Q. Yin, D. Wu, Y. Hou, Y. Ding, J. Song, D. G. Musaev, C. L. Hill, T. Lian, *J. Am. Chem. Soc.* **2011**, *133*, 2068-2071; **p)** R. M. Kellett, T. G. Spiro, *Inorg. Chem.* **1985**, *24*, 2373-2377; **q)** R. S. Khnayzer, V. S. Thoi, M. Nippe, A. E. King, J. W. Jurss, K. A. El Roz, J. R. Long, C. J. Chang, F. N. Castellano, *Energy Environ. Sci.* **2014**, *7*, 1477-1488; **r)** A. E. King, Y. Surendranath, N. A. Piro, J. P. Bigi, J. R. Long, C. J. Chang, *Chem. Sci.* **2013**, *4*, 1578; **s)** J. G. Kleingardner, B. Kandemir, K. L. Bren, *J. Am. Chem. Soc.* **2014**, *136*, *4*; **t)** M. A. Lawrence, M. J. Celestine, E. T. Artis, L. S. Joseph, D. L. Esquivel, A. J. Ledbetter, D. M.

- Cropek, W. L. Jarrett, C. A. Bayse, M. I. Brewer, A. A. Holder, *Dalton Trans* **2016**, *45*, 10326-10342; **u)** S. Losse, J. G. Vos, S. Rau, *Coord. Chem. Rev.* **2010**, *254*, 2492-2504; **v)** I. Ozcesmeci, A. Demir, D. Akyuz, A. Koca, A. Gul, *Inorg. Chim. Acta* **2017**, *466*, 591-598; **w)** O. Pantani, S. Naskar, R. Guillot, P. Millet, E. Anxolabehere-Mallart, A. Aukauloo, *Angew. Chem., Int. Ed.* **2008**, *47*, 9948-9950; **x)** Q. X. Peng, L. Z. Tang, S. T. Ren, L. P. Ye, Y. F. Deng, S. Z. Zhan, *Chem Phys Lett* **2016**, *662*, 152-155; **y)** A. Rodenberg, M. Oraziotti, B. Probst, C. Bachmann, R. Alberto, K. K. Baldridge, P. Hamm, *Inorg. Chem.* **2015**, *54*, 646; **z)** S. Schnidrig, C. Bachmann, P. Müller, N. Weder, B. Spingler, E. Joliat-Wick, M. Mosberger, J. Windisch, R. Alberto, B. Probst, *ChemSusChem* **2017**, *10*, 4570; **aa)** W. M. Singh, T. Baine, S. Kudo, S. Tian, X. A. Ma, H. Zhou, N. J. DeYonker, T. C. Pham, J. C. Bollinger, D. L. Baker, B. Yan, C. E. Webster, X. Zhao, *Angew. Chem., Int. Ed.* **2012**, *51*, 5941; **ab)** B. D. Stubbert, J. C. Peters, H. B. Gray, *J. Am. Chem. Soc.* **2011**, *133*, 18070; **ac)** Y. Sun, J. P. Bigi, N. A. Piro, M. L. Tang, J. R. Long, C. J. Chang, *J. Am. Chem. Soc.* **2011**, *133*, 9212.
- [18] **a)** N. A. Eberhardt, H. Guan, *Chem Rev* **2016**, *116*, 8373-8426; **b)** Y. Han, H. Fang, H. Jing, H. Sun, H. Lei, W. Lai, R. Cao, *Angew Chem Int Ed Engl* **2016**, *55*, 5457-5462; **c)** H. N. Kagalwala, E. Gottlieb, G. Li, T. Li, R. Jin, S. Bernhard, *Inorg Chem* **2013**, *52*, 9094-9101; **d)** J.-W. Wang, W.-J. Liu, D.-C. Zhong, T.-B. Lu, *Coordination Chemistry Reviews* **2017**; **e)** S. Wiese, U. J. Kilgore, M.-H. Ho, S. Raugei, D. L. DuBois, R. M. Bullock, M. L. Helm, *ACS Catalysis* **2013**, *3*, 2527-2535; **f)** C. F. Wise, D. Liu, K. J. Mayer, P. M. Crossland, C. L. Hartley, W. R. McNamara, *Dalton Trans* **2015**, *44*, 14265-14271.
- [19] **a)** P. Zhang, M. Wang, C. Li, X. Li, J. Dong, L. Sun, *Chem Commun.* **2010**, *46*, 8806-8808; **b)** H. Lei, H. Fang, Y. Han, W. Lai, X. Fu, R. Cao, *ACS Catal.* **2015**, *5*, 5145-5153; **c)** T. Fang, H.-X. Lu, J.-X. Zhao, S.-Z. Zhan, Q.-Y. Lv, *J. Mol. Catal. A. Chem.* **2015**, *396*, 304-309; **d)** S. Rajak, O. Schott, P. Kaur, T. Maris, G. S. Hanan, A. Duong, *Polyhedron* **2020**, *180*.
- [20] **a)** M.-a. H. a. K. S. Hironobu Ozawa, *J Am Chem Soc* **2006**, *128*, 4926; **b)** H. Ozawa, K. Sakai, *Chemistry Letters* **2007**, *36*, 920-921; **c)** C. V. Suneesh, B. Balan, H. Ozawa, Y. Nakamura, T. Katayama, M. Muramatsu, Y. Nagasawa, H. Miyasaka, K. Sakai, *Phys Chem Chem Phys* **2014**, *16*, 1607-1616.
- [21] **a)** T. Kowacs, L. O'Reilly, Q. Pan, A. Huijser, P. Lang, S. Rau, W. R. Browne, M. T. Pryce, J. G. Vos, *Inorg. Chem.* **2016**, *55*, 2685-2690; **b)** M. G. Pfeffer, B. Schafer, G. Smolentsev, J. Uhlig, E. Nazarenko, J. Guthmuller, C. Kuhnt, M. Wachtler, B. Dietzek, V. Sundstrom, S. Rau, *Angew Chem Int Ed Engl* **2015**, *54*, 5044-5048; **c)** M. G. Pfeffer, C. Pehlken, R. Staehle, D. Sorsche, C. Streb, S. Rau, *Dalton Trans* **2014**, *43*, 13307-13315.
- [22] **a)** T. Stoll, C. E. Castillo, M. Kayanuma, M. Sandroni, C. Daniel, F. Odobel, J. Fortage, M.-N. Collomb, *Coordination Chemistry Reviews* **2015**, *304-305*, 20-37; **b)** H. M. Rogers, S. M. Arachchige, K. J. Brewer, *Chemistry* **2015**, *21*, 16948-16954.
- [23] **a)** E. Rousset, D. Chartrand, I. Ciofini, V. Marvaud, G. S. Hanan, *Chem Commun (Camb)* **2015**, *51*, 9261-9264; **b)** E. Rousset, I. Ciofini, V. Marvaud, G. S. Hanan, *Inorg Chem* **2017**, *56*, 9515-9524; **c)** A. Fihri, V. Artero, M. Razavet, C. Baffert, W. Leibl, M. Fontecave, *Angew. Chem. Int. Ed.* **2008**, *47*, 564-567; **d)** L. Petermann, R. Staehle, M. Pfeifer, C.

- Reichardt, D. Sorsche, M. Wachtler, J. Popp, B. Dietzek, S. Rau, *Chem.Eur.J* **2016**, 22, 8240-8253; **e)** K. L. Mulfort, *C. R. Chim.* **2016**, Ahead of Print; fK. L. Mulfort, L. M. Utschig, *Acc. Chem. Res.* **2016**, 49, 835-843.
- [24] O. S. Wenger, *Coordination Chemistry Reviews* **2009**, 253, 1439-1457.
- [25] **a)** P. Zhang, P. A. Jacques, M. Chavarot-Kerlidou, M. Wang, L. Sun, M. Fontecave, V. Artero, *Inorg Chem* **2012**, 51, 2115-2120; **b)** A. Panagiotopoulos, K. Ladomenou, D. Sun, V. Artero, A. G. Coutsolelos, *Dalton Trans* **2016**, 45, 6732-6738; **c)** D. W. Wakerley, E. Reisner, *Physical Chemistry Chemical Physics* **2014**, 00, 1-3; **d)** A. Bhattacharjee, M. Chavarot-Kerlidou, J. L. Dempsey, H. B. Gray, E. Fujita, J. T. Muckerman, M. Fontecave, V. Artero, G. M. Arantes, M. J. Field, *Chemphyschem* **2014**, 15, 2951-2958; **e)** J. L. Dempsey, B. S. Brunschwig, J. R. Winkler, H. B. Gray, *Acc Chem Res* **2009**, 42, 1995-2004.
- [26] **a)** Z. H. Souvik Roy, Asamanjoy Bhunia, Ashleigh Castner, Arvind K. Gupta, Xiaodong, S. O. Zou, *American chemical society* **2019**; **b)** S. Roy, Z. Huang, A. Bhunia, A. Castner, A. K. Gupta, X. Zou, S. Ott, *J Am Chem Soc* **2019**, 141, 15942-15950.
- [27] X. Su, Y. Chen, L. Ren, Y. He, X. Yin, Y. Liu, W. Yang, *ACS Sustainable Chemistry & Engineering* **2019**, 7, 11166-11174.
- [28] X.-F. Liu, Y.-X. Zhang, J. Yan, *Transition Metal Chemistry* **2015**, 40, 305-311.
- [29] **a)** S. Roy, M. J. Sarma, B. Kashyap, P. Phukan, *Chem Commun (Camb)* **2016**, 52, 1170-1173; **b)** C. Y. Lin, J. C. Fettinger, P. P. Power, *Inorg Chem* **2017**, 56, 9892-9902.
- [30] **a)** P. Meng, M. Wang, Y. Yang, S. Zhang, L. Sun, *Journal of Materials Chemistry A* **2015**, 3, 18852-18859; **b)** C. D. Windle, H. Kumagai, M. Higashi, R. Brisse, S. Bold, B. Jousselme, M. Chavarot-Kerlidou, K. Maeda, R. Abe, O. Ishitani, V. Artero, *J Am Chem Soc* **2019**, 141, 9593-9602; **c)** S. Lyu, J. Massin, M. Pavone, A. B. Muñoz-García, C. Labrugère, T. Toupane, M. Chavarot-Kerlidou, V. Artero, C. Olivier, *ACS Applied Energy Materials* **2019**, 2, 4971-4980; **d)** Z. Ji, M. He, Z. Huang, U. Ozkan, Y. Wu, *J Am Chem Soc* **2013**, 135, 11696-11699.
- [31] O. Schott, A. K. Pal, D. Chartrand, G. S. Hanan, *Chemsuschem* **2017**, 10, 4436-4441.
- [32] M. Razavet, V. Artero, M. Fontecave, *Inorganic Chemistry* **2005**, 44, 4786-4795.
- [33] Y. Santiago-Rodríguez, M. C. Curet-Arana, *Reaction Kinetics, Mechanisms and Catalysis* **2015**, 116, 351-370.
- [34] **a)** E. Coropceanu, A. Rija, V. Lozan, I. Bulzac, G. Duca, V. C. Kravtsov, P. Bourosh, *Crystal Growth & Design* **2016**, 16, 814-820; **b)** K. Kumar, B. D. Gupta, *Journal of Organometallic Chemistry* **2011**, 696, 2280-2286; **c)** N. Wang, X. Sun, D. Wan, J. Chen, B. Li, *Acta Crystallogr Sect E Struct Rep Online* **2012**, 68, m204-205.
- [35] N. R. B. s. Sreltsova, V. K., *Act Cryst.* **1993**, C49, 4.
- [36] **a)** L. L. L. Merrit, Jr and Elma, *Act Cryst.* **1952**, 5, 6; **b)** W. Hamilton, *Acta Cryst.* **1961**.

- [37] B. D. Gupta, K. Qanungo, T. Barclay, W. Cordes, *Journal of Organometallic Chemistry* **1998**, *560*, 6.
- [38] C. Lopez, S. Alvarez, X. Solans, M. Font-Altaba, *Inorganic Chemistry* **1986**, *25*, 2962-2969.
- [39] A. Z. Bigotto, Ennio ; Randaccio,Lucio., *Journal of Chemical Society, Dalton Transactions* **1976**, *8*.
- [40] S. Pizarro, M. Araya, A. Delgadillo, *Polyhedron* **2018**, *141*, 94-99.
- [41] J. Chen, P. H. L. Sit, *Catal. Today* **2018**, *314*, 179-186.
- [42] **a)** K. Ikeda, W. Liu, Y. R. Shen, H. Uekusa, Y. Ohashi, S. Y. Koshihara, *J Chem Phys* **2005**, *122*, 141103; **b)** G. N. Schrauzer, L. P. Lee, J. W. Sibertl, *J. Am. Chem. Soc.* **1969**, *92*, 8.
- [43] G. Smolentsev, B. Cecconi, A. Guda, M. Chavarot-Kerlidou, J. A. van Bokhoven, M. Nachtegaal, V. Artero, *Chemistry* **2015**, *21*, 15158-15162.
- [44] D. M. Cropek, A. Metz, A. M. Muller, H. B. Gray, T. Horne, D. C. Horton, O. Poluektov, D. M. Tiede, R. T. Weber, W. L. Jarrett, J. D. Phillips, A. A. Holder, *Dalton Trans* **2012**, *41*, 13060-13073.
- [45] S. Shi, L. M. Daniels, J. H. Espenson, *Inorg Chem* **1991**, *30*, 3.
- [46] E. Deponti, M. Natali, *Dalton Trans* **2016**, *45*, 9136-9147.
- [47] B. Probst, M. Guttentag, A. Rodenberg, P. Hamm, R. Alberto, *Inorg Chem* **2011**, *50*, 3404-3412.
- [48] C. Tsay, B. N. Livesay, S. Ruelas, J. Y. Yang, *J Am Chem Soc* **2015**, *137*, 14114-14121.
- [49] **a)** D. W. W. a. E. Reisner*, **2014**; **b)** N. Queyriaux, R. T. Jane, J. Massin, V. Artero, M. Chavarot-Kerlidou, *Coord Chem Rev* **2015**, *304-305*, 3-19.
- [50] W. T. Eckenhoff, *Coordination Chemistry Reviews* **2018**, *373*, 295-316.
- [51] **a)** K. Kuhar, L. A. Fredin, P. Persson, *J Phys Chem B* **2015**, *119*, 7378-7392; **b)** L. A. Fredin, P. Persson, *J Chem Phys* **2016**, *145*, 104310; **c)** A. O. Dohn, K. S. Kjaer, T. B. Harlang, S. E. Canton, M. M. Nielsen, K. B. Moller, *Inorg Chem* **2016**, *55*, 10637-10644; **d)** E. S. Wiedner, M. B. Chambers, C. L. Pitman, R. M. Bullock, A. J. Miller, A. M. Appel, *Chem Rev* **2016**, *116*, 8655-8692.
- [52] G. N. Schrauzer, L. P. Lee, J. W. Sibert, *Journal of the American Chemical Society* **1970**, *92*, 8.

4.10 Supporting information

Olivier Schott*, Vincent Picard*, Daniel Chartrand, Garry S. Hanan

Département de Chimie, Université de Montréal, 2900 Boulevard Edouard-Montpetit, Montréal, Québec H3T 1J4
(Canada)

*Co first author

Table of Contents

Electrochemistry	193
Cyclic voltammetry	194
<i>Figure 77: Reduction voltammograms of Co(dmgH)₂(Pyr)Cl</i>	194
<i>Figure 78: Reduction voltammograms of Co(dmgH)₂(DMAP)Cl</i>	194
<i>Figure 79: Reduction voltammogram of Co(chgH)₂(Pyr)Cl</i>	195
<i>Figure 80: Reduction voltammogram of Co(chgH)₂(DMAP)Cl</i>	195
<i>Figure 81: Reduction voltammogram of Co(chgH)₂Cl₂</i>	196
Spectro-electrochemistry	
<i>Figure 82: Spectro-electrochemistry spectra of the Co(dmgH)₂(Pyr)Cl</i>	197
<i>Figure 83: Spectro-electrochemistry spectra of the Co(dmgH)₂(DMAP)Cl</i>	197
<i>Figure 84: Spectro-electrochemistry spectra of the Co(chgH)₂(Pyr)Cl</i>	198
<i>Figure 85: Spectro-electrochemistry spectra of the Co(chgH)₂(DMAP)Cl</i>	198
Table 10. Report of interest points of spectro-Echem analysis on complex 1 to 4	199
Crystallographic study	
Table 11. Crystallographic information's for Co(chgH) ₂ (dmap)Cl.	200
<i>Figure 86 : View of the Co(chgH)₂(DMAP)Cl with hydrogen atoms, atoms are represented at the 50 % probability level. The disorder of position for cyclohexyl conformers is illustrated by two conformers that are modelized with different occupancies.</i>	201

<i>Figure 87: View of the Co(chgH)₂(DMAP)Cl with hydrogen atoms, atoms are represented at the 50 % probability level. The disorder of position for cyclohexyl conformers is illustrated by two conformers that are modeled with different occupancies.</i>	202
Table 12. Selected angles and bond lengths of crystal structures Co(III)(ChgH)₂CIDMAP , the dimer Co(III)(ChgH)₂Cl₂(4-4bipyridine) and an other structure of the dimer Co(III)(ChgH)₂Cl₂(4-4bipyridine)	204
<i>Figure 88. Orientation of N-Heterocycle on cobaloxime derivatives. View of the Co(chgH)₂(DMAP)Cl with an indication of the torsion angle between Co-NOxime and C-N of DMAP. Plan 1 describes the common orientation of 6 membered N-heterocycle on the cobaloxime crystal structure^[9]. Plan 2 is rare.....</i>	205
Preparation of photoreactions and set up of gas chromatography	206
Table 13. Maxima, width band of emission spectra, and photon flux of used L.E.D.'s.	207
NMR studies.....	207
<i>Figure 89: NMR-H¹ of the Co(dmgH)₂(pyr)Cl</i>	208
<i>Figure 90: NMR-H¹ of the Co(dmgH)₂(dmap)Cl</i>	209
<i>Figure 91: NMR-H¹ of the Co(chgH)₂(pyr)Cl.....</i>	210
<i>Figure 92: NMR-H¹ of the Co(chgH)₂(dmap)Cl</i>	211
<i>Figure 93: 2D ¹HNMR Noesy of Co(chgH)2PyrCl CDCl₃ 400 MHZ. The resolution of the scalar coupling has been decreased to notice the most intense coupling between the protons on the β-carbon positions and δ-carbon of the cyclohexyl moiety.</i>	
References	212

4.10.1 Electrochemistry

Electrochemical measurements were performed in pure dimethylformamide purged with argon at room temperature with an SP-50 Biologic potentiostat. The cell has been placed in the oven at 140°C at least 30 minutes before the experiment and is blanketed in a nitrogen atmosphere immediately thereafter. The electrolyte (5 mL of Et₄NPF₆, 0.1 M as supporting electrolyte) is inserted with a syringe on the nitrogen septum and the solution is purged for at least 10 min before any measurement. A glassy carbon electrode was used as a working electrode, the counter electrode

was a Pt wire and the silver wire was the pseudo-reference electrode. The concentrations of complexes were analyzed at 1 mM. The reference of electrochemical potential was set using 1 mM ferrocene as an internal standard and the values of potentials are reported vs. SCE^[1]. The nitrogen atmosphere is kept above the solution during the measurement. Cyclic voltammograms were obtained at a scan rate of 100 mV s⁻¹ and a current amplitude of 100 mA.

4.10.2 Cyclic voltammetry

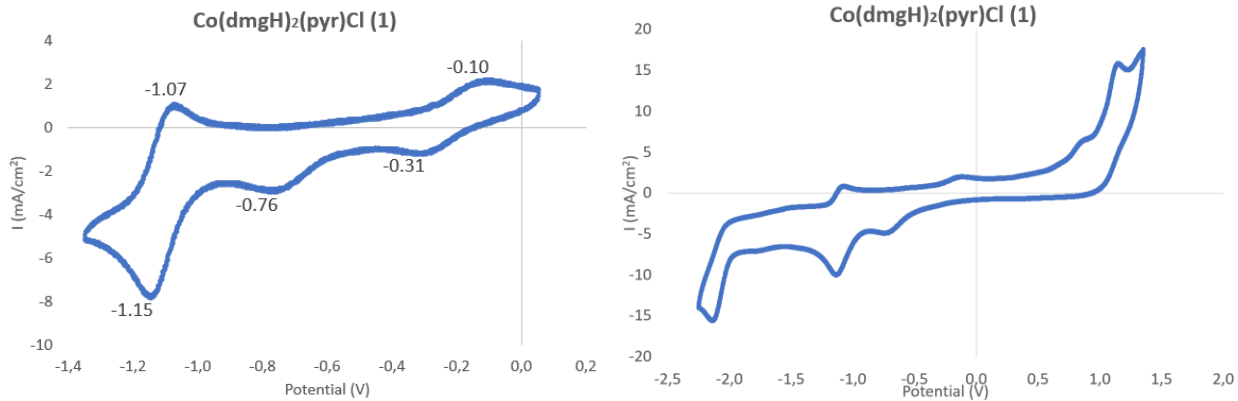


Figure 77. Reduction voltammograms of $\text{Co}(\text{dmgH})_2(\text{pyr})\text{Cl}$ in DMF with triethylammonium PF_6^- as supporting electrolyte

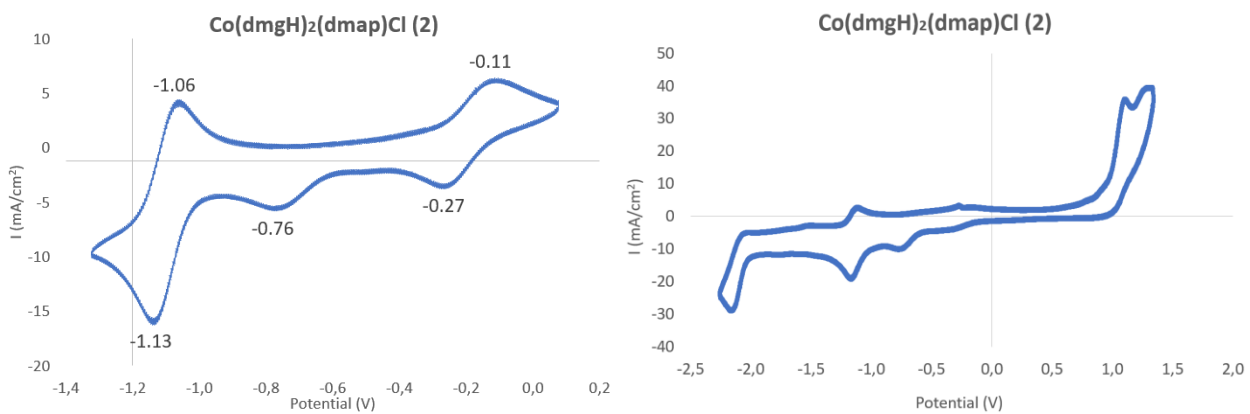


Figure 78. Reduction voltammograms of $\text{Co}(\text{dmgH})_2(\text{DMAP})\text{Cl}$ in DMF with triethylammonium PF_6^- as supporting electrolyte

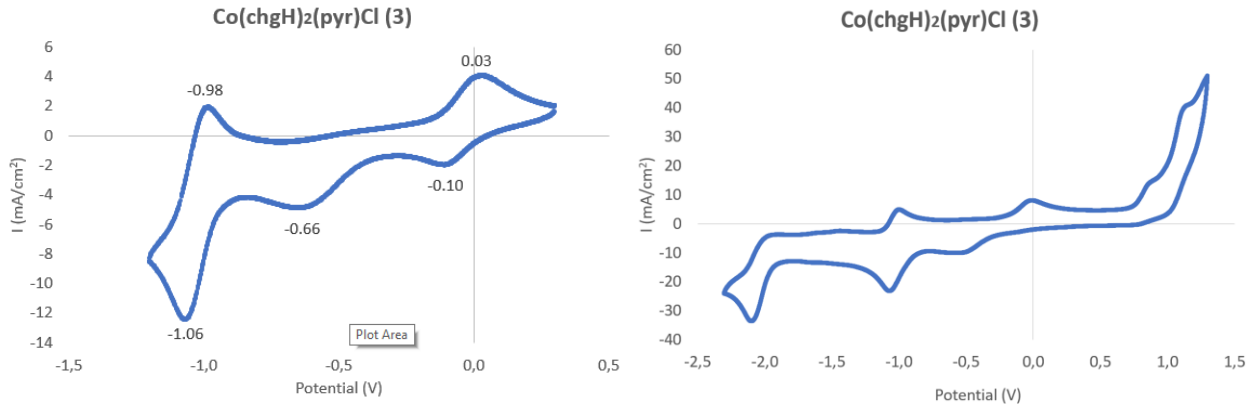


Figure 79. Reduction voltammograms of $\text{Co}(\text{chgH})_2(\text{pyr})\text{Cl}$ in DMF with triethylammonium PF_6^- as supporting electrolyte

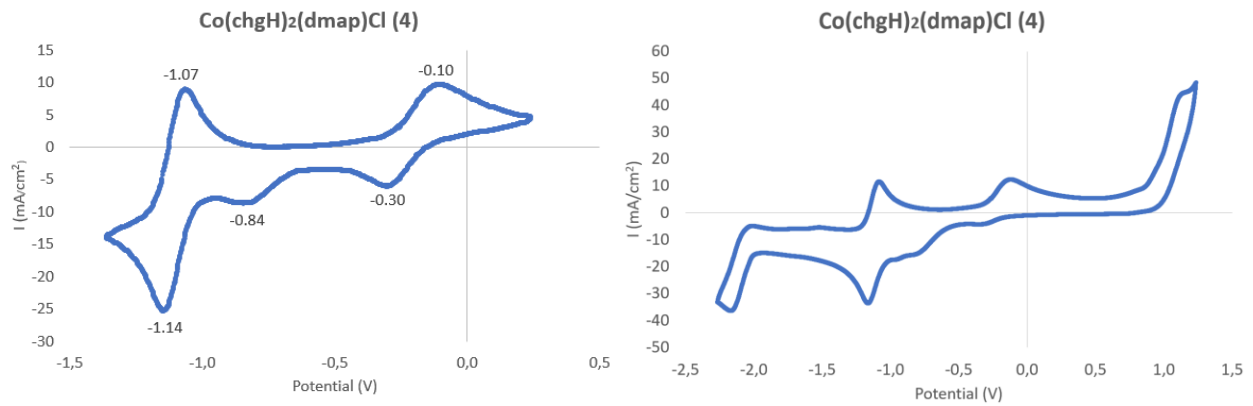


Figure 80. Reduction voltammograms of $\text{Co}(\text{chgH})_2(\text{DMAP})\text{Cl}$ in DMF with triethylammonium PF_6^- as supporting electrolyte

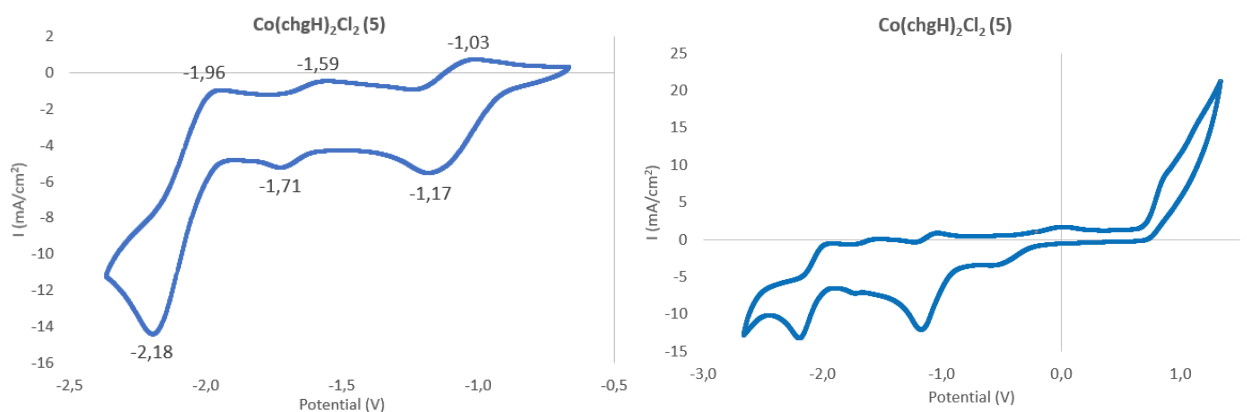


Figure 81. Reduction voltammograms of $\text{Co}(\text{chgH})_2\text{Cl}_2$ (5) in DMF with triethylammonium PF_6^- as supporting electrolyte

4.10.3 Spectro-electrochemistry

The Quartz cell is conditioned two times with the solution before the analysis. A blank sample was run with the solvent and electrolyte before the analysis and was subtracted from the results. Then we run the sample of catalysis at 3mM (around 2 mg of catalyst in 1.5 mL of solvent, with 0.1 M of tetrabutylammonium PF_6^-). Potentials of 0 V (Co^{III}), -0.7 V (Co^{II}), and -1.1 V (Co^{I}) are applied 5 min before the analysis and are kept active during all data collection. A Cary 600i UV-vis-NIR spectrometer was used for the measurements.

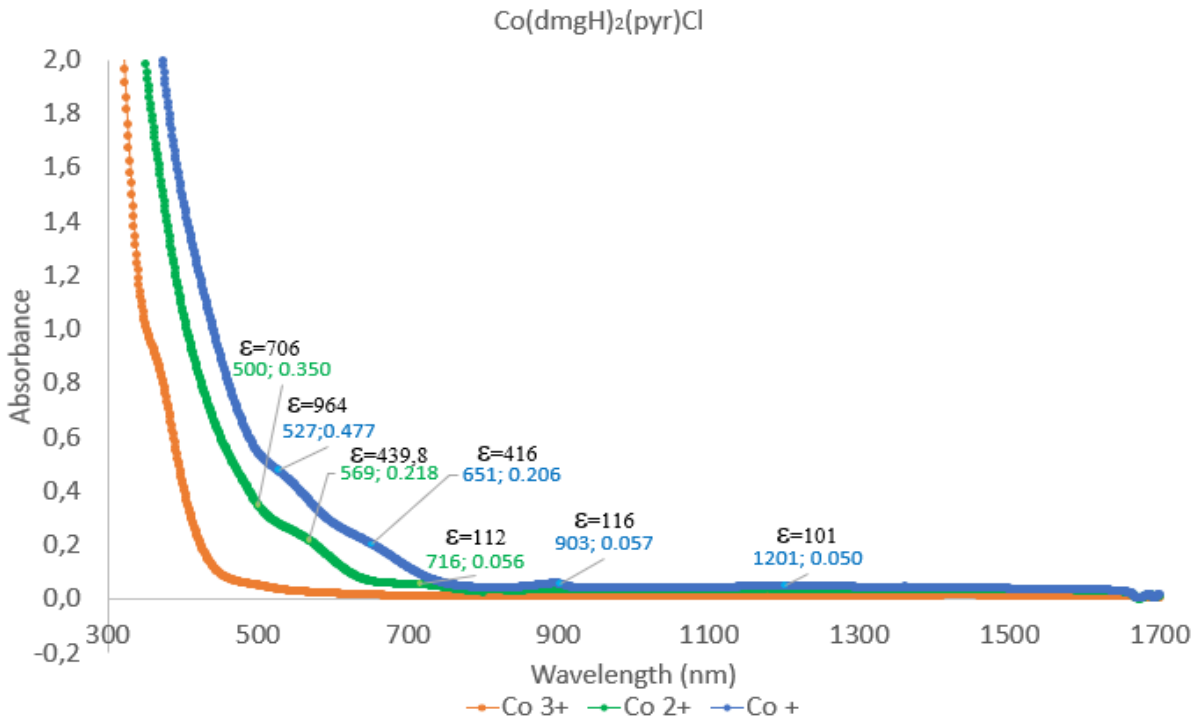


Figure 82. Spectro-electrochemistry spectra of the $\text{Co}(\text{dmgH})_2(\text{Pyr})\text{Cl}$

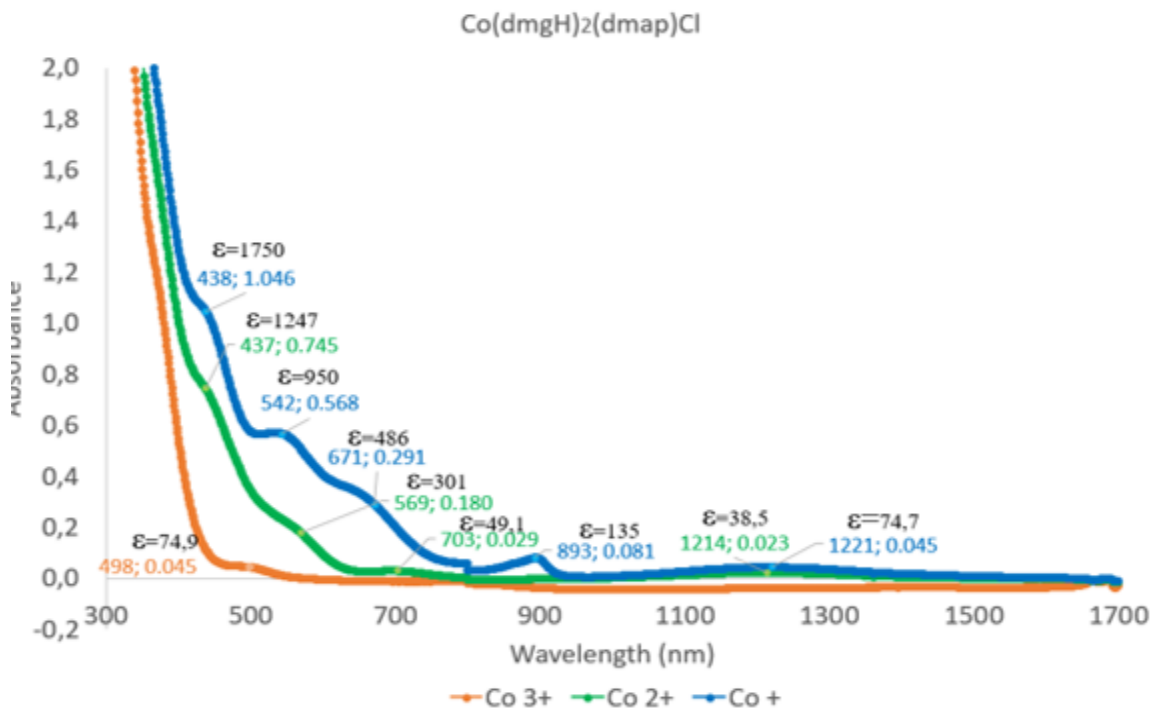


Figure 83. Spectro-electrochemistry spectra of the $\text{Co}(\text{dmgH})_2(\text{DMAP})\text{Cl}$

Chapitre 4: Efficient Ru/Co molecular photocatalytic system driven by cyclohexyl-based cobaloximes as HER catalysts

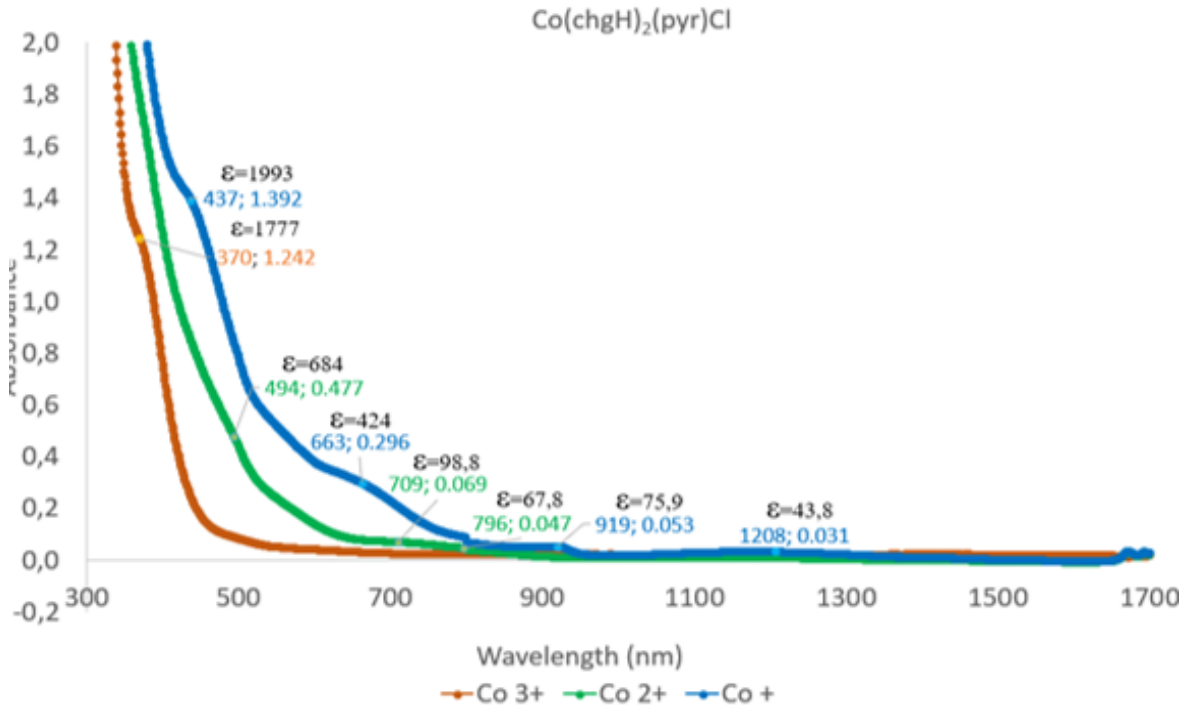


Figure 84. Spectro-electrochemistry spectra of the $\text{Co}(\text{chgH})_2(\text{Pyr})\text{Cl}$

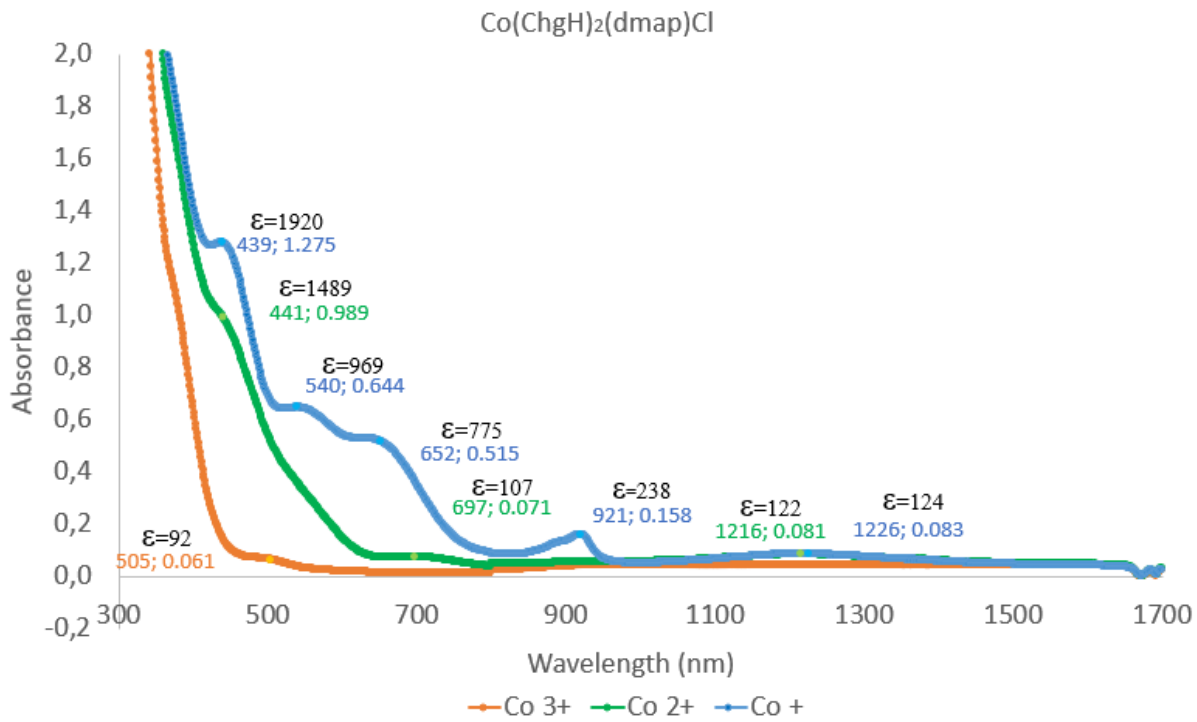


Figure 85. Spectro-electrochemistry spectra of the $\text{Co}(\text{chgH})_2(\text{DMAP})\text{Cl}$

Tableau 10. – Report of interest points of spectro-Echem analysis on complex 1 to 4

[1] Co(dmgH) ₂ (pyr)Cl			[2] Co(dmgH) ₂ (dmap)Cl			[3] Co(chgH) ₂ (pyr)Cl			[4] Ch(chgH) ₂ (dmap)Cl		
Major Co form : Co ⁺											
λ	A	ε	λ	A	ε	λ	A	ε	λ	A	ε
1201	0.050	101	1221	0.045	77	1208	0.031	44	1226	0.083	125
903	0.057	116	893	0.081	140	919	0.053	76	921	0.158	238
651	0.206	416	671	0.291	503	663	0.296	425	652	0.515	775
527	0.478	964	542	0.568	983	437	1.392	1997	540	0.644	969
			438	1.046	1812				439	1.275	1920
Major Co form : Co ²⁺											
λ	A	ε	λ	A	ε	λ	A	ε	λ	A	ε
716	0.056	112	1214	0.023	40	796	0.047	68	1220	0.080	121
569	0.218	440	703	0.029	51	709	0.069	99	703	0.071	107
500	0.350	706	569	0.180	311	494	0.477	685	441	0.989	1489
			437	0.745	1291						
Major Co form : Co ³⁺											
λ	A	ε	λ	A	ε	λ	A	ε	λ	A	ε
			498	0.045	78	370	1.242	1780	505	0.061	92

4.10.4 Crystallographic study

Crystallographic data for **Co(chgH)₂(dmap)Cl** were collected at 100 K using a Bruker Venture MetalJet diffractometer equipped with a Photon 100 CMOS area detector. For data collection, determination of cell parameters, cell refinement, and data reduction *APEX3* and *SAINT* (Bruker, 2007) were used. Absorption and corrections were applied using SADABS and TWINABS (Bruker 2001)^[2]. Structure solutions were performed using intrinsic phasing with SHELXT (Sheldrick, (2008 and 2015)^[3] and refined on F^2 by full-matrix least-squares using *SHELXL2014* (Sheldrick, 2008 and 2015)^[3]. *OLEX2* (Dolomanov *et al.*, 2009)^[4]. The material was prepared for publication using *PLATON* (Spek, 2009)^[5], and Mercury^[6].

Tableau 11. – Crystallographic information's for Co(chgH)₂(dmap)Cl, (**4**)

Identification	Co(chgH) ₂ DMAPCl
CCDC Number	1515336
Empirical formula	C ₁₉ H _{28,2} ClCoN ₆ O _{4,1}
Formula weight	500,65
Temperature/K	100.0
Crystal system	Tetragonal
Space group	P-42 ₁ c
a/Å	22.9073 (8)
b/Å	22.9073 (8)
c/Å	8.5149 (3)
α/°	90
β/°	90
γ/°	90
Volume/Å ³	4468.1(3)
Z	8
ρ _{calc} g/cm ³	1.489
μ/mm ⁻¹	5.085
F(000)	2088.0
Crystal size/mm ³	0.5 × 0.03 × 0.02
Radiation	GaKα (λ = 1.34139)
2Θ range for data collection/°	4.746 to 143.092
Index ranges	-30 ≤ h ≤ 20, -29 ≤ k ≤ 30, -11 ≤ l ≤ 11
Reflections collected	56922
Independent reflections	5839 [R _{int} = 0.0538, R _{sigma} = 0.0323]
Data/restraints/parameters	5839/128/347
Goodness-of-fit on F ²	1.069
Final R indexes [I>=2σ (I)]	R ₁ = 0.0294, wR ₂ = 0.0752
Final R indexes [all data]	R ₁ = 0.0322, wR ₂ = 0.0766
Largest diff. peak/hole / e Å ⁻³	0.43/-0.17
Flack parameter	0.034(5)

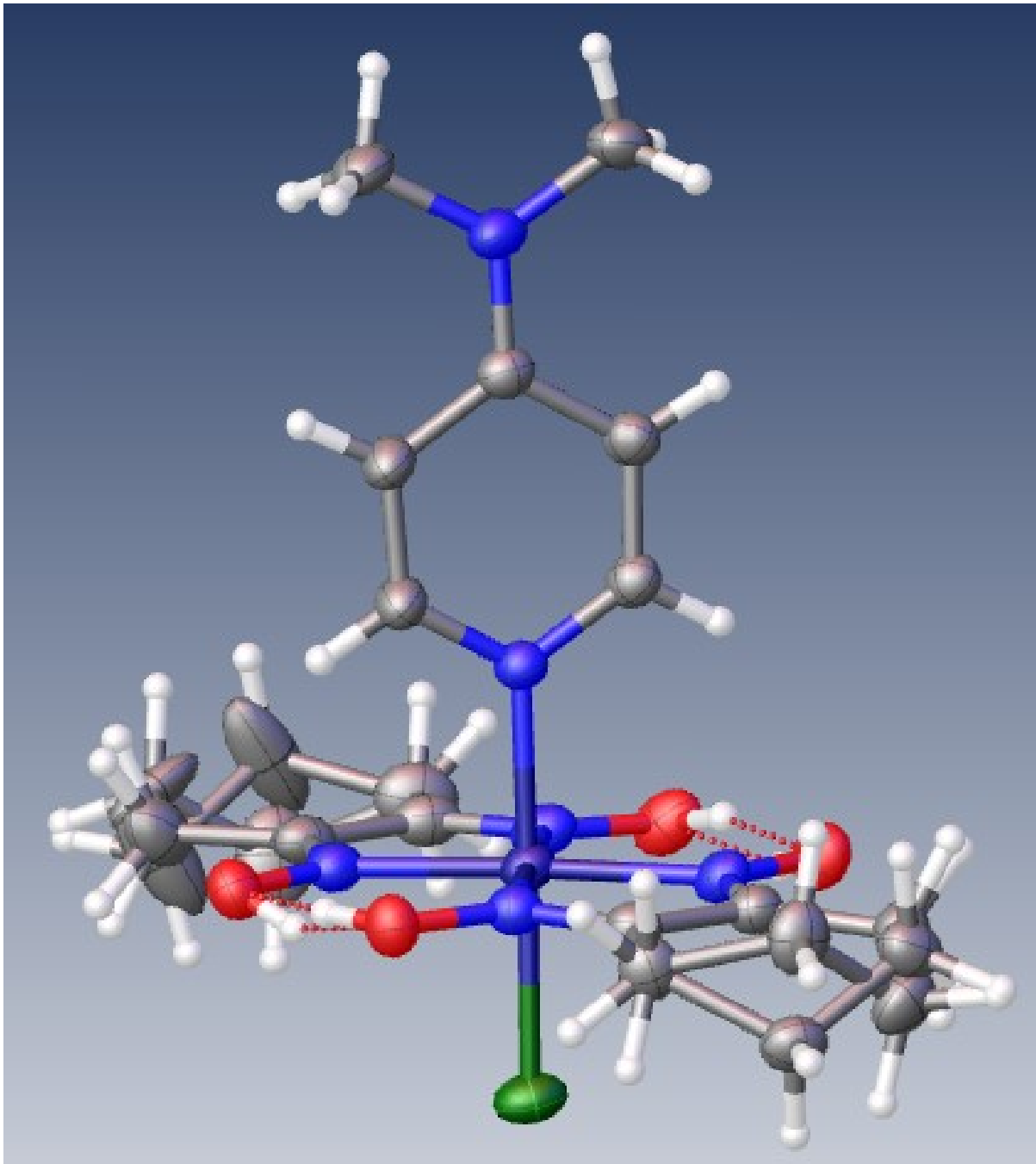


Figure 86. View of the $\text{Co}(\text{chgH})_2(\text{DMAP})\text{Cl}$ with hydrogen atoms, atoms are represented at the 50 % probability level. The disorder of position for cyclohexyl conformers is illustrated by two conformers that are modelized with different occupancies.

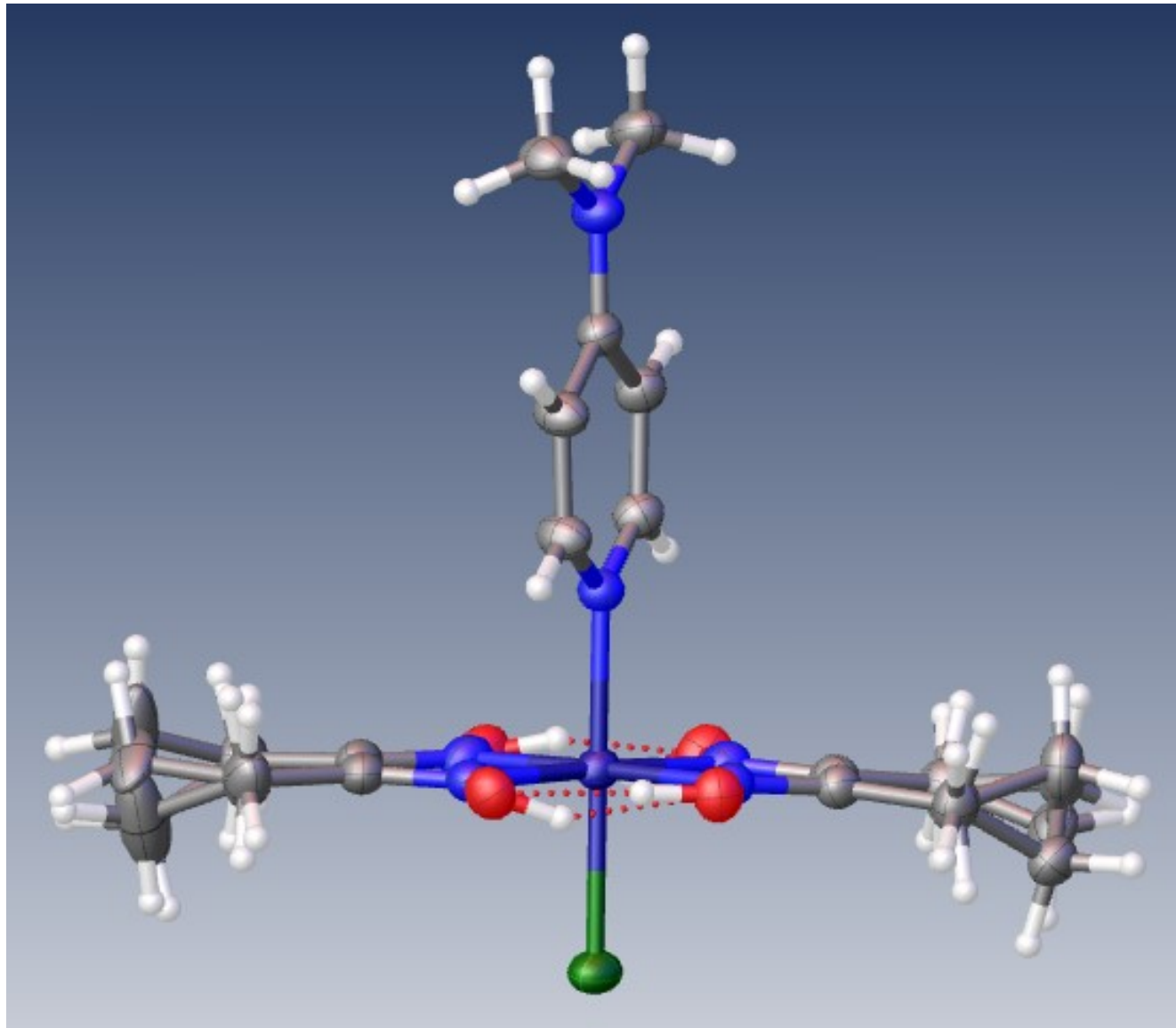


Figure 87. View of the $\text{Co}(\text{chgH})_2(\text{DMAP})\text{Cl}$ with hydrogen atoms, atoms are represented at the 50 % probability level. The disorder of position for cyclohexyl conformers is illustrated by two conformers that are modelized with different occupancies.

Brown well-shaped needles of **Co(chgH)₂(DMAP)Cl** are growing by slow evaporation of the acetone solution of the complex. Absence of twinning was verified by Platon TwinRotMat. The flack parameter 0,034(5) did not affect the merging of the model and components of the reciprocal domain. Restraints were used to model pseudo-rotational disorders of cyclohexyl conformers. Model of pseudo-rotational disorders required similar directions and amplitudes of thermal parameters for the same atoms. SADI command is used to uniform the C-C bond. For the case of the 2 cyclohexyl δ-carbons, 4 positions of carbons or two conformers for each cyclohexyl are described by ratios of free refinement of occupancies 18/82 and 30/70 respectively for each cyclohexyl. (See fig 86 et 87.). Considering the H-bonded pseudo-macrocycle, one proton of two oximes close to each other and one proton of the couple of oxime in the other side of the Co described a part to balance the probability of the presence of protons. The free refinement gave a ratio of 34/66 between the two parts. The free refinement of the occupancy of a water molecule reached 0.1054 and was rounded and finally constrained to 0.1 for the final refinement. The R1 factor reached the value of 2.94 %.

Tableau 12. – Selected angles and bond lengths of crystal structures $\text{Co(III)(ChgH}_2\text{ClDMAP}$, the dimer $\text{Co(III)(ChgH}_2\text{Cl}_2\text{(4-4bipyridine)}$ and an other structure of the dimer $\text{Co(III)(ChgH}_2\text{Cl}_2\text{(4-4bipyridine)}$.

Bond lengths in Å	$\text{Co}^{\text{III}}(\text{chgH})_2$	$\text{Co}^{\text{III}}(\text{chgH})_2\text{Cl}_2$	$\text{Co}^{\text{III}}(\text{chgH})_2\text{Cl}_2$
	(dmap)Cl	(4-4bipyridine)^[7]	(4-4bipyridine)^[8]
Co(1)–Cl	2.245 (6)	2.239 (1)	2.245 (4)
Co(1)–N1 (oxime)	1.894 (2)	1.896 (5)	1.920 (1)
Co(1)–N2 (oxime)	1.891 (2)	1.885 (5)	1.879 (1)
Co(1)–N3 (oxime)	1.894 (3)	1.925 (4)	1.878 (1)
Co(1)–N4 (oxime)	1.892 (2)	1.905 (5)	1.920 (1)
Co(1)–N5 (Pyridine derivative)	1.974 (2)	1.971 (4)	1.914 (9)

Angles (°)	$\text{Co}^{\text{III}}(\text{chgH})_2$	$\text{Co}^{\text{III}}(\text{chgH})_2\text{Cl}_2$	$\text{Co}^{\text{III}}(\text{chgH})_2\text{Cl}_2$
	(DMAP)Cl	(4-4bipyridine)¹	(4-4bipyridine)²
N1-Co(1)-N2	81.92 (8)	82.7 (2)	81.4 (7)
N3-Co(1)-N4	82.19 (1)	80.63(7)	80.4 (5)
N1-Co(1)-N3	98.62 (9)	98.0 (2)	98.6 (6)
N2-Co(1)-N4	97.19 (9)	98.6 (2)	99.5 (7)
N5-Co(1)-N4	91.35 (8)	88.42 (2)	91.6 (4)
N5-Co(1)-N3	90.63 (8)	89.55 (2)	91.2 (4)
N5-Co(1)-N2	92.09 (8)	91.97 (2)	89.8 (4)
N5-Co(1)-N1	90.37 (8)	92.34 (2)	90.3 (4)
Cl-Co(1)-N4	89.86 (6)	90.37 (1)	88.7 (4)
Cl-Co(1)-N3	88.31 (6)	88.86 (1)	88.9 (3)
Cl-Co(1)-N2	88.99 (6)	89.24 (1)	89.6 (4)
Cl-Co(1)-N1	88.43 (6)	89.30 (1)	89.9 (3)
N2-Co(1)-N3	177.23 (8)	177.7 (2)	178.5 (5)
N4-Co(1)-N1	178.09 (8)	179.2 (2)	178.3 (5)
N5-Co(1)-Cl	178.26 (6)	177.51 (1)	178.5 (5)

¹ CCDC 1018442 Measurement of angles are selected to compare the same geometric parameters of all structures.

² CCDC 996320

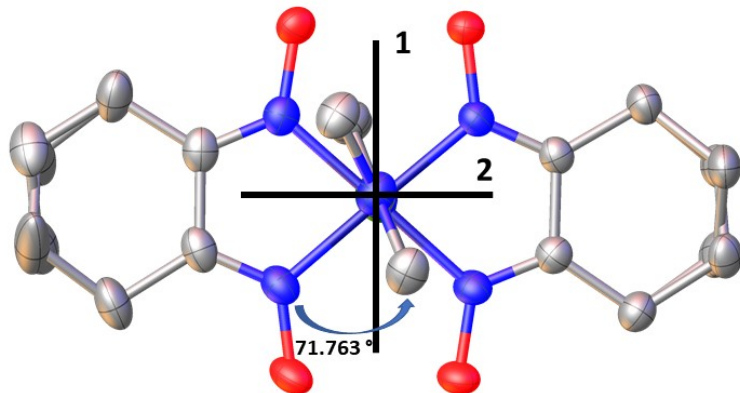


Figure 88. Orientation of N-Heterocycle on cobaloxime derivatives. View of the $\text{Co}(\text{chgH})_2(\text{DMAP})\text{Cl}$ with an indication of the torsion angle between Co-NOxime and C-N of DMAP. Plan 1 describes the commonly observed orientation of 6 membered N-heterocycle on the cobaloxime crystal structure^[9]. Plan 2 is rare.

4.10.5 Preparation of photoreactions and set up of gas chromatography

Monitoring of hydrogen evolution is measured using a Perkin Elmer Clarus-480 gas chromatograph (GC) with a thermal conductivity detector, argon as carrier, and eluant gas, a 7' HayeSep N 60/80 pre-column, a 9' molecular sieve 13x45/60 column, and a 2 mL injection loop. Three distinct solutions were prepared, 1) photosensitizer, 2) catalyst and 3) sacrificial donor and acid source (HBF_4 48% water) to obtain 5 mL of sample solutions in standard 20 mL headspace vials. The resulting molar concentration of photocatalytic components are: 0.005 mM for the photosensitizers $\text{Ru}(\text{bpy})_3(\text{PF}_6)_2$, 0.5 mM for **1**, **2**, **3**, and **4**, 1 M for triethanolamine and 0.1 mM for HBF_4 . The vials are placed on LED panel in a thermostatic bath set at 20°C. They were sealed with a rubber septum pierced with two stainless steel tubes. The first tube carried an argon flow pre-bubbled in spectrograde solvent. The flow was set to 10 mL/min (adjusted with a manual flow controller (Porter, 1000) and referenced with a digital flowmeter (Perkin Elmer FlowMark). The second tube leads the flow to the GC sample loop through a 2 mL overflow protection vial, then through an 8-port stream select valve (VICCI), and finally to the GC sample loop. A microprocessor (Arduino Uno) coupled with a custom PC interface allowed for timed injections. For calibration of H_2 production rate at a specific argon flow, a syringe pump (New Era Pump) equipped with a gas-tight syringe (SGE) and a 26s gauge needle (Hamilton) was used to bubble different rates of pure hydrogen gas into the sample, to a minimum of 0.5 $\mu\text{L}/\text{minute}$. This gave a linear fit for peak area for H_2 versus the flow rates of H_2 . For calibration testing, stock cylinders of known concentration of H_2 in argon replaced the argon flow (inserted at the pre-bubbler, to keep the same vapor matrix). The measured results, independent of flow rate (under same pressure) can be easily converted into a rate of hydrogen following equation 1.

Equation. 1: Rate of production of H_2 ($\mu\text{L}/\text{min}$) = [H₂ standard] (ppm) × Ar flow rate (L/min)

Tableau 13. – Maxima, width band of emission spectra, and photon flux of used L.E.D.’s.

<i>Blue</i>	
$\lambda_{\text{max em}}$ (nm)	452
$\Delta\lambda$ (nm)	150
<i>Photon flux in $\mu\text{Einstein}.\text{min}^{-1}.\text{cm}^{-2}$</i> [a]	20.5

[a] An analog power-meter PM100A (THORLABS) associated with a compact photodiode power head with silicon detector S120C is used to evaluate the photon flux for each LEDs. Photo-diode detector is placed at the same distance from the LED surface than the bottom of illuminated vial 0.7 cm.

4.10.6 NMR studies

NMR studies show that we may have more resonances form in the cyclohexyl catalysts. In fact, we observe the two expected bumps that are dues to the two non-equivalent CH₂. However, those “peaks” are really divided, suggesting that we have more than a single quintuplet around 2.83ppm and 3.06ppm. In a first time, we can observe those two different peaks, that are dues to the fact that protons above and under the cobalt center are not equivalents, as expected. This division of the peaks suggest that somehow, carbons are moving slowly, making the peaks move a little. The x-ray studies show us more about this surprising fact.

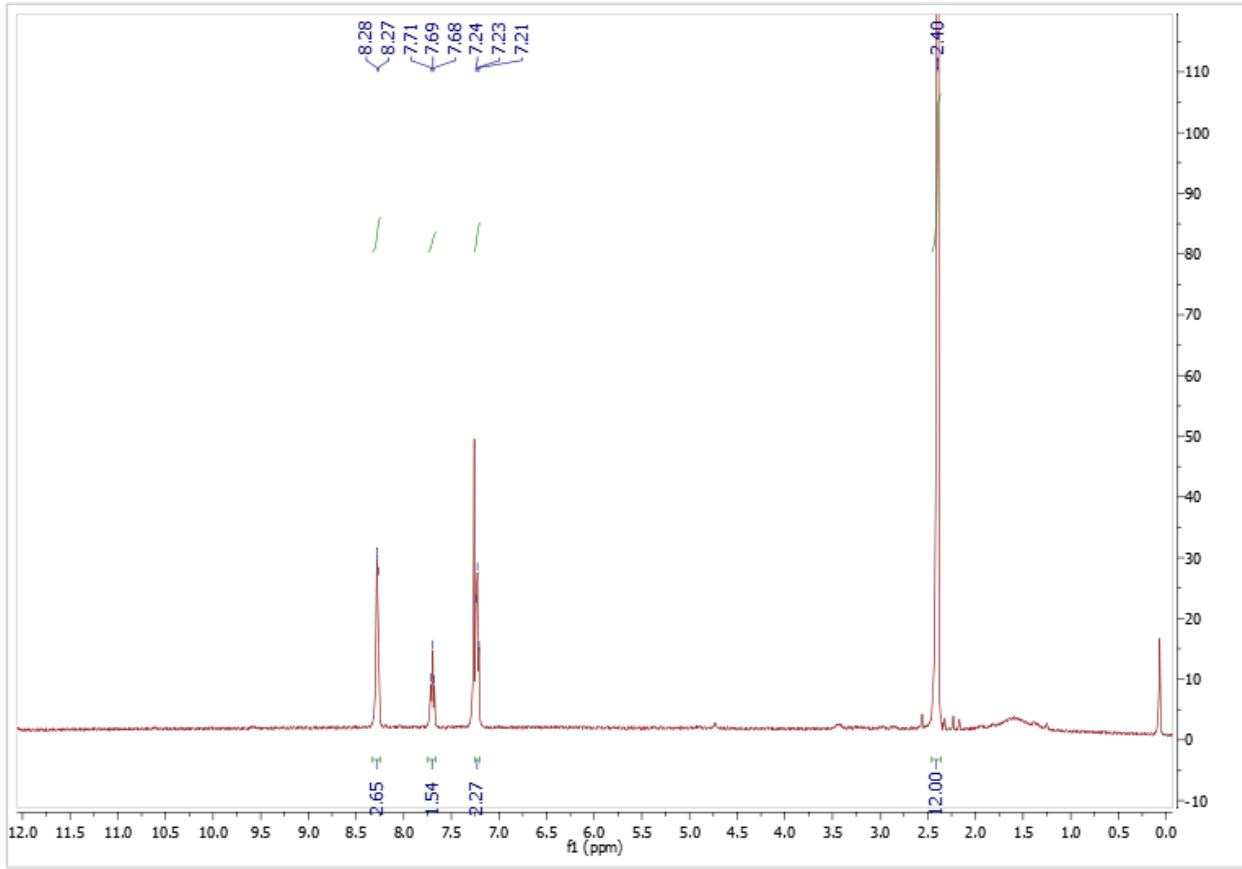


Figure 89. ^1H NMR-H¹ of the $\text{Co}(\text{dmgH})_2(\text{pyr})\text{Cl}$

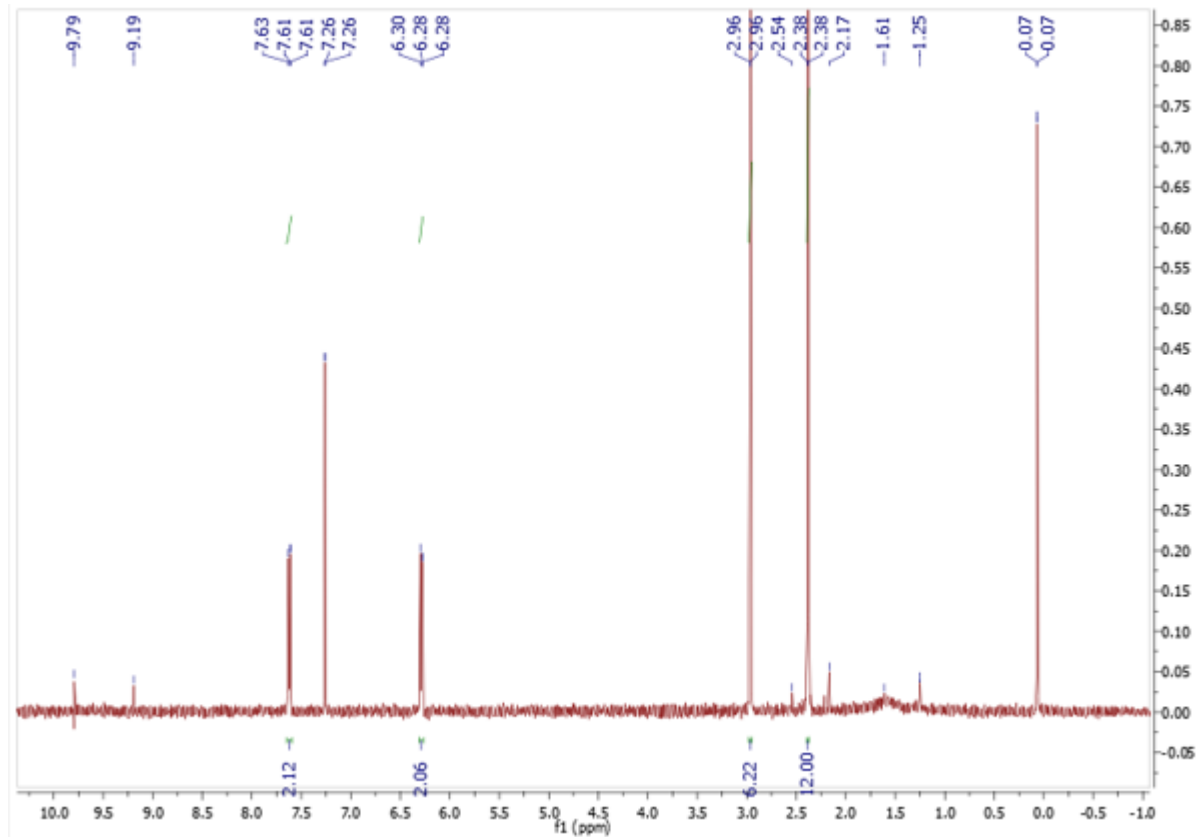


Figure 90. ${}^1\text{H}$ NMR-H¹ of the $\text{Co}(\text{dmgH})_2(\text{dmap})\text{Cl}$

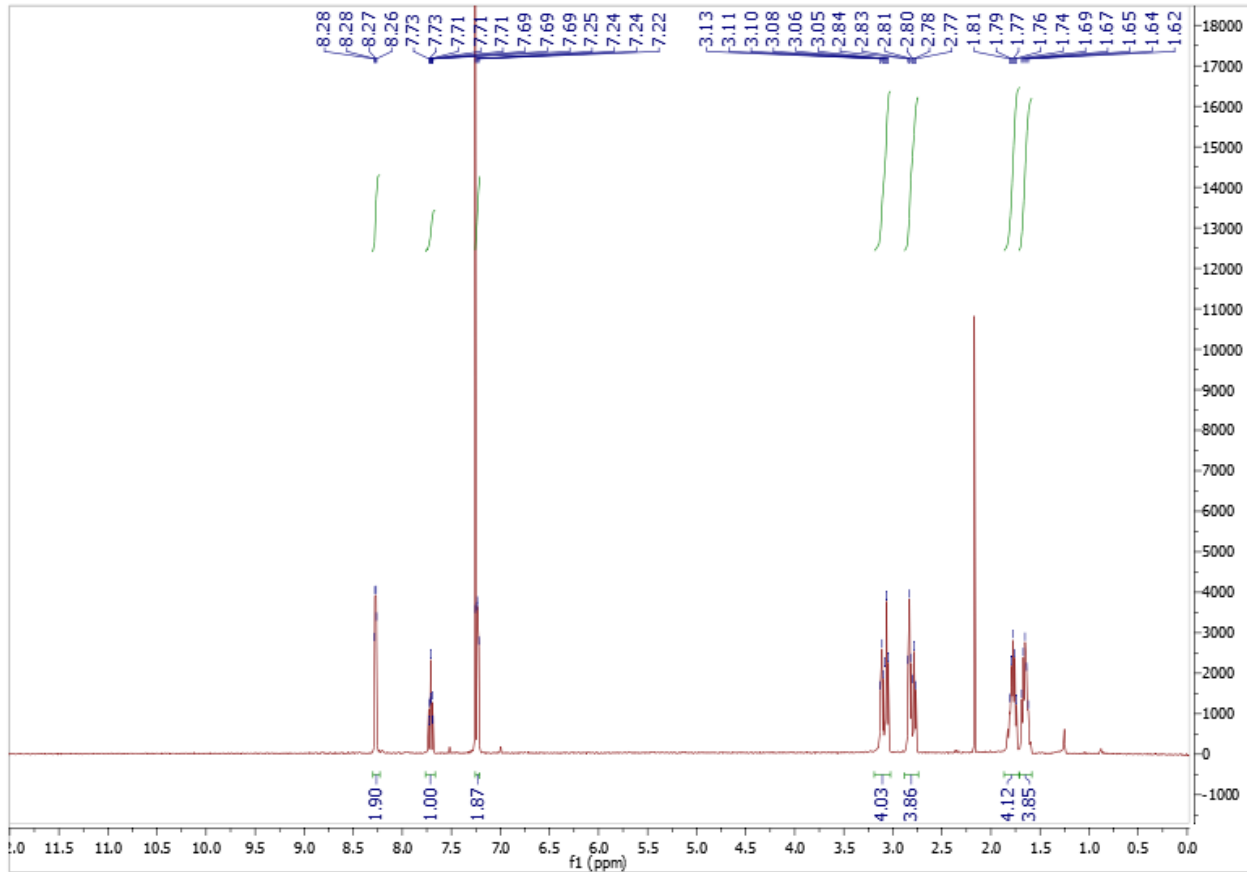


Figure 91. ${}^1\text{H}$ NMR-H¹ of the $\text{Co}(\text{chgH})_2(\text{pyr})\text{Cl}$

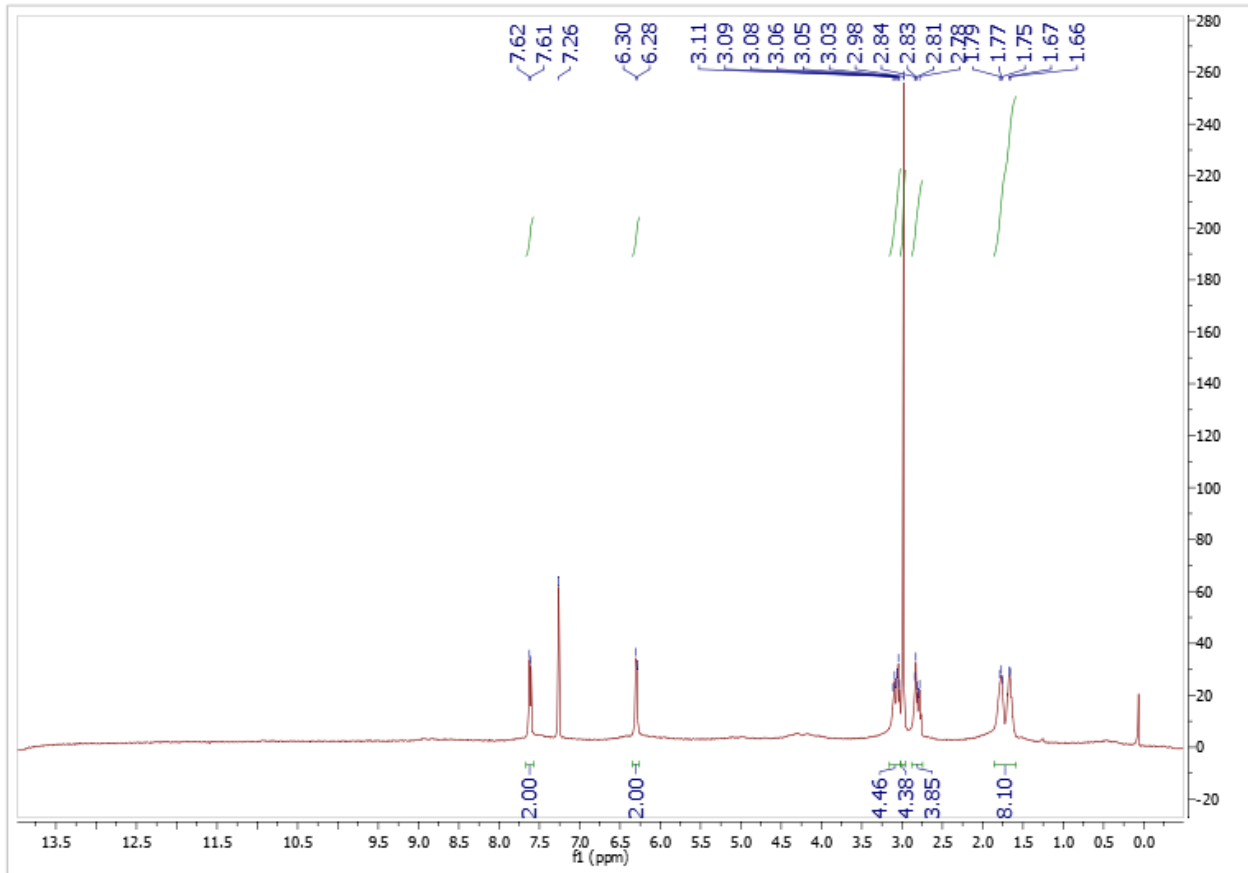


Figure 92. ^1H NMR-H¹ of the $\text{Co}(\text{chgH})_2(\text{dmap})\text{Cl}$

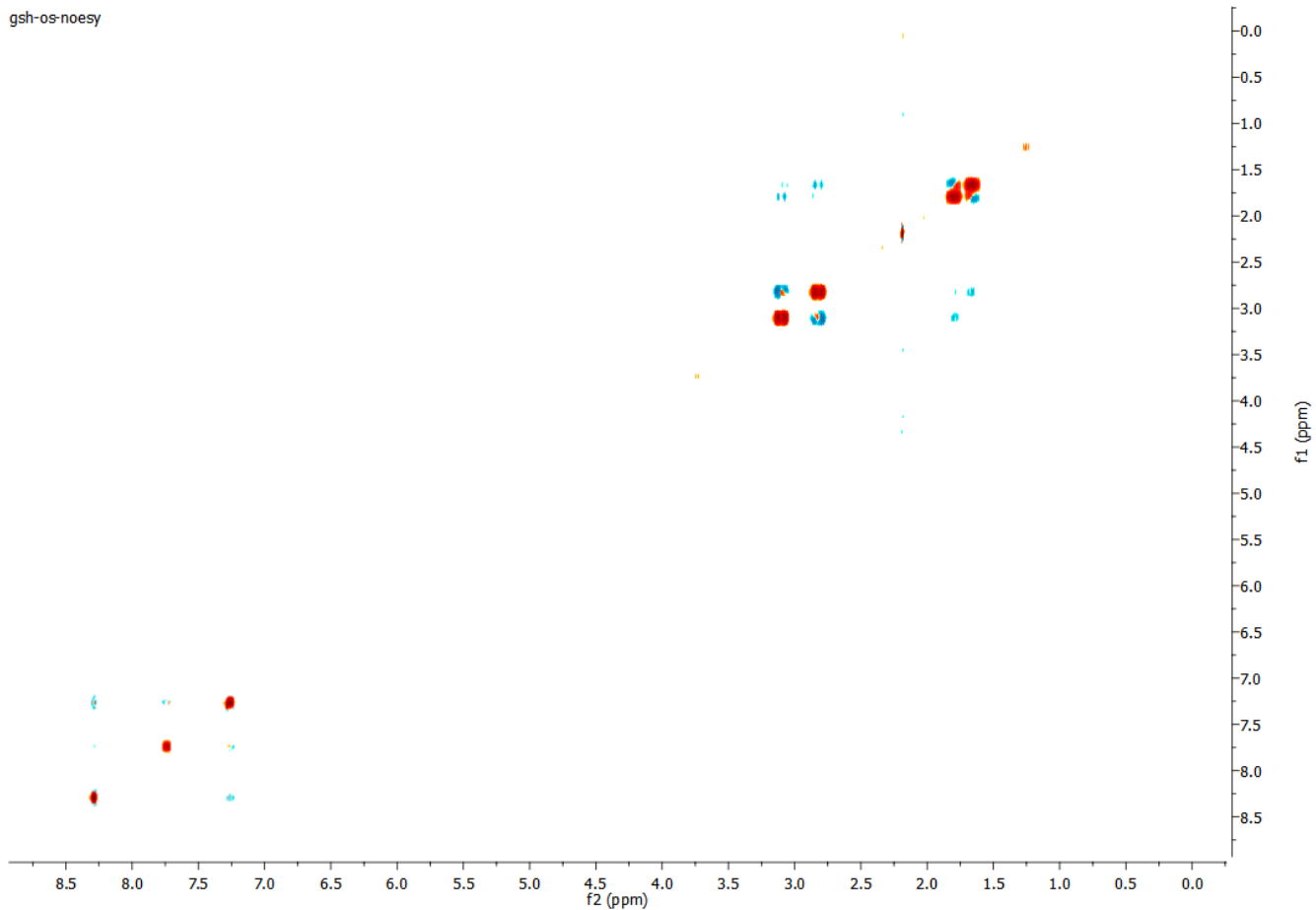


Figure 93. 2D ^1H NMR Noesy of $\text{Co}(\text{chgH})_2\text{PyrCl}$ CDCl_3 400 MHZ. The resolution of the scalar coupling has been decreased to notice the most intense coupling between the protons on the β -carbon positions and δ -carbon of the cyclohexyl moiety.

4.10.7 References

- [1] N. G. Connelly, W. Geiger, *Chem. Rev.* **1996**, *96*, 877-910.
- [2] *Bruker SADABS and TWINABS*, Bruker AXS Inc.: Madison, Wisconsin, USA., **2001**.
- [3] aG. M. Sheldrick, *Acta Crystallogr A* **2008**, *64*, 112-122; bG. M. Sheldrick, *Acta Crystallogr A Found Adv* **2015**, *71*, 3-8.
- [4] O. V. Dolomanov, L. J. Bourhis, R. J. Gildea, J. A. K. Howard, H. Puschmann, *Journal of Applied Crystallography* **2009**, *42*, 339-341.
- [5] A. L. Spek, *Acta Crystallogr D Biol Crystallogr* **2009**, *65*, 148-155.
- [6] *CCDC Mercury 3.1 - 3.3*, **2001-2003**.
- [7] X.-F. Liu, Y.-X. Zhang, J. Yan, *Transition Metal Chemistry* **2015**, *40*, 305-311.
- [8] E. Coropceanu, A. Rija, V. Lozan, I. Bulzac, G. Duca, V. C. Kravtsov, P. Bourosh, *Crystal Growth & Design* **2016**, *16*, 814-820.
- [9] C. Lopez, S. Alvarez, X. Solans, M. Font-Altaba, *Inorganic Chemistry* **1986**, *25*, 2962-2969.

5) Chapitre 5 - Properties and hydrogen evolution of N-imidoylamidine ligand cobalt(II) containing complexes

5.1 Abstract

Photocatalytic reduction of water is a promising way to generate hydrogen. Herein, we study two new Cobalt N-imidoylamidine complex ($\text{Co}(\text{Py}_2\text{ImAm})_2$ and $\text{Co}_3(\text{Pm}_2\text{ImAm})_2\text{Cl}_4 \times 5\text{H}_2\text{O}$) and their properties. As N-imidoylamidine complexes were never tested for hydrogen production, standard catalysts and photosensitizer were used as references. Electrochemical analysis reveals that Co^{II} to Co^{I} transition appears at -1.43 and -0.90 mV, respectively, while irreversible conversion of our complex from Co^{II} to Co^{III} occurs at 0.32 and 0.72 V. The irreversible transition may explain why our complex degrades fast when exposed to blue light. Those two molecules were tested as hydrogen evolution catalysts ($1 \times 10^{-5}\text{M}$) in DMF, with $1 \times 10^{-4}\text{M}$ of $[\text{Ru}(\text{bpy})_3]^{2+}$ and triethanolamine as a sacrificial donor. Hydrogen evolution leads to a maximum TOF of 315 and 130 ($\text{mmolH}_2 \times \text{mol}^{-1}_{\text{HEC}} \times \text{min}^{-1}$) and a maximum TON of 16 and 4 ($\text{molH}_2 \times \text{mol}^{-1}_{\text{HEC}}$), respectively, in DMF. Tests in water lead to, respectively, a maximum TOF of 210 and 115 ($\text{mmolH}_2 \times \text{mol}^{-1}_{\text{HEC}} \times \text{min}^{-1}$) and a maximum TON of 8 and 5.

Keywords: Photocatalyst, Electronic properties, Hydrogen production, N-imidoylamidine, Spectro-electrochemistry, Electrochemistry, Inorganic chemistry

Contribution: Pour le moment, la totalité du travail présenté a été réalisé par moi et Garry S. Hanan a procédé à la révision de l'article.

Chapitre 5 - Properties and hydrogen evolution of N-imidoylamidine ligand cobalt(II) containing complexes

Vincent Picard^a, Jaclyn Brusso^b and Garry S. Hanan^a

^a Département de Chimie, Université de Montréal 1375 Avenue Thérèse-Lavoie-Roux, Montréal, Québec, H2V-0B3, Canada. Email: Garry.hanan@umontreal.ca

^b Department of Chemistry and Biomolecular Sciences, University of Ottawa, 150 Louis Pasteur, Ottawa, Ontario, Canada K1N 6N5, Canada. Email: jbrusso@uottawa.ca

Manuscript ready for submission but for comments from our collaborator Pr. Jaclyn Brusso

Chapitre 5 - Properties and hydrogen evolution of N-imidoylamidine ligand cobalt(II) containing complexes

5.2 Introduction:

The sun allowed life on our planet for at least 3,770 million years.¹ As the main source of energy for living beings, it may be our greatest resource to feed our constantly increasing power needs. As nature did way before us, we need to learn how to use this energy to cover humankind's growth.² Balzani once said that if we can cover 0.16% of lands with 10% efficient solar-conversion systems, it would be more than enough for our actual needs.³ Steam reforming, a way to produce H₂ that also produces CO₂, is responsible for 40% of hydrogen generation worldwide and more than 95% in the United States.^{4,5} We mainly use steam reforming to produce hydrogen, because this hydrogen can be generated at a cost comparable with the production cost of fossil fuels. With that being said, we need to improve our actuals photocatalytic systems to increase their efficiency and allow a comparable production price against steam reforming. We need three distinct components for hydrogen generation: a photosensitizer (PS)⁶ to collect light from the sun, a catalyst (HEC)^{7,8} to increase reaction speed and efficiency, and a sacrificial electron donor (SED)⁹ to feed our system with electrons. While we may find plenty of sacrificial electrons donor, their efficiency mainly depends on the solvent used, except for those in water, which may require a specific pH depending on the other components to produce an optimal amount of hydrogen.^{10,11} As for PS's, [Ru(bpy)₃]²⁺ is a good reference to test those new catalysts, as ruthenium catalysts showed incredible properties and still have a good tunability.^{12–14} We find a few examples that last up to 10 days, but none of them have such a lifetime in water.¹⁵ Although [Ru(bpy)₃](PF₆)₂ may not be optimal as a PS, because of his low quantum yield and a short excited-state lifetime, which leads to a quick degradation, it is still one of the most popular references as PS to test catalysts for hydrogen production.^{16–20} Catalysts are more of a problem as none of them are able to either stabilize the PS or lasting long enough to accompany PS degradation and generate a suitable and efficient system.

Herein, we report two new catalysts that belong to a new group of Co^{II} N-imidoylamidine catalysts, that were never tested for photocatalytic hydrogen generation.²¹ N-imidoylamidine usually leads to luminescence properties when we associate them with metals. This feature is interesting because luminescent molecule sometimes makes useful PS.^{22,23} A few examples of N-imidoylamidine complex are found in the literature, but as far as we know, this kind of complex has never been tested as an HEC.²⁴⁻²⁹ We hope that this research leads to a better characterization of N-imidoylamidine complex and promotes their use for the hydrogen generation process.

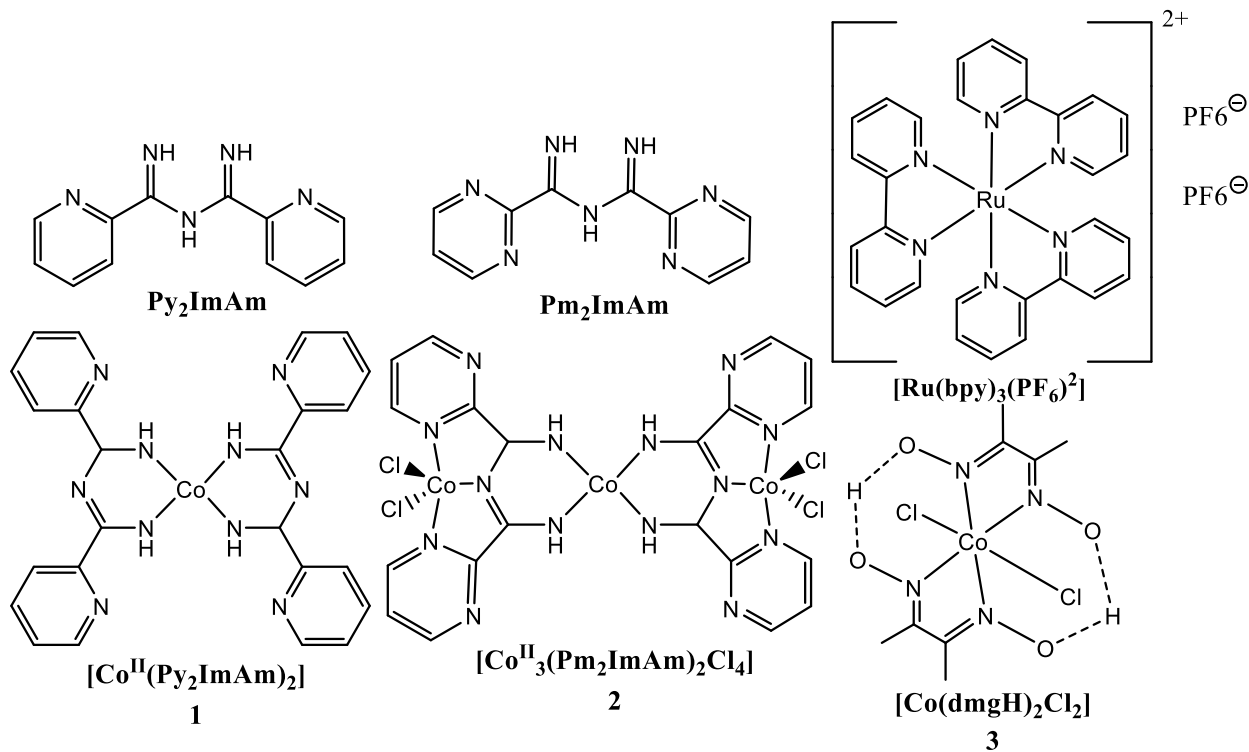


Figure 94. Structure of N-imidoylamidine (ImAm) ligands, catalysts and photosensitiser presented herein

5.3 Results and discussion

Synthesis and structural characterizations. N-imidoylamidine (Py_2ImAm and Pm_2ImAm) were prepared as we reported earlier, without metal ion assistance.²¹ Oxidation of all metallic centers for $\text{Co}(\text{Py}_2\text{ImAm})_2$ and $\text{Co}_3(\text{Pm}_2\text{ImAm})_2$ were proved by magnetic analysis (vide infra) to be Co^{II} . Purity was proved previously by x-ray powder diffraction.²¹

5.3.1 Electrochemistry

All the cyclic voltammograms and square waves of the compounds are collected in dry DMF with 1M of the electrolyte TBAPF₆ and referenced to ferrocene standard potential (See ESI Fig 99 to Fig 102). Reporting on similar complexes do not contain any cyclic voltammetry^{30,31} However, we may expect two events for each compound: oxidation of the compound from Co^{II} to Co^{III} and reduction of the compound from Co^{II} to Co^{I} . Also, for the Co_3 compound, we may reasonably expect to see two distinct transitions for cobalt, as surrounding ligands change the required potential for both oxidation and reduction, but it may be hard to distinguish them. As far as we know, no cyclovoltammetry data for heteroleptic complexes involving two inequivalent metals with these ligands has been published.^{31,32} For the mono-cobalt compound, we observe a transition at -1.43 V (0.07 V), corresponding to the reduction of cobalt metallic center from Co^{II} to Co^{I} . We also see irreversible oxidation of Co^{II} to Co^{III} at 0.32 V. This transition may explain the fast degradation of the catalyst in hydrogen generation, as the catalyst usually needs to go through Co^{III} oxidation state before producing hydrogen, then go back to Co^{I} .⁸ If the compound can't go back to Co^{II} , it may explain why we observe a single cycle for both complexes. For the tri-cobalt compound, we see the same redox waves as for mono cobalt, but both are more centered (oxidation and reduction require less energy to occur). Reduction of cobalt centers occur at -0.9 V (0.14 V) and oxidation occur at 0.72 V. Furthermore, we can expect both types of cobalt (centered and

peripherals) to reduce at different potentials, but we observe a peak that is 2-3 times as width as a normal peak, meaning that both waves are too close to distinguish. With cyclic voltammetry data alone, we are unable to say that there is more than a single wave implicated but when we took the square wave spectrum, (see ESI fig 103 and 104) we could see two waves, respectively, at -1.10 and -1.82 V. Although we may predict that centered cobalt would be easier to reduce as the bridging imidoylamidines are bridging two metal centres and thus do not donate as much electron density to the central Cobalt (ESI Fig 102), the only thing that can be said here is that we see two transitions and that those redox waves probably belong to both types of cobalt in our complex.

Tableau 14. – Electrochemical potentials of the studied complexes (in V vs Fc/Fc⁺ in DMF)

Cyclic voltammetry

Complex	Co ^{III} /Co ^{II}	Co ^{II} /Co ^I
Co(dmgH) ₂ PyrCl	-0.20 (0.18)	-1.11 (0.07)
Co(dmgH) ₂ dmapCl	-0.19 (0.16)	-1.10 (0.07)
Co(Py ₂ ImAm) ₂	0.32	-1.43 (0.07)
Co ₃ (Pm ₂ ImAm) ₂ x 5H ₂ O	0.72	-0.9 (0.14)

Square wave voltammetry

	Oxidation	Reduction
Co(Py ₂ ImAm) ₂	0.39 and -1.29	-1.30
Co ₃ (Pm ₂ ImAm) ₂ x 5H ₂ O	0.98	-1.10 and -1.82v

5.4 Spectro-Electrochemistry

To understand the properties of those new complexes regarding hydrogen evolution performances, we performed spectroelectrochemical measurements, monitoring changes in absorption as we apply a definite current. As for complex **1**, few transitions were observed (see Fig 95 to 97 and ESI Fig 105 to 111). As oxidation of our complex is irreversible, we started with the reduction sweep. At first, we may see two peaks at 375nm (π to π^*) and 500nm (MLCT transitions), and both decrease when we reach -1.2 V, confirming that they are possible only in Co^{II} oxidation state. When we reach the Co^I state, we can see 3 new peaks respectively at 600, 800, and 900nm. While we oxidize our complex, we may observe that both peaks (375nm and 500nm) disappear up to 0.6 V. Those peaks are associated with Co^{II}, explaining why we may see it between -2 and 0.4 V. Although this species changes for a Co^I around -1.2 Vv, we can see that the peak is still there, while it disappears when changed for Co^{III}. This observation confirms that once the complex reaches Co^{III} oxidation state, it can't go back to Co^{II} and thus is unable to generate more hydrogen. The reason why we observe so many peaks is still unclear but may be related to the ligand.

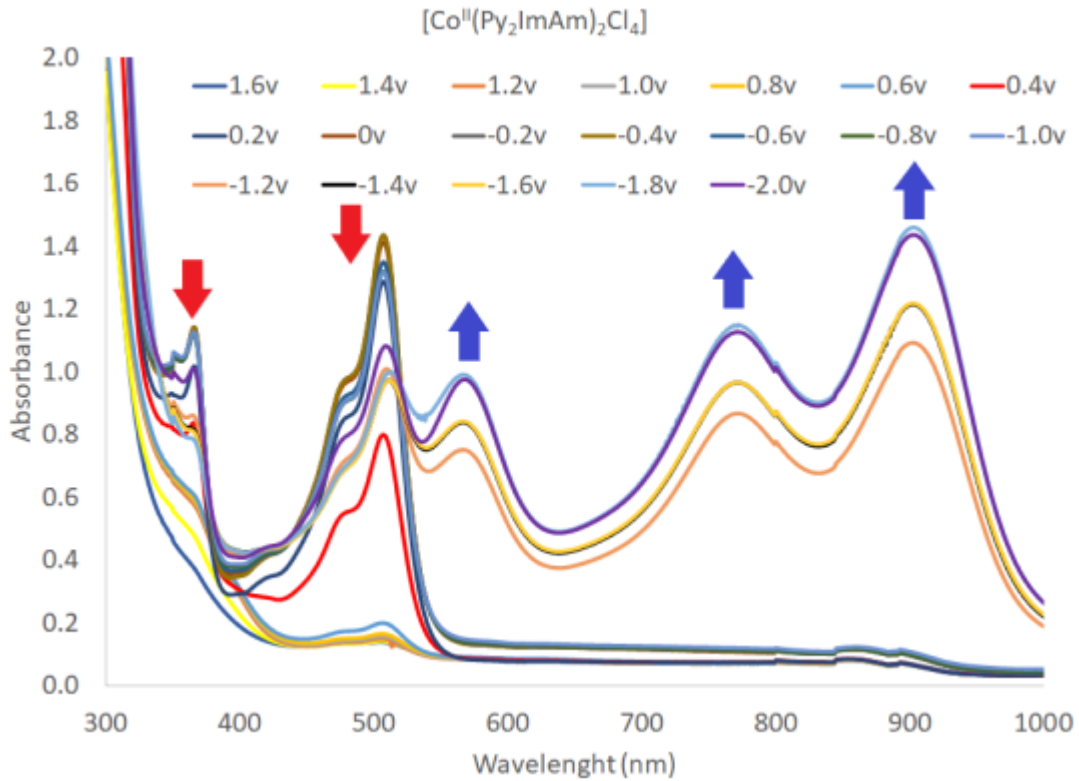


Figure 95. Spectro-electrochemistry spectra of the $[\text{Co}^{\text{II}}(\text{Py}_2\text{ImAm})_2\text{Cl}_4]$ from -2 to 1.6 V.

As for complex **2**, we did not have any peak at the start, two transitions rapidly appeared at 750 and 800 nm. We assumed that the nature of the transitions comes from the multiple transitions that are related to the three cobalt of the complex. As we oxidize the complex, the two transitions are going down while a peak at 500 nm keeps growing. This peak is assigned to Co^{III} oxidation state. Decomposed figures could be found in supplementary material (Fig 105 to 111).

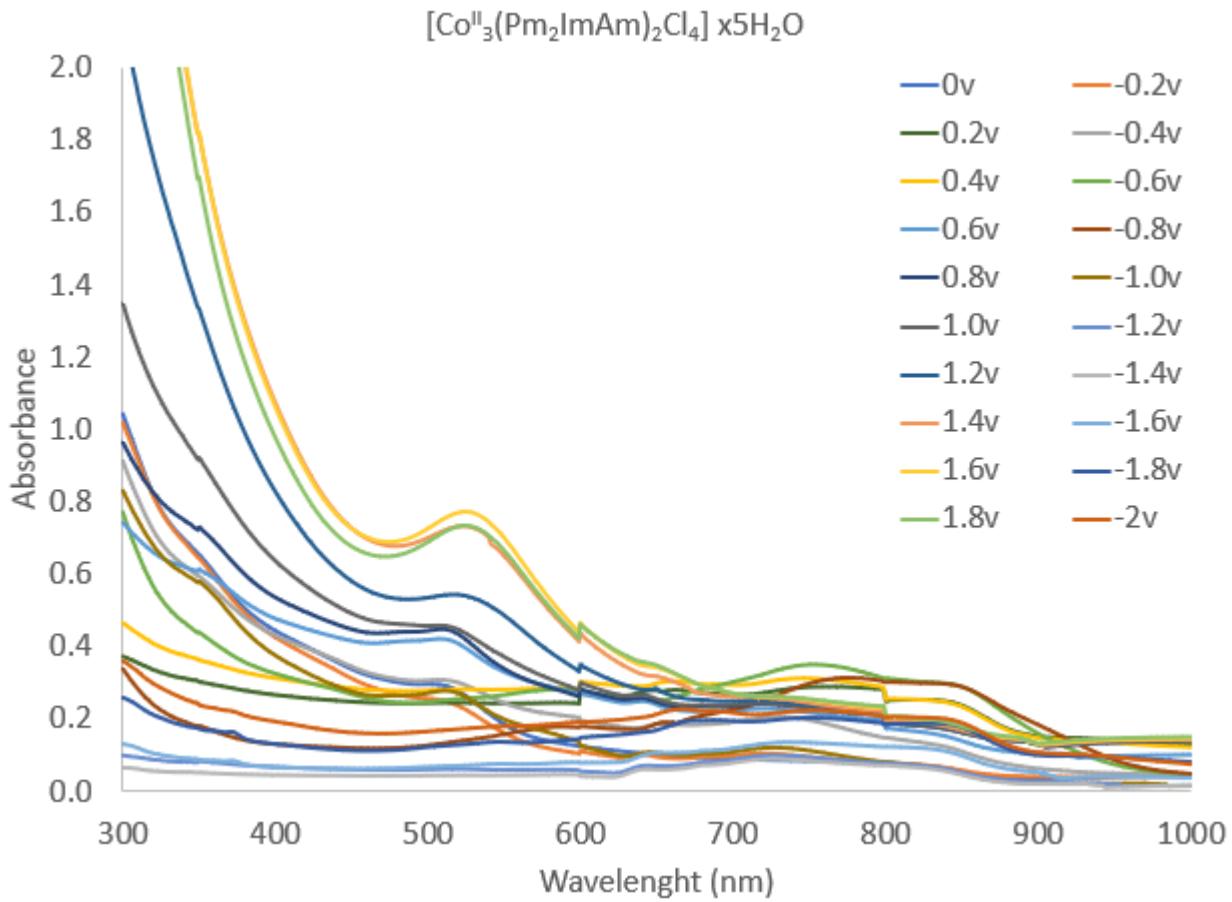


Figure 96. Spectro-electrochemistry spectra of the $[\text{Co}^{\text{II}}_3(\text{Pm}_2\text{ImAm})_2\text{Cl}_4] \times 5\text{H}_2\text{O}$ from -2 to 1.8 V

5.4.1 Photocatalytic hydrogen evolution

First, let us introduce Turn Over Number (TON) and Turn Over Frequency (TOF). TON is used to measure the ratio of hydrogen per mol of catalyst that is produced. The standard unit used are $\text{mol}_{\text{H}_2}/\text{mol}_{\text{HEC}}$, where HEC stand for Hydrogen Evolving Catalyst. The TOF measure the speed of the hydrogen production. The standard unit used are $\text{mmol}_{\text{H}_2}/\text{mol}_{\text{HEC}}/\text{min}^{-1}$. The standard units will be used herein and may be assumed to alleviate the text. The photocatalytic experiments are performed with blue Light Emitting Diodes (LEDs) centered at 452 nm irradiation. The LEDs irradiate fully the ${}^1\text{M}\text{et}\text{l-}\text{L}\text{ig}\text{a}\text{n}\text{d-}\text{C}\text{h}\text{a}\text{r}\text{g}\text{e-}\text{T}\text{r}\text{a}\text{n}\text{s}\text{f}\text{e}\text{r}$ of $\text{Ru}(\text{bpy})_3^{2+}$. The solvent of the HER is

dimethylformamide (DMF), triethanolamine 1 M is the sacrificial electron donor, HBF₄ 0.1 M and 0.56 M of water are proton sources. The Co catalysts are analyzed at 1x10⁻⁵M in association with [Ru(bpy)₃](PF₆)₂ at a concentration of 0.1mM, to see how much hydrogen the catalyst may generate and ensure that the catalyst remains the limiting factor of the hydrogen production. We ensured hydrogen production is not due to a single molecule and ran experimental blanks in each possible combination. None of them produce hydrogen. As expected, if we remove HBF₄, no hydrogen is evolved at all, as water also comes from HBF₄. No water should be present in DMF as we dried it with a molecular sieve, and we distilled it with CaH₂. The resulting DMF was left in the glovebox and small fractions were taken as needed. Without the proton source, no hydrogen is evolved at all. Those tests ensure that all compounds are essential for hydrogen production. Hydrogen was evolved in DMF and water for both compounds. All systems have a small induction period, approximately 2 minutes before hydrogen production begins. This period is attributed to the mechanism of hydrogen production, as it needs a certain state of cobalt (usually Co^{II} or Co^{III}) to produce hydrogen.⁸

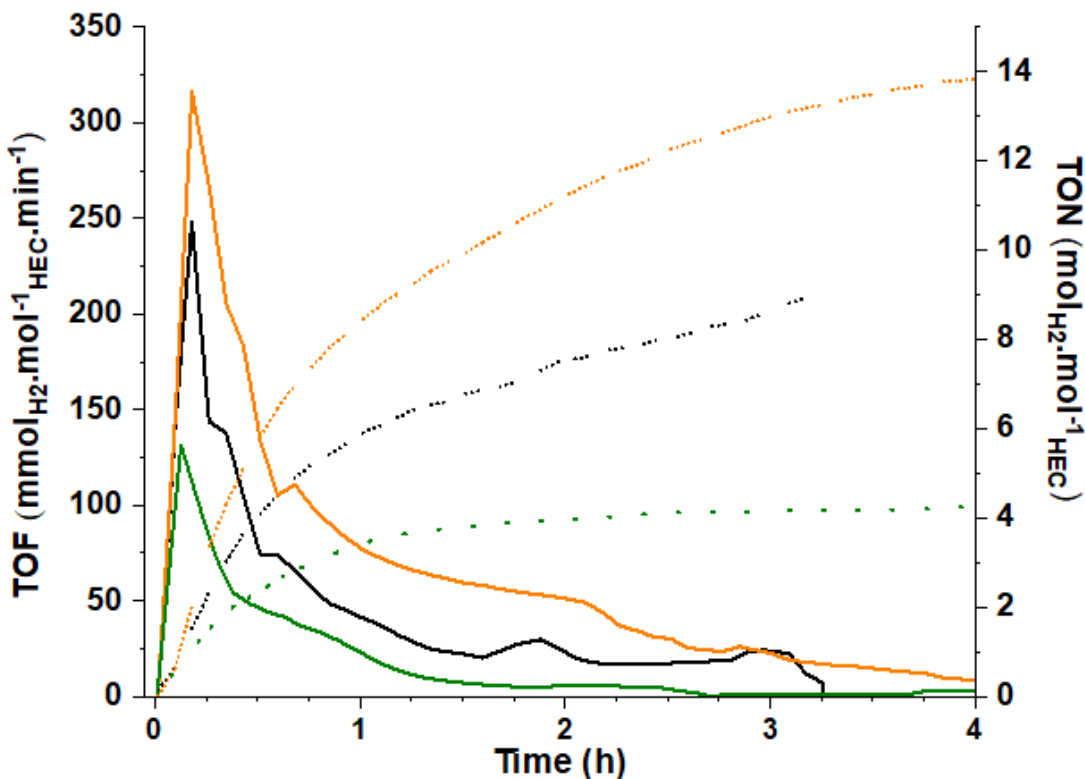


Figure 97. TON and TOF of $\text{Co}(\text{Py}_2\text{ImAm})_2$ (orange, **1-2**), $\text{Co}(\text{dmgH})_2\text{Cl}_2$ (black, **2-2**) and $\text{Co}_3(\text{Pm}_2\text{ImAm})_2 \times 5\text{H}_2\text{O}$ (green, **3-3**) in DMF with $1.0 \times 10^{-4}\text{M}$ of $[\text{Ru}(\text{bpy})_3]^{2+}$

$\text{Co}(\text{Py}_2\text{ImAm})_2$ shows a TON of approximately 2 for **1-1**, 13 for **1-2** and 146 for **1-3** and a TOF of respectively approximately 31 for **1-1**, 315 for **1-2** and 2240 for **1-3**. The hydrogen production remains constant with the amount of catalyst added for **1-1** and **1-2** but goes much higher if the photosensitiser is in large excess, like **1-3**. The main point to be noted is that when we add more catalyst, hydrogen evolution resume at different proportion. With that being said, we could probably find the optimal amount of catalyst in order to resume the hydrogen production. For run **1-1**, production gets to 75% of the initial amount. For run **1-2**, production is resumed entirely and for run **1-3**, production gets to 50% of his production, meaning mostly that the less catalyst we have, the less the production tend to resume. It is interesting to note that adding catalysts will not resume hydrogen production at all, proving that the PS is the limiting factor, presumably degrading

by reductive quenching.^{15,33,34} it has been demonstrated that when photosensitizer is in large excess or at high concentration, it tends to quench his own excited state.

$\text{Co}_3(\text{Pm}_2\text{ImAm})_2$ shows a TON of 7.3, 4.3, and 45 at different catalyst loadings (Table 15). The TOF are 304, 131, and 1024 at different catalyst loadings (Table 15). The same thing could be observed for $\text{Co}_3(\text{Pm}_2\text{ImAm})_2$ than for $\text{Co}(\text{Py}_2\text{ImAm})_2$ when we add more catalysts, as **2-1** resumes hydrogen production at 82%. However, **2-2** resume only at 18% and **2-3** resume at 56%. It is still unclear why the catalyst need a higher concentration than $\text{Co}(\text{Py}_2\text{ImAm})_2$ to resume his hydrogen production, but we believe this is related to the catalyst stability and interaction with the PS. A clear trend could be observed for the reference. The less catalyst we use, the more the hydrogen production is resumed. **3-1** is resumed at 43%, **3-2** is resumed at 34 and 30%, **3-3** is resumed at 69%. (For more data, see ESI Fig 112 to 117)

Tableau 15. – Hydrogen Production Results under Blue-Light Irradiation, vs HEC (450 nm, 62 mW) in DMF

$\text{Co}(\text{Py}_2\text{ImAm})_2$							
	[HEC]	[PS]	TOF	TOF2*	TON	TON2*	N (mmol)*
1-1	1.1×10^{-4}	1.1×10^{-4}	31.2	23.0	1.68	2.68	1779
1-2	1.4×10^{-5}	1.2×10^{-4}	314	317	12.68	24.9	1832
1-3	1.1×10^{-6}	1.1×10^{-4}	2241	1198	146	209	1528
$\text{Co}_3(\text{Pm}_2\text{ImAm})_2 \times 5\text{H}_2\text{O}$							
	[HEC]	[PS]	TOF	TOF2	TON	TON2	N (mmol)
2-1	5.0×10^{-5}	1.0×10^{-4}	304	282	7.33	30.0	3704
2-2	1.0×10^{-5}	1.0×10^{-4}	131	23.6	4.34	3.94	2261
2-3	1.7×10^{-6}	1.0×10^{-4}	1024	570	45.0	68.0	1152

Co(dmgH)₂Cl₂							
	[HEC]	[PS]	TOF	TOF2	TON	TON2	N (mmol)
3-1	1.2 x10 ⁻⁴	1.0 x10 ⁻⁴	197	86.1	3.38	13.7	4083
3-2	1.8 x10 ⁻⁵	1.0 x10 ⁻⁴	521	179	15.0	37.6	2665
3-3	7.0 x10 ⁻⁶	1.0 x10 ⁻⁴	248	170	8.61	19.5	637.9

*TON2 and TOF2 refer to the TON and TOF obtained after the PS was added to resume the hydrogen production. N (mmol) report hydrogen produced without adding PS to resume hydrogen production.

As expected, when photosensitizer is used as the comparing unit, TON and TOF go down. However, the best performance shows up with the highest concentration of catalyst. Co(Py₂ImAm)₂ shows a TON of respectively 1.67, 1.42, 1.22 and, a TOF of respectively 38.7, 30.8 and 19.4 (table 15).

Co₃(Pm₂ImAm)₂ shows a TON of respectively 7.3, 4.3, and 45. The TOF are respectively 304, 131, and 1024. The same thing could be observed for Co₃(Pm₂ImAm)₂ than for Co(Py₂ImAm)₂ when we add more catalysts, as **2-1** resumes hydrogen production at 82%. However, **2-2** resume only at 18% and **2-3** resume at 56%. As for the reference, the reverse situation could be observed. The less catalyst we use, the more the hydrogen production is resumed. **3-1** is resumed at 43%, **3-2** is resumed at 34 and 30%, **3-3** is resumed at 69%.

Tableau 16. – Hydrogen Production Results under Blue-Light Irradiation, vs PS (450 nm, 62 mW) in DMF

Co(Py₂ImAm)₂								
	[HEC]	[PS]	TOF	TOF2	TON	TON2	N (mmol)	Duration (h)
1-1	1.1 x10 ⁻⁴	1.1 x10 ⁻⁴	30.8	23.0	1.27	2.68	1779	3h52
1-2	1.4 x10 ⁻⁵	1.2 x10 ⁻⁴	38.7	39.1	1.67	3.06	1832	4h23
1-3	1.1 x10 ⁻⁶	1.1 x10 ⁻⁴	19.4	11.6	1.22	2.03	1528	4h38

Co₃(Pm₂ImAm)₂ x 5H₂O								
	[HEC]	[PS]	TOF	TOF2	TON	TON2	N (mmol)	Duration (h)
2-1	5.0 x10 ⁻⁵	1.0 x10 ⁻⁴	113	92.5	3.57	14.6	3704	2h45
2-2	1.0 x10 ⁻⁵	1.0 x10 ⁻⁴	55.6	11.2	1.29	1.93	2261	2h38
2-3	1.7 x10 ⁻⁶	1.0 x10 ⁻⁴	16.8	9.33	0.74	1.11	1152	1h55

Co(dmgH)₂Cl₂								
	[HEC]	[PS]	TOF	TOF2	TON	TON2	N (mmol)	Duration (h)
3-1	1.2 x10 ⁻⁴	1.1 x10 ⁻⁴	221	96.4	3.38	15.3	4083	2h25
3-2	1.8 x10 ⁻⁵	1.0 x10 ⁻⁴	83	29.6/25.8	1.98	6.11	2665	5h
3-3	7.2 x10 ⁻⁶	1.1 x10 ⁻⁴	16.9	11.6	0.59	1.33	638	3h15

We tried to evolve hydrogen in water with complexes **1** and **2**. However, Co(Py₂ImAm)₂ was not soluble in water in any proportions. Co₃(Pm₂ImAm)₂ was fairly soluble in water. Doing so, we repeated the procedure that we applied in DMF, as we tested respectively 5x10⁻⁵, 1x10⁻⁵, 1x10⁻⁶M of Co₃(Pm₂ImAm)₂ x 5H₂O with 1x10⁻⁴M of [Ru(bpy)₃]²⁺, using ascorbic acid as a sacrificial donor. As proved before, the optimal pH for ascorbic acid is around 5¹⁰, as above we reduce the photosensitizer, and below, cobalt hydride is formed.³⁵ The results can be found in table 17 and figure 98, below.

$\text{Co}_3(\text{Pm}_2\text{ImAm})_2$ shows a TON of respectively 3.1, 4.9, and 21.3. The TOF are respectively 77, 113, and 332. We may see that both TON and TOF go down a lot versus the hydrogen evolution in DMF. This is not surprising as most types of catalysts, except for porphyrin and polypyridyl generally don't perform well in water. With a relatively weak solubility in water, we may not be surprised that it performed poorly for hydrogen evolution. Another thing that could be noted is that the pH slightly increases after the hydrogen evolution, suggesting that some of the ascorbic acid is consumed in the process. However, the pH increase is low. To ensure that this change was not caused by degradation over time, we prepared a sample that would also get the addition of the photosensitizer after "degradation" (because we did not expose this sample to light) and measured the pH after the hydrogen evolution experiment, as same as other samples. This solution was our starting point for pH measurement. However, we may see that pH goes from 5.04 to 5.43 after 3 days of air exposure and that the ascorbic acid solution turned yellow after a few days, probably because of oxidation of ascorbic acid.

The mono-cobalt compound was not soluble in water in any proportion. Water immediately precipitates the compound at any proportion, so we dissolved all the compounds separately and added water last, to prevent precipitation. Results can be found in supplementary materials (See figure 118).

The results are a bit surprising, as we obtain a TON of respectively 11.7, 17.8, 10.6, and 7.98, with TOF of respectively 374, 277, 239, and 212.

Without any surprise, the more water we add, the weaker hydrogen production is. However, hydrogen production really goes down starting with **1-15** (15% water). Furthermore, water seem to initially quench the production in **1-5** and **1-10**, but for **1-15** and **1-25**, hydrogen production

resume normally. The fact that we add more PS, and hydrogen production resume at 200-300% of initial production, is really strange, but may suggest that adding small amount of water either quench hydrogen production or react with degradation product of $[Ru(bpy)_3]^{2+}$ to enhance hydrogen production. We cannot say clearly for now why adding water seem to affect hydrogen production, but this may be the start of an interesting studie about hydrogen production mechanism in water. The trend seems clear that the less water we add, the better hydrogen production is, as TOF are respectively 374/277/239/212. After 15%v/v of water was added to the solution, it seems that there was too much water and the catalyst started to become less soluble. **1-15** and **1-25** seem to fit with usual hydrogen production pattern, and it does not anymore produce more than initially. (for more data, see ESI Fig 118 and 119)

Tableau 17. – Hydrogen Production Results under Blue-Light, vs HEC (450 nm, 62 mW) in water

Co(Py₂ImAm)₂

*	[HEC]	[PS]	TOF	TOF2	TON	TON	N	Duration	pH	pH
					2	(mmol)	(h)	before	after	
1-5%	1.1x10 ⁻⁵	1.1 x10 ⁻⁴	374	847	11.7	144	15183	7h19	-	-
1-10%	1.1x10 ⁻⁵	1.1 x10 ⁻⁴	277	697	17.8	88.1	9619	8h05	-	-
1-15%	1.1x10 ⁻⁵	1.1 x10 ⁻⁴	239	152	10.6	24.5	2628	5h49	-	-
1-25%	1.1x10 ⁻⁵	1.1 x10 ⁻⁴	212	173/1	7.98	37.8	4057	6h34	-	-

93

* **1-5%** mean that we added **5% v/v** water to compound #1

Co₃(Pm₂ImAm)₂ x 5H₂O

	[HEC]	[PS]	TOF	TOF2	TON	TON	N	Duration	pH	pH
					2	(mmol)	(h)	before	after	
2-1	5.1x10 ⁻⁵	9.1x10 ⁻⁵	77	61	3.1	7.6	1651	1h58	4.83	4.96
2-2	1.0x10 ⁻⁵	9.1x10 ⁻⁵	113	118	4.9	16.2	534	1h30	4.84	4.87
2-3	6x10 ⁻⁶	9.6x10 ⁻⁵	332	293	21.3	45.3	2109	6h31	5.04	5.38

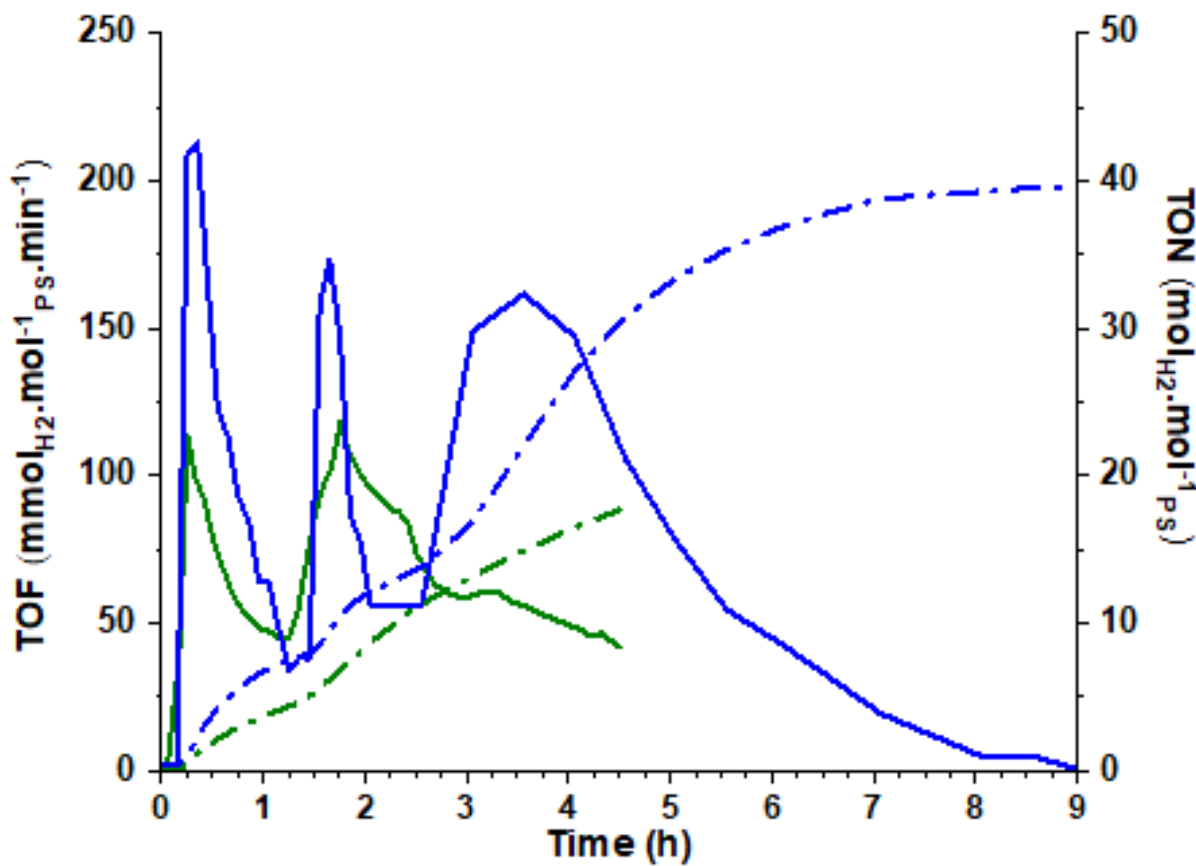


Figure 98. TON and TOF of $\text{Co}(\text{Py}_2\text{ImAm})_2$ (blue) with 25% water and DMF as solvent and $\text{Co}_3(\text{Pm}_2\text{ImAm})_2 \times 5\text{H}_2\text{O}$ (green) in water with $1.0 \times 10^{-4}\text{M}$ of $[\text{Ru}(\text{bpy})_3]^{2+}$

5.5 Conclusion

We tested two new N-imidoylamidine catalysts for hydrogen production in DMF and water. Both catalysts ($\text{Co}(\text{Py}_2\text{ImAm})_2$ and $\text{Co}_3(\text{Pm}_2\text{ImAm})_2 \times 5\text{H}_2\text{O}$) were irradiated with blue light and tested with $1 \times 10^{-4}\text{M}$ of $[\text{Ru}(\text{bpy})_3]^{2+}$ as photosensitizer and triethanolamine as electron sacrificial donor (DMF) or ascorbic acid (Water). Both compounds have a much better hydrogen production in DMF than in water. Electronics properties have been tested and both compounds exhibit $\text{Co}^{\text{II}}/\text{Co}^{\text{III}}$ and $\text{Co}^{\text{II}}/\text{Co}^{\text{I}}$ transitions. Furthermore, new MLCT transitions could be observed with spectro-electrochemistry.

5.6 Acknowledgment

We thank the Natural Sciences and Engineering Research Council of Canada for its financial support. We would also like to thank Dr. Daniel Chartrand for the instrumentation.

5.7 Bibliography

- (1) Dodd, M. S.; Papineau, D.; Grenne, T.; Slack, J. F.; Rittner, M.; Pirajno, F.; O’Neil, J.; Little, C. T. S. Evidence for Early Life in Earth’s Oldest Hydrothermal Vent Precipitates. *Nature* **2017**, *543* (7643), 60–64. <https://doi.org/10.1038/nature21377>.
- (2) Berardi, S.; Drouet, S.; Francas, L.; Gimbert-Surinach, C.; Guttentag, M.; Richmond, C.; Stoll, T.; Llobet, A. Molecular Artificial Photosynthesis. *Chem Soc Rev* **2014**, *43* (22), 7501–7519. <https://doi.org/10.1039/c3cs60405e>.
- (3) Balzani, V.; Credi, A.; Venturi, M. Photochemical Conversion of Solar Energy. *ChemSusChem* **2008**, *1* (1–2), 26–58. <https://doi.org/10.1002/cssc.200700087>.
- (4) Pantoleontos, G.; Kikkilides, E. S.; Georgiadis, M. C. A Heterogeneous Dynamic Model for the Simulation and Optimisation of the Steam Methane Reforming Reactor. *Int. J. Hydron. Energy* **2012**, *37* (21), 16346–16358. <https://doi.org/10.1016/j.ijhydene.2012.02.125>.
- (5) Han, B.; Wei, W.; Li, M.; Sun, K.; Hu, Y. H. A Thermo-Photo Hybrid Process for Steam Reforming of Methane: Highly Efficient Visible Light Photocatalysis. *Chem Commun Camb* **2019**, *55* (54), 7816–7819. <https://doi.org/10.1039/c9cc04193a>.
- (6) Yuan, Y.-J.; Yu, Z.-T.; Chen, D.-Q.; Zou, Z.-G. Metal-Complex Chromophores for Solar Hydrogen Generation. *Chem. Soc. Rev.* **2017**, *46* (3), 603–631. <https://doi.org/10.1039/C6CS00436A>.
- (7) Dalle, K. E.; Warnan, J.; Leung, J. J.; Reuillard, B.; Karmel, I. S.; Reisner, E. Electro- and Solar-Driven Fuel Synthesis with First Row Transition Metal Complexes. *Chem Rev* **2019**, *119* (4), 2752–2875. <https://doi.org/10.1021/acs.chemrev.8b00392>.
- (8) Artero, V.; Chavarot-Kerlidou, M.; Fontecave, M. Splitting Water with Cobalt. *Angew Chem Int Ed Engl* **2011**, *50* (32), 7238–7266. <https://doi.org/10.1002/anie.201007987>.
- (9) Fabrice Odobel, Y. P. Sacrificial electron donor reagents for solar fuel production | Elsevier Enhanced Reader <https://reader.elsevier.com/reader/sd/pii/S1631074816000734?token=764D62F9C0A846A73AFA6B790759C9AF4AB5ACEF9EBCB8BB72CDB7C70925F26006C79FFABF6D501F27F392DD6435E74B&originRegion=us-east-1&originCreation=20211027224253> (accessed 2021 -10 -27). <https://doi.org/10.1016/j.crci.2015.11.026>.
- (10) Natali, M. Elucidating the Key Role of PH on Light-Driven Hydrogen Evolution by a Molecular Cobalt Catalyst. *ACS Catal.* **2017**, *7* (2), 1330–1339. <https://doi.org/10.1021/acscatal.6b03087>.
- (11) Beyene, B. B.; Hung, C.-H. Photocatalytic Hydrogen Evolution from Neutral Aqueous Solution by a Water-Soluble Cobalt(II) Porphyrin. *Sustain. Energy Fuels* **2018**, *2* (9), 2036–2043. <https://doi.org/10.1039/c8se00253c>.
- (12) Goldberg, V.; Kaplan, M.; Soltzberg, L.; Genevich, J.; Berry, R.; Bukhari, A.; Chan, S.; Damour, M.; Friguglietti, L.; Gunn, E.; Ho, K.; Johnson, A.; Lin, Y. Y.; Lowenthal, A.;

- Suth, S.; To, R.; Yopak, R.; Slinker, J. D.; Malliaras, G. G.; Flores-Torres, S.; Abruña, H. D. Degradation of Ru(Bpy) 3^{2+} -Based OLEDs. In *Materials Research Society Symposium Proceedings*; 2005; Vol. 846, pp 301–306.
- (13) Deponti, E.; Natali, M. Photocatalytic Hydrogen Evolution with Ruthenium Polypyridine Sensitizers: Unveiling the Key Factors to Improve Efficiencies. *Dalton Trans* **2016**, *45* (22), 9136–9147. <https://doi.org/10.1039/c6dt01221c>.
- (14) K. Prier, C.; A. Rankic, D.; W. C. MacMillan, D. Visible Light Photoredox Catalysis with Transition Metal Complexes: Applications in Organic Synthesis.
- (15) Rupp, M.; Auvray, T.; Rousset, E.; Mercier, G. M.; Marvaud, V.; Kurth, D. G.; Hanan, G. S. Photocatalytic Hydrogen Evolution Driven by a Heteroleptic Ruthenium(II) Bis(Terpyridine) Complex. *Inorg. Chem.* **2019**, *58* (14), 9127–9134. <https://doi.org/10.1021/acs.inorgchem.9b00698>.
- (16) Fihri, A.; Artero, V.; Razavet, M.; Baffert, C.; Leibl, W.; Fontecave, M. Cobaloxime-Based Photocatalytic Devices for Hydrogen Production. *Angew. Chem. Int. Ed.* **2008**, *47* (3), 564–567.
- (17) Rajak, S.; Schott, O.; Kaur, P.; Maris, T.; Hanan, G. S.; Duong, A. Design of a [FeFe] Macroyclic Metallotecton for Light-Driven Hydrogen Evolution Reaction. *Int. J. Hydrot. Energy* **2020**, *45* (4), 2699–2708. <https://doi.org/10.1016/j.ijhydene.2019.11.141>.
- (18) Varma, S.; Castillo, C. E.; Stoll, T.; Fortage, J.; Blackman, A. G.; Molton, F.; Deronzier, A.; Collomb, M.-N. Efficient Photocatalytic Hydrogen Production in Water Using a Cobalt(III) Tetraaza-Macroyclic Catalyst: Electrochemical Generation of the Low-Valent Co(I) Species and Its Reactivity toward Proton Reduction. *Phys. Chem. Chem. Phys.* **2013**, *15* (40), 17544–17552. <https://doi.org/10.1039/C3CP52641K>.
- (19) Bergamini, G.; Natali, M. Homogeneous vs. Heterogeneous Catalysis for Hydrogen Evolution by a Nickel(II) Bis(Diphosphine) Complex. *Dalton Trans* **2019**, *48* (39), 14653–14661. <https://doi.org/10.1039/c9dt02846c>.
- (20) Lucarini, F.; Fize, J.; Morozan, A.; Marazzi, M.; Natali, M.; Pastore, M.; Artero, V.; Ruggi, A. Insights into the Mechanism of Photosynthetic H₂ Evolution Catalyzed by a Heptacoordinate Cobalt Complex. *Sustain. Energy Fuels* **2020**. <https://doi.org/10.1039/c9se00434c>.
- (21) Castañeda, R.; Rouzières, M.; Clérac, R.; Brusso, J. L. Controlling the Nuclearity and Topology of Cobalt Complexes through Hydration at the Ppm Level. *J. Mater. Chem. C* **2020**, *8* (13), 4401–4407. <https://doi.org/10.1039/C9TC06261K>.
- (22) Sarova, G. H.; Bokach, N. A.; Fedorov, A. A.; Berberan-Santos, M. N.; Kukushkin, V. Y.; Haukka, M.; Silva, J. J. R. F. da; Pombeiro, A. J. L. A New Family of Luminescent Compounds: Platinum(II) Imidoamidinates Exhibiting PH-Dependent Room Temperature Luminescence. *Dalton Trans.* **2006**, No. 31, 3798–3805. <https://doi.org/10.1039/B602083F>.
- (23) Yousaf, M.; Yutronkie, N. J.; Castañeda, R.; Klein, J. A.; Brusso, J. Boratriazines: Inducing Luminescence through Boron Incorporation into a Terpy-Type Framework. *New J. Chem.* **2017**, *41* (20), 12218–12224. <https://doi.org/10.1039/C7NJ02462B>.
- (24) Kopylovich, M. N.; Pombeiro, A. J. L.; Fischer, A.; Klooo, L.; Kukushkin, V. Yu. Facile Ni(II)/Ketoxime-Mediated Conversion of Organonitriles into Imidoamidine Ligands. Synthesis of Imidoamidines and Acetyl Amides. *Inorg. Chem.* **2003**, *42* (22), 7239–7248. <https://doi.org/10.1021/ic0349813>.
- (25) Kopylovich, M. N.; Tronova, E. A.; Haukka, M.; Kirillov, A. M.; Kukushkin, V. Yu.; Fraústo da Silva, J. J. R.; Pombeiro, A. J. L. Identification of Hexameric Water and Hybrid

- Water–Chloride Clusters Intercalated in the Crystal Hosts of (Imidoylamidine)Nickel(II) Complexes. *Eur. J. Inorg. Chem.* **2007**, *2007* (29), 4621–4627. <https://doi.org/10.1002/ejic.200700462>.
- (26) Bokach, N. A.; Kuznetsova, T. V.; Simanova, S. A.; Haukka, M.; Pombeiro, A. J. L.; Kukushkin, V. Yu. Nitrile–Amidine Coupling at Pt(IV) and Pt(II) Centers. An Easy Entry to Imidoylamidine Complexes. *Inorg. Chem.* **2005**, *44* (14), 5152–5160. <https://doi.org/10.1021/ic050037q>.
- (27) Kang, S.-G.; Kim, J.-S.; Kim, J.-K. Oxidative Dehydrogenation of Hexaaza Macroyclic Nickel(II) Complexes Bearing Two N-Alkyl Pendant Arms: Preparation of New Complexes Containing Imidoylamidine Linkages. *Bull. Korean Chem. Soc.* **2007**, *28* (6), 1053–1056. <https://doi.org/10.5012/bkcs.2007.28.6.1053>.
- (28) Castañeda, R.; Harriman, K. L. M.; Wong, J. W. L.; Gabidullin, B.; Murugesu, M.; Brusso, J. L. Rational Design of Tetranuclear Complexes Employing N-Imidoylamidine Based Ligands. *Eur. J. Inorg. Chem.* **2019**, *2019* (7), 963–972. <https://doi.org/10.1002/ejic.201801412>.
- (29) Kopylovich, M. N.; Haukka, M.; Kirillov, A. M.; Kukushkin, V. Yu.; Pombeiro, A. J. L. Unsymmetrical NiII–Imidoylamidine Complexes Derived from a Novel Oxime-Mediated Single-Pot Reaction of Nitriles. *Chem. – Eur. J.* **2007**, *13* (3), 786–791. <https://doi.org/10.1002/chem.200600765>.
- (30) Boéré, R. T.; Roemmele, T. L.; Yu, X. Unsymmetrical 1λ3-1,2,4,6-Thiatriazinyls with Aryl and Trifluoromethyl Substituents: Synthesis, Crystal Structures, EPR Spectroscopy, and Voltammetry. *Inorg. Chem.* **2011**, *50* (11), 5123–5136. <https://doi.org/10.1021/ic2003996>.
- (31) Kajiwara, T.; Kamiyama, A.; Ito, T. Complexed Bridging Ligand , {Cu(Bptap) 2 }, as a Ferromagnetic Coupler. *Chem. Commun.* **2002**, *0* (12), 1256–1257. <https://doi.org/10.1039/B202967G>.
- (32) Tong, M.-L.; Wu, Y.-M.; Tong, Y.-X.; Chen, X.-M.; Chang, H.-C.; Kitagawa, S. Rational Design of a Ferromagnetic Trinuclear Copper(II) Complex with a Novel in-Situ Synthesised Metalloligand. *Eur. J. Inorg. Chem.* **2003**, *2003* (13), 2385–2388. <https://doi.org/10.1002/ejic.200300197>.
- (33) Lewandowska-Andralojc, A.; Polyansky, D. E. Mechanism of the Quenching of the Tris(Bipyridine)Ruthenium(II) Emission by Persulfate: Implications for Photoinduced Oxidation Reactions. *J. Phys. Chem. A* **2013**, *117* (40), 10311–10319. <https://doi.org/10.1021/jp407573d>.
- (34) Khnayzer, R. S.; Thoi, V. S.; Nippe, M.; King, A. E.; Jurss, J. W.; El Roz, K. A.; Long, J. R.; Chang, C. J.; Castellano, F. N. Towards a Comprehensive Understanding of Visible-Light Photogeneration of Hydrogen from Water Using Cobalt(Ii) Polypyridyl Catalysts. *Energy Env. Sci* **2014**, *7* (4), 1477–1488. <https://doi.org/10.1039/c3ee43982h>.
- (35) Krishnan, C. V.; Sutin, N. Homogeneous Catalysis of the Photoreduction of Water by Visible Light. 2. Mediation by a Tris(2,2'-Bipyridine)Ruthenium(II)-Cobalt(II) Bipyridine System. *J Am Chem Soc* **1981**, *103* (8), 2141–2142. <https://doi.org/10.1021/ja00398a066>.

5.8 Supporting information

Vincent Picard^a, Jaclyn Brusso^b and Garry S. Hanan^a

^a Département de Chimie, Université de Montréal 1375 Avenue Thérèse-Lavoie-Roux, Montréal, Québec, H2V-0B3, Canada.

Email: Garry.hanan@umontreal.ca

^b Department of Chemistry and Biomolecular Sciences, University of Ottawa, 150 Louis Pasteur, Ottawa, Ontario, Canada K1N 6N5, Canada. Email: jbrusso@uottawa.ca

Table of content

Synthesis.....	234
Electrochemistry.....	235
<i>Figure 99: Reduction voltammograms of Co(dmgH)₂(Pyr)Cl</i>	235
<i>Figure 100: Reduction voltammograms of Co(dmgH)₂(dmap)Cl</i>	236
<i>Figure 101: Reduction voltammograms of Co(Py₂ImAm)₂.....</i>	236
<i>Figure 102: Reduction voltammograms of Co₃(Pm₂ImAm)₂</i>	237
<i>Figure 103: Square wave voltammograms of Co(Py₂ImAm)₂ in DMF with triethylammonium PF₆ as supporting electrolyte</i>	237
Figure 104: Square wave voltammograms of Co ₃ (Pm ₂ ImAm) ₂ in DMF with triethylammonium PF ₆ as supporting electrolyte	238
Spectro-electrochemistry.....	238
Figure 105: Spectro-electrochemistry spectra of the [Co ^{II} (Py ₂ ImAm) ₂ Cl ₄] from 0 to -2v ..	239
Figure 106: Spectro-electrochemistry spectra of the [Co ^{II} (Py ₂ ImAm) ₂ Cl ₄] from 0 to 1.6v	240
Figure 107: Zoom-in of the spectro-electrochemistry spectra of the [Co ^{II} (Py ₂ ImAm) ₂ Cl ₄] (0 to 1.6v)	240
Figure 109: Spectro-electrochemistry spectra of the [Co ^{II} ₃ (Pm ₂ ImAm) ₂ Cl ₄] x5H ₂ O from 0 to -2v.....	242
Figure 110: Spectro-electrochemistry spectra of the [Co ^{II} ₃ (Pm ₂ ImAm) ₂ Cl ₄] x5H ₂ O from 0 to 1.8v.....	243

Figure 111: Spectro-electrochemistry spectra of the $[Co^{II}_3(Pm_2ImAm)_2Cl_4] \times 5H_2O$ from -2 to 1.8v.....	244
Preparation of photoreactions and set up of gas chromatography	244
<i>Figure 112: Turn Over Frequency of hydrogen evolution for $Co(dmgH_2)Cl_2$ in association with $1x10^{-4}M [Ru(bpy)_3]^{2+}$ in DMF.....</i>	245
<i>Figure 113: Turn Over Frequency of hydrogen evolution for $Co(Py_2ImAm)_2Cl_2$ in association with $1x10^{-4}M [Ru(bpy)_3]^{2+}$ in DMF.....</i>	246
<i>Figure 114: Turn Over Frequency of hydrogen evolution for $Co_3(Pm_2ImAm)_2Cl_2$ in association with $1x10^{-4}M [Ru(bpy)_3]^{2+}$ in DMF</i>	247
<i>Figure 115: Turn Over Frequency of hydrogen evolution for $1x10^{-4}M$ catalyst ($5x10^{-5}M$ for $Co_3(Pm_2ImAm)_2$) in association with $1x10^{-4}M [Ru(bpy)_3]^{2+}$in DMF.....</i>	248
<i>Figure 116: Turn Over Frequency of hydrogen evolution for $1x10^{-5}M$ catalyst in association with $1x10^{-4}M [Ru(bpy)_3]^{2+}$in DMF.....</i>	249
<i>Figure 117: Turn Over Frequency of hydrogen evolution for $1x10^{-6}M$ catalyst in association with $1x10^{-4}M [Ru(bpy)_3]^{2+}$ in DMF</i>	250
<i>Figure 118: Turn Over Frequency of hydrogen evolution for $1x10^{-5}M Co(Py_2ImAm)_2$ in association with $1x10^{-4}M [Ru(bpy)_3]^{2+}$in DMF, with different amounts of water</i>	251
<i>Figure 119: Turn Over Frequency of hydrogen evolution for $Co_3(Pm_2ImAm)_2$ in association with $1x10^{-4}M [Ru(bpy)_3]^{2+}$ in water</i>	252

5.8.1 Synthesis

Synthesis of the $(Py_2ImAm)^{1,2}$, $Co(Py_2ImAm)_2^3$ and $Co_3(Pm_2ImAm)_2^3$ was done according to the literature procedure reported earlier.

5.8.2 Electrochemistry

Electrochemical measurements were performed in pure dimethylformamide purged with argon at room temperature with an SP-50 Biologic potentiostat. DMF was dried and distilled before use. The cell has been placed in the oven at 140°C at least 30 minutes before the experiment and is blanketed in a nitrogen atmosphere immediately thereafter. The electrolyte (5 mL of Et₄NPF₆, 0.1 M as supporting electrolyte) is inserted with a syringe on the septum and the solution is purged for at least 10 min before any measurement. A glassy carbon electrode was used as a working electrode, the counter electrode was a Pt wire, and the silver wire was the pseudo-reference electrode. The concentrations of complexes were analyzed at 1 mM. The reference of electrochemical potential was set using 1 mM ferrocene as an internal standard and the values of potentials are reported vs. SCE^[1]. The nitrogen atmosphere are kept above the solution during the measurement. Cyclic voltammograms were obtained at a scan rate of 100 mv.s⁻¹ and a current amplitude of 100 mA.

5.8.3 Cyclic voltammetry

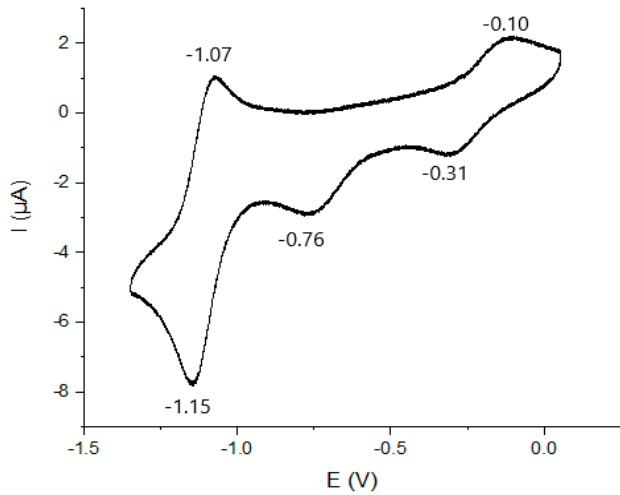


Figure 99. Reduction voltammograms of Co(dmgH)₂(pyr)Cl in DMF with triethylammonium PF₆ as supporting electrolyte

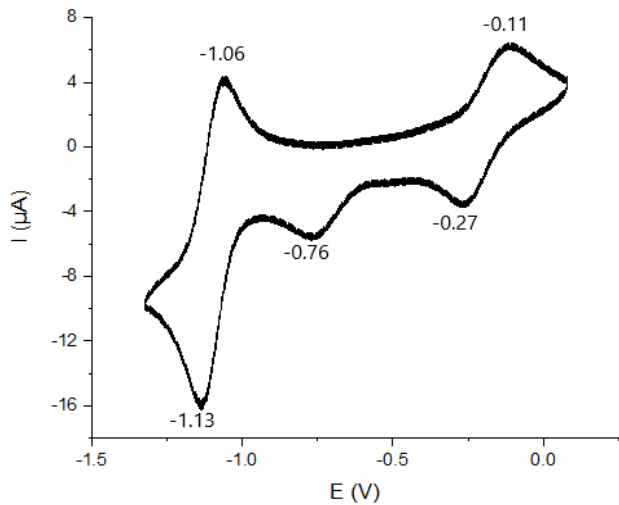


Figure 100. Reduction voltammograms of $\text{Co}(\text{dmgH})_2(\text{pyr})\text{Cl}$ in DMF with triethylammonium PF_6^- as supporting electrolyte

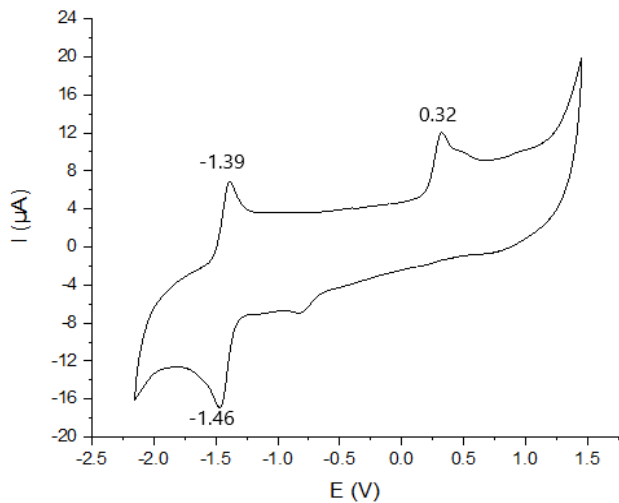


Figure 101. Reduction voltammograms of $\text{Co}(\text{Py}_2\text{ImAm})_2$ in DMF with triethylammonium PF_6^- as supporting electrolyte

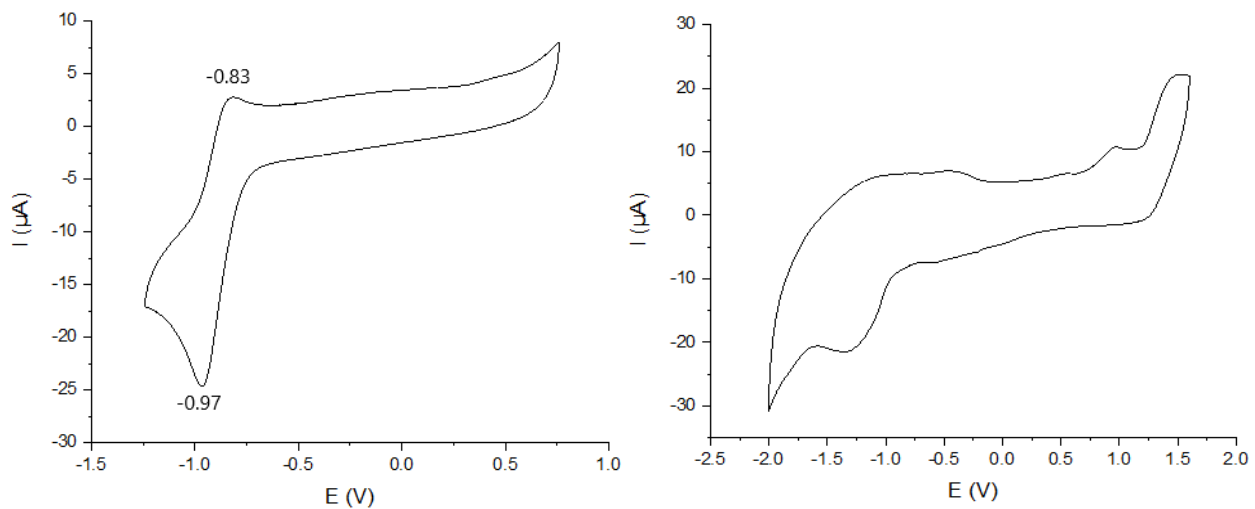


Figure 102. Reduction voltammograms of $\text{Co}_3(\text{Pm}_2\text{ImAm})_2$ in DMF with triethylammonium PF_6^- as supporting electrolyte

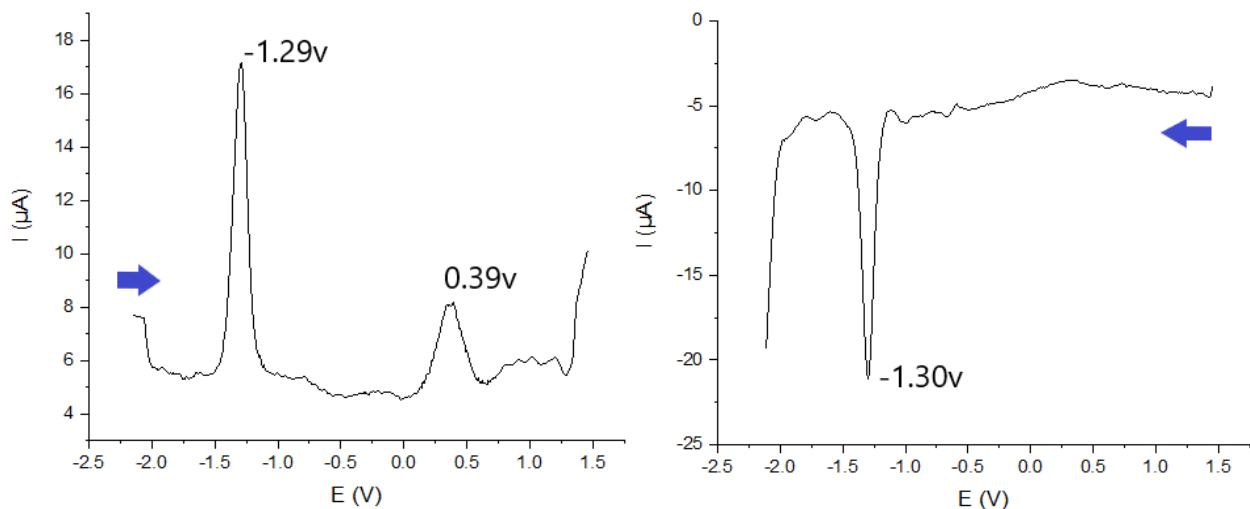


Figure 103. Square wave voltammograms of $\text{Co}(\text{Py}_2\text{ImAm})_2$ in DMF with triethylammonium PF_6^- as supporting electrolyte

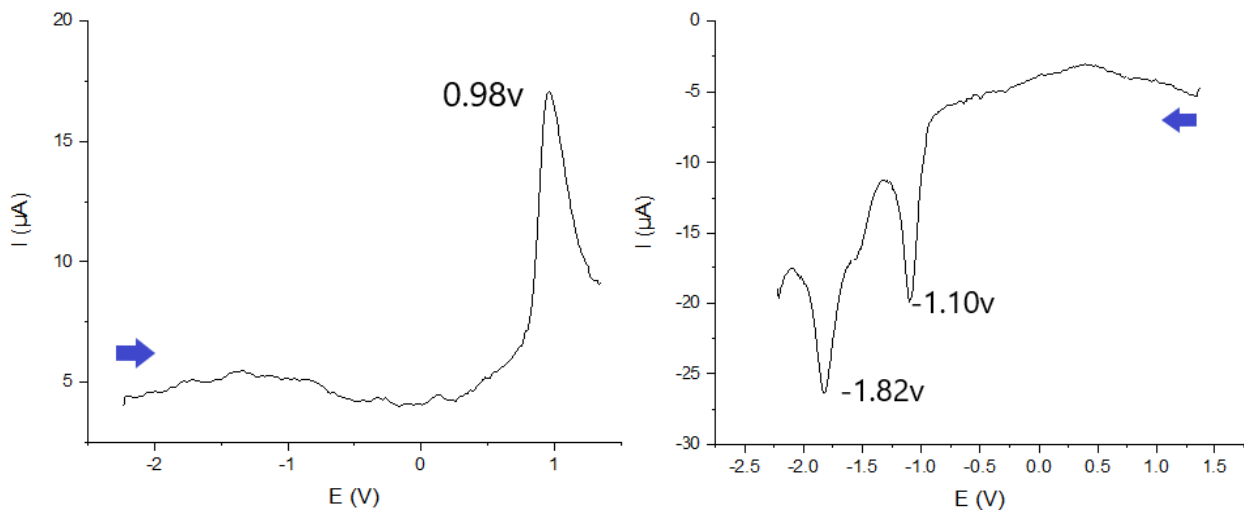


Figure 104. Square wave voltammograms of $\text{Co}_3(\text{Pm}_2\text{ImAm})_2$ in DMF with triethylammonium PF_6^- as supporting electrolyte

5.8.4 Spectro-electrochemistry

The Quartz cell is conditioned two times with the solution before the analysis. A blank sample was run with the solvent and electrolyte before the analysis and was subtracted from the results. Then we run the sample of catalysis at 3mM (around 2 mg of catalyst in 1.5 mL of solvent, with 0.1 M of tetrabutylammonium PF_6^-). Potentials of 0 V (for the Co^{III}), -0.7 V (for the Co^{II}), and -1.1 V (for the Co^{I}) are applied 5 min before the analysis and is kept active during all data collection. A Cary 600i UV-vis-NIR spectrometer was used for the measurements.

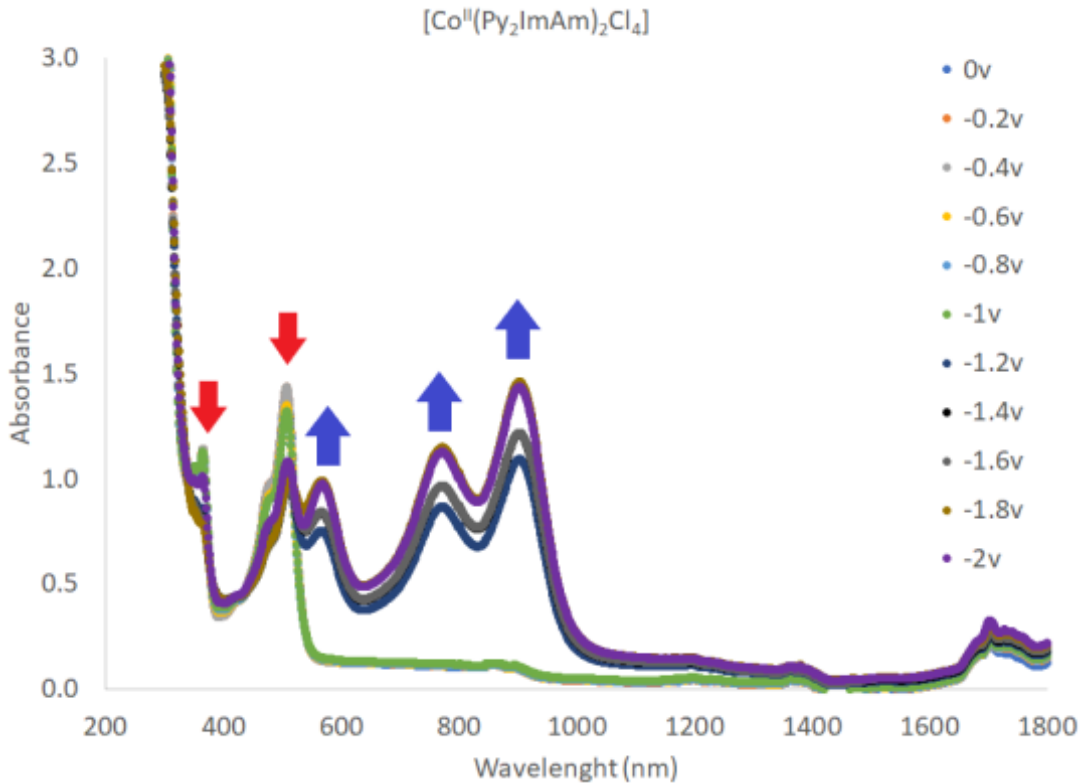


Figure 105. Spectro-electrochemistry spectra of the $[\text{Co}^{\text{II}}(\text{Py}_2\text{ImAm})_2\text{Cl}_4]$ from 0 to -2v

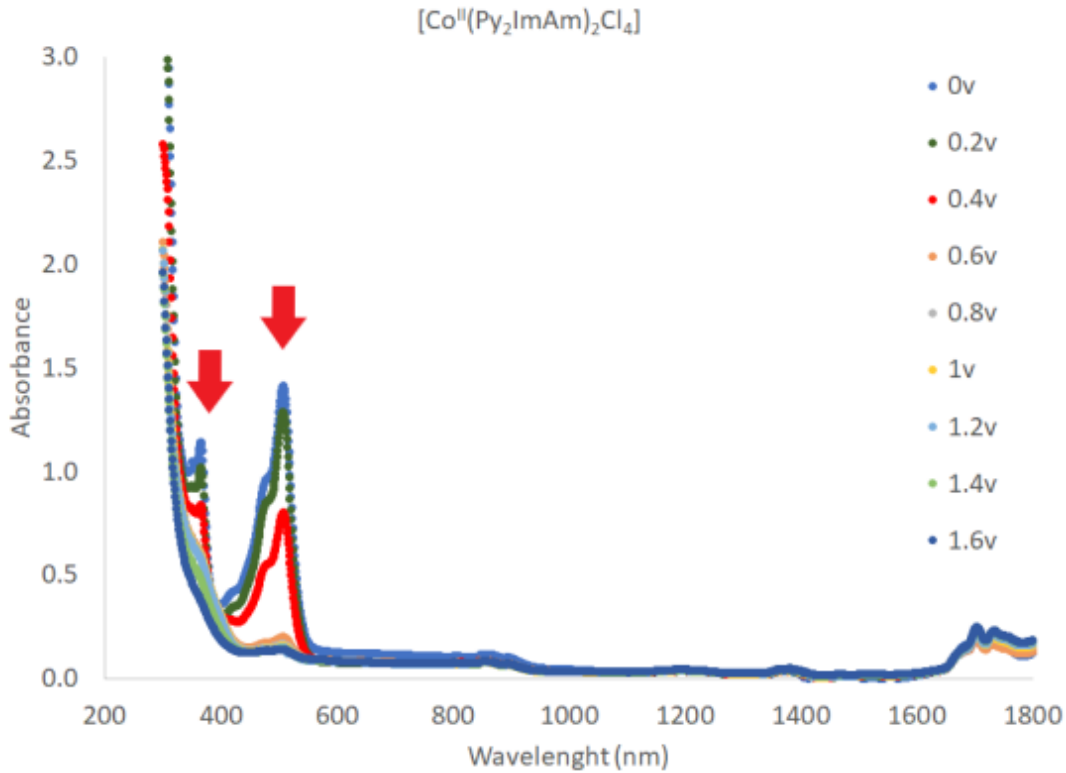


Figure 106. Spectro-electrochemistry spectra of the $[\text{Co}^{\text{II}}(\text{Py}_2\text{ImAm})_2\text{Cl}_4]$ from 0 to 1.6v

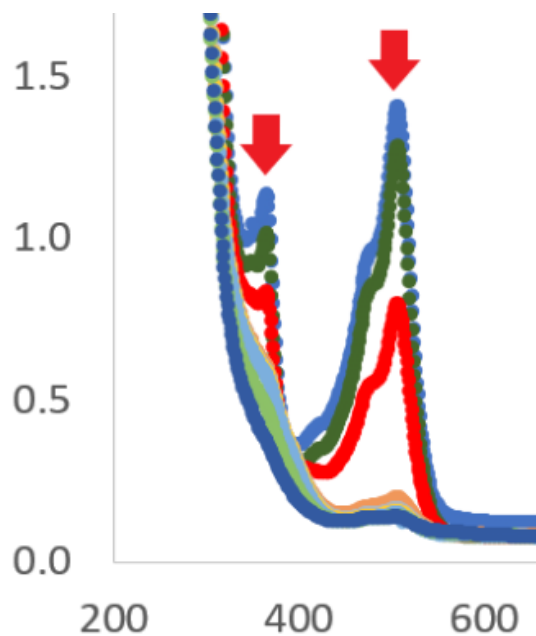


Figure 107. Zoom-in of the spectro-electrochemistry spectra of the $[\text{Co}^{\text{II}}(\text{Py}_2\text{ImAm})_2\text{Cl}_4]$ (0 to 1.6v)
Chapitre 5 - Properties and hydrogen evolution of N-imidoylamidine ligand cobalt(II) containing complexes

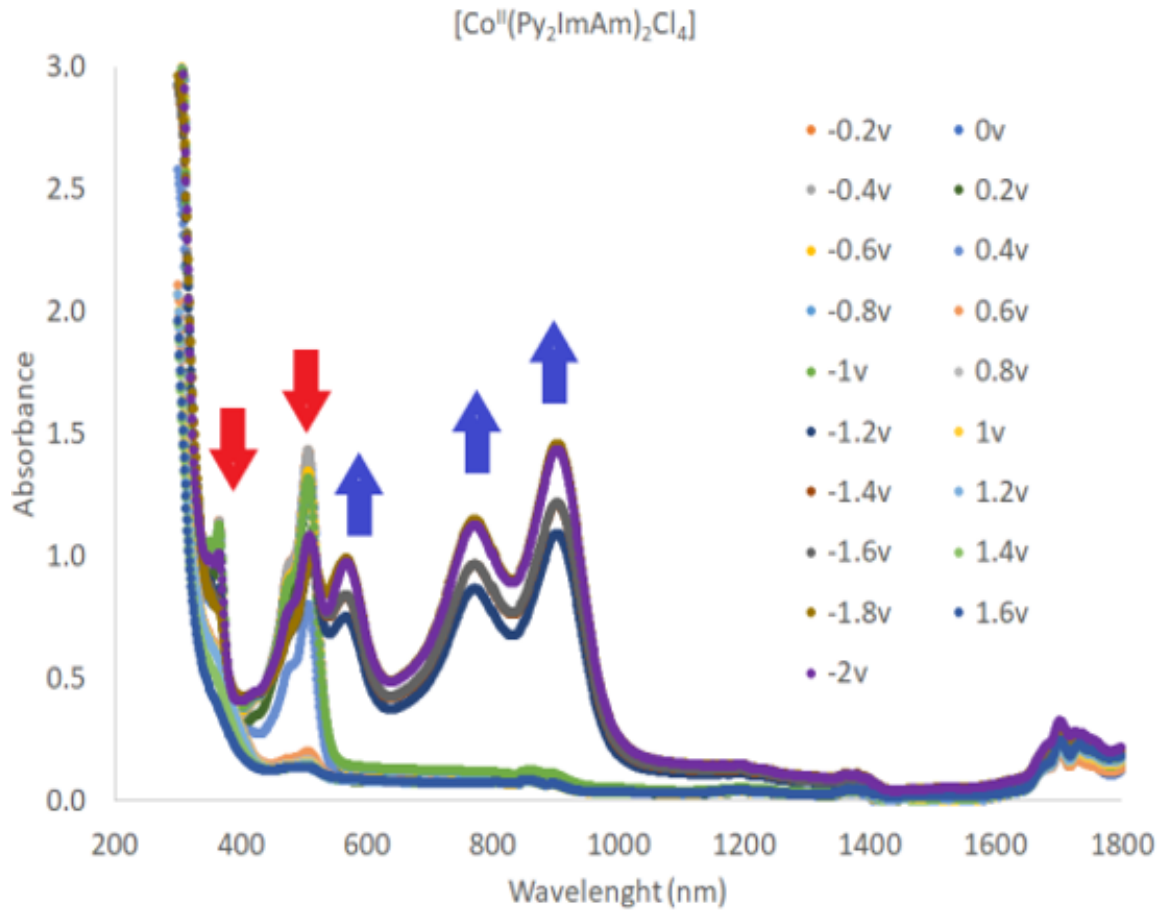


Figure 108. Spectro-electrochemistry spectra of the $[\text{Co}^{\text{II}}(\text{Py}_2\text{ImAm})_2\text{Cl}_4]$ from -2 to 1.6v

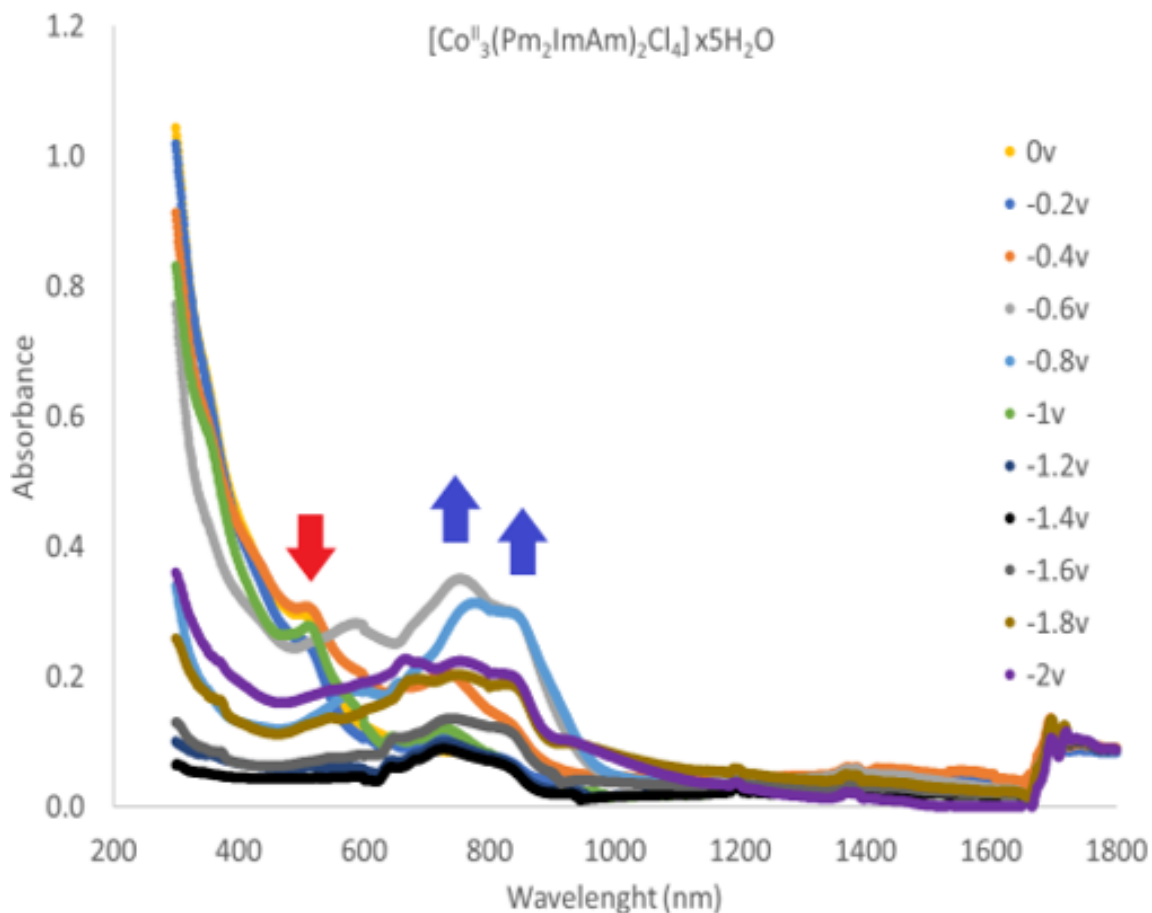


Figure 109. Spectro-electrochemistry spectra of the $[\text{Co}^{\text{II}}_3(\text{Pm}_2\text{ImAm})_2\text{Cl}_4] \times 5\text{H}_2\text{O}$ from 0 to -2v

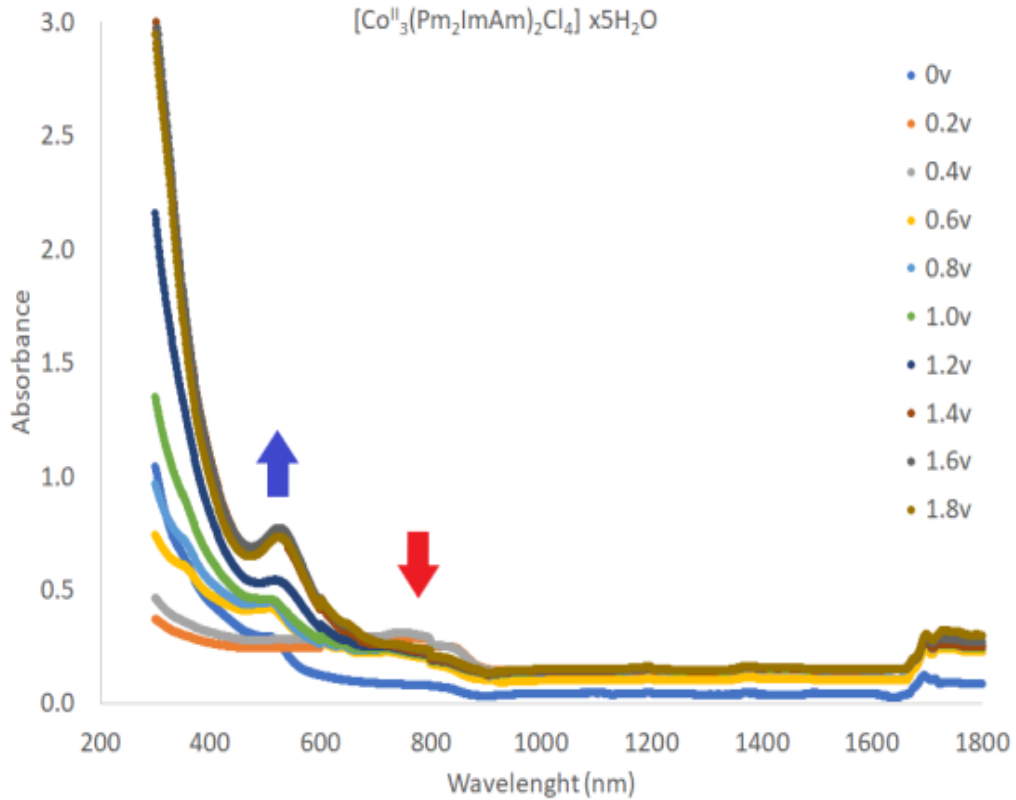


Figure 110. Spectro-electrochemistry spectra of the $[\text{Co}^{\text{II}}_3(\text{Pm}_2\text{ImAm})_2\text{Cl}_4] \times 5\text{H}_2\text{O}$ from 0 to 1.8v

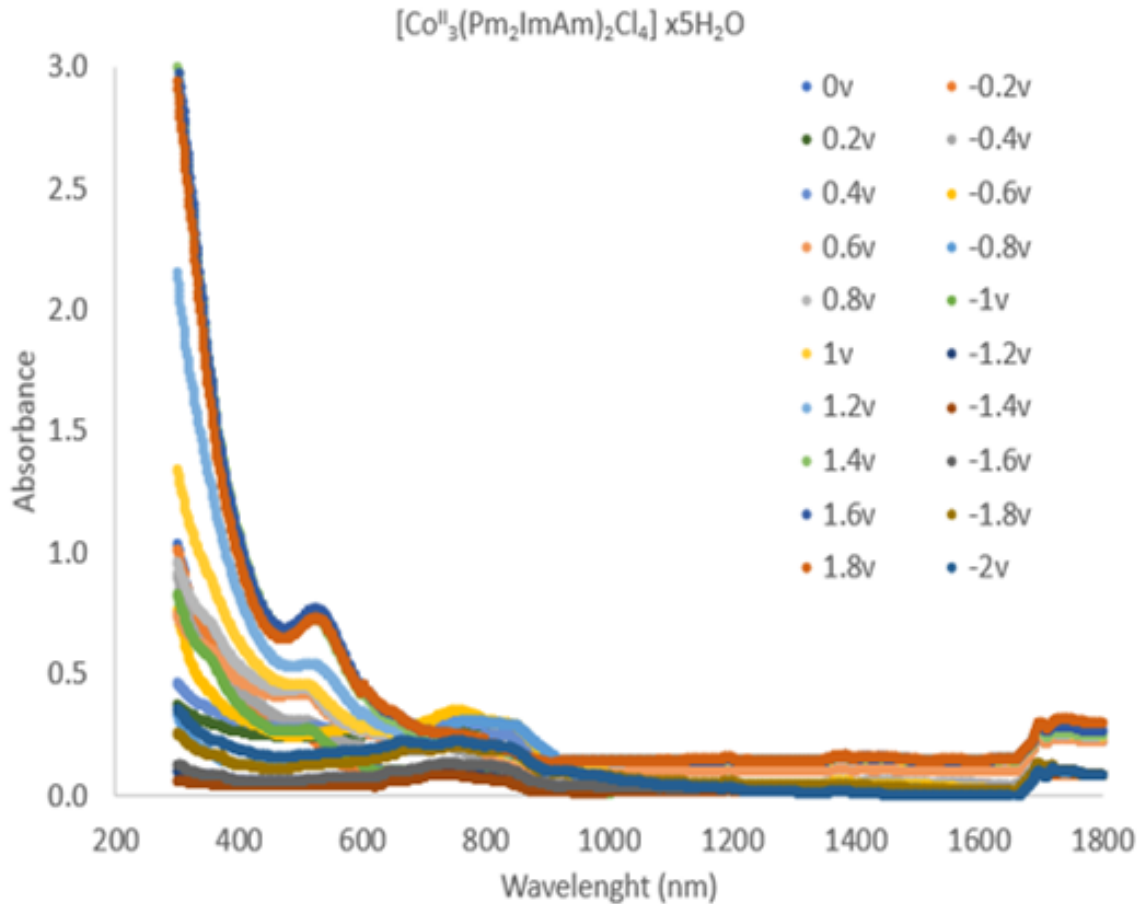


Figure 111. Spectro-electrochemistry spectra of the $[\text{Co}^{\text{II}}_3(\text{Pm}_2\text{ImAm})_2\text{Cl}_4] \times 5\text{H}_2\text{O}$ from -2 to 1.8v

5.8.5 Preparation of photoreactions and set up of gas chromatography

Monitoring of hydrogen evolution is measured using a Perkin Elmer Clarus-480 gas chromatograph (GC) with a thermal conductivity detector, argon as a carrier, and eluant gas, a 7' HayeSep N 60/80 pre-column, a 9' molecular sieve 13x45/60 column, and a 2 mL injection loop. Three distinct solutions were prepared, 1) photosensitizer, 2) catalyst and 3) sacrificial donor and acid source (HBF_4 48% water) to obtain 5 mL of sample solutions in standard 20 mL headspace vials. The resulting molar concentration of photocatalytic components are 0.1 mM for the photosensitizers $\text{Ru}(\text{bpy})_3(\text{PF}_6)_2$, respectively 0.1, 0.01, and 0.001 mM for all compounds, except for the tri-cobalt catalyst, where the 0.1mM was replaced for 0.05mM because of solubility. The sacrificial electron donor was 1 M of TEOA (in DMF) and 0.1M of A.A (in water). The proton source used was 0.1 mM of HBF_4 and 0.56M of water.

The vials are placed on LED panel in a thermostatic bath set at 20°C. They were sealed with a rubber septum pierced with two stainless steel tubes. The first tube carried an argon flow pre-bubbled in spectrograde solvent. The flow was set to 5 mL/min (adjusted with a manual flow controller (Porter, 1000) and referenced with a digital flowmeter (Perkin Elmer FlowMark). The second tube leads the flow to the GC sample loop through a 2 mL overflow protection vial, then through an 8-port stream select valve (VICCI), and finally to GC sample loop. A microprocessor (Arduino Uno) coupled with a custom PC interface allowed for timed injections. For calibration of H₂ production rate at a specific argon flow, a syringe pump (New Era Pump) equipped with a gas-tight syringe (SGE) and a 26s gauge needle (Hamilton) was used to bubble different rates of pure hydrogen gas into the sample, to a minimum of 0.5 μL/minute. This gave a linear fit for peak area for H₂ versus the flow rates of H₂. For calibration testing, stock cylinders of known concentration of H₂ in argon replaced the argon flow (inserted at the pre-bubbler, to keep the same vapor matrix).

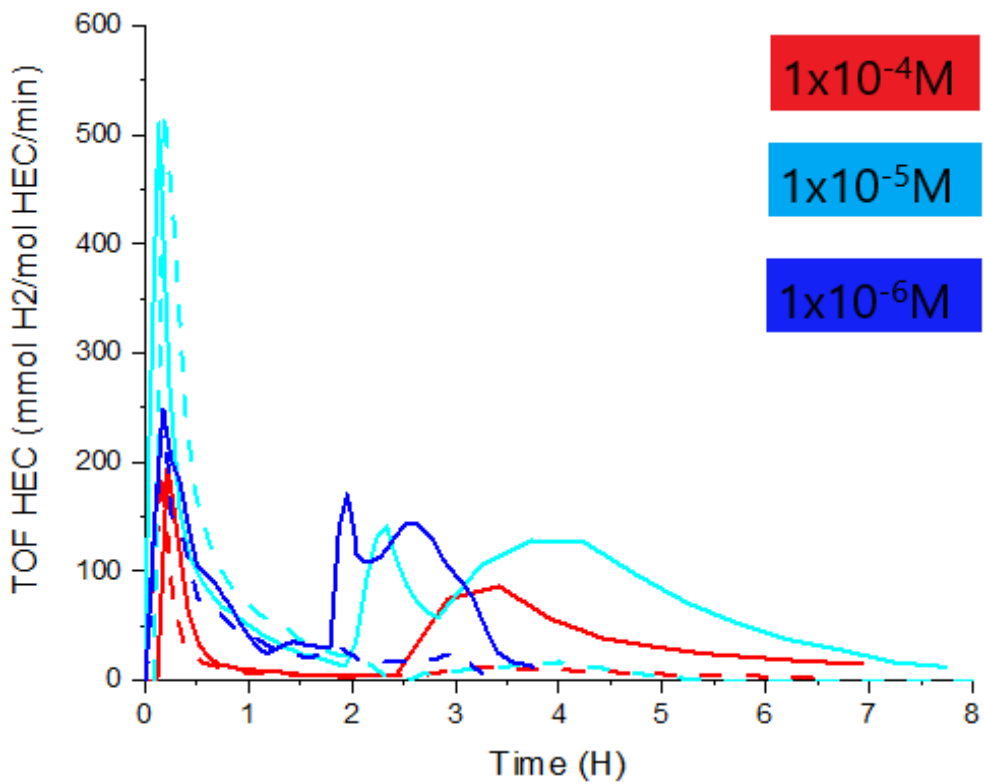


Figure 112. Turn Over Frequency of hydrogen evolution for Co(dmgH₂)Cl₂ in association with 1x10⁻⁴M [Ru(bpy)₃]²⁺ in DMF

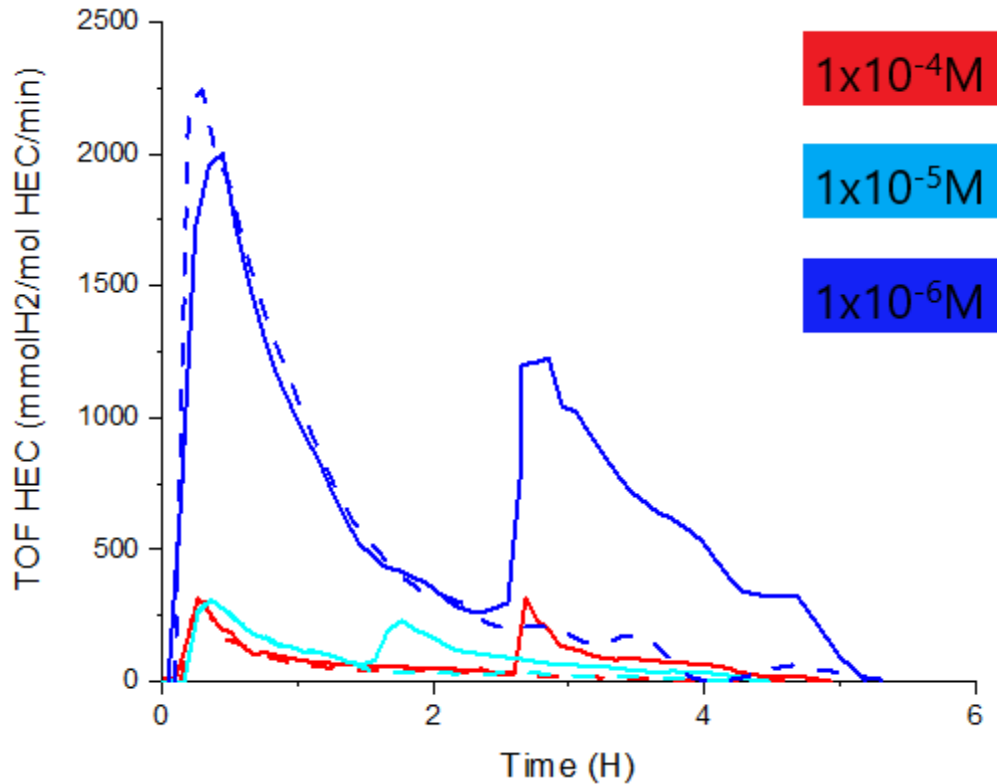


Figure 113. Turn Over Frequency of hydrogen evolution for Co(Py₂ImAm)₂Cl₂ in association with 1x10⁻⁴M [Ru(bpy)₃]²⁺ in DMF

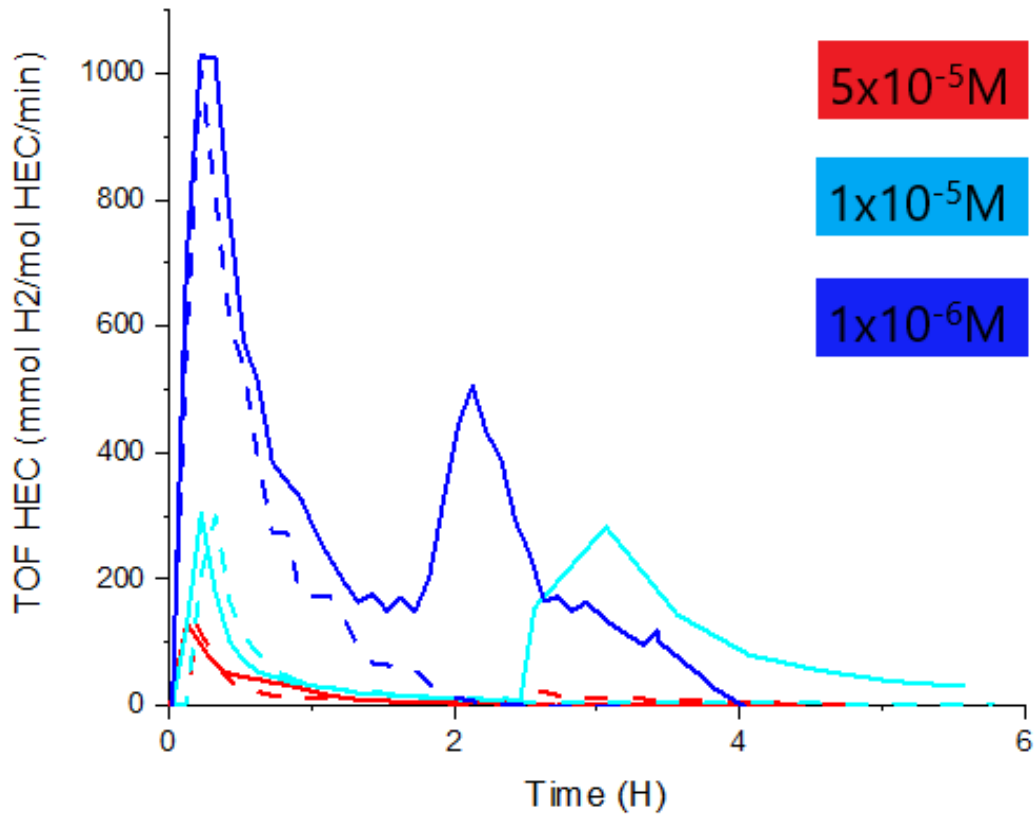


Figure 114. Turn Over Frequency of hydrogen evolution for $\text{Co}_3(\text{Pm}_2\text{ImAm})_2\text{Cl}_2$ in association with $1 \times 10^{-4} M [\text{Ru}(\text{bpy})_3]^{2+}$ in DMF

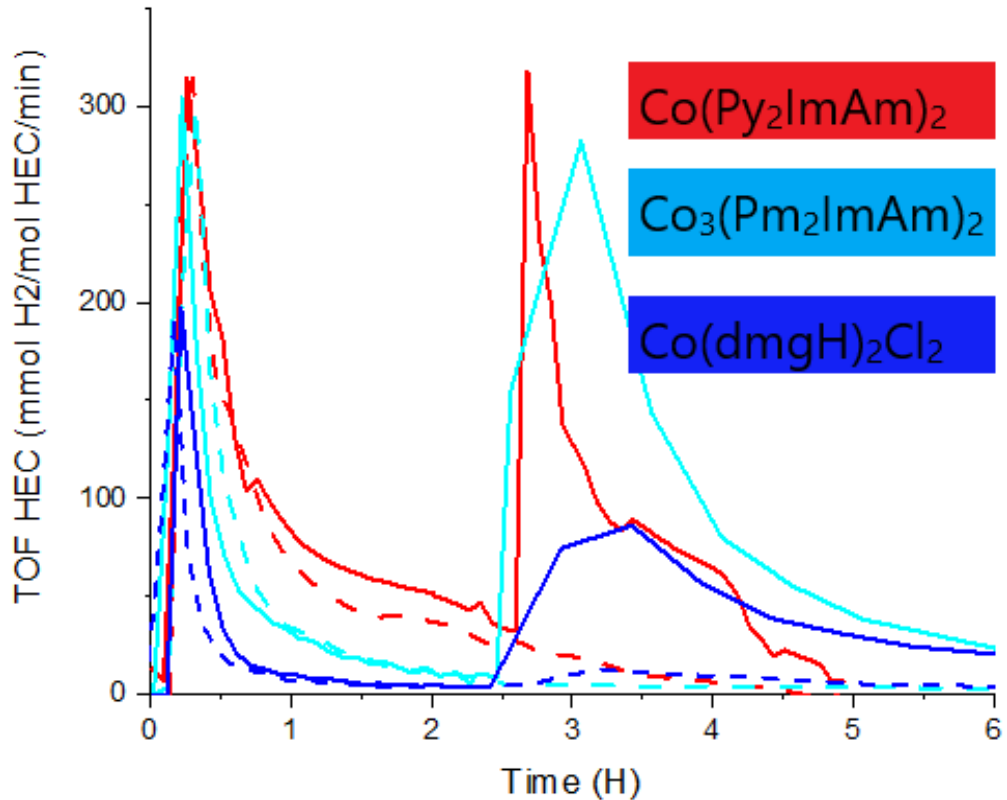


Figure 115. Turn Over Frequency of hydrogen evolution for $1 \times 10^{-4}\text{M}$ catalyst ($5 \times 10^{-5}\text{M}$ for $\text{Co}_3(\text{Pm}_2\text{ImAm})_2$) in association with $1 \times 10^{-4}\text{M} [\text{Ru}(\text{bpy})_3]^{2+}$ in DMF

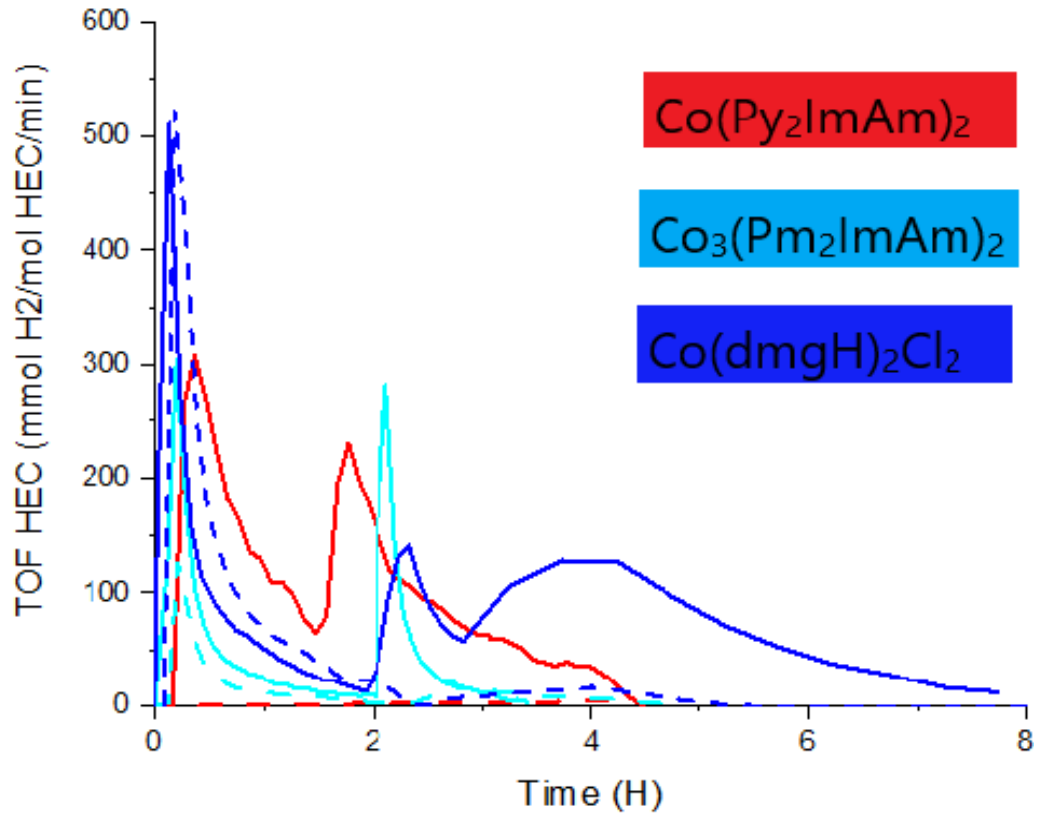


Figure 116. Turn Over Frequency of hydrogen evolution for 1×10^{-5} M catalyst in association with 1×10^{-4} M $[\text{Ru}(\text{bpy})_3]^{2+}$ in DMF

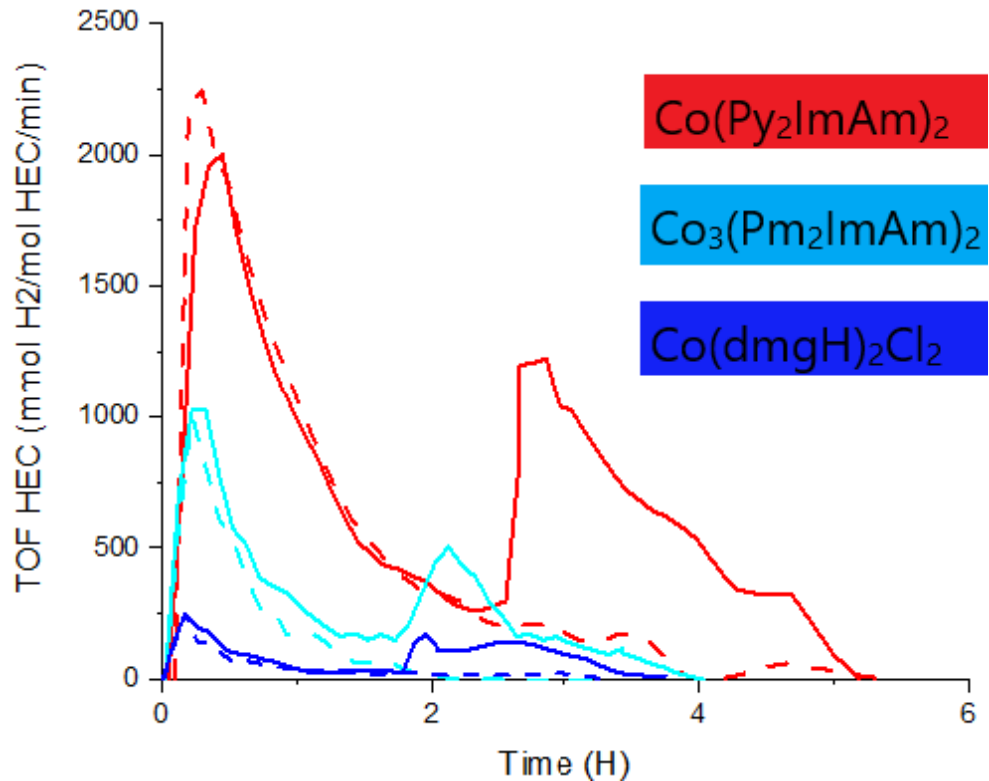


Figure 117. Turn Over Frequency of hydrogen evolution for $1 \times 10^{-6}\text{M}$ catalyst in association with $1 \times 10^{-4}\text{M} [\text{Ru}(\text{bpy})_3]^{2+}$ in DMF

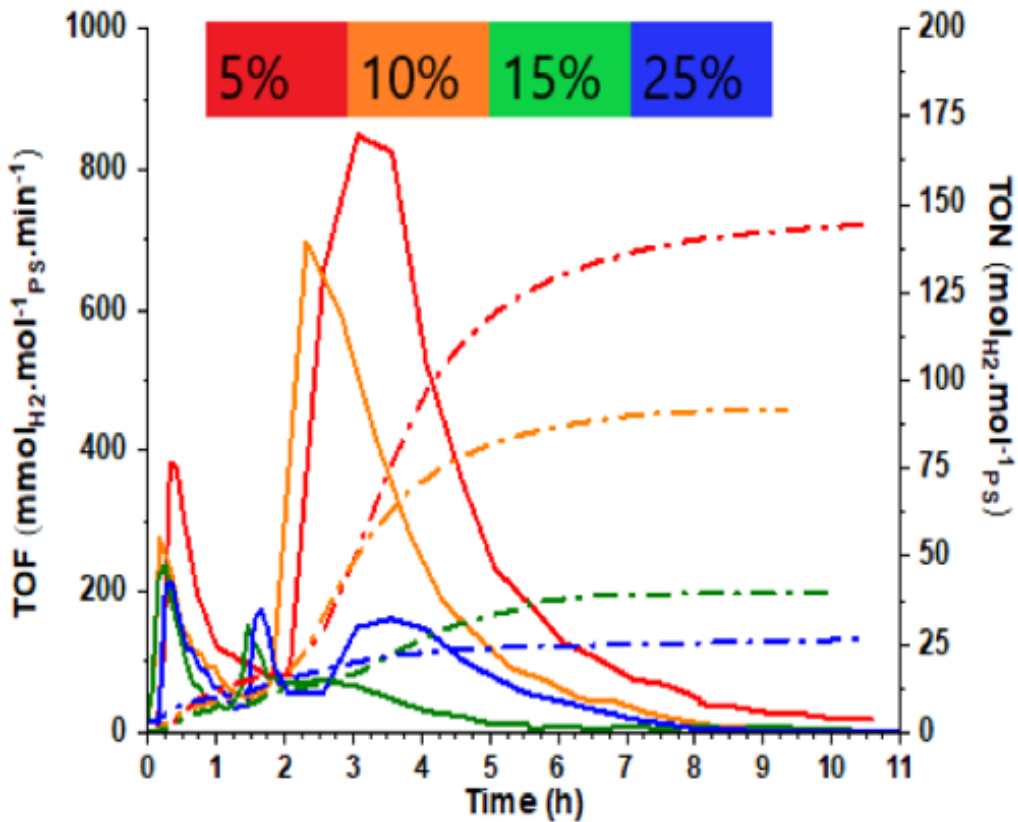


Figure 118. Turn Over Frequency of hydrogen evolution for 1×10^{-5} M $\text{Co}(\text{Py}_2\text{ImAm})_2$ in association with 1×10^{-4} M $[\text{Ru}(\text{bpy})_3]^{2+}$ in DMF, with different amounts of water

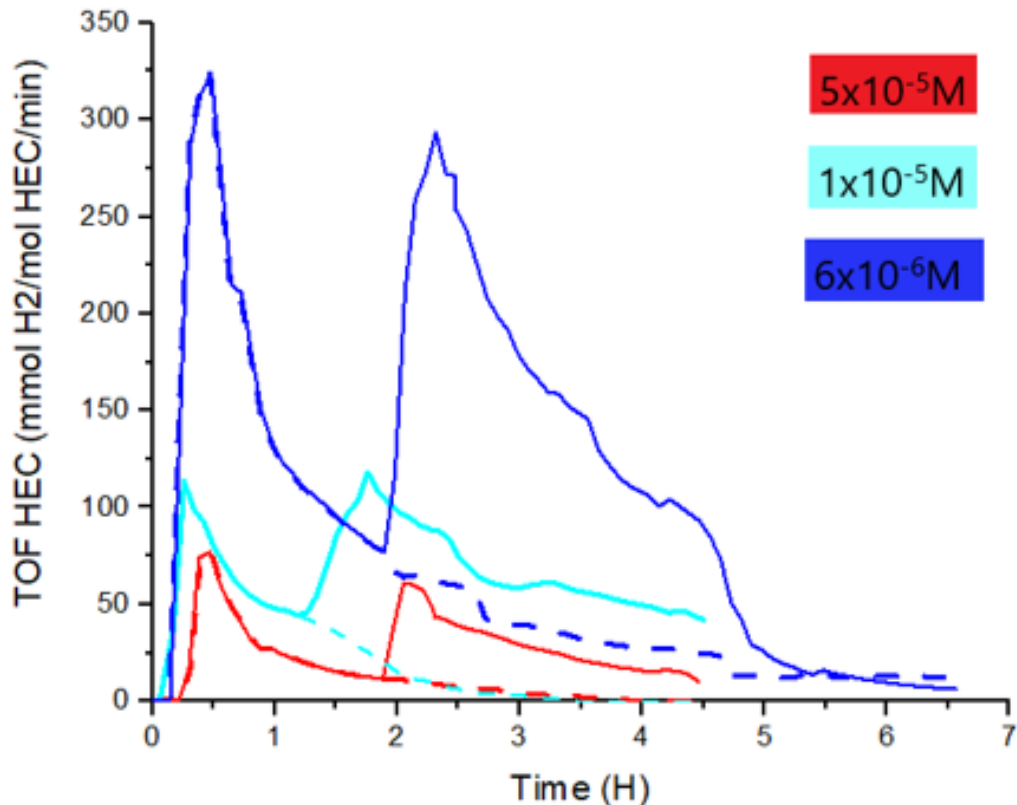


Figure 119. Turn Over Frequency of hydrogen evolution for $\text{Co}_3(\text{Pm}_2\text{ImAm})_2$ in association with $1 \times 10^{-4}\text{M} [\text{Ru}(\text{bpy})_3]^{2+}$ in water

References

- (1) Yousaf, M.; Yutronkie, N. J.; Castañeda, R.; Klein, J. A.; Brusso, J. Boratriazines: Inducing Luminescence through Boron Incorporation into a Terpy-Type Framework. *New J. Chem.* **2017**, *41* (20), 12218–12224. <https://doi.org/10.1039/C7NJ02462B>.
- (2) Castañeda, R.; Hollingshead, A.; Gabidullin, B.; Brusso, J. L. Probing the Coordination Chemistry of N-2-Pyridylimidoyl-2-Pyridylamidine: A Versatile Ligand with Multiple Coordination Sites. *Cryst. Growth Des.* **2017**, *17* (12), 6572–6578. <https://doi.org/10.1021/acs.cgd.7b01232>.
- (3) Castañeda, R.; Rouzières, M.; Clérac, R.; Brusso, J. L. Controlling the Nuclearity and Topology of Cobalt Complexes through Hydration at the Ppm Level. *J. Mater. Chem. C* **2020**, *8* (13), 4401–4407. <https://doi.org/10.1039/C9TC06261K>.

6) Chapitre 6 – Conclusions et perspectives

6.1 Sommaire

Les propriétés de plusieurs types de catalyseurs ont été étudiés principalement pour leurs propriétés catalytiques pour la génération d'hydrogène par photocatalyse. Les catalyseurs étudiés incluent les catalyseurs à base de polypyridyl, les cobaloximes et les N-imydoylamidine. Parmis les types de catalyseurs étudiés, les catalyseurs de type polypyridyl sont les plus prometteurs dans l'eau. Toutefois, l'étude de ces catalyseurs nous a permis de constater le potentiel limité de modification applicable sur ces catalyseurs. Ce faisant, l'étude des cobaloximes, bien que souffrant de leur instabilité en solution et de leur insolubilité dans l'eau, pourraient s'avérer très prometteurs si on intègre des cycles rigides tels que les cyclohexyl pour stabiliser la molécule, jumelé à des fonctions hydro-solubles tels que des acides carboxyliques ou des sels. Finalement, l'étude des catalyseurs à base de N-imidoamidine a démontré qu'ils sont une nouvelle catégorie de catalyseurs prometteurs et qu'il est possible de les modifier de sorte qu'ils soient solubles dans l'eau. Ce faisant, il pourrait également être possible de les modifier par des fonctions hydrosolubles et d'approfondir l'étude de leur potentiel dans l'eau. Toutefois, il faudrait améliorer leur stabilité et la réversibilité catalytique afin de mener ce projet à bien, puisqu'ils semblent se dégrader dès qu'ils sont sous forme de Co^{III}, en raison de leur géométrie carré plan. Les compétences du groupe Hanan dans le transfert d'électron directionnel pourraient définitivement permettre ces modifications et amener un nouveau projet inédit et prometteur. Finalement, retourner aux sources et intégrer ces connaissances à des catalyseurs à base de chlorophylles pourrait peut-être être une solution intéressante si on applique ce qui a été appris ici.

Dans l'objectif d'une vue plus globale du sujet, d'autres membres de notre groupe sont concentrés respectivement sur l'aspect de la pénurie des matériaux ainsi que de la stabilité des systèmes et de

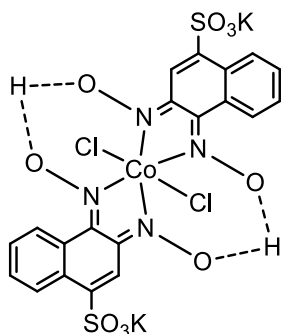
la récupération de la lumière. Dans le premier cas, l'étude des photosensibilisateurs potentiels à base de fer jumelé avec des ligand à base de guanidine est envisagée. L'objectif est de découvrir une molécule permettant de remplir la fonction de photosensibilisateur en utilisant le fer comme centre métallique, de manière à éliminer l'utilisation du ruthénium ou de l'iridium en tant que centre métallique, ceux cis étant plutôt rare et dispendieux. Le second cas de figure a un double objectif. En premier, utiliser la lumière rouge plutôt que la lumière bleue permet de réduire l'énergie des systèmes utilisés, de manière à réduire les risques de décomposition et de réaction secondaire. En second, l'utilisation de la lumière rouge par intermédiaire de systèmes conjugués permet de faciliter le passage à l'état excité des photosensibilisateur, ce qui confèrerais théoriquement une plus grande vitesse de cyclage aux systèmes. Toutefois, il faut être prudent avec cette seconde affirmation, car dans certains cas, la réduction du centre du catalyseur est le facteur limitant et cette modification pourrait amener les systèmes à devenir inactif plus rapidement, par l'entremise de la dégradation rapide du photosensibilisateur.¹

Bien que nous ne sommes pas vraiment plus près qu'avant de résoudre les multiples problèmes inhérents à la production d'hydrogène par photolyse de l'eau, des pistes intéressantes ont été amenés et les explorer pourraient permettre de résoudre partiellement les problèmes reliés à la production d'hydrogène par photolyse de l'eau. La recherche sur la photolyse de l'eau étant encore loin de son point critique, il faudra certainement encore plusieurs années avant que celle-ci soit mené à la phase de carburant au niveau industriel.

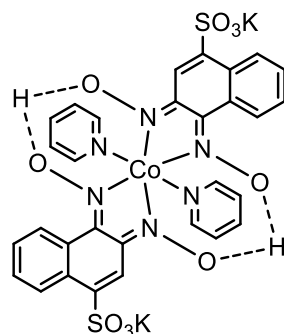
6.2 Perspectives

Le présent projet de maîtrise a permis plusieurs avancées, mais tous les projets commencés n'ont pas été menés à terme. Voici donc quelques projets qui ont été entrepris dans le cadre du présent travail.

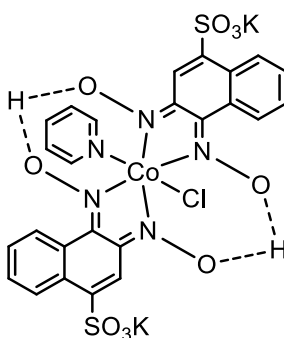
Un projet intégrant des catalyseurs hydrosolubles à base de cobaloxime a été tenté, mais a dû être abandonné en raison des nombreuses difficultés rencontrées. Il a été jugé préférable de se concentrer sur les autres projets et de mener à bien ceux-ci en premier. Voici les structures qui étaient attendus.



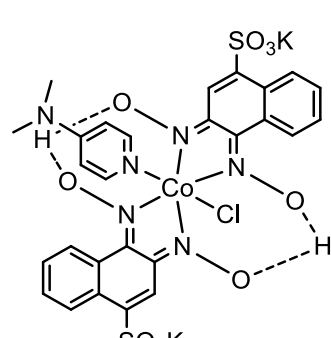
Co(k)Cl₂



Co(k)(Py)₂



Co(k)(Py)Cl



Co(k)(dmap)Cl

Figure 120. Structure des catalyseurs cobaloxime à base de sels de potassium prévue dans un projet précédent

Le problème principal était relié à la synthèse de la fonction oxime. Lors de la synthèse du précurseur, il n'était pas clair dans le travail de référence que la molécule obtenue était hors de tout doute celle qui était attendue.² Cela nous a amené à croire initialement que la synthèse avait effectivement fonctionné, mais suite à l'obtention d'une structure rayon X du produit final de la synthèse de la fonction oxime, nous avons de bonne raison de croire que la fonction alcool n'avait pas réagis et qu'il faut développer une méthode plus détaillée afin de prouver le produit de la réaction. L'utilisation du spectromètre de masse est une solution envisagée. Voici la structure rayon X obtenue.

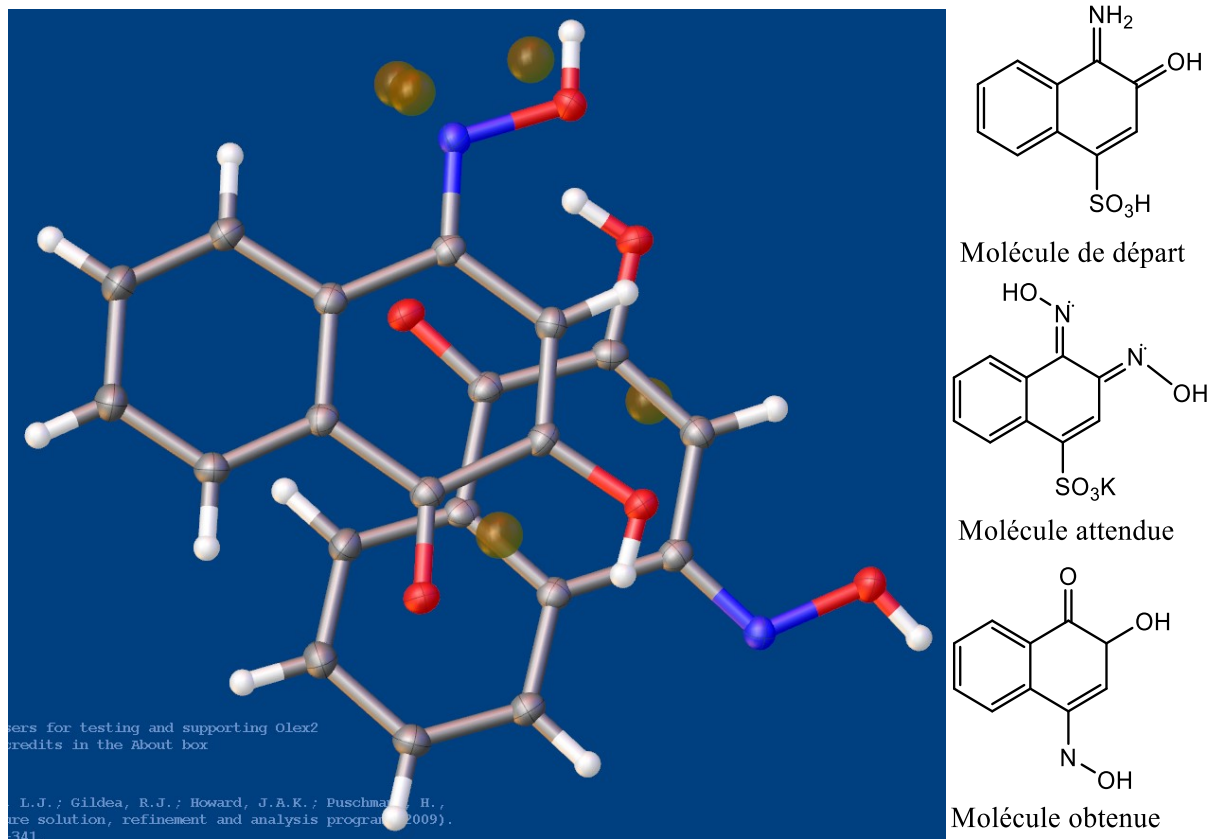


Figure 121. Structure rayon-x et chemdraw de la molécule obtenue vs la molécule attendue

Le chemin synthétique envisagé est présenté à la figure 121. Pour la synthèse de la fonction oxime, il est démontré que la sulfonation est facilement réversible en condition aqueuse, ce qui pourrait permettre de faire sauter la fonction SO_3K , même si ce ne semblait pas le cas, lors des différents tests effectués. De plus, une synthèse démarrant avec le même réactif et donnant un produit similaire à celui qui a été obtenus utilise le NaOH en tant que réactif.³ Il serait donc recommandé de faire la synthèse en utilisant plutôt une catalyse acide. L'utilisation de conditions anhydres serait recommandée pour de futurs essais. Effectivement, le produit obtenu avait une couleur jaune plutôt que vert sombre, ce qui pourrait être le signe d'un produit différent. Nous n'avons pas réussi à faire cristalliser ce produit ni à synthétiser le complexe à partir de ce produit, de sorte que toute idée n'est pour le moment qu'une supposition. Quelques articles pourraient être utile pour la suite du projet.⁴⁻⁶

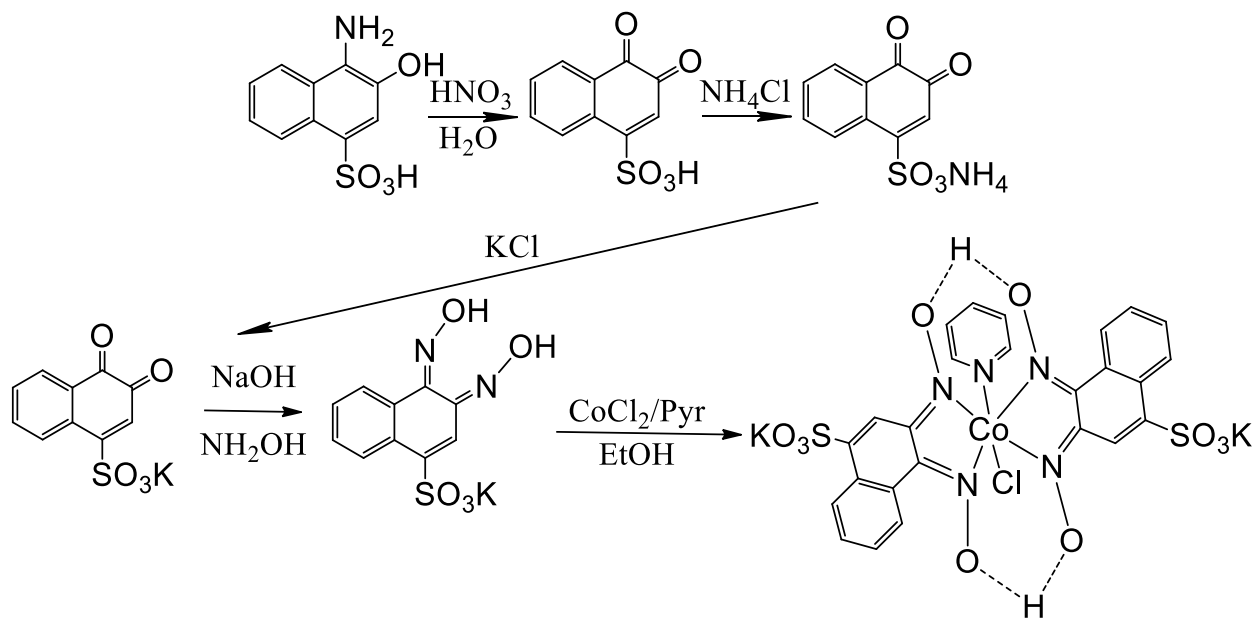
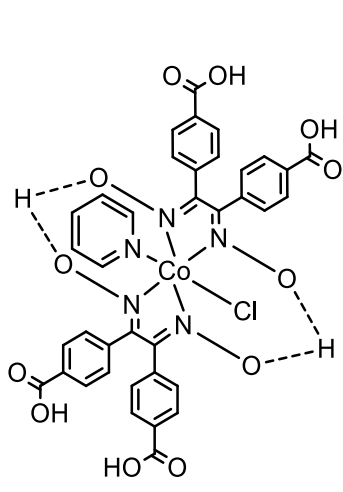


Figure 122. Chemin réactionnel envisagé pour l'obtention du catalyseur aquasoluble à base de cobaloxime

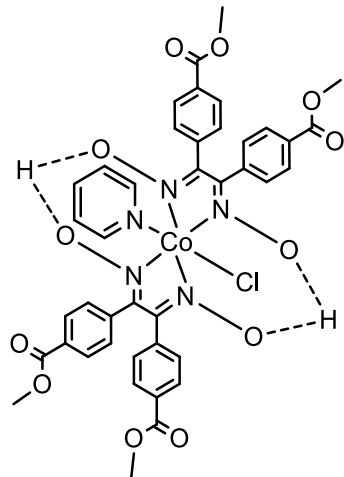
Un second projet a été lancé dans l'optique de faire des catalyseurs aquasolubles à base de cobaloxime. Bien que plusieurs références rapportent la même molécule⁷⁻⁹, ce projet fut jonché d'embuches. Les méthodes de synthèses rapportées dans ces articles ne donnent pas le même résultat lorsqu'exécuté par notre groupe. Également, de nombreuses conditions réactionnelles ont été omis, de sorte qu'il a fallu les découvrir ou les déduire par nous-même, afin que les synthèses soient un succès. Ce second projet était presque complet lorsque cette thèse a été déposée, mais il a été jugé préférable de l'écartier en raison des contraintes de temps. L'article sera tout de même publié, mais ne fera malheureusement pas partie de la présente thèse de maitrise. Les contraintes de temps nous ont poussé à favoriser l'article des N-imidoyl amidine, dans l'optique d'un meilleur travail plutôt que de compléter les deux projets mais avec une qualité moindre.



Co(A)(Py)Cl

Chemical Formula: C₃₇H₂₇ClCoN₅O₁₂

Exact Mass: 827,07



Co(E)(Py)Cl

Chemical Formula: C₄₁H₃₅ClCoN₅O₁₂

Molecular Weight: 884,13

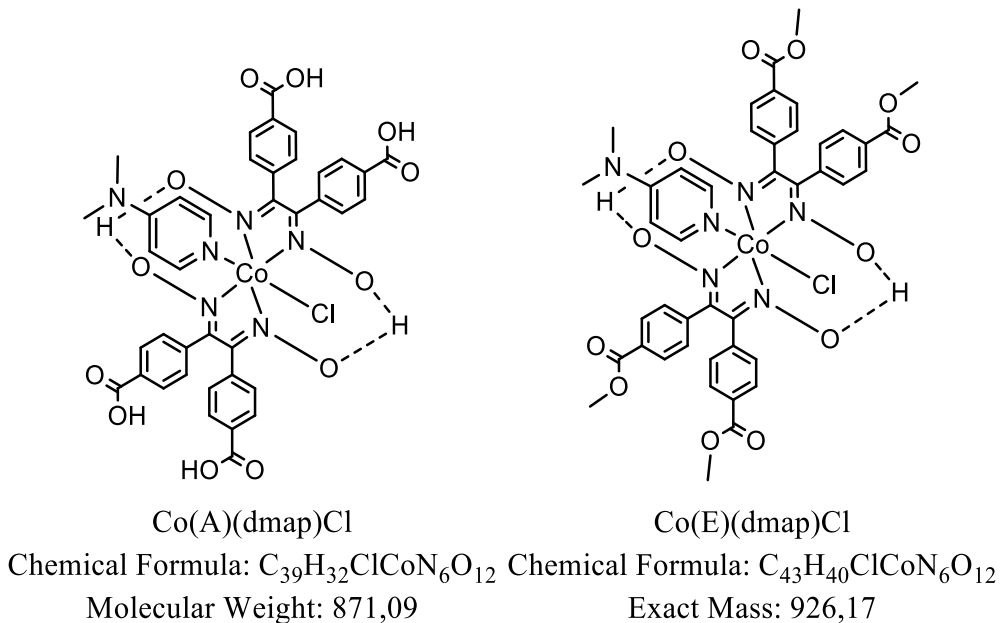


Figure 123. Structure des catalyseurs à base de cobaloxime avec fonctions hydrosolubles intégrés

Finalement, plusieurs catalyseurs à base de porphyrine (dérivé de la chlorophylle α) ont été étudiés.^{10–13} Plusieurs rapportent des fonctions hydrosolubles ainsi que des stabilités à long terme. Pour améliorer cette stabilité, il conviendrait d'étudier le mécanisme de dégradation et de s'inspirer de la structure pour améliorer la stabilité des catalyseurs à base de cobaloxime. Afin de changer des conditions acides perpétuellement proposés dans la littérature, pourquoi ne pas intégrer des fonctions sels, plutôt que des fonctions acides. Cela permettrait d'être compatible avec tous les donneurs d'électrons sacrificiels, ce qui nous donnerait davantage de possibilités. Il est également possible que ces catalyseurs soient actifs en milieu basique ou neutre. Voici donc deux exemples de molécules possibles.

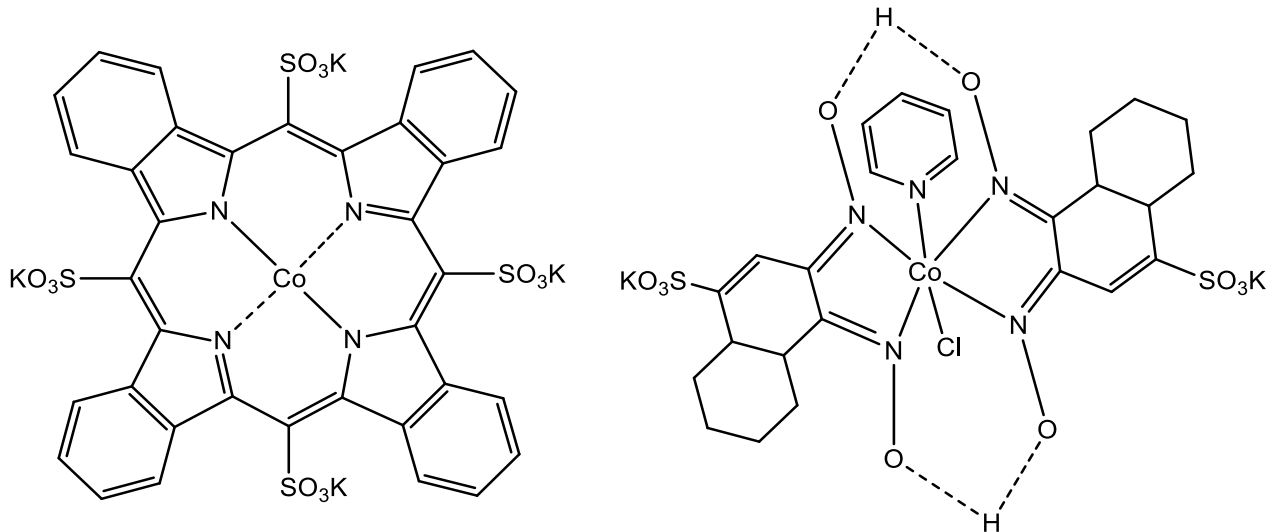


Figure 124. Structure proposée par l'auteur pour de futures expériences

Deux solutions sont envisagées pour améliorer les performances catalytiques des cobaloximes. La première est effectivement d'y intégrer des fonctions telles que le cyclohexyl, le rendant plus stable et plus difficile à dégrader. La seconde serait de le jumeler avec des photosensibilisateurs pour diminuer les niveaux énergétiques et ainsi potentiellement inhiber partiellement les risques de dégradation.

De plus, les structures par assemblages supramoléculaires sont à envisager. Elles permettent d'augmenter grandement les possibilités de structures possibles ainsi que les transferts d'électrons directionnel, ce qui pourrait s'avérer bénéfique dans l'élucidation des mécanismes réactionnels. Notre groupe a effectivement l'expertise pour de tels projets et c'est pourquoi de telles suggestions pourraient être pertinentes.

6.3 Références bibliographiques

- (1) Rousset, E.; Ciofini, I.; Marvaud, V.; Hanan, G. S. Facile One-Pot Synthesis of Ruthenium(II) Quaterpyridine-Based Photosensitizers for Photocatalyzed Hydrogen Production. *Inorg. Chem.* **2017**, *56* (16), 9515–9524. <https://doi.org/10.1021/acs.inorgchem.7b00771>.
- (2) 1,2-NAPHTHOQUINONE-4-SULFONATE, AMMONIUM AND POTASSIUM. *Org. Synth.* **1941**, *21*, 91. <https://doi.org/10.15227/orgsyn.021.0091>.
- (3) 2-HYDROXY-1,4-NAPHTHOQUINONE. *Org. Synth.* **1941**, *21*, 56. <https://doi.org/10.15227/orgsyn.021.0056>.
- (4) Petersen, M. H.; Gevorgyan, S. A.; Krebs, F. C. Thermocleavable Low Band Gap Polymers and Solar Cells Therefrom with Remarkable Stability toward Oxygen. *Macromolecules* **2008**, *41* (23), 8986–8994. <https://doi.org/10.1021/ma801932a>.
- (5) Pan, Y.; Fu, Y.; Liu, S.; Yu, H.; Gao, Y.; Guo, Q.; Yu, S. Studies on Photoinduced H-Atom and Electron Transfer Reactions of o-Naphthoquinones by Laser Flash Photolysis. *J. Phys. Chem. A* **2006**, *110* (23), 7316–7322. <https://doi.org/10.1021/jp055308x>.
- (6) Osadchenko, I. M.; Tomilov, A. P. Phase-Transfer Catalysis in Synthesis of Oximes. *Russian Journal of Applied Chemistry* **2002**, *75* (3), 511–512. <https://doi.org/10.1023/A:1016140131717>.
- (7) Xie, L. S.; Park, S. S.; Chmielewski, M. J.; Liu, H.; Kharod, R. A.; Yang, L.; Campbell, M. G.; Dincă, M. Isoreticular Linker Substitution in Conductive Metal–Organic Frameworks with Through-Space Transport Pathways. *Angewandte Chemie International Edition* **2020**, *59* (44), 19623–19626. <https://doi.org/10.1002/anie.202004697>.
- (8) Pizarro, S.; Gallardo, M.; Gajardo, F.; Delgadillo, A. Electrochemical Reduction of Lindane Using a Cobaloxime Containing Electron-Withdrawing Groups. *Inorganic Chemistry Communications* **2019**, *99*, 164–166. <https://doi.org/10.1016/j.inoche.2018.10.014>.
- (9) Roy, S.; Huang, Z.; Bhunia, A.; Castner, A.; Gupta, A. K.; Zou, X.; Ott, S. Electrocatalytic Hydrogen Evolution from a Cobaloxime-Based Metal–Organic Framework Thin Film. *J Am Chem Soc* **2019**, *141* (40), 15942–15950. <https://doi.org/10.1021/jacs.9b07084>.
- (10) Chen, Z.; Wang, J.; Zhang, S.; Zhang, Y.; Zhang, J.; Li, R.; Peng, T. Porphyrin-Based Conjugated Polymers as Intrinsic Semiconducting Photocatalysts for Robust H₂ Generation under Visible Light. *ACS Appl. Energy Mater.* **2019**, *2* (8), 5665–5676. <https://doi.org/10.1021/acsaem.9b00811>.
- (11) Zhang, X.; Cibian, M.; Call, A.; Yamauchi, K.; Sakai, K. Photochemical CO₂ Reduction Driven by Water-Soluble Copper(I) Photosensitizer with the Catalysis Accelerated by Multi-Electron Chargeable Cobalt Porphyrin. *ACS Catal.* **2019**, *9* (12), 11263–11273. <https://doi.org/10.1021/acscatal.9b04023>.
- (12) Beyene, B. B.; Hung, C.-H. Photocatalytic Hydrogen Evolution from Neutral Aqueous Solution by a Water-Soluble Cobalt(II) Porphyrin. *Sustainable Energy Fuels* **2018**, *2* (9), 2036–2043. <https://doi.org/10.1039/C8SE00253C>.
- (13) Wu, Z.-Y.; Xue, H.; Wang, T.; Guo, Y.; Meng, Y.-S.; Li, X.; Zheng, J.; Brückner, C.; Rao, G.; Britt, R. D.; Zhang, J.-L. Mimicking of Tunichlorin: Deciphering the Importance of a β-Hydroxyl Substituent on Boosting the Hydrogen Evolution Reaction. *ACS Catal.* **2020**, *10* (3), 2177–2188. <https://doi.org/10.1021/acscatal.9b03985>.
